Surface Relief and Bulk Birefringence Gratings in Photo-sensitive Polymer Films

in-situ Probing and Manipulation in Real Time

KUMULATIVE DISSERTATION

zur Erlangung des akademischen Grades
“doctor rerum naturalium”
(Dr. rer. nat.)
in der Wissenschaftsdisziplin Experimentalphysik

eingereicht an der
Mathematisch-Naturwissenschaftlichen Fakultät
Institut für Physik und Astronomie
der Universität Potsdam

von

Dipl.-Phys. Joachim Jelken

Potsdam, den 7. Oktober 2020

Betreuer (Supervisor):
Professor Doctor Svetlana Santer
Faculty of Mathematics & Natural Sciences
Chair of the Experimental Physics
Institute of Physics and Astronomy
Universität Potsdam
Germany

Gutachter (Reviewer):
Privatdozent Doctor Marina Grenzer (Saphiannikova)
Leibniz-Institute of Polymer Research Dresden Germany

Gutachter (Reviewer):
Professor Doctor Arri Priimägi
Faculty of Engineering and Natural Sciences
Chair of the Smart Photonic Materials
Tampere University
Finland

Published online on the
Publication Server of the University of Potsdam:
https://doi.org/10.25932/publishup-48398
https://nbn-resolving.org/urn:nbn:de:kobv:517-opus4-483988

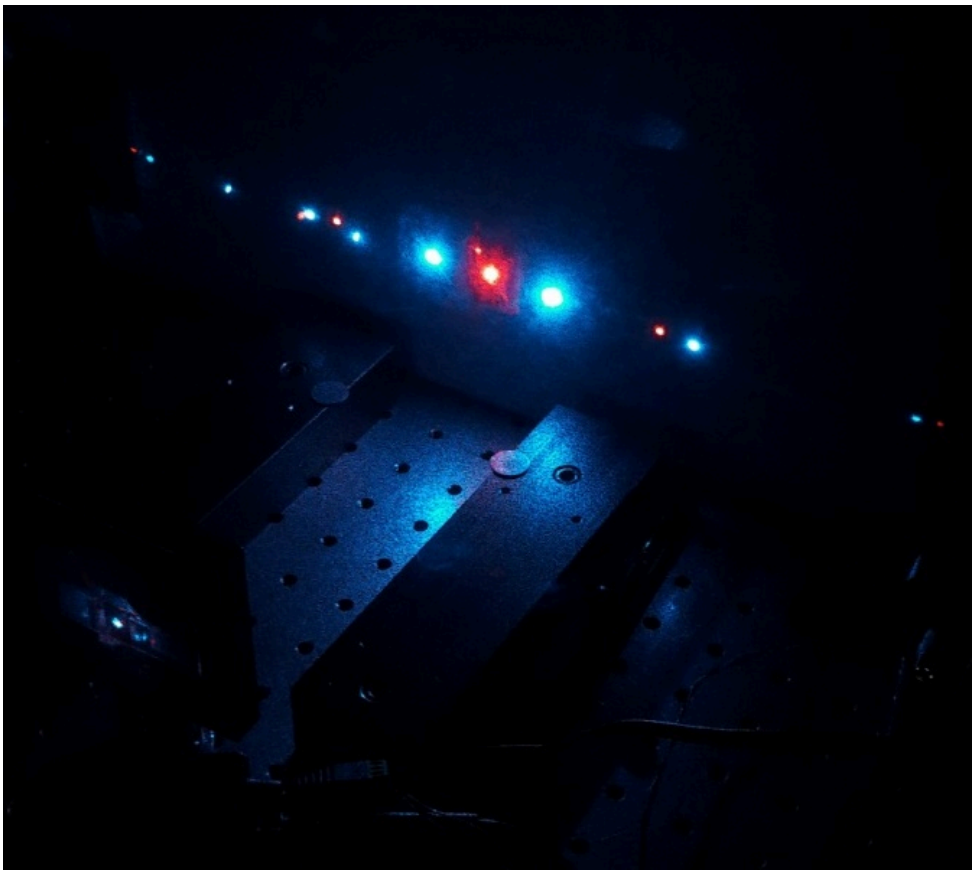

“The man who is swimming against the stream knows the strength of it.”

Woodrow Wilson

Abstract

This thesis is focused on a better understanding of the formation mechanism of bulk birefringence gratings (BBG) and a surface relief gratings (SRG) in photo-sensitive polymer films. A new set-up is developed enabling the *in situ* investigation how the polymer film is being structured during irradiation with modulated light. The new aspect of the equipment is that it combines several techniques such as a diffraction efficiency (DE) set-up, an atomic force microscope (AFM) and an optical set-up for controlled illumination of the sample. This enables the simultaneous acquiring and differentiation of both gratings (BBG and SRG), while changing the irradiation conditions in desired way.

The dissertation is based on five publications (see list of publication on page lxxv). The first publication (I) is focused on the description of the set-up and interpretation of the measured data. A fine structure within the 1st-order diffraction spot is observed, which is a result of the inhomogeneity of the inscribed gratings.

In the second publication (II) the interplay of BBG and SRG in the DE is discussed. It has been found, that, dependent on the polarization of a weak probe beam, the diffraction components of the SRG and BBG either interfere constructively or destructively in the DE, altering the appearance of the intensity distribution within the diffracted spot.

The third (III) and fourth (IV) publications describe the light-induced reconfiguration of surface structures. Special attention is payed to conditions influencing the erasure of topography and bulk gratings. This can be achieved via thermal treatment or illumination of the polymer film. Using the translation of the interference pattern (IP) in a controlled way, the optical erase speed is significantly increased. Additionally, a dynamic reconfigurable surface is generated, which could move surface attached objects, by the continuous translation of the interference pattern during irradiation of the polymer films.

The fifth publication (V) deals with understanding of polymer deformation under irradiation with SP-IP, which is the only IP generating a half-period topography grating (compared to the period of the IP) on the photo-sensitive polymer film. This mechanism is used, e.g. to generate a SRG below the diffraction limit of light. It also represents an easy way of changing the period of the surface grating just by a small change in polarization angle of the interfering beams without adjusting the optical pass of the two beams. Additionally, complex surface gratings formed in mixed polarization- and intensity interference patterns are shown.

Zusammenfassung

In dieser kumulativen Dissertation, basierend auf fünf Publikationen (siehe Publikationsliste auf Seite lxxv), geht es darum ein Verständnis über die grundlegenden Mechanismen zu entwickeln, welche hinter der Entstehung von Oberflächen- und Volumengittern in amorphen photo-sensitiven Polymerfilmen stehen. Hierzu wurde ein neuer Versuchsaufbau entwickelt, welcher *in situ* (d.h. während der Belichtung mit einem Interferenzgitter) Messungen der zeitlichen Entwicklung (Entstehung oder Löschung) von Volumen- als auch Oberflächengittern unabhängig voneinander ermöglicht. Dies stellt einen erheblichen Vorteil gegenüber dem gängigen Verfahren der Beugungseffizienzmessung dar, weil dort die Anteile der beiden Gitter durch aufwendige mathematische Behandlung voneinander getrennt werden müssen. Hierzu wurde ein Rasterkraftmikroskop (AFM, atomic force microscope) in einen optischen Aufbau zur Erzeugung eines Interferenzgitters, welches zur Belichtung des Polymerfilms benutzt wird, integriert. Zusätzlich wurde außerdem die Beugung eines Sondenstrahls an den entstehenden Gittern detektiert.

Die erste Publikation (I) beschäftigt sich mit der grundsätzlichen Interpretation der mit diesem neuen Messaufbau erzielten Ergebnisse. Es wurde eine Feinstruktur in dem räumlichen Profil der ersten Beugungsordnung gemessen, deren Ursprung aus der Inhomogenität der erzeugten Gitter herrührt.

In der zweiten Publikation (II) wird die Kopplung von Oberflächen- und Volumengitter in der aufgezeichneten Beugungseffizienz untersucht. Es wird gezeigt, dass, abhängig von der Polarisation des Sondierungsstrahls, diese Kopplung sowohl konstruktiv als auch destruktiv sein kann, was auch die in der ersten Publikation beschriebene Feinstruktur beeinflusst.

Die dritte (III) und vierte (IV) Publikation beschäftigen sich mit dem dynamischen Umbau von Oberflächenstrukturen. Hierzu muss das erzeugte Oberflächengitter möglichst schnell wieder gelöscht werden können. Dies kann sowohl thermisch, als auch optisch erfolgen. Durch eine definierte Translation des Interferenzgitters konnte hier die optische Löschgeschwindigkeit signifikant gesteigert werden. Zum anderen wird auch die Möglichkeit des Transports oberflächenadsorbierter Objekte durch die Erzeugung einer dynamisch modulierten Oberfläche (mittels einer kontinuierlichen Translation des Interferenz- und dadurch des Oberflächengitters) aufgezeigt. Die Hypothese des Massentransports wird hierbei kritisch untersucht.

Die fünfte Publikation (V) widmet sich dem SP-Interferenzgitter, welches als einziges Gitter eine Periode der Oberflächenstruktur ausbildet, die der Hälfte der Periode des optischen Interferenzgitters entspricht. Diese Eigenschaft kann zum einen für die Erzeugung von Oberflächengittern unterhalb der optischen Auflösungsgrenze benutzt werden, zum anderen erlaubt sie die Periode der Oberflächenstruktur einfach zu ändern, indem die Beleuchtung zu einem anderen Interferenzgitter geschaltet wird. Zusätzlich wird auch die Erzeugung von komplexen Oberflächengittern durch Misch-Interferenzgitter (Mischung aus Polarisations- und Intensitäts-Interferenzgitter) diskutiert.

Table of Contents

Nomenclature

Abbreviations

Eq.	equation
IP	interference pattern
IIP	intensity interference pattern
PIP	polarization interference pattern
AFM	atomic force microscope
DE	diffraction efficiency
SRG	surface relief grating
BBG	bulk birefringence grating
LC	liquid crystal
PAZO	poly{1-4[4-(3-carboxy-4-hydroxyphenylazo)benzenesulfonamido]-1,2-ethanediyl sodium salt}
PDR1	Poly[(methyl methacrylate)-*co*-(Disperse Red 1 acrylate)]
PMMA	Poly(methyl methacrylate)
PDMS	Polydimethylsiloxane
$AzoC_6$	Azobenzene containing cationic surfactant with a spacer of six methylene groups between the positively charged trimethylammonium bromide head group
DSC	differential scanning calorimetry
DMA	dynamic mechanical analysis
SEM	scanning electron microscope
T_g	glass transition temperature
SS	intensity interference pattern, two vertical (0°) polarized pump beams
PP	intensity interference pattern, two horizontal (90°) polarized pump beams
SP	polarization interference pattern, one pump beam vertical (0°) and the second one horizontal (90°) polarized
±45	polarization interference pattern, one pump beam +45° and the second one -45° linearly polarized

RL	polarization interference pattern, one pump beam right-handed circularly and the second one left-handed circularly polarized
P probe	horizontal (90°) polarized probe beam
S probe	vertical (0°) polarized probe beam
RCP probe	right-handed circularly polarized probe beam
LCP probe	left-handed circularly polarized probe beam
$\Lambda/2$-shift	translation of the interference pattern by *half* the grating period
$\Lambda/4$-shift	translation of the interference pattern by a *quarter* of the grating period
irr.	irradiation
DFB	distributed feedback
SLM	spatial light modulator
DMD	digital micromirror device
STED	stimulated emission depletion
av.	average

Symbols

I	intensity
d	film thickness
Λ	grating period of IP
λ_{pump}	wavelength of the pump beam
λ_{probe}	wavelength of the probe beam
S	order parameter
D	photo-induced dichroism
n	refractive index
$n_{\parallel}$	refractive index in the direction of the chromophore orientation (slow axis)
$n_{\perp}$	refractive index in the direction perpendicular to the chromophore orientation (fast axis)
Δn	photo-induced birefringence ($\Delta n = n_{\parallel} - n_{\perp}$)
Δd	SRG amplitude

A	absorbance
$A_{\parallel}$	absorbance probed along the chromophore orientation
$A_{\perp}$	absorbance probed perpendicular to the chromophore orientation
$\vec{E}$, $\boldsymbol{E}$	electric field of the illumination
$J_n(\Delta\phi)$, $J_n(u)$	*n*th-order Bessel function

1. Introduction

In the last two decades considerable progress has been made in the development of smart and functional materials, triggered by an external stimulus and being inspired from the dynamics and behavior of living systems. A change in temperature,[1–4] pH,[5–7] humidity,[8,9] magnetic[10–13] or electric field[14–17] results in a change in material properties such as swelling/deswelling, contraction/expansion, mechanical stiffening or softening, conductivity, color or fluorescence. A perfect candidate for such an external stimulus is light. It can be modulated in terms of wavelength, intensity and polarization permitting non-contact adjustable control over a broad range of parameters. The applications are manifold, ranging from photo-lithography,[18–20] self-healing films,[21–23] micro-swimmers,[24–27] artificial muscles,[28–30] porous membranes[31,32] to optical data storage.[33,34] In many of these approaches, the light couples to certain molecular units of the material, e.g. chromophores that switch their properties under irradiation with light in the visible range. These reversible conformational changes between two or more (meta)stable states can be found in e.g. azobenzene,[35,36] spiropyran,[37–39] stilbene,[40,41] diarylethenes[42–44] etc. The photo-switching of the azobenzene molecule is stable, without side products and can be repeated many times. It converts optical- into mechanical energy and permits the design of artificial intelligence[45,46] or induces macroscopic motion.[47,48] Systems for drug delivery[49–51] or smart surfaces, where the wettability can be controlled by light,[52–54] were presented as well.

The azobenzene molecule absorbs light very strongly and is often used as a dye to color cloth.[55] The irradiation with linearly polarized light results in a photo-orientation of the molecule perpendicular to the polarization of the light after several isomerization cycles. The azobenzene is incorporated into systems via doping into polymer matrices or e.g. covalent bonding in the side-chain of a polymer backbone, which makes the whole polymer photo-sensitive. This results in fascinating properties. The photo-orientation leads to a dichroism[56] and birefringence,[57] which can be used e.g. for optical data storage.[33,58,59] The pixel is set either as isotropic or birefringent. The difference can be optically probed and full isotropy is created after heating above the glass transition temperature. The full volume of the material can be encoded with many layers of 2D data one by one, which is achieved by moving the

optical focal plane through the material.[33,60–62] The attractive feature of photo-sensitive polymer films is that they are easy to process and the supra-molecular structure can be designed for certain specific requirements.

The photo-orientation can also result in a surface patterning when the polymer film is illuminated with an interference pattern (IP, the local light field shows a gradient in intensity or polarization).[63–65] These optically induced surface relief gratings (SRGs) can be used in many ways. For some applications reversibility is not required and the surface structure is permanently fixed due to cross-linking.[32] In other applications, reversibility is required and it is possible to erase the SRG by light illumination[66] or thermal treatment[67] of the polymer film. The relief is formed anew after another exposure to an IP. This is of interest e.g. for biological applications, where the cell seeding/ growth is guided by a surface grating.[68–71] The gratings are used as optical polarizers,[72] couplers for optical devices[73] or create lasers, where the emission wavelength is tunable by changing the grating period.[62,74–77] The SRG can act as a master for replica molding with e.g. PDMS.[78–80] It aligns liquid crystals (LCs) or colloids are arranged in its grooves,[62,81–84] where they might, e.g. form nano-wires.[79,85] These nano-sized wires shrink the size of electronic circuits in electronic devices.

The illumination with a special IP (SP-IP, first pump beam S- and the second P-polarized, polarization interference pattern) generates a local field, that results in a period of the surface structure which is half the period of the IP.[86] This permits to create sub-micrometer structures below the diffraction limit using far-field illumination.[87,88] Azobenzene containing polymer films are sensitive to near-field irradiation which generates even smaller structures.[89] The near-field is structured by, e.g. surface plasmons,[8,90–92] or with a scanning near-field optical microscope.[93]

The exact mechanism behind the SRG inscription is still unclear though several different models were proposed during the years.[94–99] The SRG is stable (after the inscription), indicating an irreversible, plastic deformation of the polymer film. Large photo-induced stresses have to be generated in order to overcome the yield point of the polymer that indicates the transition from elastic to plastic deformation, and to irreversible structure the photo-sensitive film. Photo-induced stresses large enough to crack thin metal layers, which were deposited on the polymer film, were observed during the grating inscription.[100,101] The same experiment was repeated with a graphene layer placed on the polymer film, acting as

a stress gauge, and reveals photo-induced stresses of ~1GPa.[102,103] In another experiment these stresses lead to chain scission.[104,105] Only a few of the proposed models are able to explain such large photo-induced stresses.[106] In addition, a wide variety of material-specific responses has been observed. No model seems to be able to explain the entire zoology of the responses to the IPs, in particular those including polarization gradients. The question if the deformation appears only on the surface or also in the bulk of the polymer film is still unanswered. A survey of these different models and approaches will be presented in the next chapter.

The focus of this dissertation is the generation and analysis of surface structures on azobenzene containing side-chain polymer films. The examination of the different proposed models is helping to develop an understanding of the driving force behind the SRG formation. Usually the formation of the SRG (surface relief grating) and bulk birefringence grating (BBG, orientation grating) is probed by monitoring the diffraction efficiency (DE) of the gratings as a function of time.[107,108] Therefore, a weak probe laser, with a wavelength falling out of the absorption spectrum of the polymer film, is focused on the sample. The diffraction signal contains information about both the BBG and SRG which however can be split up into its components after adopting some approximate models[109,110] or performing a polarization analysis of the diffraction efficiency using a specific probe beam polarization (see **Appendix**).

Taking into account the above discussion, the following questions will be addressed in the present dissertation:

- Understanding optical diffraction data
    - How is the probe geometry influencing the diffraction efficiency? What phenomena arise in the case of a spatially inhomogeneous BBG and SRG (amplitude variation)? Does the size and spatial profile of the probe beam (Gaussian beam profile) matter?
    - How do SRG and BBG contribute to the total diffraction efficiency? How do they depend on the polarization of the probe beam and the interference pattern?

- Disentangling surface relief and bulk birefringence grating
    - How is the SRG formed? Is there first a bulk orientation leading to mechanical stresses and a deformation which finally results in the SRG formation? Is there a way to disentangle the kinetics of these two gratings in the optical data?
    - How is the assignment of the local optical polarization of the writing field to the SRG and BBG for different interference patterns, especially for polarization interference patterns? Is it consistent with the picture of molecular migration along the field polarization?[98,111]
- Reversing the surface grating growth
    - How to erase an inscribed grating? What is the difference between the methods? How to increase the erase speed?
    - Is there a protocol for the complete and fast optical erasure of the SRG and BBG? Can the SRG get selectively erased, so that only the BBG remains?
    - How to design a dynamically reconfigurable surface and what would be the application?
- Complex surface gratings in mixed polarization- and intensity interference patterns
    - The illumination with a SP interference pattern (polarization interference pattern) inscribes a surface grating with a period which is half the period of the IP. Why it is like that and what is the difference to the ±45-IP (polarization interference pattern whose electric field is just rotated by 45° relative to the SP pattern) where the SRG forms with the normal period? Is there a correlation to the local polarization of the writing field?
    - What kind of surface gratings will be formed by using mixed interference patterns made of polarization- and intensity interference pattern? How does a gradient in intensity and polarization influence the SRG formation? What information may this reveal about the driving force of the SRG inscription?

In order to address these questions, a new set-up is developed that combines SRG writing and analysis. It consists of three parts: a two-beam interference set-up for topographic structuring, an atomic force microscope (AFM) for *in situ* monitoring (during irradiation) of the surface morphology and a diffraction efficiency (DE) set-up which enables to obtain

information about the bulk birefringence grating at the same time. This permits the direct measurement of the SRG and BBG inscription and simplifies the interpretation of the DE.

The overall aim is to further understand the process of SRG formation on azobenzene containing polymer films by analyzing the kinetics of topographic changes and of changes in optical properties. Here, of special interest is the formation of a birefringence grating in the bulk. Final goal is the practical use of the findings of this thesis.

The dissertation is based on five publications, in which the raised problems will be explored (see **list of publications** on page lxxv). Briefly, the first (I) and second (II) publication deal with the understanding of the diffraction efficiency recorded with the new designed set-up in the case of a ±45-IP (one pump beam +45° and the second -45° polarized, polarization interference pattern). A fine structure in the 1st-order diffraction spot is theoretically predicted and experimentally observed. The second publication is showing how this fine structure depends on the polarization of the probe. The theoretical model is extended, explaining the separate contribution of BBG and SRG to the total DE. Additionally, the model permits to assign the local polarization of the IP to the SRG and BBG, which is recovering conclusions of earlier experiments. From the assignment information about the driving force behind the SRG formation are obtained.
The third (III) and fourth (IV) publication are dedicated to the erasure of the SRG and BBG, which are created by the illumination with the RL-IP (one pump beam right- and the second left-handed circularly polarized, polarization interference pattern). Here, a protocol for a selective and fast optical erasure of the SRG and BBG, based on the translation of the IP, is presented. This technique also reveals the different kinetics for the two gratings (the chromophore orientation responsible for the BBG reacts faster than the SRG). By combining with the knowledge of publication II, the assignment of the relative position of IP, BBG and SRG in the RL configuration could be clarified. It is possible to create a dynamic reconfigurable surface using the IP translation technique which could permit e.g. the transport of surface attached objects along the surface.

In the last paper (V) the response to an SP-IP is analyzed. The appearance of the half-period SRG is explained and the influence of gradients in intensity and polarization (mixed IP) is discussed.

The dissertation is organized as follows. Chapter 2 gives an overview about the azobenzene molecule itself and the properties of azobenzene containing polymer films as well as the basic concepts of SRG formation and analysis. Summaries of publications, composing this cumulative dissertation, are presented in chapter 3. The reprints of the published papers (main text and supplementary materials) constitute chapter 4. Chapter 5 provides a discussion of the obtained results and draws conclusions. In the Appendix, additional results which complement the findings of the presented publications are shown.

2. Basics and theoretical concepts

2.1. Azobenzene

The azobenzene molecule consists of two phenyl rings which are linked by an azo-bond (N=N, nitrogen double bond). It can be reversible isomerized by light absorption between the thermally stable *trans* (E) configuration and the metastable *cis* (Z) form. Using light within the *trans* absorption band (e.g. UV light) switches the dye from *trans* to *cis* configuration. The back-conversion is caused either by the absorption of a photon which wavelength falls into the *cis* absorption band (e.g. visible light) or by thermal relaxation.

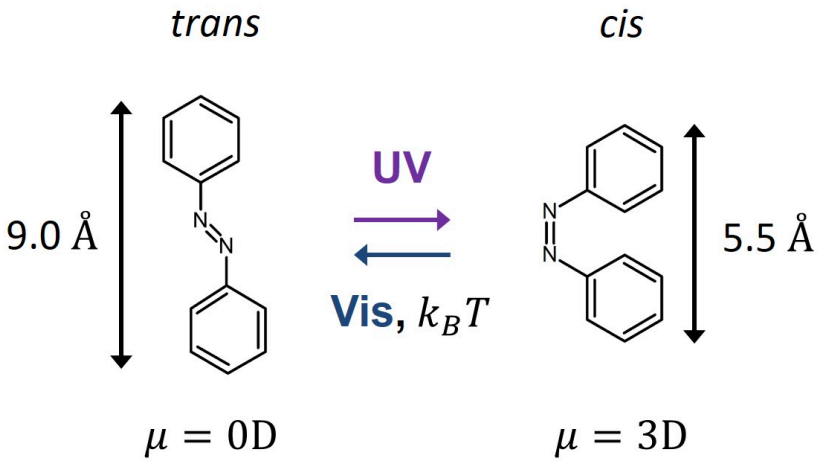

Figure 2.1. Molecular photo-dynamics of azobenzene with the structural conformation of the two isomers of azobenzene. The illumination with ultraviolet (UV) light changes from *trans* to *cis* conformation, while the relaxation into *trans* state happens via irradiation with visible light or is thermal driven.

The two isomers have different shape, molecular length and dipole moments. The *trans* azobenzene is planar and in the *cis* configuration the phenyl rings are twisted by 90° relative to the C-N=N-C plane.[112] The distance between the 4 and 4' position reduces from 0.9nm in the *trans* form to 0.55nm in the *cis* configuration due to the photo-isomerization.[113] The geometrical change results also in an increase of the dipole moment from $|\vec{\mu}| = 0$ in the *trans* state to $|\vec{\mu}| = 3.1$D in the *cis* form.[114]

The electronic absorption spectrum of the *trans* form shows a strong ππ* absorption and a much lower intensity of the nπ* band (see **Figure 2.2**). In the *cis* absorption spectrum the ππ* transition is blue shifted and much weaker while the nπ* transition is slightly red shifted and more pronounced than in the *trans* form.

The *trans* isomer of the azobenzene molecule corresponds to lower energy minimum indicating that this form is more stable and that most of the molecules are in *trans* form in dark. The photo-isomerization reaction usually requires several picoseconds while the thermal back-relaxation is slower.[115–117] In the latter case the time scale depends on the substitution of the phenyl rings and local environment. Typical relaxation times ranging from milliseconds to hours.[118] The energy barrier at room temperature for the thermal back-relaxation (*cis*-to-*trans*) is about 90 kJ/mol.[35,119]

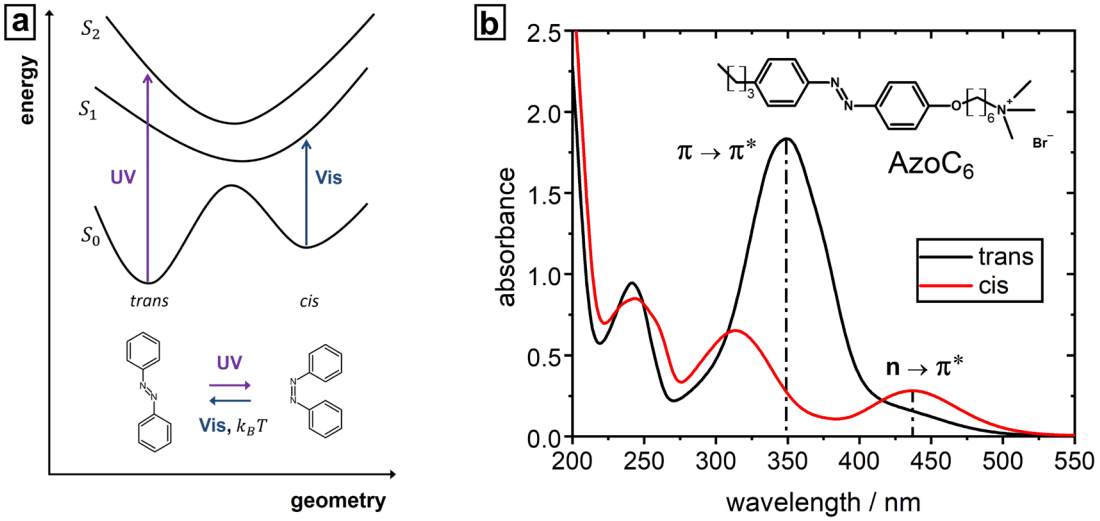

Figure 2.2. (a) Schematic view on the lowest singlet potential energy of azobenzene, namely S_0, S_1 and S_2. The *trans* and *cis* isomers are shown together with excitations usually employed for isomerizations (illumination with ultraviolet (UV) light of the *trans* isomer and visible (Vis) light of the *cis* isomer). (b) Typical absorption spectrum of a azobenzene containing surfactant ($AzoC_6$, chemical structure shown in the inset). The black curve is showing the initial state (dark, all *trans*) and the red curve the photo-stationary state after applying UV light (9% *trans*). The ππ* and nπ* transitions are indicated.

An ensemble of azobenzene molecules reaches a photo-stationary state upon irradiation with a steady state *trans-cis* composition. The photo-stationary state is defined by the competing effects of photo-isomerization to *cis* state, a thermal back-relaxation into *trans* state and a light induced *cis* reconversion. The steady-state *trans-cis* ratio is unique for each system and depends on e.g. the illumination intensity, wavelength, temperature and matrix (e.g. solution, polymer matrix etc.).[35] The absorption spectrum is changing during illumination because it is a composition of *trans* and *cis* spectra. Analyzing the temporal change can give the *cis* fraction in steady state (assuming that all molecules are in *trans* form in dark).[35]

The electronic absorption spectra of *trans* and *cis* can be tuned by ring substitution.[120–122] The substitution with electron-donating and electron-withdrawing groups results in a strong asymmetric electron distribution. This "push-pull" configuration affects the *trans* and *cis* absorption spectra and for a certain substitution the absorption spectra of these two isomers overlap. Then, a single wavelength excites the forward and reverse reaction resulting in a continuous *trans-cis-trans* photo-isomerization with a mixed photo-stationary state.[57,123,124]

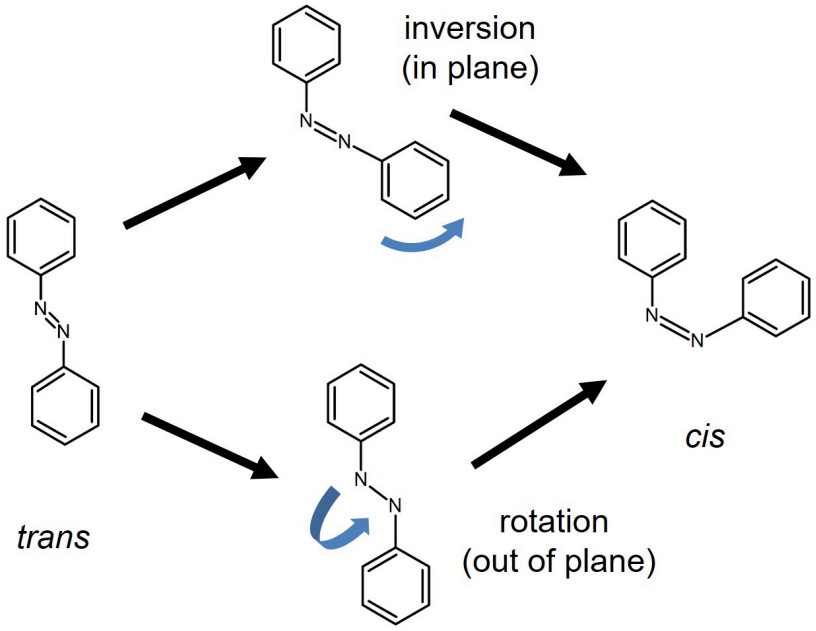

Figure 2.3. Isomerization of azobenzene from *trans* to *cis* state via inversion or rotation. The rotation mechanism involves the rupture of the N=N double bond to a N-N single bond and free rotation of the single bond. The inversion mechanism involves a transition state, such that the N=N-C angle is 180° and there is a sp-hybridization of the nitrogen atom.

Two pathways of the photo-isomerization have been found. It can take place through rotation around the N-N single bond, with a rupture of the double bond (π bond), or through inversion, where the π bond remains intact (see **Figure 2.3**).[125] The thermal back-relaxation appears via rotation.[126] The volume requirement of the inversion mechanism is much smaller than of the rotation mechanism and explains why isomerization can take place even in rigid matrices.

2.2. Azobenzene containing polymers

The azobenzene molecules are incorporated into amorphous,[58] crystalline[127] or liquid crystalline[128,129] (LC) polymeric systems via doping into a polymer matrix or e.g. covalent bonding to the polymer.[130,131] In the doped system the azobenzene concentration is controlled up to a certain limit via the dopant concentration. Increasing the concentration further results in a phase separation. Higher azobenzene concentrations in the system are achieved e.g. via covalent bonding of the chromophore to the polymer. Here, the azobenzene is either attached as side-chain or incorporated in the backbone of the polymer.[132] A polymer film is prepared via spin coating,[133] Langmuir-Blodgett technique[134] or self-assembling monolayers.[135] The annealing above the glass transition temperature of the polymer removes any incorporated solvent and anisotropy.

2.3. Photo-orientation

The irradiation of the azobenzene chromophores with linearly polarized light results in a photo-orientation of the chromophores perpendicular to the polarization of the light.[136,137] This is a statistically driven process as a result of the cyclic photo-isomerization of the azobenzene chromophores. The photo-sensitive dye switches from *trans* to *cis* configuration once it is absorbing the light. The back-relaxation into the *trans* form occurs in a new random direction. The azobenzene-unit absorbs light polarized along the long axis (transition dipole axis). Chromophores oriented perpendicular to the polarization of the light are not absorbing.[138] The consequence is a depletion of the chromophores aligned along the light polarization and a photo-orientation of the azobenzene-unit perpendicular to the light

polarization with time. The re-orientation is not completed after one isomerization cycle, indeed several cycles are required. The result of the photo-orientation is a strong anisotropy in the absorbance (dichroism)[56,139,140] and refractive index (photo-induced birefringence).[141–143]

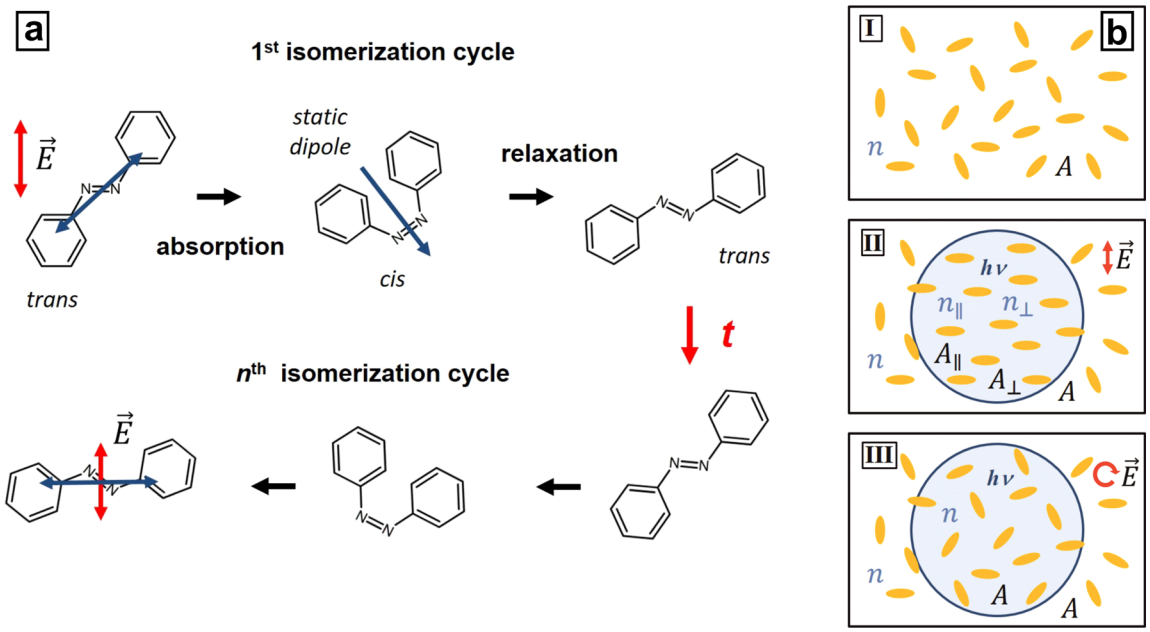

Figure 2.4. (a) Photo-isomerization from *trans* to *cis* form of azobenzene upon irradiation with linearly polarized light. The chromophores, which are not perpendicular aligned to the linear polarization, are absorbing the light. The relaxation back into the *trans* form results in a different orientation of the molecule. The cyclic *trans-cis-trans* photo-isomerization aligns the azobenzene perpendicular to the polarization of the light after several isomerization cycles. (b) Schematic representation of the photo-orientation in an amorphous azobenzene containing polymer film. The chromophores (yellow rods) are initially randomly oriented (I, isotropic state). The homogeneous illumination with linearly polarized light aligns the azobenzene chromophores perpendicular to the polarization of the light, so that they are not absorbing anymore (II). This results in a photo-induced anisotropy with different refractive index n and absorbance A parallel ($A_{\parallel}$, $n_{\parallel}$) and perpendicular ($A_{\perp}$, $n_{\perp}$) to the chromophore orientation. An isotropic state in the plane parallel to the film surface is achieved after exposure to circularly polarized light (III).

The photo-induced orientation is reversible and can be modified by changing the polarization angle or even erased using circularly polarized light which again creates a random chromophore orientation in the plane parallel to the film surface.[144] The latter case also aligns a certain amount of chromophores in the plane perpendicular to the film surface (direction of light propagation) which results in an anisotropy.[145,146]

The photo-induced anisotropy is probed by measuring polarization sensitive absorbance spectra. Therefore, the illumination with a linearly polarized pump beam, with a wavelength falling into the absorption band of the sample, is generating an anisotropy due to the photo-orientation. Afterwards, the absorbance is probed in two directions (parallel and perpendicular to the pump beam polarization (chromophore orientation), respectively) using a weak linearly polarized probe beam, with a wavelength falling into the absorbance range of the polymer film (usually with a wavelength corresponding to the absorption maximum of the polymer film). The chromophores align perpendicular to the polarization of the pump beam so that they are not absorbing anymore. This results in a drop in the absorbance of the probe beam polarized perpendicular to the molecule orientation and in an increase of absorbance when the light is polarized in the same direction as the long axis of the dye (see **Figure 2.5a**). Initially the chromophores are randomly oriented so that no difference in the absorbance of the probe beam is measured. After the generation of the anisotropy the absorption spectrum splits. The irradiation of the polymer film with the pump beam only for a short time and probing the absorbance afterwards permits to determine the kinetics of the photo-orientation.

The irradiation with a circularly polarized pump beam is not generating a dichroism in the plane parallel to the surface but a certain amount of chromophores orient in the plane of the incident light. Surprisingly, some polymers do not show a symmetric splitting of the absorbance, only after previous exposure to circularly polarized light (see **Appendix, Figure A.1**). This might be explained by an increased orientation in the plane of the incident light. The strength of the photo-induced dichroism (D) is calculated from the absorption coefficient for parallel ($A_{\parallel}$) and perpendicular ($A_{\perp}$) to the molecular axis polarized light:[56]

$$D = \frac{A_{\parallel} - A_{\perp}}{A_{\parallel} + A_{\perp}} \tag{2.1}$$

The macroscopic order parameter S varies typically between 0 for samples with isotropic and 1 for samples with anisotropic orientation and is defined by:[147]

$$S = \frac{A_{\parallel} - A_{\perp}}{A_{\parallel} + 2A_{\perp}} \tag{2.2}$$

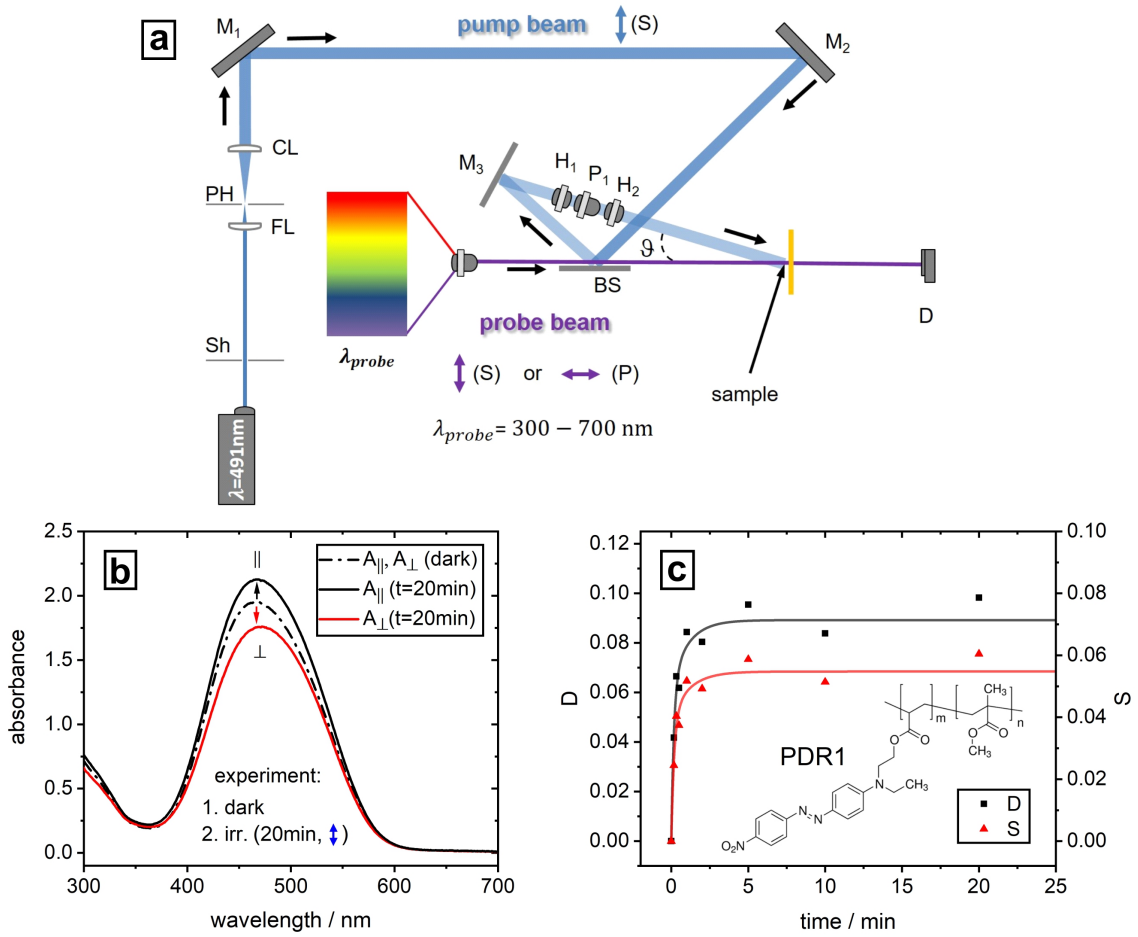

Figure 2.5. (a) Schematic representation of the experimental set-up for probing the photo-induced dichroism. The pump beam (S(0°)-polarized) is absorbed by the polymer film and generates an anisotropy due to the photo-orientation (chromophore orientation perpendicular to the polarization of the pump beam). The probe beam, with a wavelength falling into the absorption band of the polymer film, is measuring the absorbance perpendicular ($A_\perp$, S-polarized probe beam) and parallel ($A_\parallel$, P-polarized probe beam) to the chromophore orientation. (b) Photo-induced splitting of the PDR1 absorption spectrum after 20min of irradiation with linearly polarized light ($d = 600\text{nm}$, $\lambda_{\text{pump}} = 457\text{nm}$, $I = 100\text{mW/cm}^2$). (c) Dynamics of the photo-induced dichroism (D) and order parameter (S). The fitting is performed with a single exponential function ($\tau = 18\text{s}$). The inset is showing the structure of the PDR1. (Sh = shutter, M = mirror, D = detector, P = polarizer, H = half-wave-plate, BS = beam splitter, CL = collimating lens, FL = focusing lens, PH = pin hole)

Another technique to probe the generated anisotropy is to measure the photo-induced birefringence (Δn), defined by the difference ($\Delta n = n_\parallel - n_\perp$) of the refractive indices for a parallel ($n_\parallel$) or perpendicular ($n_\perp$) to the chromophore orientation (long axis) polarized

probe beam. The refractive index probed along the chromophore long axis is larger ($n_{\parallel}$, *slow* axis) compared to that along the perpendicular direction ($n_{\perp}$, *fast* axis).

The probe beam should not disturb the chromophore orientation. Therefore, a weak and linearly polarized laser beam (S-polarized (0°)), with a wavelength falling outside of the absorption band of the polymer, is focused on the film. The pump beam (+45° linearly polarized) aligns the chromophores in -45° direction. Due to the photo-induced anisotropy a phase shift of π between the components of the probe beam traveling along the *fast*- (lower refractive index, $n_{\perp}$) and *slow*-axis (higher refractive index, $n_{\parallel}$) exists. This rotates the polarization of the probe beam so that the transmitted light is P-polarized which is analyzed by adding a polarizer in 90° (P-polarization) orientation afterwards. The light which passes this cross-polarized configuration is detected with a photodiode. The increase of this signal with time yields directly the kinetics of the photo-orientation process and provides an absolute value for the induced birefringence (see **Figure 2.7**).

Assuming S-polarization, the electric field vector of the incident probe beam has the form:

$$\boldsymbol{E}_{in} = \begin{pmatrix} E_{in,x} \\ E_{in,y} \end{pmatrix} = \begin{pmatrix} 0 \\ E_0 \end{pmatrix}. \tag{2.3}$$

The *fast* axis of the material is oriented in $\hat{f}$ and the *slow* axis in $\hat{s}$ direction (chromophore orientation, see **Figure 2.6**). Then, the projection of the illuminating field on the *fast* and *slow* axis is expressed as:

$$\boldsymbol{E}_{in} = E_{in,f}\hat{f} + E_{in,s}\hat{s} = E_0(\hat{f}\sin\alpha + \hat{s}\cos\alpha). \tag{2.4}$$

Thereby, α is the angle between the *slow* axis and the S-polarized light. Both components are real in the case of linearly polarized light. The transmitted electric field is calculated by adding a phase shift

$$\boldsymbol{E}_{out} = E_{out,f}\hat{f} + E_{out,s}\hat{s} = E_{in,f}e^{i\frac{2\pi}{\lambda}n_f d}\hat{f} + E_{in,s}e^{i\frac{2\pi}{\lambda}n_s d}\hat{s}. \tag{2.5}$$

Here, d is the polymer film thickness and n_f (n_s) the refractive index along the *fast* (*slow*) axis, respectively. The cross-polarized component (projection of this field on the x-axis, P-polarization) is given by:

$$E_{out,x} = E_{out,f}\cos(\alpha) - E_{out,s}\cos(90° - \alpha) \tag{2.6}$$

Assuming an angle of $\alpha = 45°$ between the light polarization and the chromophore orientation the equation is simplified to the following:

$$E_{out,x} = \tfrac{1}{2}E_0 e^{i\frac{2\pi}{\lambda}n_f d} - \tfrac{1}{2}E_0 e^{i\frac{2\pi}{\lambda}n_s d}. \tag{2.7}$$

The refractive index along the *fast* axis is defined as $n_f = n_0 - \frac{\Delta n}{2}$ and along the *slow* axis as $n_s = n_0 + \frac{\Delta n}{2}$. Thereby, n_0 is the effective refractive index and the difference $\Delta n = n_s - n_f > 0$ is called the birefringence. Now, **Eq. 2.7** is expressed as

$$E_{out,x} = -\tfrac{1}{2}E_0 e^{i\frac{2\pi}{\lambda}n_0 d}\left(-e^{-i\frac{\pi}{\lambda}\Delta n d} + e^{+i\frac{\pi}{\lambda}\Delta n d}\right) = -iE_0 e^{i\frac{2\pi}{\lambda}n_0 d}\sin\left(\frac{\pi}{\lambda}\Delta n d\right). \tag{2.8}$$

Therefore, the intensity is:[148]

$$I = |E_x^2| = I_0 \sin^2\left(\frac{\pi\Delta n d}{\lambda}\right) \tag{2.9}$$

where I_0 is the intensity of the incident probe beam, λ its wavelength and d the film thickness.

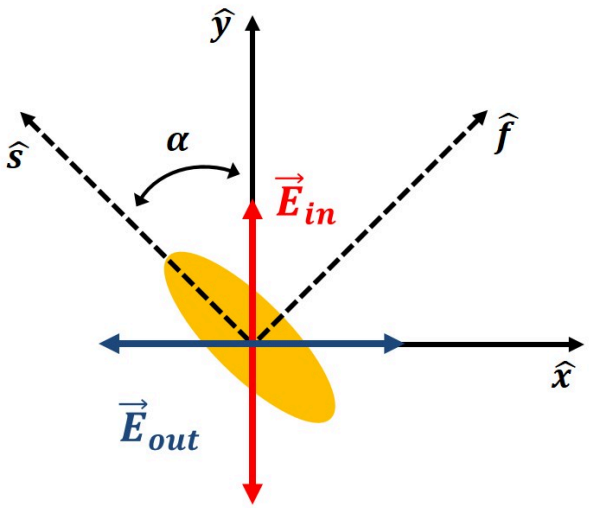

Figure 2.6. Sketch of the chromophore orientation (yellow rod) and the incident probe beam (red vector). The photo-induced anisotropy generates a *fast*-axis $\hat{f}$ and *slow*-axis $\hat{s}$. To probe the birefringence, the transmitted light is measured along a 90° rotated polarization direction (blue vector).

Amorphous polymers with a high glass transition temperature (T_g) show a good stability of the photo-induced orientation.[149] The anisotropy is erased after heating above T_g.[150] A short spacer between the chromophore and the polymer backbone decreases the birefringence due to hindered motion of the side-chain.[128,151]

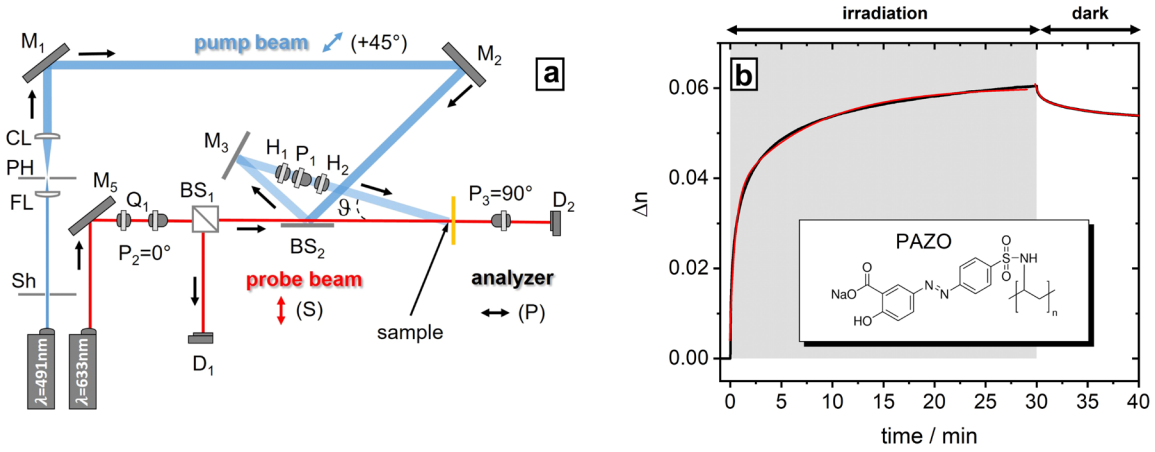

Figure 2.7. (a) Schematic representation of the experimental set-up for probing the photo-induced birefringence. The +45°-polarized pump beam ($\lambda_{\mathrm{pump}} = 491\mathrm{nm}$, $I = 100\mathrm{mW/cm^2}$) is absorbed by the polymer film and generates an anisotropy due to the photo-orientation (chromophore orientation perpendicular to the polarization of the pump beam). The S(0°)-polarized probe beam ($\lambda_{\mathrm{probe}} = 633\mathrm{nm}$) is not absorbed by the polymer film. An angle of 45° is formed between its polarization and the induced anisotropy, which rotates the polarization by 90° (due to the photo-induce birefringence) probed with a polarizer in P(90°)-orientation. (b) Photo-induced birefringence of a PAZO film ($d = 1\mu\mathrm{m}$). The fitting is performed with a double exponential function: $\tau_1 = 30\mathrm{s}$, $\tau_2 = 464\mathrm{s}$ (illumination), $\tau_1 = 295\mathrm{s}$, $\tau_2 = 24\mathrm{s}$ (dark). (Sh = shutter, M = mirror, D = detector, P = polarizer, H = half-wave-plate, Q = quarter-wave-plate, BS = beam splitter, CL = collimating lens, FL = focusing lens, PH = pin hole)

2.4. Surface relief and bulk birefringence gratings

It is now more than 20 years back that the surface relief grating (SRG) formation on photo-sensitive polymer films was discovered.[63] Here, the film is irradiated with a spatially varying light pattern, usually generated by the interference of two coherent beams. The period of the interference pattern (Λ) is defined by the angle between the two interfering beams (2ϑ) and given by

$$\Lambda = \frac{\lambda}{2\sin\vartheta} \tag{2.10}$$

where λ is the wavelength of the pump beam.

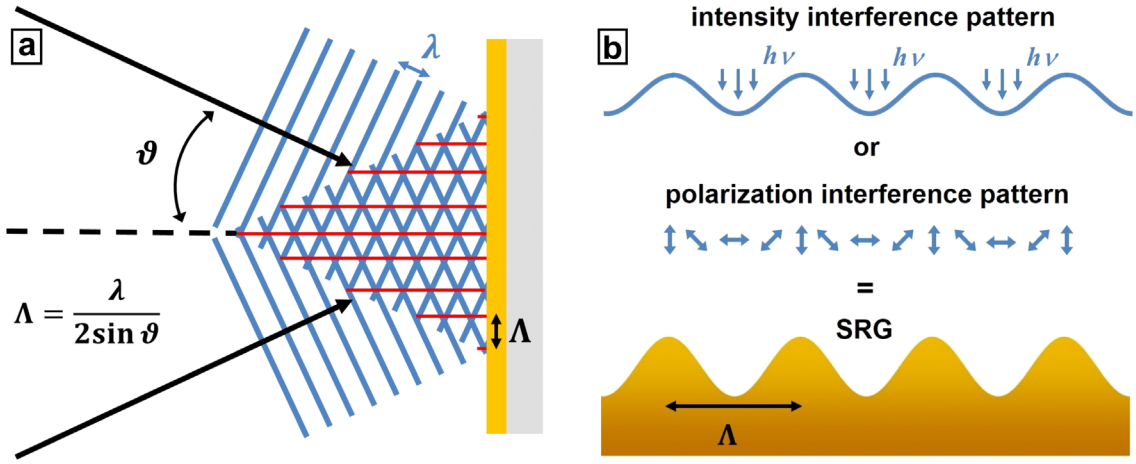

Figure 2.8. (a) The interference of two coherent laser beams results in an intensity- or polarization interference pattern dependent on the polarization of each of the interfering beams. (b) A gradient in intensity or polarization creates a surface grating.

These days spatial light modulators[152,153] or scanning stages[154] are also used in order to generate the light pattern. The sinusoidal intensity modulation creates a sinusoidal surface grating on the polymer film with a peak-to-valley amplitude of several hundred nanometers (dependent on the illumination parameters) and a large period in the micrometer range (controlled by the period of the IP). This indicates a mesoscopic deformation of the polymer film. The process appears at room temperature (well below the glass transition temperature T_g) and using comparable low irradiation intensities ($I = 200\text{mW/cm}^2$) for minutes to

hours. The SRG formation is only observed in glassy systems while the photo-orientation is reported for viscous solution,[155,156] liquid crystals,[56,157] and glassy polymers.[158] The molecular weight of the polymer also has to fall within a certain range. No SRG formation is observed using small azobenzene containing molecules[57] and only a poor grating is inscribed when the weight is "too" high.[64] In the latter case entanglements of the polymers chains might hinder the grating formation. The substitution of the phenyl-rings of the azobenzene chromophores slows down the SRG formation kinetics.[159,160] This shows the importance of the environment on the SRG inscription because the reduced kinetic is attributed to a larger volume requirement of the chromophore. Additionally, in guest-host systems made of a polymer matrix and small azobenzene containing molecules the SRG formation is usually week compared to azobenzene side-chain polymers. This is associated with the lower azobenzene concentration in these system and on the other hand with a poor translational motion.[161,162]

The above mentioned experimental facts lead to the "orientation" model[163,164] which describes the SRG formation in azobenzene containing side-chain polymer films. Here, the SRG generation is explained as a multi-step process which occurs on different time- and length-scales. The irradiation with the interference pattern isomerizes the azobenzene-chromophores in the bright areas from *trans*- to *cis* form (on a time scale < 1s). This corresponds with a conformational change on angstrom scale. A *cis-trans* grating[107] (so called "chemical" grating) is formed due to a different photo-stationary state in the bright and dark areas. The grating will fade when the illumination is switched off because of the relaxation of the chromophores into the *trans* state. Further illumination photo-aligns the azobenzene-chromophores in the side-chain of the polymer film in the bright areas of the IP perpendicular to the polarization of the light. This process results in the formation of a bulk birefringence grating (BBG, second grating).[107,165] The photo-orientation appears in the ~nm range and in the timescale of ~s. Here, the refractive index is spatially changing according to the orientation of the azobenzene-units and the light polarization. The photo-orientation of the azobenzene-chromophores is effecting the orientational order of the polymer backbone (azobenzene functionalized polymers) or results in a deformation of the polymer matrix in a doped-system (guest-host system). This is the origin of macroscopic (in the range of micrometer) deformation of the polymer film which finally results in the formation of the surface relief grating[80,107] (third grating) within minutes to hours. At the same time also a

density grating[107,166,167] (fourth grating) is forming. It appears that the photo-orientation and deformation of the polymer film leads to the formation of LC seeding aggregates acting as a kind of nucleation centers for a subsequent slow ordering process. It was found that they are growing into larger-scale density variations during thermal treatment of the SRG. The density grating is only accessible with X-ray diffraction technique.[168] In contrast the SRG can be optically probed by visible light diffraction[165] or directly measured with an AFM.[169] It was found that a cyclic *trans* to *cis* isomerization is required for an effective SRG formation.[57,123]

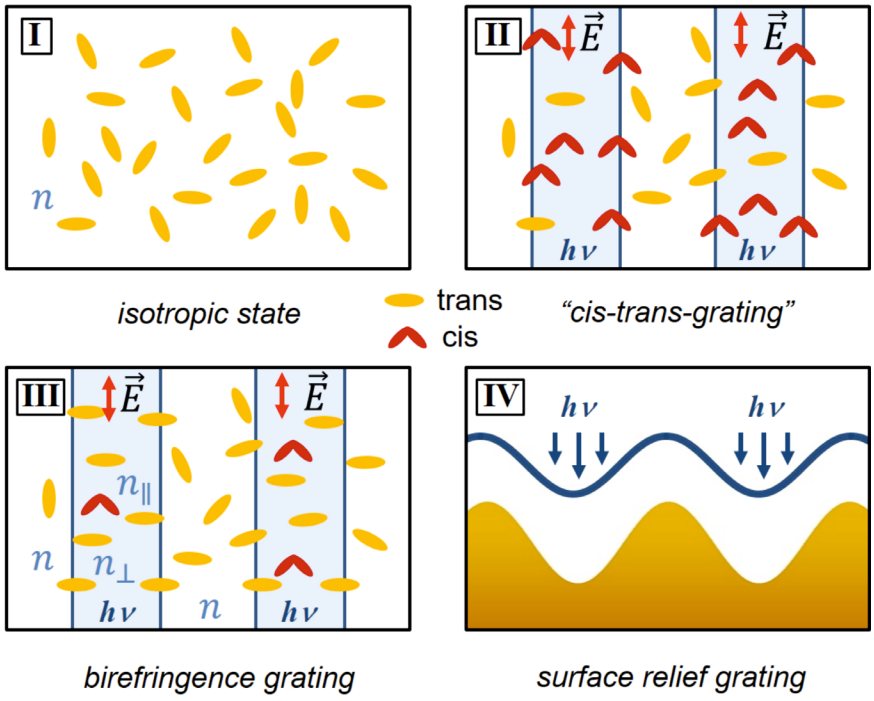

Figure 2.9. The three steps of SRG formation in case of irradiation with an intensity interference pattern. The azobenzene-chromophores (yellow rods) are initially randomly oriented (I). The holographic exposure excites the chromophores (from *trans* to *cis*) in the bright areas which are not aligned perpendicular to the polarization of the light. A "chemical" grating is formed due to a different photo-stationary state in the bright and dark areas (II). The cyclic *trans-cis-trans* photo-isomerization aligns the azobenzene-chromophores perpendicular to the polarization of the light. In this orientation they are not absorbing the light. The photo-orientation results in a spatially modulation of the refractive index, the "birefringence grating" (III), and strong mechanical stresses are generated. These stresses are the origin of a macroscopic deformation of the polymer film forming the surface relief grating (IV).

Interestingly, azobenzene containing polymer films respond not only to a gradient in light intensity, also a gradient in polarization creates a SRG.[87,88,170] Additionally, near-field illumination is also used to create structures within the polymer film below the diffraction limit of light.[89] The near-field is structured by, e.g. surface plasmons,[8,90–92] or with a scanning near-field optical microscope.[93]

The surface gratings are stable in time but the deformation can be reversed. Heating above the glass transition temperature of the polymer or the irradiation with circularly polarized light creates a flat surface again and the grating can be optically rewritten.[66,150,171] The SRG is very stable in polymers having no glass transition temperature.[149] Surprisingly, it is found that for some LC systems the grating amplitude is increasing upon thermal treatment of the film (after illumination with the IP).[172] This might indicate that the heat enables the motion and aggregation of the chromophores.

The assignment of the IP to the SRG and BBG is an important parameter in order to develop an understanding about the grating formation in photo-sensitive polymer films. Here, some polymers show a deformation away from the bright areas and for other polymers this behavior is inverted.[173] Usually the response of the polymer film on light is probed by the irradiation through a mask. A dent in the film (probe with an atomic force microscope after the illumination) indicates a deformation away from the light intensity while a hill shows the opposite behavior. It is found that in LC systems the phase behavior is inverted (alignment along the light polarization) in comparison with amorphous polymers (alignment perpendicular to light polarization).[174–176] Also high intensity illumination (>300mW/cm^2) is inverting the phase behavior (direction of deformation towards light intensity) in amorphous polymers.[177] But the individual response is material-specific so that no general rule is formulated.

A deformation is not only generated through the illumination with an IP. Single beam exposure with linear polarization can also create an elongated trench.[65,178–180] The SRG inscription does only depend on the energy dose, independent if this dose is provided on a short or long time.[181] This rule does not apply for very high or low intensities and short interrupted illumination. It was found that for very short illumination ($< 2s$) no permanent grating is formed, even after repeated exposure.[182] This indicates an elastic deformation in addition to a plastic flow.

Different types of interference patterns

Dependent on the polarization of each of the two interfering beams in the holographic set-up several different combinations are possible. The electric fields, $\boldsymbol{E}_1(\boldsymbol{r})$ and $\boldsymbol{E}_2(\boldsymbol{r})$, of the two plane waves corresponding to these two laser beams are given by

$$\boldsymbol{E}_1(\mathbf{r}) = \boldsymbol{E}_{01} \exp(ik_{1x}x + ik_{1z}z) \tag{2.11}$$

$$\boldsymbol{E}_2(\mathbf{r}) = \boldsymbol{E}_{02} \exp(ik_{2x}x + ik_{2z}z) \tag{2.12}$$

where k_{1i} and k_{2i} $(i = x, z)$ are the corresponding components of the wave vectors in x and z direction, $\boldsymbol{r}$ is the position vector in the overlapping space, $\boldsymbol{E}_{01}$ and $\boldsymbol{E}_{02}$ are the electric field amplitudes. At the overlapping area of the two beams, the intensity of the interference pattern (IP) is the sum of the electric fields of the individual plane waves

$$I(\boldsymbol{r}) = |\boldsymbol{E}_1(\boldsymbol{r}) + \boldsymbol{E}_2(\boldsymbol{r})|^2. \tag{2.13}$$

The phase difference between these two waves is defined as:

$$\delta = k_{1,x} \cdot x - k_{2,x} \cdot x, \qquad \text{with} \quad k_{2x} = -k_{1x} \quad \text{and} \quad k_{1z} = k_{2z} \tag{2.14}$$

Here, the beams incident symmetrically with respect to the normal to the film. The polarization (e.g. linear or circular) of the two interfering beams is defined by the amplitude $\boldsymbol{E}_{01}$ and $\boldsymbol{E}_{02}$.[183]

The different interference patterns are distinguished between intensity- and polarization-interference patterns. In the case of intensity interference patterns (IIP) the intensity is sinusoidal modulated along the surface of the polymer film but the orientation of the local polarization is constant (see **Figure 2.10**, calculated across one period Λ of the optical grating). Typical IIPs are: SS (both pump beams are S(0°)-polarized), PP (both pump beams are P(90°)-polarized), +45+45 (both beams are +45°-polarized), RR (both beams are right-handed circularly polarized), LL (both beams are left-handed circularly polarized).

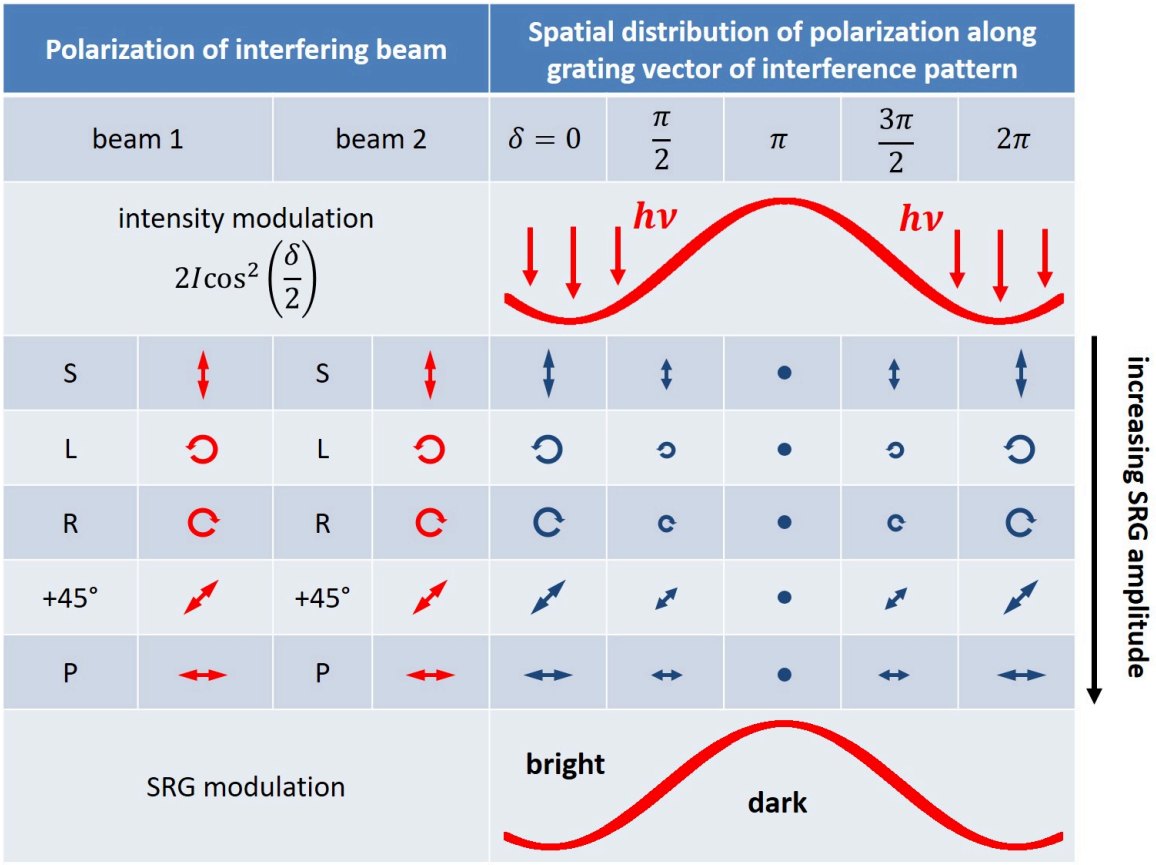

Figure 2.10. Local electric field in the case of intensity interference patterns and corresponding SRG amplitude for a photo-sensitive polymer which shows a deformation direction away from the bright area, e.g. PAZO. The interference patterns are sorted by the resulting SRG amplitude and the intensity modulation is calculated across one period Λ of the optical grating.

The second type of IPs are polarization interference patterns (PIP, see **Figure 2.11**).[170] Here, the intensity along the film surface is constant but the local polarization is changing with the period of the interference pattern (calculated across one period Λ of the optical grating). Typical PIPs are: SP (one of the pump beams is S while the second one is P-polarized), ±45 (one of the pump beams is polarized in +45° direction while the second one polarized in -45° direction) and RL (one pump beam is right-handed and the second one left-handed circularly polarized).

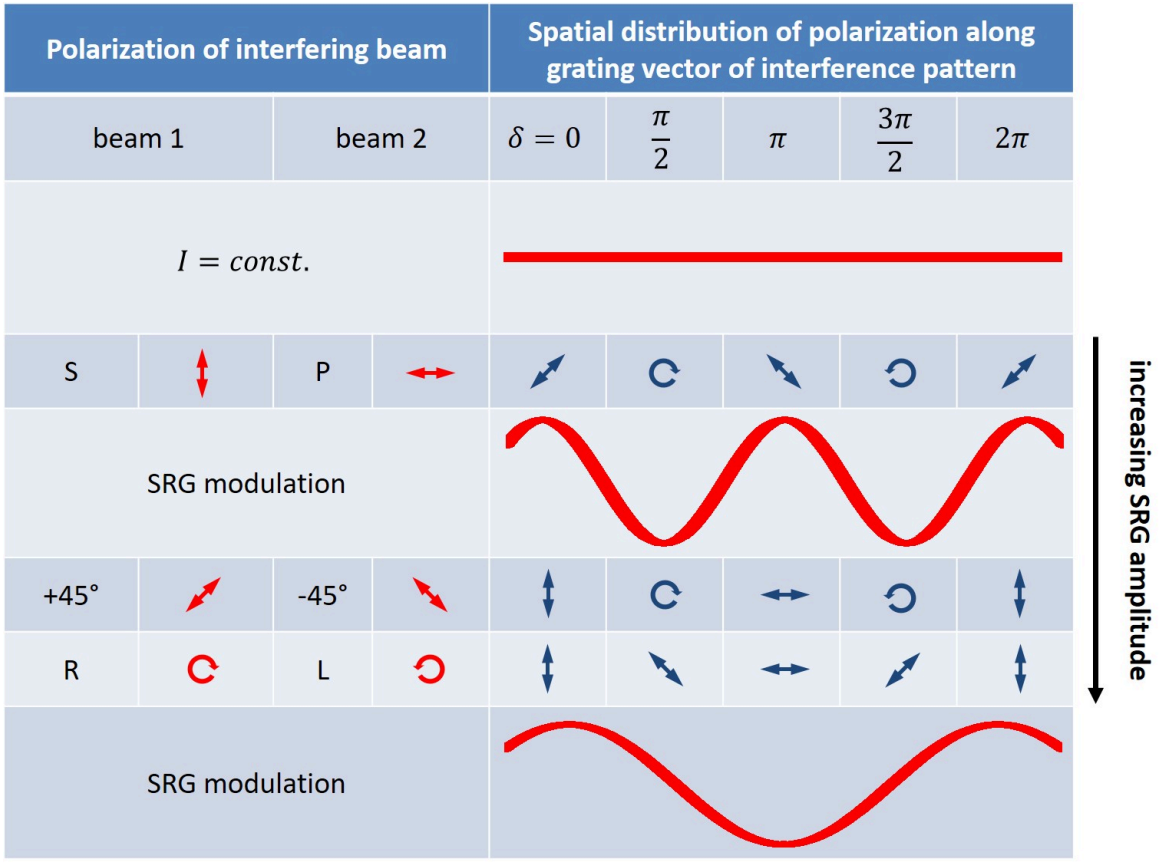

Figure 2.11. Local polarization in the case of polarization interference patterns. The interference patterns are sorted by the resulting SRG amplitude (PAZO film). The calculation is performed across one period Λ of the optical grating and neglecting the small vertical polarization component.

Both types of IPs create a SRG on the photo-sensitive polymer film but the kinetics as well as the final SRG amplitude is different for each of these IPs (see **Appendix**, **Figure C.4**, **Figure C.5**). The SS-IP (as well as the RR-, LL-IP)[169,178] is producing a poor SRG, indicating that a component of the local polarization in the direction of the grating vector (intensity modulation) is necessary (by comparison with the PP-IP, which results in the largest surface modulation for illumination with IIPs). Higher surface modulations are achieved with PIPs, e.g. the ±45- and RL-IP.[178] A special IP is the SP-IP. It generates a SRG with a period which is half the period of the IP.[88,86]

The exact polarization- and intensity pattern within the polymer film is unknown, but it is an important parameter in order to understand the SRG formation. **Figure C.9** (see **Appendix**) shows an attempt to model the local electric field within the film for different IPs based on the assumption of a reflection of the incident light field (IP) at the plane polymer-air interface. The result is an intensity modulation that appears also in the bulk perpendicular to the film surface.

Probing the SRG and BBG formation

In order to understand the driving force behind the SRG formation it is important to measure the grating inscription kinetics for the different IPs. This is usually done by measuring the diffraction efficiency (DE) as a function of time. Therefore, a non-absorbing probe beam (HeNe-laser, $\lambda_{\mathrm{probe}} = 633\mathrm{nm}$) is focused on the polymer film. The interpretation of the DE is usually challenging because it contains information about several gratings. The probe beam is sensitive to:

- the chemical grating[107] (higher *cis* concentration in the bright- compared to dark-areas which results in a different photo-stationary state),
- the birefringence grating[107,165] (phase grating in the bulk due to a spatial variation of the refractive index),
- surface relief grating[80,107] (periodic variation of optical length due spatial variation in the film height)
- and density grating[107,166,167] (variation in density).

The chemical grating is usually not detected because of the low modulation amplitude and fast response time. The density grating became accessible using small angle X-ray diffraction.[167,168,184] The separation of the SRG and BBG component in the DE is in general not trivial and involves a complicated theoretical treatment of the data, e.g. like Jones calculus.[86,109,110,165,171,185]

Isotropic gratings are categorized as either thick or thin. Thick gratings show Bragg diffraction and their diffraction efficiency is approximated analytically using Kogelnik's coupled wave theory,[186] which is valid close to the Bragg angle (energy and momentum are

conserved). Here, only one diffraction peak appears. The simplified diffraction efficiency η (normal incidence, only a BBG is considered) is given by[187]

$$\eta = \sin^2\left(\frac{\pi \Delta n d}{\lambda}\right) \tag{2.15}$$

where Δn is the amplitude of birefringence grating, λ the wavelength of the probe beam, d the polymer film thickness.

Thin isotropic gratings show Raman-Nath[188] diffraction with several diffraction orders. The transmitted optical electric field $\boldsymbol{E}_{out}(\boldsymbol{r}, t)$ (after transmission through the polymer film) is calculated by adding a phase to the electric field of the incident probe beam $\boldsymbol{E}_{in}(\boldsymbol{r}, t)$ (normal incidence):

$$\boldsymbol{E}_{out}(\boldsymbol{r}, t) = \boldsymbol{E}_{in}(\boldsymbol{r}, t)\exp[i\phi(\boldsymbol{r}, t)] \tag{2.16}$$

here ϕ is the spatially modulated phase. The diffraction pattern in the far field is calculated using the Fraunhofer-Kirchhoff approximation:

$$I(\boldsymbol{q}, t) = \left|\widetilde{\boldsymbol{E}}_{out}(\boldsymbol{q}, t)\right|^2 \tag{2.17}$$

where $\widetilde{\boldsymbol{E}}_{out}(\boldsymbol{q}, t)$ is the Fourier transform of $\boldsymbol{E}_{out}(\boldsymbol{r}, t)$.

For simplicity a sinusoidal homogeneous phase grating in the bulk oriented along the x-axis is considered. The diffraction in the case of an inhomogeneous grating (Gaussian shaped envelope of the modulation amplitude) will be addressed in publication I and II. Then, the variation of the refractive index is expressed as

$$n(x, t) = n_0 \pm \frac{\Delta n(t)}{2} \cos\left(\frac{2\pi\, x}{\Lambda}\right) \tag{2.18}$$

where $\frac{\Delta n}{2}$ is the amplitude of the BBG and n_0 the average refractive index of the polymer at the respective light wavelength λ. Λ is the period of the IP, determined by the angle 2ϑ between the two pump beams, $\Lambda = \frac{\lambda}{2 \cdot \sin(\vartheta)}$. The ± sign indicates the position of the BBG (e.g. as a function of the probe beam polarization and becomes an important parameter when the SRG is added). Then, the phase modulation (in reflection configuration, $2d_0$) is expressed, as

$$\phi(x,t) = \frac{2\pi}{\lambda} n(x,t) 2d_0 \tag{2.19}$$

where d_0 is the polymer thickness. Using this expression, the electric field of the outgoing wave can be written in the form:

$$\boldsymbol{E}_{out}(\boldsymbol{r},t) = R \cdot \boldsymbol{E}_{in}(\boldsymbol{r},t) \exp\left[\pm \frac{2\pi i}{\lambda} \Delta n(t) \cos\left(\frac{2\pi x}{\Lambda}\right) d_0\right]. \tag{2.20}$$

Here, R is a constant reflection amplitude and a global phase is left out. The exponential function can be expanded in a Fourier series (Jacobi Anger expansion)

$$\begin{aligned} &\exp\left[\pm \frac{2\pi i}{\lambda} \Delta n(t) \cos\left(\frac{2\pi\, x}{\Lambda}\right) d_0\right] \\ &= \sum_n J_n\left(\pm \frac{2\pi}{\lambda} \Delta n(t)\, d_0\right) \exp\left(in \frac{2\pi\, x}{\Lambda}\right) \exp\left(i \frac{n\pi}{2}\right) \end{aligned} \tag{2.21}$$

with coefficients $J_n(\Delta\phi) = J_n\left(\pm \frac{2\pi}{\lambda} \Delta n(t) d_0\right)$ given by Bessel functions. If the incoming wave is a plane wave

$$\boldsymbol{E}_{in}(\boldsymbol{r}) = \boldsymbol{E}_{in} \exp(i\boldsymbol{k}_{in} \cdot \boldsymbol{r}) \tag{2.22}$$

the outgoing wave contains the wave vectors

$$\boldsymbol{k}_n = \boldsymbol{k}_0 + n\boldsymbol{G} \qquad \text{with } \Lambda = 2\pi/G. \tag{2.23}$$

Introducing the diffraction angle θ_n via $k_{n,x} = k \sin\, \theta_n$, with the wavenumber $k = \frac{2\pi}{\lambda}$, leads to the discrete diffraction orders under the angles (Bragg-Laue condition)

$$\sin\theta_n - \sin\theta_0 = \frac{nG\lambda}{2\pi}. \tag{2.24}$$

For an infinite grating the diffraction efficiencies are thus given by the squared coefficients of **Eq. 2.21**:

$$\eta_n \equiv \frac{I_n}{I_{in}} = |R|^2 \left|J_n\left(\frac{2\pi}{\lambda} \Delta n(t)\, d_0\right)\right|^2 = |R|^2 |J_n(\Delta\phi)|^2 \tag{2.25}$$

The Bessel function shows several oscillations as a function of modulation height resulting in a nonlinear dependence of the DE on the grating height (see **Figure 2.12**).

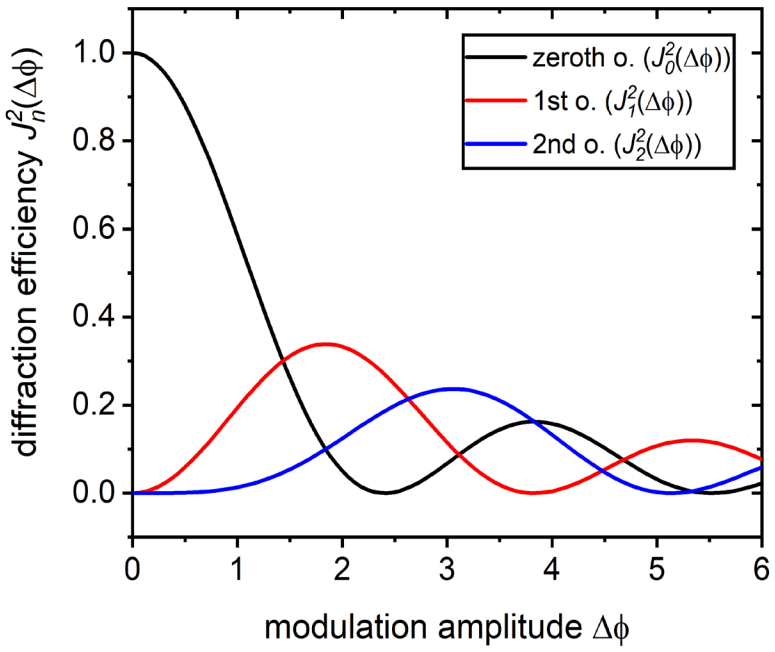

Figure 2.12. Plot of the zeroth-, 1st- and 2nd-order diffraction efficiency according to the Raman-Nath approximation.

Now, an additional SRG with a sinusoidal surface modulation will be considered

$$d(x,t) = d_0 + \frac{\Delta d(t)}{2}\cos\left(\frac{2\pi\, x}{\Lambda}\right), \tag{2.26}$$

where $\frac{\Delta d(t)}{2}$ is the amplitude of the SRG. The spatial shift between the BBG and SRG is defined with the help of the ± sign in **Eq. 2.18**, which corresponds to constructive (+) and destructive (-) interference of these two gratings in the total DE. The combined phase modulation is expressed in terms of

$$\phi(x,t) = \frac{2\pi}{\lambda}\left(2n_0 d_0 + [n_0\Delta d(t) \pm d_0\Delta n(t)]\cos\left(\frac{2\pi\, x}{\Lambda}\right)\right) \tag{2.27}$$

This leads to the same expression of the n'th order diffraction efficiency like in **Eq. 2.25**:

$$\eta_n = |R'|^2 |J_n(\Delta\phi_{tot})|^2 \tag{2.28}$$

with $\Delta\phi_{tot} = \frac{2\pi}{\lambda}[n_0\Delta d(t) \pm d_0\Delta n(t)]$.

Furthermore, the kinetics of the BBG ($\Delta n(t)$) and SRG ($\Delta d(t)$) formation is expressed by an exponential function of the form[108]

$$\Delta n(t) = \Delta n_{\max}\left[1 - \exp\left(-\frac{t}{\tau_1}\right)\right] \tag{2.29}$$

$$\Delta d(t) = \Delta d_{\max}\left[1 - \exp(-\frac{t}{\tau_2})\right] \tag{2.30}$$

where τ_1 and τ_2 are two characteristic grating inscription time constants, and $\Delta n_{\max}$ and $\Delta d_{\max}$ are the maximum refractive index- and thickness-modulations for given experimental conditions, e. g. light intensity, wavelength, grating period, sample thickness and polymer typ.

The time constant of the faster process τ_1 is describing the rate of angular molecular redistribution of the chromophores and the slower process τ_2 the polymer deformation resulting in the SRG formation. A plot of **Eq. 2.28** in the case of constructive (plus sign in $\Delta\phi_{tot}$) and destructive (minus sign in $\Delta\phi_{tot}$) interference of SRG and BBG is shown in **Figure 2.13**.

In order to categorize gratings as either thick or thin for finite values of d, one may look for a parameter that indicates whether the analytical approximations for Bragg or Raman-Nath diffraction are reasonable. This is done by comparing d_0 and the wavelength λ with the average index of refraction n_0 or birefringence Δn and the grating period Λ. Most often, the Klein-Cook parameter[189,190]

$$Q = \frac{2\pi d_0 \lambda}{n_0 \Lambda^2} \tag{2.31}$$

is used and the grating is considered thin when $Q < 1$ and thick when $Q > 10$.

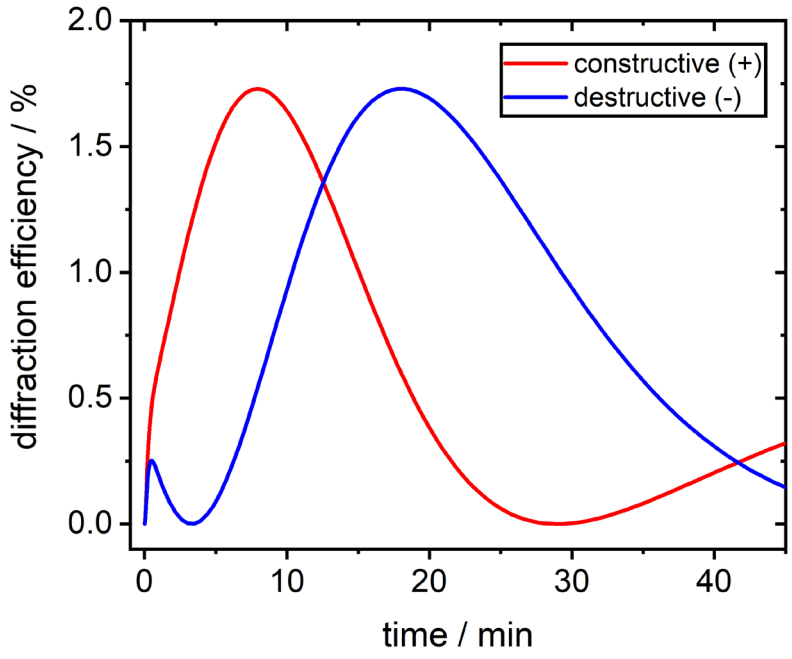

Figure 2.13. Plot of the diffraction efficiency according to **Eq. 2.28** in the case of constructive interference of the SRG and BBG (red curve, plus sign in $\Delta\phi_{tot}$). The blue curve represents the situation of destructive interference (minus sign in $\Delta\phi_{tot}$). The following typical parameters are used: $\tau_1 = 10\text{s}$, $\tau_2 = 27\text{min}$, $\Delta n_\infty = 0.058$, $\Delta h_\infty = 300\text{nm}$.

Another frequently used parameter is:[189]

$$\rho = \frac{\lambda^2}{n_0 \Delta n \Lambda^2} \tag{2.32}$$

For which $\rho < 1$ is considered as thin and $\rho \gg 1$ as thick.

Typical values are $d_0 = 1\mu\text{m}$, $\lambda = 633\text{nm}$, $n_0 = 1.6$ and $\Lambda = 2\mu\text{m}$. Then, the Klein-Cook parameter with these values is $Q = 0.62 < 1$ (and $\rho \approx 1.04$), indicating that the Raman-Nath approximation holds.

An alternative approach to the DE measurement in order to determine SRG kinetics is the direct *in situ* scan of the polymer film surface (while irradiating with an IP) with an atomic force microscope[169] (AFM). Here, the SRG amplitude as a function of irradiation time is directly measured. Nevertheless, no information about the BBG is obtained. Using a

scanning near-field optical microscope[191–193] (SNOM) an additional optical signal beside the topography is recorded. This permits to assign the intensity of the IP to the SRG (in the case of an intensity interference pattern) but still no information about the bulk orientation is obtained. The scanning probe technique is also relatively slow (time resolution ~1s) which is the reason why nowadays a digital holographic microscope[194] (DHM) is utilized to analyze the change in the SRG amplitude (time resolution ~ms). Here, the optical holography signal contains beside the SRG also the BBG, but the deconvolution is still complicated.

Combining the scanning probe technique with DE measurements permits to record *in situ* the temporal change of the BBG and SRG independently. The DE carries the information about the BBG and SRG. Subtracting the SRG component (with the help of the *in situ* recorded AFM data) yields directly the modulation amplitude of the BBG as a function of time. This permits to obtain information about the driving force behind the SRG formation by comparing the bulk orientation with the surface modulation.

The new designed set-up consists of three parts (see **Figure 2.14**). The first part is the two-beam interference set-up. Here, well defined spatial intensity- or polarization interference patterns are generated by the interference of two coherent beams of the same intensity. Therefore, the diode pumped solid state laser (Cobolt Calypso, $\lambda_{\mathrm{pump}} = 491\mathrm{nm}$) is first focused on a pinhole with the help of an objective-lens and collimated afterwards. This configuration acts as a spatial filter and beam expander at the same time. The beam diameter is set to 4mm. A 50:50 beam splitter is separating the initial single beam into two beams of the same intensity. These coherent beams than pass through a set of wave plates and polarizers enabling the independent control of intensity and polarization until they interfere on the surface of the polymer film. A piezo stack is integrated into one of the beam path in order to control the position of a mirror (M_4) on the nanometer-scale (see **Figure 2.14**). This permits to introduce a phase shift between the two interfering beams on demand, which results in a translation of the whole interference pattern along the polymer film surface. The set-up additionally owns a Pockels cell acting as a fast optical switch by applying the half-wave-plate voltage. This permits to block one beam on demand and switches from the two-beam interference to the single beam irradiation configuration of the set-up.

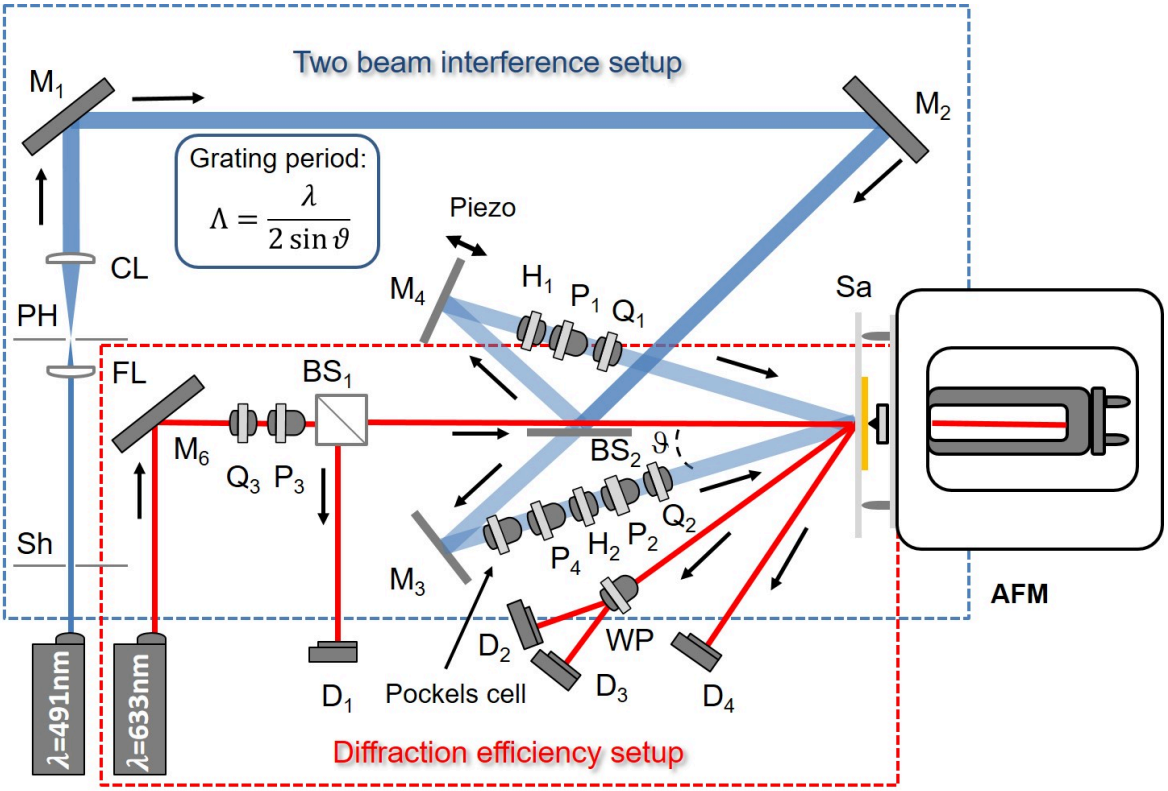

Figure 2.14. Scheme of the experimental set-up consisting of three parts: (1) a two-beam interference part for generation of the interference pattern (blue laser line), (2) an atomic force microscope (AFM) for *in situ* (during irradiation) surface morphology detection and (3) a diffraction efficiency (DE) set-up (red laser line) enabling the collection of information about the BBG *in situ*. The two-beam interference set-up contains additionally a Pockels cell in order to switch fast to the single beam erase configuration of the set-up. The interference pattern is translated with the help of a piezo stack. (Sh = shutter, Sa = sample, M = mirror, D = detector, P = polarizer, H = half-wave-plate, Q = quarter-wave-plate, BS = beam splitter, CL = collimating lens, FL = focusing lens, PH = pin hole, WP = Wollaston-prism).

The second part of the set-up is the integrated atomic force microscope (AFM) which permits *in situ* measurements of changes in polymer topography, e.g. under varying irradiation conditions. The sample is oriented with the polymer surface pointing towards the AFM tip, such that the irradiation is through the glass substrate. The SRG amplitude is determined from the surface profile (obtained from the AFM scan) by measuring the difference in height between hills and valleys of the SRG. A plot of this value as a function of time gives the kinetics of the SRG formation.

In order to simultaneously probe the bulk orientation a red probe laser is integrated into the set-up to probe the diffraction efficiency of the inscribed gratings as a function of time (third part). Its wavelength falls outside the absorption band of the polymers and the intensity is low enough not to affect the polymer film. A Wollaston-prism permits to analyze the DE for its polarization.

The interplay of light, light sensitive chromophore and embedding matrix is the key of understanding the photo-induced orientation and SRG formation. This question will be addressed in this thesis by the *in situ* acquisition of the BBG- and SRG amplitude.

Optimization of grating inscription[191,195,196]

An interesting effect appears when the polymer film is illuminated with an additional (assisting) beam, beside the irradiation with an interference pattern and whose wavelength falls into the absorption band of the polymer. The assisting beam is causing a significant increase in SRG height, even when the surface grating is already saturated.[191,195,196] Here, the explanation is that the additional beam is used to control the photo-isomerization in order to increase the photo-orientation dynamic (mobility). Using an UV laser results in a faster relaxation of the *cis*-isomers (produced by the pump beam) into the *trans* form. It was found that the polarization of the assisting laser has to be same as the pump beam in order to optimize the grating inscription. A laser, whose wavelength is in the visible range, also increases the modulation of the inscribed gratings. The pump beam (interference pattern) aligns the azobenzene-chromophores perpendicular to the local linear polarization. Therefore, the Vis-assisting laser is perpendicular polarized, compared to the pump beam, in order to reach these chromophores.

Applying a strong electric field during illumination with an interference pattern is optimizing the SRG inscription in a photo-sensitive polymer film.[197] The Corona poling aligns the azobenzene-chromophores which results in a significant increase in the modulation amplitude of the inscribed gratings. It is assumed that surface charges tend to move to a valley of the SRG where they are closer to the conductive substrate (oppositely charged). These accumulated charges are producing an additional force which increases the SRG amplitude.

Photo-induced stresses

One of the key question in understanding the grating formation in glassy azobenzene containing side-chain polymer films is the estimation of photo-induced stresses which result in the plastic deformation of the polymer film. The Young's modulus of these polymer films is usually high (~GPa, see **Appendix.B**) while the intensity of the IP rather low (~200mW/cm^2). This indicates that large photo-induced forces are present during the grating formation. Several different approaches were proposed in the last years in order to measure these forces.[198] The most impressive one is the rupturing of thin gold layers (~10nm) deposited on the surface of an azobenzene containing polymer film.[100,101,199] During the grating inscription (illumination from the back side with an IP) small cracks appear in the gold layer indicating that the photo-induced stresses are large enough to rupture thin metallic layers.

A first estimation of the stresses acting during the SRG formation became accessible after the deposition of a graphene layer on the polymer surface.[102,103] During the SRG inscription this layer is stretched which results in a shift of the graphene G-band in the Raman spectrum. It is found that the shift corresponds to a photo-induced stress of at least 1GPa. Another approach to visualize and estimate the opto-mechanical stresses is the illumination of a polymer coated AFM cantilever (see **Appendix**, **Figure B.5**). The irradiation with linearly polarized light results in a deformation of the polymer layer which is bending the cantilever upwards. Recording the cantilever deflection (with a calibrated cantilever) permits to estimate the photo-induced stresses to ≈16 MPa. This value is much smaller compared to the one obtained from the experiment with the graphene layer. It might be that the polymer film is less bonded on the cantilever which results in a poor force transmittance or the cantilever spring constant is "too" low in order to estimate the real photo-induced forces.

2.5. Models to explain mechanical stress

During the last twenty years several models were proposed to explain the SRG formation, but none of them is able to explain all experimental observations. The challenge here is the connection between the isomerization of the azobenzene and the appearance of a force which causes the macroscopic polymer film deformation. The next paragraph will try to give an overview about these models and shows which questions are still unanswered.

Photo-softening[200–202]

In order to explain the macroscopic polymer film deformation well below the glass transition temperature it was postulated that the *trans-cis-trans* photo-isomerization cycle results in a photo-softening[99,201] (athermal phase transition) of the polymer film which enhances the polymer chain mobility or that a thermal gradient is forming the SRG. This photo-softening was several times reported, but has to be critically discussed, because it cannot explain the polarization dependency of the surface deformation. Indentation[203] or dynamic mechanical analysis[204] (DMA) measurements reveal that there is a reduction in the Young's modulus upon illumination of the polymer film (e.g. from 3.4 GPa to 0.9 GPa, see also **Appendix Figure B.2**),[201] but the change is not enough to cause a phase transition. SRGs are also formed using low laser intensities, less then $200\mathrm{mW/cm^2}$, in order to avoid heating.

One could speculate that the isomerization enables the localized molecular motion, by generating free volume which is then occupied by the neighboring chromophore. This enables a net flow of the material similar like the hopping transport of electrons in an organic semiconductor.[205] The temperature increase due to absorption depends on the intensity and on the polymer structure. It is found to stay below 10K for the polymers used in this thesis (measured at room temperature, see **Appendix**, **Figure B.1**), which is far away from the glass transition temperature (e.g. $T_g \approx 102°\mathrm{C}$) and too low to cause significant changes in the Young's modulus. On the other hand, it is also reported, that the viscosity in azobenzene containing systems is changing significantly upon illumination,[206,207] which might explain the increase in polymer chain mobility. Both viscosity and Young's modulus are temperature dependent. An increase in temperature reduces these two values. Here, it might be of interest

to study the change in both parameters as a function of temperature and illumination, in particular, if the yield point (transition point from elastic to plastic deformation) is effected by illumination.

Isomerization pressure[62,64,94,200]

Another approach to describe the SRG formation is that the isomerization generates a pressure because of the greater free volume requirement of the *cis* state.[64,94,208] The light intensity gradient generates a pressure gradient, because the pressure is proportional to the intensity, which results finally in a pressure-driven deformation. This approach is also able to explain the SRG formation under illumination with a polarization interference pattern. Linearly polarized light excites less chromophores than circularly polarized light and leads to a lower pressure, explaining the grating formation e.g. in the case of the ± 45-IP. The generated pressure must be greater then the yield point of the polymer in order to irreversible deform the material. The mass transport is described by solving the Navier-Stokes equation for a laminar flow of a viscous fluid

$$\rho \frac{\partial \bar{v}}{\partial t} = -\text{grad}\, P + \mu \Delta \bar{v}. \tag{2.33}$$

Here, ρ is the density, v the velocity, P the pressure and μ the viscosity. The viscosity term is acting against the mass flow (generated by to the pressure gradient). Nevertheless, this approach cannot explain all experimental observations, e.g. why the SS- and PP-IP lead to SRG's of different height.

Permittivity gradient theory[62,95,200,209]

In this model it is assumed that a spatial modulation of refractive index (permittivity) is induced in the film.[95,209] This generates a force, which is proportional to the intensity in the direction of the deformation and to the gradient in permittivity itself (similar to electrostriction, but here $\vec{E}^2$ is the average over the optical period):

$$\vec{f} = -\frac{\varepsilon_0}{2} \vec{E}^2 \vec{\nabla} \varepsilon \tag{2.34}$$

with $\vec{f}$ being the force density, $\vec{E}$ the electric field, $\vec{\nabla}\varepsilon$ the gradient in the permittivity within the polymer film and ε_0 the vacuum permittivity.

This results in a deformation away from the bright into the dark area. The approach can be applied to any system with a spatial variation in refractive index. Therefore, the azobenzene chromophore is not required for the grating formation. This is experimentally not observed.[57] If the gradient in permittivity $\vec{\nabla}\varepsilon$ is created by the birefringence grating, the force is nonlinear in intensity which is also not observed. Additionally, a rough estimation reveals that the force density (~0.1 N/m^3) is much too small. The permittivity gradient is proportional to $\vec{\nabla}\varepsilon \sim n\Delta n/\Lambda$, with n being the refractive index (≈ 1.7), Δn the photo-induced birefringence (≈ 0.06), Λ the grating period (2µm) and using an intensity of $I = 200\,\mathrm{mW/cm^2}$.

Gradient electric force[62,96,200,210,211]

In this model a component of the electric field (E_j) in the direction of the grating vector is required, which is in agreement to the experimental observations. The spatial variation of light intensity leads to a polarization (P_i) of the material. The induced polarization is related to the light intensity and the local susceptibility tensor χ_{ij} by:

$$P_i = \varepsilon_0 \chi_{ij} E_j \tag{2.35}$$

The electric field generates a forces acting on the material and the time average is given by:[210]

$$\vec{f} = \langle (\vec{P} \cdot \nabla)\vec{E} \rangle \tag{2.36}$$

The important parameters are the induced polarization, the magnitude and gradient of the electric field. This model includes the dependency on the polarization of the light, but the force density predicted by this model (~100 N/m^3) is much too small to cause a deformation of a real system ($I = 100\mathrm{mW/cm^2}$, $\lambda_{\mathrm{pump}} = 488\mathrm{nm}$).[212]

Asymmetric diffusion[62,98,111,200]

The model assumes that the SRG is formed due to an orientational concentration gradient. The rapid and cyclic photo-isomerization of the azobenzene-chromophores enables a random ("inchworm") motion of the chromophores preferentially along their long axis. The probability of undergoing such a random walk step is proportional to the probability of isomerization, which depends on the light intensity and the angle between the chromophore dipole and the polarization of the incident light. This results in a flux of molecules out of the illuminated areas into the dark region which is in agreement with some experimental observations (dependent on the photo-sensitive polymer). This model provides the best explanation for small molecules, while it fails in the case of polymers.

Mean-Field theory[62,97,200,213]

This model assumes that each chromophore is exposed to an external potential (mean-field potential) resulting from the interaction of all other chromophores in the material (Maier-Saupe).[214] The irradiation aligns the azobenzene-unit leading to an orientation potential, that also arranges other chromophores. Additionally, there is an attractive force between side-by-side chromophores that are aligned similarly, which leads to order and aggregation. This model predicts an accumulation of chromophores in the illuminated area. Dependent on the polymer this is in agreement with the experimental observations.[173] The model on the other hand includes the polarization state of the light. Therefore, it is able to explain the SRG formation using polarization interference patterns. An attractive interaction between the chromophores which is stabilizing the SRG and BBG against the angular diffusion is assumed. The exact origin of the interaction is not clear. The bulk viscosity η is connected with the angular diffusion D via[163]

$$\eta \sim \frac{(kT/D)}{L^3}. \tag{2.37}$$

Here, L is the length of the chromophores ($\sim 0.9\text{nm}$), T the temperature, k the Boltzmann-constant and η is of the order $\sim 10^{12}$ Pa s. Then, the time scale of angular diffusion is $1/D \sim 10^5 \text{s}$ which is quite stable, indicating that angular diffusion results not in an instability of the gratings.

Orientation approach[99,106,163,215]

The "orientation approach" is following similar line like the mean-field theory. An external potential aligns the chromophores (entropic mean-field). The orientation potential results from the statistical distribution of the chromophores. From the potential the force/ angular momentum acting on the chromophore is obtained which results in the alignment. The temperature induced motion is working against this orientation process.

The probability $P(\Theta)$ that a chromophore is oriented at an angle Θ with respect to the linearly polarized light is described by an exponential function

$$P(\Theta) \cong C \exp\left[-\frac{V(\Theta)}{kT}\right] \tag{2.38}$$

where T is the absolute temperature, k the Boltzmann constant and the effective potential $V(\Theta)$ has the form (Maier-Saupe):[214]

$$V(\Theta) = V_0 \cos^2\Theta\,. \tag{2.39}$$

Here, V_0 is the strength of the potential. The value of V_0 is determined by the intensity of the laser I and is estimated as

$$V_0 = C \cdot I \tag{2.40}$$

where C is the constant of proportionality. The interaction of the chromophores with polarized light results in an orientation anisotropy of polymer chains due to covalent bonding of chromophores to the chain backbones. The mechanical stress σ is determined by the free energy of the system $F = F(\varepsilon)$ which is a function of the strain ε:

$$\sigma(\varepsilon) = -\frac{\partial F(\varepsilon)}{\partial \varepsilon}\,. \tag{2.41}$$

Using a modified expression of the potential $U(\theta,\psi) = N_{ch} V_0 u(\theta,\psi)$, where N_{ch} is the number of chromophores and $u(\theta,\psi) \equiv \langle \cos^2\Theta(\theta,\psi)\rangle$, the free energy F is expressed as:

$$F = nkT \int d\Omega\, f(\Omega) \ln f(\Omega) + n \int d\Omega\, f(\Omega) U(\Omega) + \frac{E\varepsilon^2}{2} \tag{2.42}$$

where n is the number of oligomers in a unit volume, $f(\Omega)$ the orientation distribution function of the oligomers with $\Omega \equiv (\theta, \psi)$. The first term is the orientation entropy of oligomers and the second term is the energy of all chromophores in the illuminated area. The third term is caused by the elasticity of a glassy polymer, with E being the Young's modulus. One can also define an order parameter

$$S = \langle P_2(\theta) \rangle \equiv \int d\Omega \, f(\Omega) \frac{3\cos^2\theta - 1}{2}. \tag{2.43}$$

Therefore, the photo-induced stress results from a change in the order parameter with time.[163] The above defined potential is able to generate photo-mechanical stresses ranging ~100MPa up to ~1GPa using reasonable values for the parameters.[163] It is the first theory which provides light induced stresses which are larger than the yield stress for these polymers (10-50MPa).[215] In addition, these values are also in good agreement with experimental observations.[215] The approach also explains the SRG formation. Therefore, the whole surface is divided in small parts where the intensity or the direction of light polarization is constant. The local deformation of each part is a result of two factors: the interaction of the molecules with the homogeneous light in each part and a balance between stresses appearing in the neighboring parts. The orientation of molecules in each part leads to the deformation of that part. As a result, the molecules are moved to another part with another different light intensity (or polarization). The deformation of each part results in the translational movement of molecules. The SRG formation is a combination of the orientation approach and a mass transport. This model is able to explain the difference in SRG height for the illumination with a SS- or PP-IP. In the case of the PP-IP the light polarization vector is oriented in the direction of the gradient in light intensity, so that each small part is deforming along the electric field vector. In the case of an SS-IP, the polarization vector lies perpendicular to the gradient vector of the light intensity and the intensity along this vector is constant. Therefore, the stresses appearing in the neighboring parts along the polarization vector are the same. Hence the deformation is strongly suppressed due to the balance between stresses appearing in the neighboring parts.

3. Summary of publications

3.1. Publication I: Understanding optical diffraction data

- **Solving an old puzzle: fine structure of diffraction spots from an azo-polymer surface relief grating**

  J. Jelken, C. Henkel and S. Santer, *Applied Physics B*, **125** (2019), 218

This work deals with the interpretation of the results which are obtained with the new designed set-up. It combines the *in situ* acquisition of the surface relief grating (SRG) amplitude with the help of an atomic force microscope and diffraction efficiency (DE) of the inscribed gratings during irradiation with an interference pattern. The results show that the SRG amplitude is continuously increasing during the illumination with an ±45-IP. This leads to a deep phase modulation of the probe beam, so that the 1st-order DE shows several extrema. Changes in the spatial profile of the 1st-order diffraction spot starting from Gaussian to a ring structure ("donut") and finally to a ring structure with a bright center ("Saturn"-like structure) are observed as a function of grating modulation when a probe beam with a large diameter (e.g. equal in size with the pump beam, ≈ 4mm) is used (see **Figure 3.1**). The transformations in the spatial profile are correlated with changes in the DE by recording the +1st-order diffraction spot with a CMOS camera and the -1st-order DE with a photodiode simultaneously. Here it is important to say that the DE of these two different diffraction spots is the same for this IP and probe beam polarization.

The ±45-IP is a polarization interference pattern, meaning that the intensity along one grating period is constant, only the local polarization is periodically changing. Further experiments and theoretical calculations confirmed the assumption that the origin of the fine structure in the diffraction spot is a Gaussian shaped intensity modulation of the interference pattern by using two pump beams of finite size (see **Figure 3.2**). This results in an inhomogeneous amplitude of the bulk birefringence grating (BBG) and SRG, since the modulation amplitude is mimicking the intensity profile. The consequence is a spatially inhomogeneous diffraction efficiency, because the kinetics of the SRG and BBG strongly depends on the intensity of the writing beam.

A simple "reflecting phase screen" model is proposed for the theoretical prediction of the 1st-order DE. Here, the diffraction of the SRG and BBG is described by a thin phase grating (in Raman-Nath approximation) with a common phase modulation amplitude (constructive interference of the SRG and BBG in the DE). Additionally, the special geometry of the set-up (recoding of the diffraction efficiency in reflection configuration) doubles the optical length, which results in the deep phase modulation (together with the large SRG amplitude). It turns out that the spatial profile of the diffraction spot does not represent the Fourier transform of the diffracted light in the far-field. The diffraction spot is a "shadow" of the writing field and shows the inhomogeneous grating profile. Therefore, it represents, at a given time, a scan over different energy doses. This can be avoided experimentally by working, e.g. with a small probe beam, where the energy dose is a function of the exposure time.

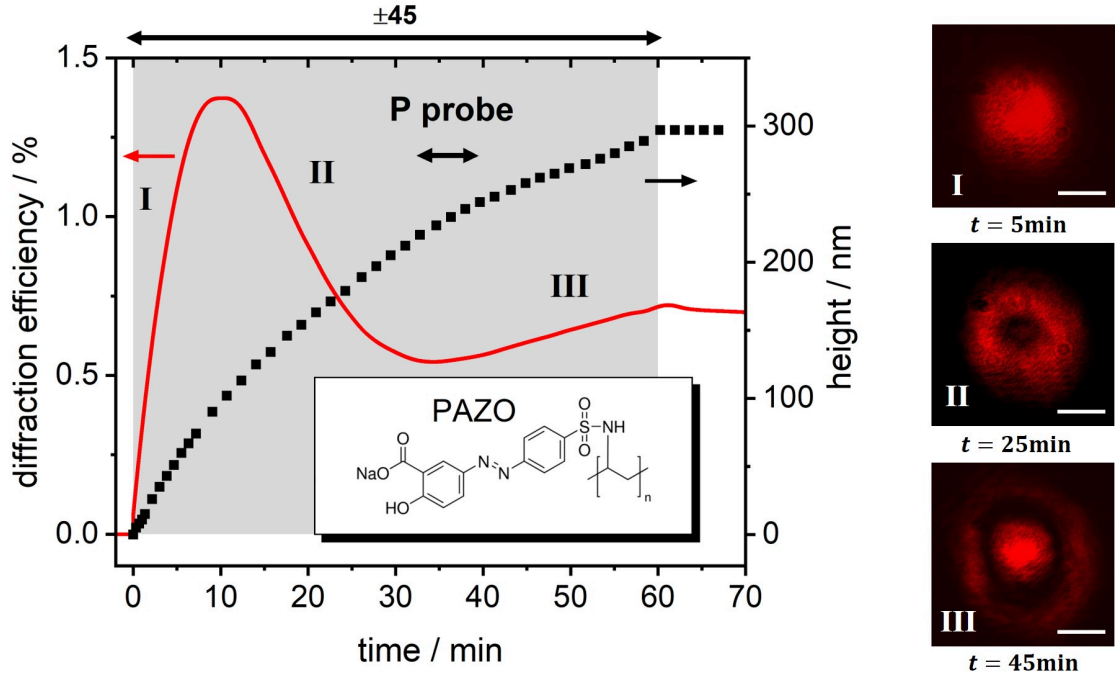

Figure 3.1. *In situ* recorded 1st-order DE (red curve) and SRG amplitude (black dots) as a function of irradiation time with the ±45-IP (left). The grey rectangle marks the irradiation sequence of the film. The inset is showing the chemical structure of the azobenzene containing polymer PAZO. On the right side the spatial profile of the diffraction spot is show at different stages of the temporal evolution of the DE ($\lambda_{\mathrm{pump}} = 491\mathrm{nm}$, $\lambda_{\mathrm{probe}} = 633\mathrm{nm}$, total pump intensity $I = 200\mathrm{mW/cm^2}$, SRG period $\Lambda = 2\mu\mathrm{m}$, film thickness $d = 1\mu\mathrm{m}$).

Using a probe with a large diameter the inhomogeneous grating can be seen. Assuming a probe beam which matches in size with the pump beam confirms the experimental observations. For small modulations a Gaussian profile of the 1st-order diffraction spot is observed (see green curve in **Figure 3.2a**). Further increase in the modulation amplitude results first in the drop of the DE in the center ("donut" structure, black curve in **Figure 3.2a**) and then in the translation of the minimum to the side (appearance of the "Saturn"-like structure, yellow curve in **Figure 3.2a**), as it is experimentally observed. The theoretical calculations show that the size of the probe beam has a large influence on the total DE (integral over the total spot size, see **Figure 3.2b**). For a very small probe beam the DE for a homogeneous grating (first-order Bessel function) is observed. As soon as the probe beam diameter is increased the DE differs (assuming an inhomogeneous (Gaussian) modulation amplitude of the SRG and BBG). A shift of the maximum to the right to larger relief amplitudes takes place as well as a strong derivation from the homogeneous grating.

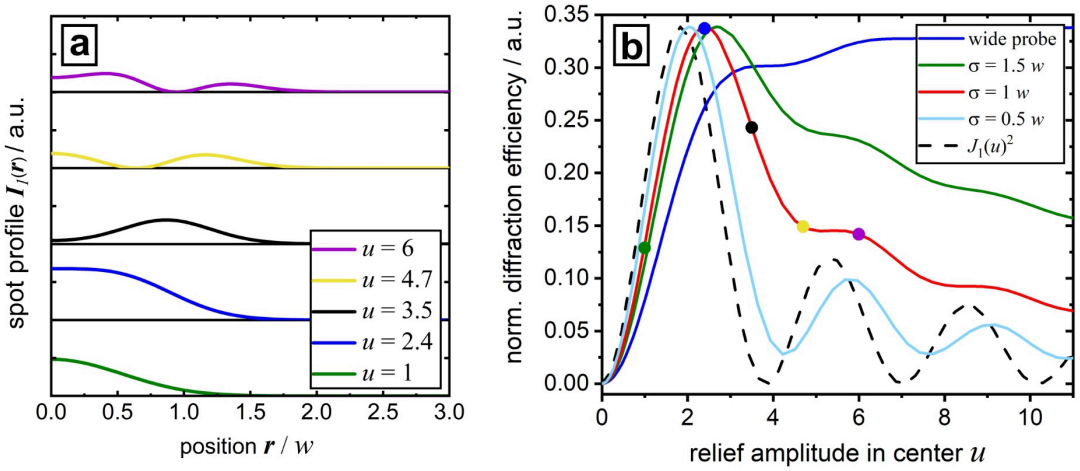

Figure 3.2. (a) Theoretical prediction of the spatial fine structure in the 1st-order diffraction spot. The parameter u gives the modulation depth at the center of the phase grating, w is the radius of the irradiated grating area (assuming a Gaussian profile). (b) Diffraction efficiency as a function of grating modulation u (in the center), for different sizes σ of the probe beam. Solid lines: numerical calculation, integrating the diffracted intensity over the area of the 1st-order diffraction spot. Dashed line: comparison to the Bessel function $J_1(u)^2$ evaluated at the grating center (see publication I for the definition of the parameters). All efficiencies are normalized to their maximal value. The dots mark the parameters chosen in (a).

Contribution of J. Jelken:

J. Jelken has planned the experiments, prepared and characterized the samples, built the experimental set-ups, performed all the measurements composing this publication and analyzed the obtained results. He has designed and assembled all figures, written the first version of the manuscript, actively participated in the discussion and wrote a reply to the comments of the reviewers.

3.2. Publication II: Disentangling surface relief and bulk birefringence gratings

- **Polarization controlled fine structure of diffraction spots from an optically induced grating**

  J. Jelken, C. Henkel and S. Santer, *Applied Physics Letters*, **116** (2020), 051601

In this publication it is demonstrated that by using the same interference pattern (IP) for the illumination like in publication I (±45-IP), but changing the polarization of the probe beam from P- to S-polarization, one senses a different azobenzene-chromophore orientation in the bulk. The photo-orientation is introducing a slow axis (higher refractive index, slower phase velocity) along the chromophore orientation and a fast axis (lower refractive index, higher phase velocity) perpendicular to the orientation of the azobenzene-unit. The probe beam is sensing a higher or lower refractive index dependent on its polarization or the chromophore orientation. This can result in a spatial shift between the SRG and BBG dependent on the polarization of the probe beam, because the maximum of the BBG is shifting. The shift results in a destructive interference of the SRG and BBG in the DE (in contrast to publication I, see **Figure 3.3**). At the beginning of illumination, only the bulk birefringence grating (BBG) contributes to the DE, because the SRG amplitude is too low to have a significant impact on the DE. The surface modulation increases with time, but due to the destructive interference of the contributions of SRG and BBG the overall DE drops. At a certain point the SRG component starts to dominate the DE which results in an increase of the signal. In the case of a P-polarized probe beam (sensing a high refractive index from the chromophores aligned in the direction of the grating vector), there is no phase shift between SRG and BBG resulting in a constructive interference of these two signals in the total DE. Switching the polarization of the probe beam cyclically between S- and P-polarization permits the *in situ* acquisition of the diffraction efficiency for these two polarizations together with the surface grating amplitude.

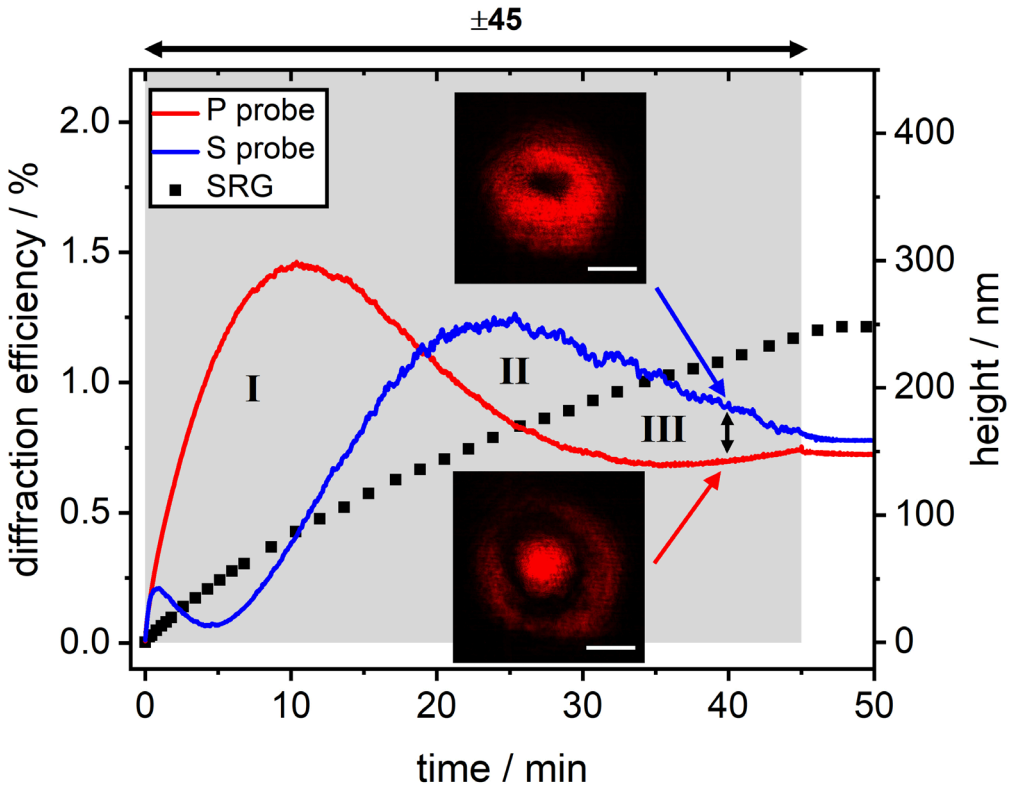

Figure 3.3. *In situ* recorded SRG amplitude and 1st-order diffraction efficiency with a P- (red curve) or S-polarized (blue curve) probe beam. The grey rectangle marks the irradiation sequence of the film. The roman numbers indicate the appearance of the Gaussian (I), "donut" (II) and "Saturn" (III) spatial profile in the diffraction spot of a P-polarized probe beam. The scale bar is 1mm (PAZO, same parameters as **Figure 3.1**).

The spatial profile of the 1st-order diffraction spot for an S-polarized probe beam shows the same change in the beam profile (Gaussian, "donut" (bright ring with dark spot in the center), "Saturn" (bright ring with a bright center)) with time as it is reported in publication I for the P-polarized probe beam, but due to the destructive interference there is a certain delay. This permits to switch between the Gaussian and "donut" or "donut" and "Saturn" structure by simply changing the polarization of the probe beam. The different spot profiles are stable in time. When the pump beam is switched off a certain relaxation in the intensity of the diffraction spot becomes noticeable, but the spatial profile remains unchanged. This indicates that the SRG, as well as the BBG are permanent and the spatial profile of the diffraction spot can be inverted by a change in the polarization of the probe beam (without

illumination with the pump beam), making it of high interest for applications in photonic devices, e.g. it can act as a spatial light modulator.

The recorded DE is described theoretically as well. The proposed model of publication I is thus extended by considering two gratings, the SRG and BBG. Dependent on the probe beam polarization a phase shift is added, so that the experimentally recorded DE for both polarizations of the probe beam is reproduced with a very good agreement (see **Figure 3.4**). The extracted parameters have reasonable values. Here, the probe beam coincides in size with the pump beam and a Gaussian shaped envelope of the SRG and BBG modulation amplitude is considered. A big difference to the use of a narrow probe beam is observed (represented by the dotted curves).

The proposed model also permits to assign the IP to the SRG and BBG, as a result from the spatial shift between these two gratings dependent on probe beam polarization. It is found that the SRG maxima are forming at local vertical (S) polarization and the minima at local horizontal (P) polarization.

Contribution of J. Jelken:

J. Jelken has planned the experiments, prepared and characterized the samples, built the experimental set-ups, performed all the measurements composing this publication and analyzed the obtained results. He has designed and assembled all figures, written the first version of the manuscript, actively participated in the discussion and wrote a reply to the comments of the reviewers.

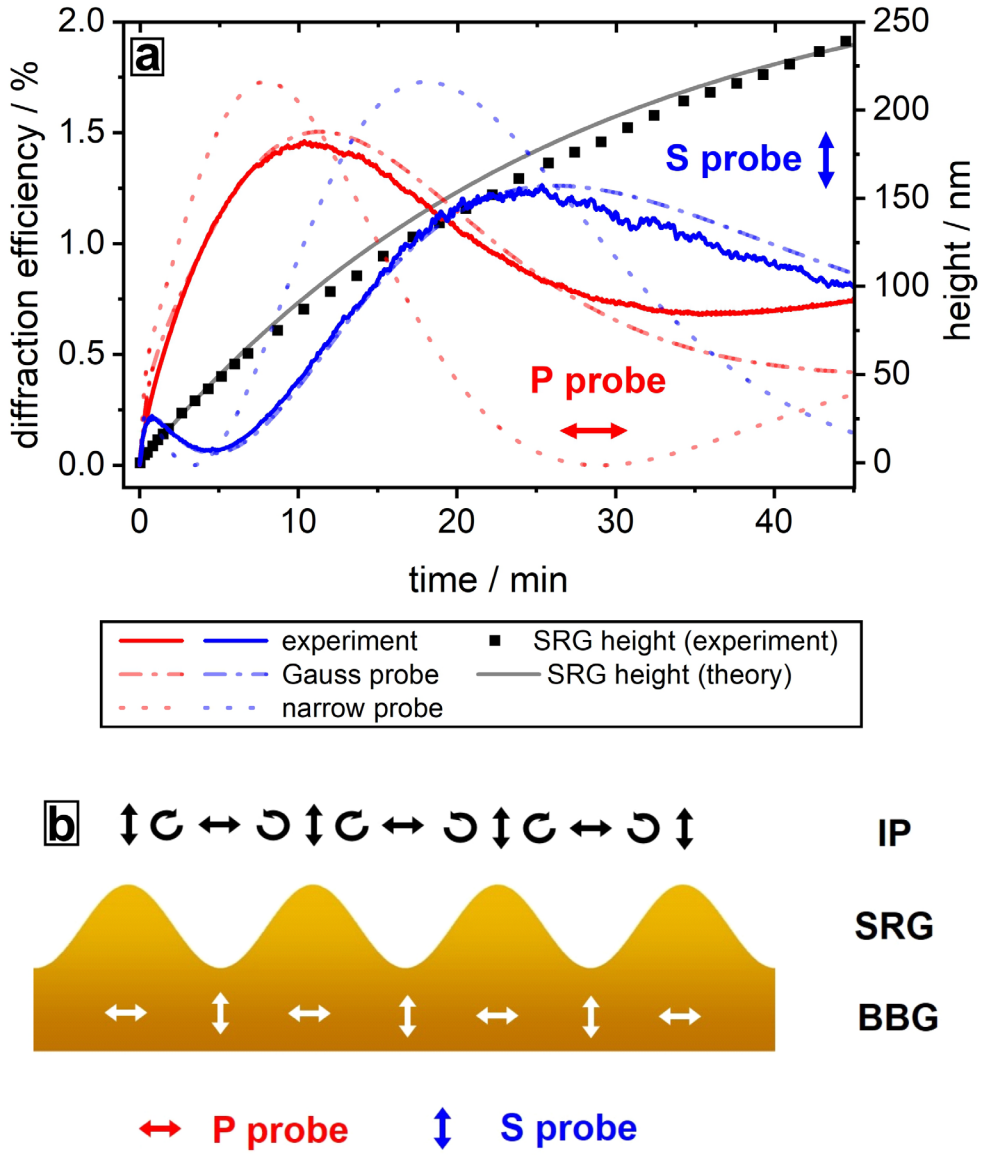

Figure 3.4. (a) Fit of the experimental data of **Figure 3.3** with the model proposed in this publication. The solid curve is showing the *in situ* recorded 1st-order DE for a P- (red curve) or S-polarized probe beam (blue curve). The dotted lines are showing the predicted DE for a narrow probe beam, while the dash-dotted lines give the DE obtained with a Gaussian profile of the probe beam. The ratio between probe and pump beam diameters is $\sigma/\omega = 0.8$ (see publication II for the definition of the parameters). The black dots are showing the *in situ* recorded SRG height, while the solid black line is the fitted SRG amplitude. Comparing experimental results with the model shows a very good matching. (b) Scheme of the SRG with the distribution of the electrical field vector (arrows on the top) for the $\pm$45-IP. White arrows within the SRG depict the photo-stationary orientation of the azobenzene chromophores in the bulk during irradiation (bulk birefringence grating, BBG). Polarizations and orientations are projected onto the film surface.

3.3. Publication III: Reversing the surface grating growth

- **Light induced reversible structuring of photosensitive polymer films**

  J. Jelken and S. Santer, *RSC Advances*, **9** (2019), 20295

Photo-sensitive polymer films enable to create a dynamically reconfigurable surface (response time: ~min) which is of high interest for many applications, e.g. it could permit the transport of surface attached objects along the surface[81] or allows the control of cell seeding in biological applications.[68–71] For this purpose, the SRG has to be inscribed and erased as fast as possible (~min), which is usually challenging. In this publication a new way of fast optical erasing of the surface structure (erase time is comparable with the grating inscription time) is presented by performing a translation of the interference pattern (IP) by *half* the grating period (Λ/2, "anti-phase" shift). The shift is achieved by integrating a piezo-stack into the beam path of one beam of the two-beam-interference set-up. The piezo drive is connected to a mirror which permits to change its position on the nanometer scale. The change in position enables to control the phase relation between the two interfering beams. As a result of the mirror displacement the whole interference pattern is translated along the film surface. Depending on the speed and step length of the IP shift the inscribed SRG can follow the illumination pattern or not. Shifting the RL-IP (one beam is right- and the second one left-handed circularly polarized) continuously and slowly in a certain direction (e.g. every four minutes by a *quarter* of the grating period (Λ/4)) results in a continuous drift of the SRG (with an almost constant SRG amplitude, see **Figure 3.5b**). This generates a dynamically reconfigurable surface (similar to a water wave) and could permit e.g. the transport of silica microspheres along the surface.[81] In total the SRG is shifted by 14µm (2µm grating period) along the surface and the translation-length is only limited by the motion-range of the piezo stack. The IP can also be translated stepwise. An antiphase shift (one step translation by *half* the grating period) results in a decrease of the surface modulation amplitude because the SRG cannot follow the IP translation (see **Figure 3.5a**). Continuing the illumination generates an SRG again, but with inverted hills and valleys. This process is reversible many times. **Figure 3.5** summarizes the different behavior of the surface grating for several *half*-period- (a) and *quarter*-period- (b) translations of the interference pattern.

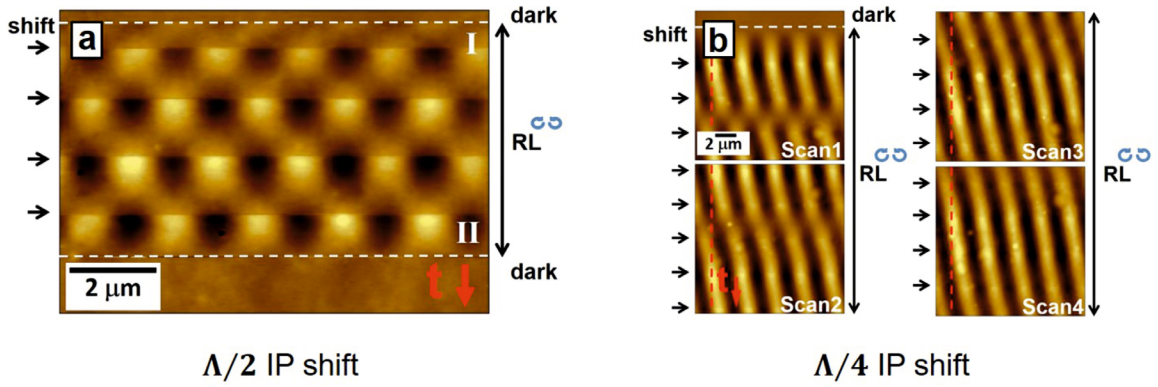

Figure 3.5. *In situ* recorded AFM micrograph of the PAZO film during irradiation with the RL-IP showing the influence of the IP translation on the formation of the surface structure (same parameters as **Figure 3.1**). In (a) the IP is translated every 60s by *half* the grating period (Λ/2). The step length is "too" large, so that the surface grating cannot follow the translation. This results in an erasure of the SRG and the formation of an inverted surface modulation. The AFM scanning starts at the top in dark with flat topography; at the time marked by the 1st (I) white dashed line, the irradiation with IP is switched on for 60s; at the time marked by the black arrow the interference pattern is shifted by $\Lambda/2$. At the bottom of the micrograph marked by the 2nd (II) dashed white line, the irradiation is switched off. (b) Translating the IP in smaller steps permits that the SRG can follow the change in illumination (without erasure). Shifting the IP very 4 min by a *quarter* of the grating period (Λ/4) results in a dynamically reconfigurable surface.

Figure 3.6 shows a typical result of a *half*-period (Λ/2) translation of the interference pattern. Here, the sample is first irradiated for 3min with an RL-IP generating an SRG of 40nm in height, showing a strong DE signal. A *half*-period-shift of the IP results in a drastic drop in the DE almost down to zero, while the SRG amplitude first rapidly increases (5nm jump) and then starts to slowly decrease. The irradiation is stopped when the SRG is completely erased (monitored with the integrated AFM). At this point the DE still shows a strong signal indicating that a new BBG is formed, although no surface structure is left. The erase process can be understood in the way that the translation of the IP re-orients the local polarization by 90° as well as the azobenzene-chromophores in the bulk, yielding a new birefringence grating, but shifted in its position. The photo-induced mechanical stresses generated by the new inscribed BBG erases the old SRG.

During the grating inscription the azobenzene-chromophores align perpendicular to the local polarization which is inactivating them. The rotation of the local polarization by 90° associated with the IP translation activates these chromophores again, so that they are

suddenly absorbing the light. This generates free volume and is the reason for the sudden 5nm jump in the SRG amplitude right after the IP translation. It also explains that the kinetics of the erase process is slightly faster compared to that of the writing process. The grating inscription starts from an isotropic state. In contrast the optical erase technique by the *half*-period translation of the IP starts from an anisotropic state because of previous grating inscription, which is more efficient.

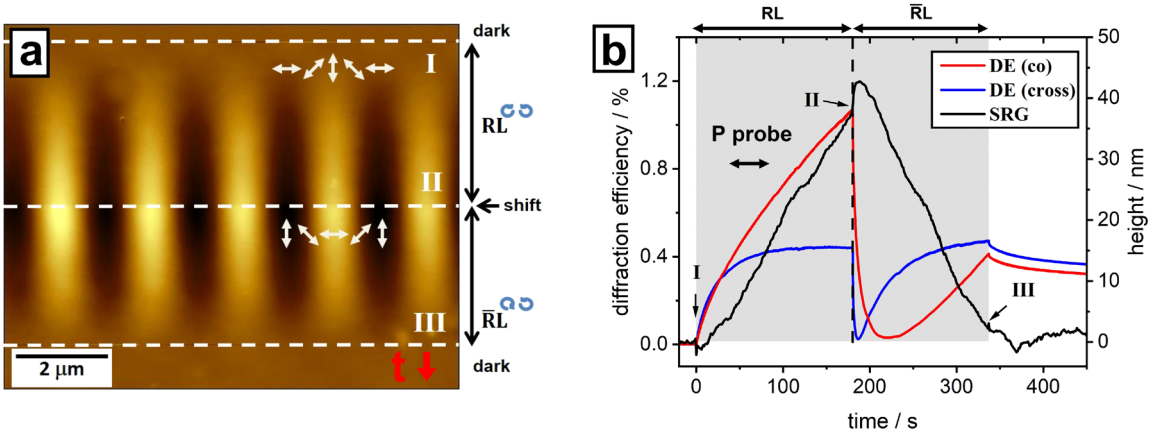

Figure 3.6. (a) *In situ* recorded AFM micrograph of the PAZO film during irradiation with RL-IP (same parameters as **Figure 3.1**), the local polarization is indicated by the white arrows. AFM scanning starts at the top in dark with flat topography; at the time marked by the 1st (I) white dashed line, the irradiation with IP is switched on for 180s; at the time marked by "shift" at the 2nd (II) dashed white line, the interference pattern is translated by *half* the grating period. The new distribution of the electrical field vector relative to the polymer topography is shown as above. The shifting of the interference pattern is equivalent to a rotation of the local polarization by 90°. At the bottom of the micrograph marked by 3rd (III) dashed white line, the irradiation is switched off. (b) *In situ* recorded SRG height (black curve) and 1st-order diffraction efficiency (co- (red curve) and cross-polarized component (blue curve)) as a function of irradiation time. The probe beam is P-polarized. The grey rectangle marks the irradiation sequence of the film. At the point where the interference pattern is translated (indicated by the dashed black line (II)), an increase in the SRG height becomes noticeable, while the diffraction efficiency decreases rapidly. The SRG is erased with time accompanied by the formation of a new inverted BBG.

The new developed optical erase process is compared with the single beam erase approach. Here, only one circularly polarized beam is utilized to illuminate the polymer film. Under this condition an isotropic distribution of the chromophore orientation in the plane parallel to the surface is generated during the irradiation (but also a certain amount of chromophores align perpendicular to the film surface). This is in contrast to the erase technique by a

translation of the IP. Here, the final state (at the point of a flat surface) is an anisotropy in the plane parallel to the surface due to the inscription of a new, inverted BBG which is overwriting the old SRG. The single beam erase process is quite slow. It is necessary to illuminate for 20h instead of 160s in the case of the IP translation to erase an SRG of the same height. Surprisingly, the surface grating formed on a PAZO film (the polymer does not have pronounced glass transition temperature (T_g)) could not be erased by a thermal treatment. In case of other polymers (pronounced glass transition temperature at ca. 100°C), the SRG is erased by heating up the sample close to T_g. The results of this publication show that the SRG and BBG are treated as two individual gratings and that the orientation of the bulk (BBG) is the source of the SRG formation.

Contribution of J. Jelken:

J. Jelken has planned the experiments, prepared and characterized the samples, built the experimental set-ups, performed all the measurements composing this publication and analyzed the obtained results. He has designed and assembled all figures, written the first version of the manuscript, actively participated in the discussion and wrote a reply to the comments of the reviewers.

3.4. Publication IV: Fast and full erasure of surface relief and bulk birefringence gratings

- **Rapid Optical Erasure of Surface Relief and Bulk Birefringence Grating in Azo-Polymer Thin Films**

  J. Jelken, M. Brinkjans, C. Henkel and S. Santer, *SPIE Proceedings*, **11367** (2020), 1136710

This publication is an extension to the previous one (publication III) and studies the DE under illumination with the RL-IP and using a S-polarized probe beam (similar like publication II in the case of the ±45-IP). On the one hand this permits to obtain the assignment of the IP with respect to the SRG, as well as BBG, and provides on the other hand a further deeper understanding of the processes and the behavior of DE in the case of a half-period translation of the IP (see also publication III). Additionally, a new technique of rapid optical erasing (~min) the SRG as well as the BBG without heating up the sample is presented.

Similar to publication II an additional peak appears in the *in situ* recorded 1st-order DE when starting the exposure to the RL-IP and using an S-polarized probe beam, based on the destructive interference of the SRG and BBG in the total DE. This delivers the same assignment of the local polarization of the writing field with respect to the surface grating for the RL-IP like it is reported for the ±45-IP (see publication II). The SRG maximum appears at local vertical (S) polarization and the minimum at local horizontal (P) polarization.

The translation of the IP by *half* of its period results in the erasure of the inscribed surface grating, because of strong photo-induced stresses generated by the formation of a new inverted BBG (see publication III). This publication following similar line, but focuses on the interpretation of the polarization sensitive recorded DE using an S-polarized probe beam (see **Figure 3.7**). Starting the grating inscription the 1st-order DE (co-polarized component, S-polarized) initially increases (due to the BBG) and afterwards decreases (despite of increasing SRG amplitude). As soon as the IP translation starts, the co-polarized component in the 1st-order DE goes through a maximum and decreases when also the SRG amplitude is

shrinking. A significant DE signal is left when the SRG is completely erased, indicating the formation of the inverted BBG.

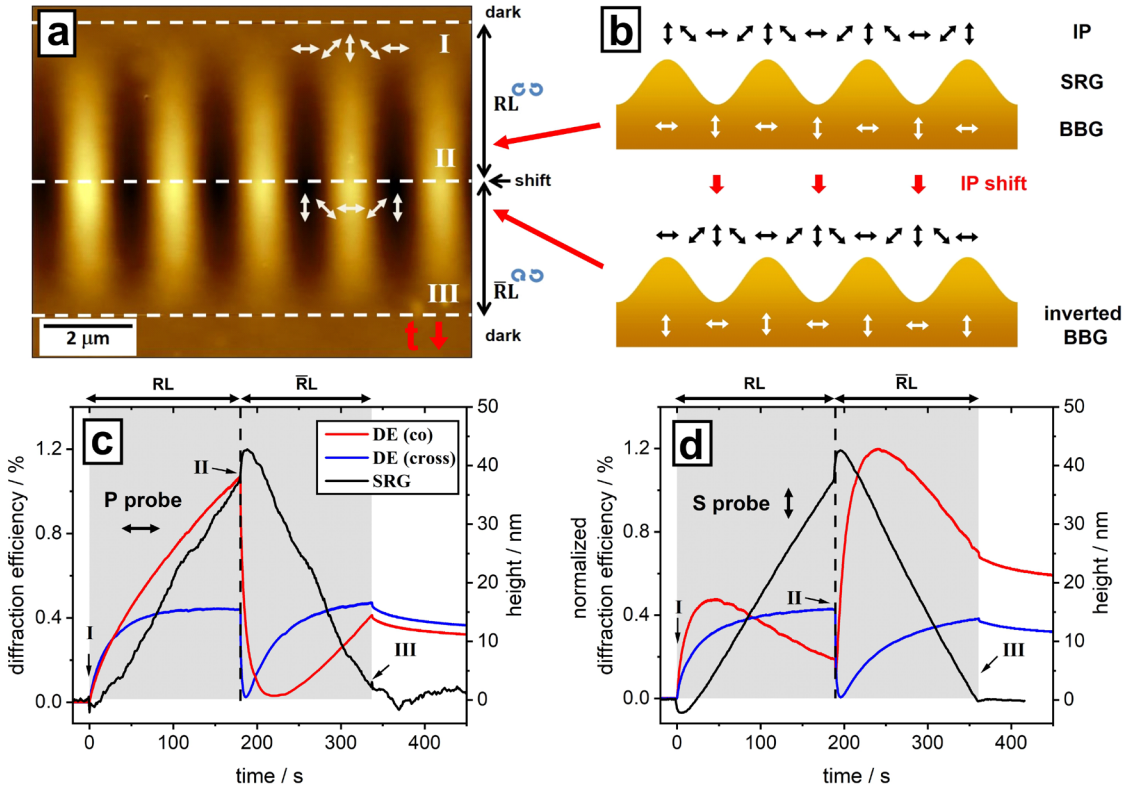

Figure 3.7. *In situ* recorded SRG amplitude and 1st-order DE for a translation of the RL-IP by *half* the grating period. The AFM micrograph is shown in (a). The scan direction is from top to bottom indicated by the small red arrow in the lower right corner. The scan starts with a flat surface. At the time of the 1st (I) white dashed line the irradiation is started. Later the interference pattern is shifted by *half* the grating period at the time of the 2nd (II) white dashed line. This translation corresponds to a rotation of the local polarization by 90° (the local polarization of the IP is indicated by the white arrows) and results in a decrease of the SRG amplitude. The irradiation is switched off at the time when the 3rd (III) white dashed line is reached. (b) Scheme of the IP translation by *half* the grating period. In the case of a P-polarized probe beam the SRG is in phase with the BBG (constructive interference, indicated by the white arrows, projection onto the film surface). By the shift of the IP and the corresponding re-orientation of the chromophores in the bulk, a phase shift of π (half the period of the IP) between SRG and BBG is generated. It results in a destructive interference of the two signals in the DE. In the case of a S-polarized probe beam one starts with destructive interference which is converted into constructive interference by the IP shift. (c) *In situ* recorded SRG amplitude (black dots) and 1st-order DE (co- (red curve) and cross-polarized (blue curve) component) for a P-polarized probe beam. The grey rectangle marks the irradiation sequence of the film. (d) The same experiment as in (c) but with an S-polarized probe beam (PAZO, same parameters as **Figure 3.1**).

The behavior of the DE can be explained with the help of the assignment of the local polarization with respect to the SRG and BBG, as illustrated in **Figure 3.7b**. The grating inscription starts with a destructive interference of the SRG and BBG in the 1st-order DE. The shift of the IP by *half* the grating period results in a fast (~s) re-orientation of the azobenzene-chromophores in the bulk (rotation of the local polarization and chromophore orientation by 90°), which removes the spatial shift between SRG and BBG. This results in a constructive interference, which explains the observed fast increase in the DE. The translation of the IP therefore changes from destructive- to constructive interference of the SRG and BBG in the 1st-order DE (co-polarized component). Afterwards the DE starts to decrease, as soon as the SRG amplitude drops due to the formation of the inverted BBG. In the case of a P-polarized probe beam the grating inscription starts with a constructive interference of the SRG and BBG in the 1st-order DE (co-polarized component) and is converted into a destructive interference (due to the IP translation) explaining the fast decrease of the signal (see **Figure 3.7c**). The DE starts increasing again, as soon as the SRG amplitude decreases (because its contribution in the destructive interfering DE is reduced). Once the inverted SRG is increasing there is a conversion back to constructive (in the case of the P-polarized probe beam) or destructive (in the case of a S-polarized probe beam) interference.

The cross-polarized component of the 1st-order DE exhibits the same behavior for an S- and P-polarized probe beam (as predicted by the proposed model, see also **Figure 3.4**). During the inscription, the signal is growing until it saturates, but immediately after the IP translation it drops down to almost zero followed by a fast recovering. This indicates the re-orientation of the azobenzene-chromophores in the bulk and the formation of the inverted BBG (the SRG is not changing the polarization of the probe beam).

The remaining birefringence grating is eliminated by a single beam irradiation afterwards. This combined erase protocol is removing both gratings within 3min, which is approx. 600 times faster than the exposure to a single beam and ends up in the same final state (isotropic orientation parallel to the surface). The erase time is now comparable with the grating inscription time. **Figure 3.8a** shows the result of such a combined experiment. This method uses the photo-induced stresses generated by an inverted BBG to reverse the SRG growth. Once the SRG amplitude crosses zero, monitored with the AFM, one can switch off the IP irradiation. The single beam just has to erase the BBG which it does rapidly.

The illumination with a circular polarized beam erases the BBG (see **Figure 3.8b**) and aligns the chromophores perpendicular to the film surface. The cross-polarized DE data show that there is no spatially periodic BBG left. But the SRG is removed much more slowly (requires several hours of exposure).

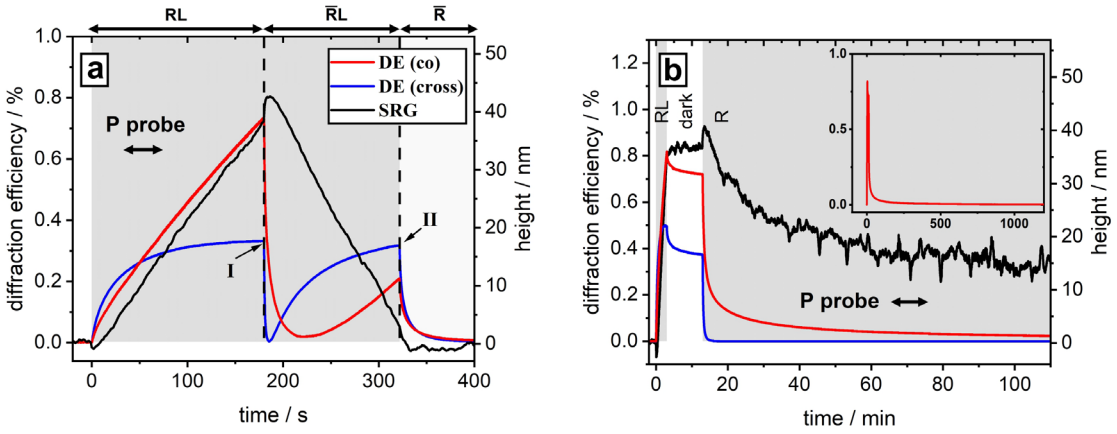

Figure 3.8. (a) *In situ* recorded relief height (SRG, black line) and 1st-order diffraction efficiency (DE, both co-(P)- and cross-(S)-polarized components are shown, P-polarized probe beam) for a combined erasing protocol of shifting the interference pattern (IP) by half the grating period, followed by single-beam exposure. The grey rectangles mark the irradiation sequence of the PAZO film with the RL-IP and single beam (dashed line II). At line I, the IP is shifted by 1µm, i.e. *half* its period. First the SRG is erased by the translation of the IP, then the remaining bulk birefringence grating is removed by ~1min of single-beam irradiation. (b) Single-beam erasure experiment for comparison. The polymer film is irradiated for 3min with the RL-IP, the SRG amplitude is then 40nm. Changes in topography and DE signal are recorded for 10min (without irradiation), followed by switching on the erase beam. After 20h of single beam exposure SRG and BBG vanish (see inset). This process is several orders of magnitude slower compared to the combined erasing protocol of (a) [single beam intensity in (a) $I = 100\ \mathrm{mW/cm^2}$, other parameters as **Figure 3.1**].

Contribution of J. Jelken:

J. Jelken has planned the experiments, prepared and characterized the samples, built the experimental set-ups, performed most of the measurements composing this publication and analyzed the obtained results. He has designed and assembled all figures, written the first version of the manuscript and actively participated in the discussion.

3.5. Publication V: Complex surface gratings in mixed polarization- and intensity interference patterns

- **Formation of Half-Period Surface Relief Gratings in Azobenzene Containing Polymer Films**

  J. Jelken, C. Henkel and S. Santer, *Applied Physics B*, **126** (2020**)**, 149

This publication is dedicated to the SP interference pattern (polarization interference pattern, one pump beam S- and the second P-polarized, see **Figure 2.11**). The irradiation with the SP-IP results in a surface grating with a period which is half the grating period of the IP. This behavior differs from all other IPs (polarization- as well as intensity interference patterns). The explanation for this unique behavior is the special orientation of the linearly polarized components of the IP. In the case of the ±45-IP these components are either S- or P-polarized, while in the SP-IP they are rotated by 45° (see **Figure 2.11**). It is found that the 1st-order DE rapidly increases and then saturates under illumination with the SP-IP, while the 2nd-order DE continuously increases with SRG amplitude (see **Figure 3.9**). The polarization analysis reveals that the 1st-order DE signal is purely cross-polarized, while the 2nd-order DE is purely co-polarized (for S- or P- polarized probe beams). The interpretation is, that the 1st-order DE, in the case of the SP-IP, carries only information about the BBG, because the SRG maintains the state of polarization in the case of an S- or P-polarized probe beam (principal polarizations). The 2nd-order DE additionally contains information regarding the SRG amplitude. The chromophore orientation of ±45° is introducing an angle of 45° between the fast- (slow-) axis, respectively, and the polarization of the probe beam (for a S- or P-polarized probe beam). The phase difference resulting from the -45° and +45° aligned chromophores rotates the light polarization by 90°.

Figure 3.9 shows that the SRG amplitude is continuously increasing while the orientation of the chromophores (BBG amplitude) is already saturated. This is surprising, because in the "orientation approach"[99] it is assumed that the photo-orientation (BBG) is the driving force for the SRG formation. Once the orientation is saturated the photo-induced stress, which results in the formation of the SRG, also disappears. This problem can be healed by adding a certain delay time of the surface deformation on the photo-orientation into the model.

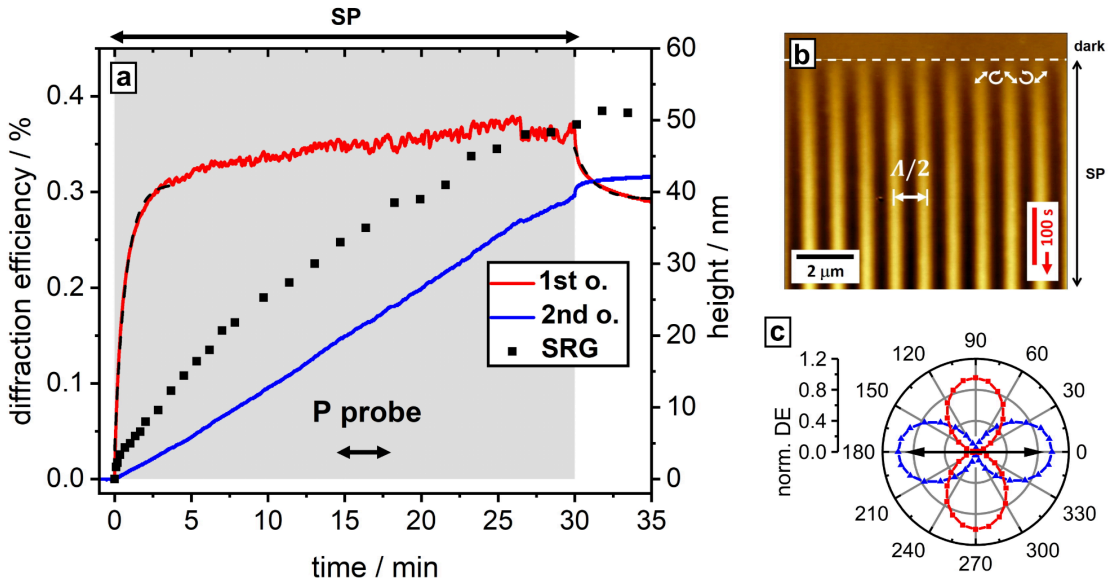

Figure 3.9. (a) *In situ* recorded SRG height (black dots) and diffraction efficiency (P-polarized probe beam) of the PAZO film under irradiation with SP-IP (same parameters as **Figure 3.1**). The grey rectangle marks the irradiation sequence of the film. The 1st-order DE (red curve) is increasing until the signal saturates after short time, while the 2nd-order DE (blue curve) is continuously growing. The SRG amplitude follows the 2nd-order DE and is also continuously increasing. The increase and the relaxation of the 1st-order DE is fitted with exponential functions (dashed line) giving the time constants $\tau_{write} = 43\text{s}$ and $\tau_{relax} = 70\text{s}$. (b) AFM micrograph of the polymer film deformation during irradiation. At the time marked by the dashed white line the irradiation with SP interference pattern is switched on. The local polarization relative to the topography maxima and minima is shown by white arrows. The surface profile after irradiation with the SP-IP ($\Lambda = 2\mu\text{m}$) appears with a half-period ($\Lambda/2 = 1\mu\text{m}$). At the end of the image (8min) the SRG amplitude reaches 20nm. (c) Polarization analysis of the 1st- and 2nd-order diffraction spot for a P-polarized probe beam. The 1st order is purely S-polarized (90° rotated) while the 2nd order is polarized in the same direction as the probe beam (black vector).

A simple calculation based on the half-period surface grating supports the assumption that the 1st-order DE only results from the BBG while the 2nd-order DE additionally also gives information about the SRG (see **Figure 3.10**). The half-period of the SRG shifts the 1st-order diffraction spot (correspondent to the SRG period) to larger diffraction angles, which coincides with the 2nd-order diffraction spot of the BBG (normal period). Therefore, the 2nd-order DE is a sum of the 2nd diffraction order of the BBG and the 1st diffraction order of the SRG. Thus, the different periods of the SRG and BBG provide a simple way of directly separating the BBG from the SRG kinetics without any complex calculations. Probing the

SRG formation with a ±45° linearly polarized probe beam shows no cross-polarization of the 1st-order DE. This is in agreement with the proposed model because in this case the probe beam is either polarized along the slow- or fast axis, which will not result in a rotation of the polarization of the probe beam.

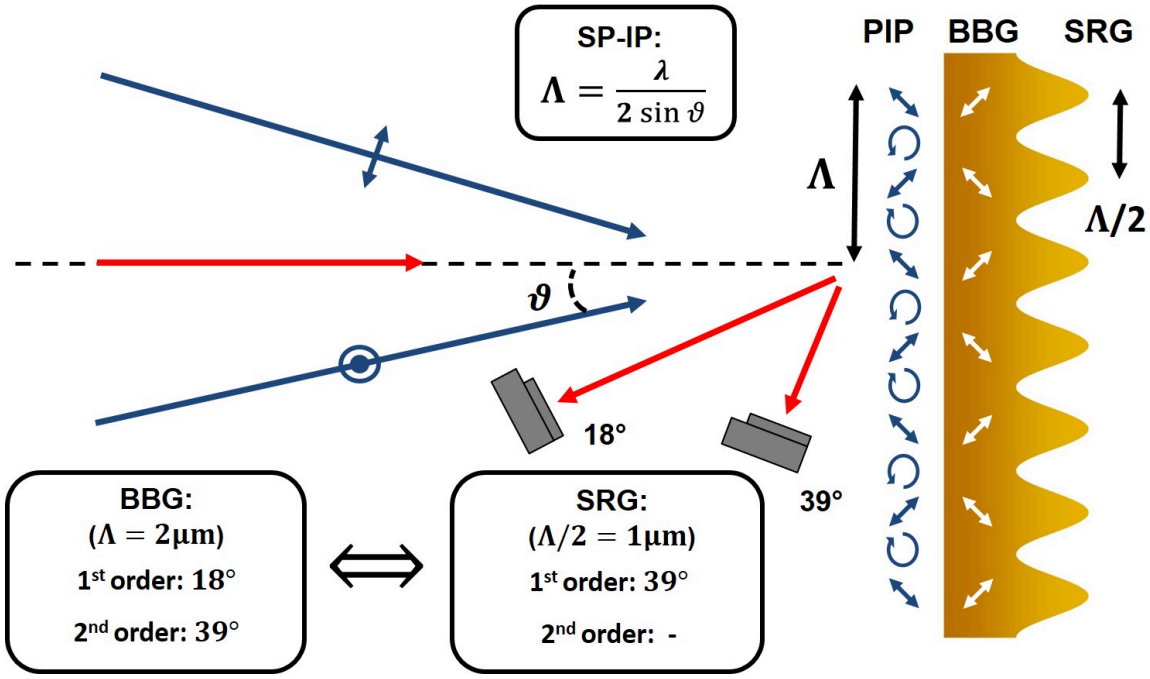

Figure 3.10. Sketch of the SRG formation in the case of the illumination with an SP-IP (polarization interference pattern, indicated by the blue arrows, projection onto the film plane). The period of the IP ($\Lambda = 2\mu m$) is set by the angle 2ϑ between the two interfering beams. Here, the intensity along the grating is constant, only the local polarization is changing with the period Λ. The surface of the polymer film responds with a half-period SRG ($\Lambda/2$). The 1st diffraction order of the BBG ($\Lambda = 2\mu m$) appears at an angle of 18° while the 2nd order at 39° ($\lambda_{probe} = 633nm$). Performing the same calculation for the SRG ($\Lambda/2 = 1\mu m$) results in a 1st-order diffraction angle of 39° while the 2nd order is evanescent. The photodiodes are placed at the angle of 18° and 39°. Therefore, the 1st-order DE (detector at 18° position) contains only information about the BBG (indicated by the white arrows, projection onto the film surface) and the 2nd-order DE (detector at 39° position) additionally carries the SRG signal.

In order to address the question why a half-period SRG is formed in the case of the SP-IP, several different experiments are performed. First, it is found, by the translation of the interference pattern (by half the grating period of the IP), that the SRG is invariant under a

rotation of the linearly polarized components of the IP by 90° and an interchange of the circularly polarized components. This is surprising, because a similar shift results in the case of the RL-IP (publication III and IV) in the erasure of the inscribed SRG. The explanation is the half period SRG as a result of the special chromophore orientation, so that no photo-induced stresses are generated to reverse the SRG growth. The 1st-order DE shows a rapid decrease as soon as the IP is translated, followed by an increase of the signal, while the SRG amplitude, as well as the 2nd-order DE, is only slightly affected (only a little jump can be seen). This indicates that the 1st-order DE shows the re-formation of the BBG. Several half- and quarter period shifts of the interference pattern are performed, in order confirm this assumption (together with the polarization analysis of the DE). Translating the IP by a quarter of the IP-period, generates photo-induced stresses to reverse SRG growth.

In publication I and II the assignment of the local polarization with respect to the SRG is determined for the ±45-IP. This information is now used for the assignment of the SP-IP to the local surface deformation. To this end, the IP is changed during the illumination from SP to ±45 (both polarization interference patterns) and the change in topography monitored. Here, it is important that in the change of the IP (rotation of the half-wave-plates) no phase shift between the two interfering beams is generated. In the case of the ±45-IP the SRG minimum appears where the local light field is P-polarized. After the change to the SP-IP the AFM micrograph shows that at this position, a linear polarization prevails and is forming an SRG maximum. The conversion of the interference pattern from SP ($\Lambda/2$ grating) to ± 45 (Λ grating) permits to change the period of the SRG by a factor of two. On the other hand this provides also a selective erase process of one of the two SRG maxima (of the SP surface grating) by changing from the SP to ±45- or $\pm 45_{\pi}$ out-of-phase-IP.

The half-period surface grating is very sensitive to small changes in the IP. The precise alignment of the polarization of the two pump beams is the important parameter in order to end up with a half-period surface grating with a constant modulation amplitude. A small deviation from the SP configuration (by 1°) results in an asymmetric grating amplitude (the grating period starts to double and coincides with the one of the IP). In a series of experiments the polarization angle between the interfering beams is stepwise reduced from 90° (SP-IP) to 0° (PP-IP). A polarization angle less than 90° results in the fading of the half-period grating and in the formation of a blazed grating (≈70°) with the period of the IP

(normal grating). The surface profile changes to a sinusoidal shape once the polarization angle has reached 45°. This shows the interplay between two processes. On the one hand the SRG formation due to a gradient in intensity and on the other hand because of a change in local polarization. The gradient in intensity becomes more and more pronounced during the change from polarization- to intensity interference pattern by reducing the polarization angle between the two interfering beams, while the polarization gradient is reducing.

Moreover, the unique half-period feature of the SP-IP enables to generate surface structures below the diffraction limit of light using far field irradiation. Increasing the angle between the two writing beams, the period of the IP decreases. The period of the surface relief can then even drop below the writing wavelength.[87,88] Structures as small as 250nm are produced, but only a few nm in amplitude. The inscription of sub-diffraction-limit structures using photo-lithography technique is of high interest, because it is easy, cheap and fast. At the same time, this also demonstrates the advantages of having both the optical probing and the scanning probe technique for the monitoring of the grating formation in azobenzene containing polymer films. Studying the DE of the inscribed gratings permits to probe at the same time the SRG and BBG formation. The disadvantage is that this method is limited by diffraction. Once the IP period equals the wavelength of the probe beam, no DE signal can be monitored. Only the AFM can be used to probe the SRG inscription of these small gratings.

Contribution of J. Jelken:

J. Jelken has planned the experiments, prepared and characterized the samples, built the experimental set-ups, performed all the measurements composing this publication and analyzed the obtained results. He has designed and assembled all figures, written the first version of the manuscript and actively participated in the discussion.

4. Reprints

4.1. Publication I: Solving an old puzzle: fine structure of diffraction spots from an azo-polymer surface relief grating

Applied Physics B (2019) 125:218
https://doi.org/10.1007/s00340-019-7331-8

Applied Physics B
Lasers and Optics

Solving an old puzzle: fine structure of diffraction spots from an azo-polymer surface relief grating

Joachim Jelken[1] · **Carsten Henkel**[1] · **Svetlana Santer**[1]

Received: 26 August 2019 / Accepted: 17 October 2019 / Published online: 1 November 2019

Abstract

We report on the experimental and theoretical interpretation of the diffraction of a probe beam during inscription of a surface relief grating with an interference pattern into a photo-responsive polymer film. For this, we developed a set-up allowing for the simultaneous recording of the diffraction efficiency (DE), the fine structure of the diffraction spot and the topographical changes, in situ and in real time while the film is irradiated. The time dependence of the DE, as the surface relief deepens, follows a Bessel function exhibiting maxima and minima. The size of the probe beam relative to the inscribed grating (i.e., to the size of the writing beams) matters and has to be considered for the interpretation of the DE signal. It is also at the origin of a fine structure within the diffraction spot where ring-shaped features appear once an irradiation time corresponding to the first maximum of the DE has been exceeded.

Graphic abstract

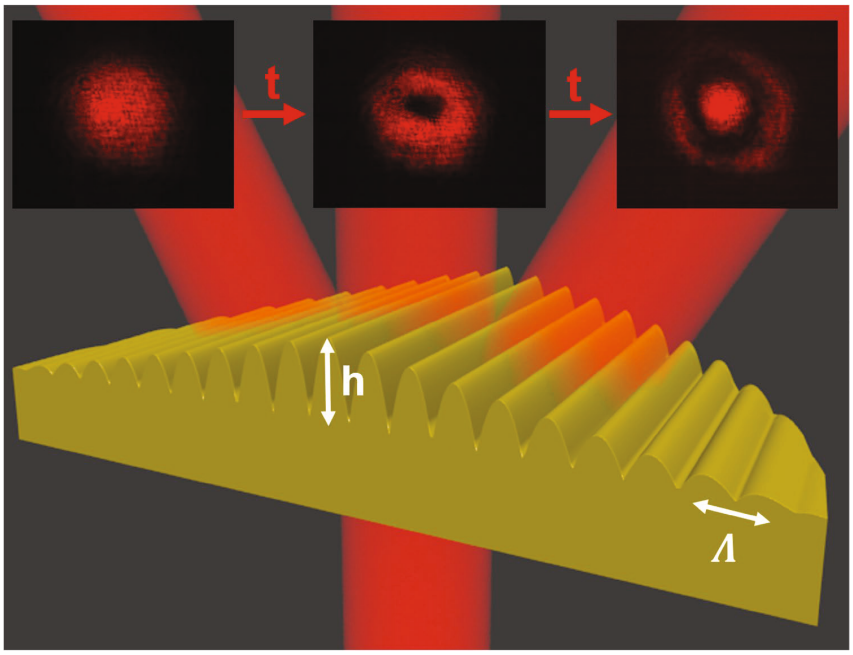

Electronic supplementary material The online version of this article (https://doi.org/10.1007/s00340-019-7331-8) contains supplementary material, which is available to authorized users.

Extended author information available on the last page of the article

1 Introduction

Azobenzene containing polymer thin films can develop significant opto-mechanical stress under irradiation with spatially modulated light [1, 2] which results in the macroscopic deformation of the surface. The deformation ranges from elongation or contraction in one direction during irradiation with linear polarized light [3] to a fine vortex-like topographical response to a complex shape of the inscribing beam [4–6]. Special relief structures can be generated by applying illumination with an interference pattern, where the incoming light shows a periodic variation of the magnitude or local orientation of the electrical field vector [7, 8]. The dynamical responsive of these polymeric materials is such that the topography deforms on time scales of seconds to minutes, mimicking the optical interference pattern, and establishes a sinusoidal profile, so-called surface relief grating (SRG), whose period is in most cases equal to the optical periodicity [9–13]. It was demonstrated that such topographical gratings can have periods as small as 125 nm for a certain polarization pattern (SP configuration: one writing beam s-polarized, the other one p-polarized), while the height of the pattern can be as large as ~ 90% of the total thickness of the polymer film (in the RL configuration: one beam with right-handed circular polarization, the other beam left-handed) [14, 15]. The process takes place in air without additional solvent or temperature softening, under rather low intensity ($I \sim 50$ mW/cm^2). This is remarkable because the polymer is in a solid (glassy) state and its mechanical modulus is several hundred of MPa. A possible explanation of such a deformation is the orientation model proposed by Saphiannikova et al. [16, 17] In this model, the SRG formation is considered as a multiscale chain of several processes starting from the small-scale motion of azobenzene molecules under cyclic *trans–cis–trans* isomerization, which causes the local alignment of azobenzene groups perpendicularly to the electrical field vector, followed by re-orientation of the polymer backbones they are connected to [18, 19]. The process ends up generating strong internal, anisotropic stress and the subsequent macroscopic opto-mechanical deformation of the film, as manifested in the SRG [20–25]. During this process, the formation of two gratings can be distinguished: a birefringence grating in the bulk due to the local alignment of azobenzene chromophores, and a surface grating as a result of topographical deformation.

Experimentally, the SRG formation process can be probed by focusing a red laser beam on the polymer film and measuring the intensity of the diffracted light as a function of irradiation time. (At the probe wavelength, the material absorption is relatively weak.) The changes in the diffraction efficiency (DE) signal follow a *n*th-order Bessel function and can be explained using a time-dependent model based on the Raman–Nath diffraction theory [26]. It has been reported, indeed, that the diffraction efficiency is not monotonously increasing as a function of irradiation time, but can drop in the course of grating development [27–32]. However, the DE signal contains information about bulk and surface gratings, and requires a quite involved de-convolution model to separate the contributions of both gratings to the time-dependent DE signal [33–36].

Recently, we have proposed a set-up where one can directly separate birefringence and surface gratings by measuring the development of DE signal and topography simultaneously and in situ, i.e., during irradiation [37]. The set-up consists of three parts (see Scheme 1): (1) a two-beam interference system for generating a well-defined intensity or polarization interference pattern; (2) a probe laser with a set of photodiodes for recording the diffraction efficiency, and (3) an atomic force microscope (AFM) for acquiring the change in surface topography during irradiation. The DE and AFM data are taken simultaneously over time scales of seconds to minutes, while the SRG grows in amplitude in the presence of the interference pattern. In this paper, complementing the above-described set-up, we report on data taken with an additional component that acquires the spatial intensity profile of the diffraction spot. Moreover, we explain a maximum and subsequent decrease in the DE that appears during the development of the SRG when its amplitude typically exceeds around 100 nm. The explanation is supported by calculations using a "reflecting phase screen" model in the Raman–Nath approximation,[26] and is based on the fact that the profile of the writing beam has a Gaussian shape. The corresponding modulation depth of the SRG changes over the inscribed area (see Fig. 4b below): the grating has a maximal amplitude in the center of the writing spot which drops radially to periphery. The size of the probe beam that records the SRG growth, relative to the inscribed area, determines the conditions where the DE signal peaks occur. Using a wide probe beam, which matches the inscribed grating area in size, one finds a fine structure in the spatial profile of the diffraction spot, which has been reported earlier by other groups [38]. The spatial profile of the diffraction spot changes as a function of the SRG height starting from a Gaussian to a hollow ring ("donut" like) and finally to a ring structure with a bright center. The hollow ring appears at the moment where the total DE signal decreases, while the ring with the bright center sets in when the DE signal starts to increase again. On the example of two different polymers, at fixed size of the writing and probe beams, we show that the decrease in the DE signal and the variation of the fine structure of the beam profile of diffraction spot starts at the same SRG height. For a very small probe beam diameter, the diffraction efficiency follows the

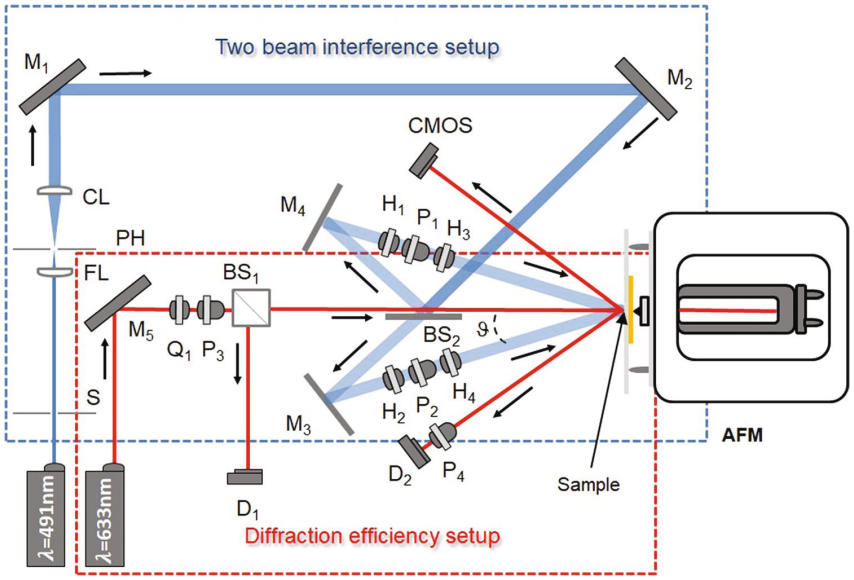

Scheme 1 Scheme of the experimental set-up consisting of three parts: (1) a two-beam interference part for generating the interference pattern (blue laser beams), (2) a diffraction efficiency (DE) set-up (red laser beams) enabling the collection of in situ information about the optical grating (periodic refractive index and surface relief), and (3) an atomic force microscope (AFM) for in situ recording of the surface morphology (during irradiation). *S* shutter, *M* mirror, *D* detector, *P* polarizer, *H* half-wave-plate, *Q* quarter-wave-plate, *BS* beam splitter, *CL* collimating lens, *FL* focusing lens, *PH* pin hole, *CMOS* camera

prediction for a homogeneous grating of infinite area (given by squares of ordinary Bessel functions).

2 Experimental part

2.1 Materials and methods

Poly[1-[4-(3-carboxy-4-hydroxyphenylazo) benzenesulfonamido]-1,2-ethanediyl, sodium salt] (Pazo) and *Poly[(methyl methacrylate)-co-(Disperse Red 1 acrylate)]* (poly(MMA-co-DR1A)) are purchased from Sigma-Aldrich. The Pazo polymer solution is prepared by dissolving 170 mg Pazo in 1 ml solution containing a mixture of 95% methoxyethanol and 5% ethylene glycol. The poly(MMA-co-DR1A) polymer is dissolved in chloroform to get a concentration of 60 mg/ml.

Sample preparation The polymer films are prepared by spin casting at 3000 rpm for one minute of 100 µl of the polymer solution on a thin glass slide. The film thickness is measured from the cross-sectional profile of atomic force microscope (AFM) micrographs along a scratch within the polymer film.

2.2 Methods

Home-made set-up for studying SRG formation in situ The set-up consists of three parts: (1) two-beam interference lithography, (2) atomic force microscopy (AFM) and (3) diffraction efficiency (DE) measurement (Scheme 1). The two-beam interference lithography with a continuous-wave diode-pumped solid-state laser (Cobolt Calypso, $\lambda = 491$ nm) allows generating well-defined spatiotemporal interference patterns by changing the polarization of two interfering beams in a controlled way. In this part of the set-up, the laser beam is spatially expanded and then collimated with a pair of focusing and collimating lenses and a pinhole (Scheme 1). The beam diameter is set to 4 mm and the total intensity is varied between 100 mW/cm^2 and 200 mW/cm^2. Additionally, a 50:50 beam splitter is added to separate the initially single beam into two beams of the same intensity. These two beams pass through a set of wave plates and polarizers allowing independent control of intensity and polarization. For instance, adding a half-wave plate to each of the beam paths of the interference set-up (H_3, H_4), one with an angle of +22.5° and the second with an angle of −22.5° with respect to the optical axis, results in the ±45° interference pattern (IP). This is a polarization interference pattern with constant intensity in the sample plane, but spatially varying distribution of polarization.

The second part of the home-made set-up is an atomic force microscope (AFM, PicoScan (Molecular Imaging) AFM operating in intermittent contact mode) enabling measurements of the polymer topography changes in situ and in real time, i.e., under varying irradiation conditions. The scan speed of the AFM is set to 1 Hz with a scan area of 10×10 µm and a resolution of 512×512 pixel. Commercial tips (Nanoworld-Point probe) with a resonance frequency of 130 kHz, and a spring constant of 15 N/m are used. The sample is oriented with the polymer surface pointing towards the AFM tip, such that irradiation is "from below", i.e., through the glass substrate (Scheme 1). The

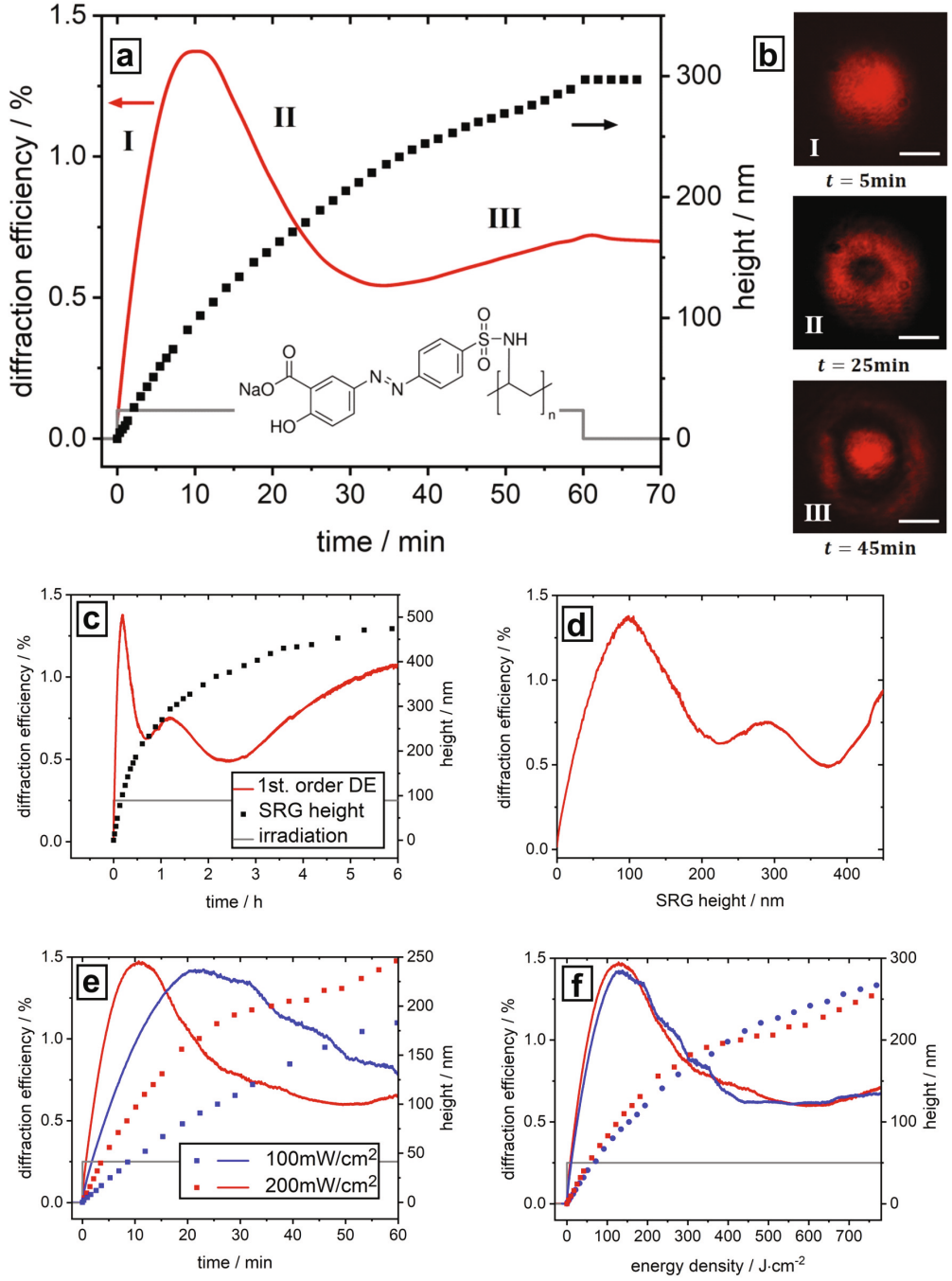

SRG amplitude is determined from the plot of the surface profile of the AFM scan by measuring the difference in height between topography maximum and minimum. A plot of this value as a function of time gives the growth kinetic of the SRG. To obtain at the same time information about the alignment of the azobenzene side chains in the polymer film, a red probe laser beam (Uniphase, HeNe, 633 nm) with a tunable beam diameter from 1 mm to 3 mm ($I = 30$ mW/cm^2) is integrated into the set-up. The wavelength of 633 nm is outside the absorption band of both polymers studied in

◂**Fig. 1** **a**, **c** In situ-recorded SRG height and diffraction efficiency (DE) under irradiation of a Pazo film with a ±45° interference pattern (IP) of $\lambda = 491$ nm light ($I = 200$ mW/cm^2, $\Lambda = 2$ µm grating period, thickness $d = 1$ µm); **a** 1st h of irradiation; **c** irradiation during 6 h. Note the non-monotonous increase and decrease in the first-order DE (red curve), while the SRG height increases continuously (black dots). The inset depicts the chemical structure of the Pazo polymer. **b** Spatial profile of the first-order diffraction spot for three irradiation times (camera images, scale bar 1 mm). The shape is Gaussian, until the maximum DE signal (SRG height of 100 ± 10 nm, micrograph marked by I) is reached. When the DE starts to decrease, there is a noticeable change in the beam profile (micrographs marked by II and III). The intensity in the center of the diffraction spot decreases, resulting in a ring-shaped distribution (II). Further irradiation changes the spot shape to a ring structure with a bright center (III). **d** Parametric representation of the data in **c**: DE (optical data) as a function of SRG height (AFM data). **e** In situ-recorded SRG height (dots) and 1st order DE (solid line) for two irradiation intensities: 200 mW/cm^2 (red) and 100 mW/cm^2 (blue). **f** Plot of the data of **e** as a function of fluence (intensity multiplied by time)

this work and its intensity is weak enough not to affect the polymer film, as proved by AFM measurements. To calibrate the DE, a beam splitter with a ratio (T:R = 90:10) is used in the DE set-up, such that 90% of the light arrives on the sample (intensity I_0) and 10% on a photodiode. The signal of this photodiode is recorded during the whole measurement for controlling the stability of the probe beam during the experiment. The diffraction efficiency is defined as the ratio of the intensity of diffraction order (I_n) and the intensity of the incoming light (I_0): $\eta_n = \frac{I_n}{I_0}$, where I_0 is 90% of the total intensity of the probe beam. The DE set-up additionally includes a quarter-wave plate converting the polarization of the probe beam from linear to circular. The polarization state of the probe beam can be set by adding a polarizer afterwards. The probe beam is P-polarized for all measurements discussed in this paper. The detector D2 measures the P-polarized component of the 1st order DE signal.

The three different set-ups: two beam interference, AFM and DE acquisition are controlled and operated with a software (Profilab-Expert, Abacom) specifically designed in the laboratory to record signals of the photodiodes, control the irradiation shutter and to synchronize DE set-up with the AFM. A computer-generated signal regulates the irradiation with the help of an AD/DA converter (Kolter Electronic, PCI-AD12 N-DAC2), which also records the signals of the photodiodes. This irradiation signal is sent to the diffraction efficiency set-up as well as to the AFM by recording the signal with the aux-input of the AFM controller, which enables to synchronize the different components.

The set-up is aligned in such a way that the AFM probe is placed in the center of the two interfering beams, using as a reference spot the red laser of the AFM optical lever focused on the cantilever. Afterwards, the probe beam is aligned to the center of the IP and AFM probe.

Silicon detectors (Thorlabs DET 100A/M) are used in the diffraction efficiency (DE) set-up to measure the intensity of the diffracted probe beam. A 600-nm long-pass filter is placed in front of each photodiode to be only sensitive to the probe beam. The intensity of the diffracted light is recorded every 200 ms.

The change in the beam profile of the first-order DE is recorded with a CMOS Camera (Thorlabs DCC1545 M) with a sensor size of 6.7 × 5.3 mm and resolution of 1280 × 1024 pixel (pixel size 5.2 µm). For these measurements, the photodiode is replaced by the CMOS camera; alternatively, the camera can be placed in the direction of the -1 diffraction order (see Scheme 1).

All experiments are carried out under yellow light in the laboratory (to avoid undesirable photo-isomerization) and under ambient conditions, *i.e.*, at room temperature with a relative humidity of 55%. The whole set-up is covered with a non-transparent encapsulation to avoid any influence of the environment on the measurement (parasitic light, air circulation and vibration).

3 Results and discussion

Figure 1 shows a typical curve recorded during irradiation of the azobenzene containing polymer film (Pazo) with the ±45° interference pattern (IP). The SRG height (black dots in Fig. 1) increases continuously, while the DE signal (1st order, red curve in Fig. 1a) has a Bessel function shape where several maxima and minima appear. Indeed, the DE signal first increases within 10 min of irradiation followed by a decrease when the SRG height reaches 100 ± 10 nm. In the course of irradiation during 6 h two maxima of the DE signal (at SRG height of 100 ± 10 nm and 300 ± 10 nm) and two minima (at 200 ± 10 nm and 400 ± 10 nm) develop (Fig. 1c, d). Similar behavior is observed for other polymers, here illustrated with poly(MMA-co-DR1A) (Figure S1b, Supporting Information). The extremal points of the DE signal appear at the same positions relative to the SRG height, although the SRG kinetic growth is much faster for the poly(MMA-co-DR1A) (Figure S1a, Supporting Information).

The DE signal typically measured is the integrated value over the whole detector area, i.e., the entire diffraction spot. The analysis of spot profile in the 1st order reveals, however, a time-dependent intensity modulation resembling “donut” structure. As long as the DE signal grows (first 10 min of irradiation), the beam profile has a Gaussian shape (micrograph I in Fig. 1b). At maximum DE signal (the SRG height is 100 ± 10 nm), the intensity in the center of the laser spot (micrograph II in Fig. 1b) starts to decrease (appearance of the “donut”). Further irradiation with an interference pattern will modify a spot profile further into a ring structure with

a bright center (after 45 min, micrograph III in Fig. 1b). The time evolution of diffraction spot profile is shown in a video (see Supporting Information, Figure S2). The DE slightly decreases when the pump beam is switched off (after 60 min of irradiation), while the SRG amplitude and the spatial profile of the first-order diffraction spot do not change. This indicates directly the relaxation of the birefringence grating. When the irradiation intensity is reduced in two times (from 200 to 100 mW/cm^2), a similar behavior of the DE signal is observed (blue curve in Fig. 1e), but at longer irradiation time where the SRG has reached to the height of 100 ± 10 nm. This behavior scales with the energy fed into the system, as illustrated by the collapse of the DE and SRG data when plotted as a function of the product of intensity and irradiation time (insert in Fig. 1f).

At constant irradiation parameters, the kinetic of the SRG growth and the maximal SRG height depends on the thickness of the polymer film. Figure 2 shows a comparison of the first-order DE and SRG height for different thicknesses of the Pazo polymer film and a fixed irradiation time of 1 h. In he case of 1-µm-thick polymer film (Fig. 2a), the DE signal increases until the SRG height of 100 ± 10 nm (13 min of irradiation at $I = 200$ mW/cm^2) is reached. The inset of Fig. 2a shows the in situ-recorded AFM micrograph during irradiation. The micrograph depicts the temporal evolution of the polymer topography with the vertical direction from top to bottom (red arrow at the bottom right corner) corresponding to the irradiation time. The AFM scanning starts in dark (flat topography), at the position marked by the dashed white line; the irradiation with ±45° interference pattern (IP) is switched on. The distribution of the electric field vector relative to the topography maxima and minima is shown by the white arrows (Fig. 2a). In the case of a 750-nm-thick polymer film, the kinetics of the SRG growth is slower. The final SRG height is 160 nm after 1 h of irradiation (see also the inset in Fig. 2b, showing the final in situ AFM micrograph). The peak in the DE appears also at the SRG height of 100 ± 10 nm (after 17 min of irradiation). Further reduction

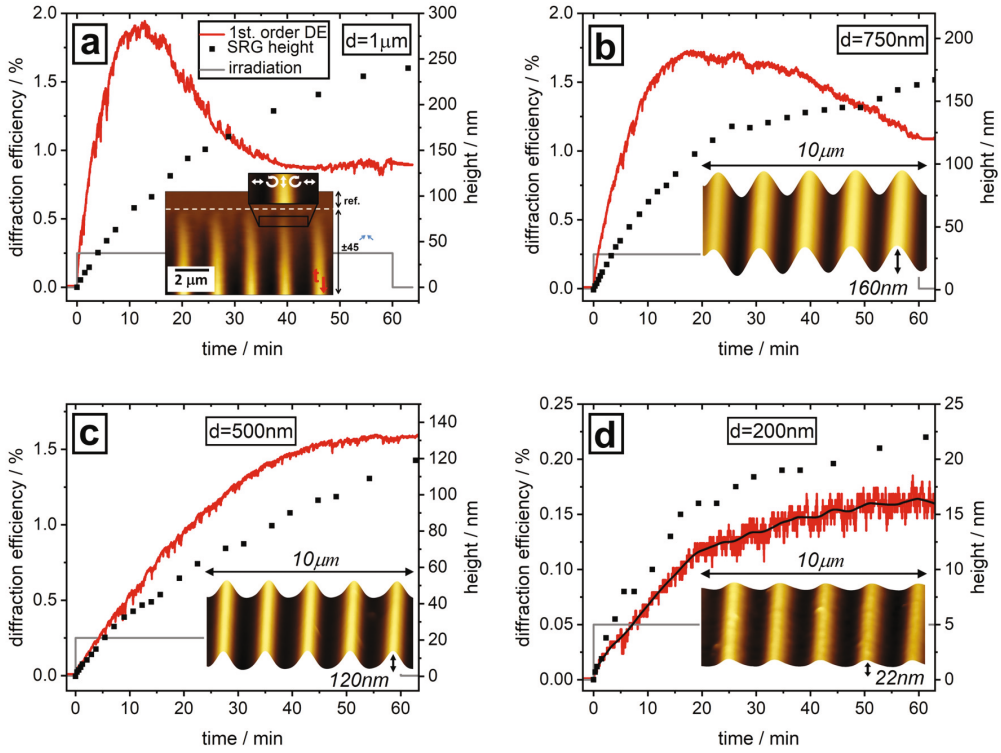

Fig. 2 *In situ*-recorded SRG height (black dots) and diffraction efficiency (1st order DE, red curve) as a function of time during irradiation with ±45° IP for different thicknesses of the Pazo polymer film: **a** 1 µm, **b** 750 nm, **c** 500 nm and **d** 200 nm. The inset in **a** shows the in situ AFM micrograph of the polymer film deformation during irradiation. The direction of scanning (indicated by the red arrow at the bottom right corner) is from top to bottom showing the temporal evolution of film topography. The AFM scanning starts without irradiation (flat film), and at the position marked by the dashed white line, the irradiation ($\lambda = 491$ nm, $I = 200$ mW/cm^2, ±45° configuration, $\Lambda = 2$ µm) is switched on. The local polarization of the electric field relative to the topography maxima and minima is shown by white arrows. The insets in **b**–**d** illustrate the topographies of the final SRG measured by AFM

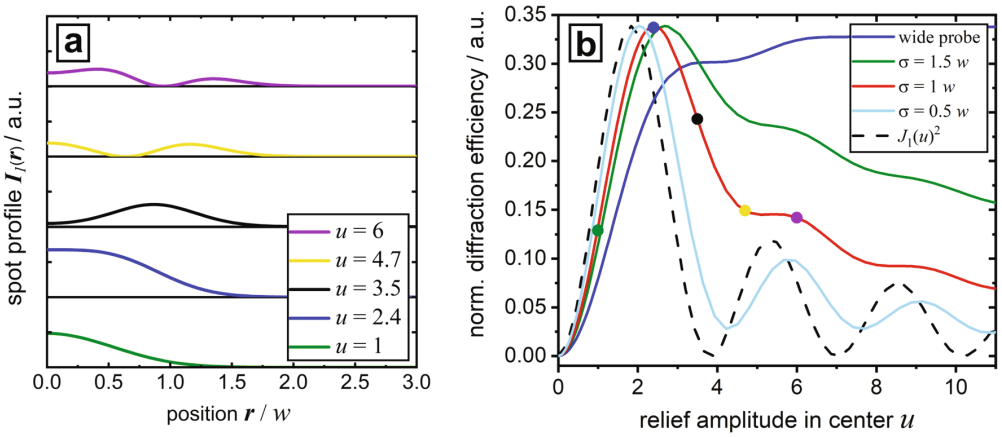

Fig. 3 **a** Theoretical prediction for the spatial fine structure of the $n = 1$ diffraction spot [Eq. (1)]. The parameter u gives the modulation depth at the center of the phase grating, w is the radius of the irradiated grating area (assuming a Gaussian profile). **b** Diffraction efficiency as a function of grating modulation u (in the center), for different sizes σ of the probe beam. Solid lines: numerical calculation based on Eq. (16), integrating the diffracted intensity over the area of the $n = 1$ spot. Dashed line: comparison to the Bessel function $J_1(u)^2$ evaluated at the grating center. All efficiencies are normalized to their maximal value. The dots mark the parameters chosen in **a**

of the film thickness to 500 nm results in a drop of the final SRG height to 120 nm (Fig. 2c). In the DE, a saturation level at the characteristic height of 100 ± 10 nm is reached. In the case of 200-nm-thick polymer film, the maximal SRG height after 1 h of irradiation is 22 nm (Fig. 2d) and the DE signal does not show any drop.

In the following, we explain that the distribution of the intensity within the diffraction spot is the result of the integration of light diffracted at different SRG modulation depths (different positions). Indeed, the grating does not have a constant modulation amplitude, u, over the inscribed area, but rather a circular shape set by the profile of the writing beams (see schematic representation in Fig. 4b), due to the Gaussian profile of the writing beam. Since the spot sizes of the writing (4 mm) and the probe beam (3 mm) are comparable, the DE signal is acquired from the whole irradiated area where the probe beam is diffracted at spatially inhomogeneous modulated SRG amplitude.

To compare the data with a theoretical model, we have computed the diffracted light wave in the far field and the near field (see Appendix for details). The basic idea is to "shrink" the azo-polymer film into a phase grating that is observed in reflection. For our setup, the intensity of the diffraction spot in the nth order is given by:

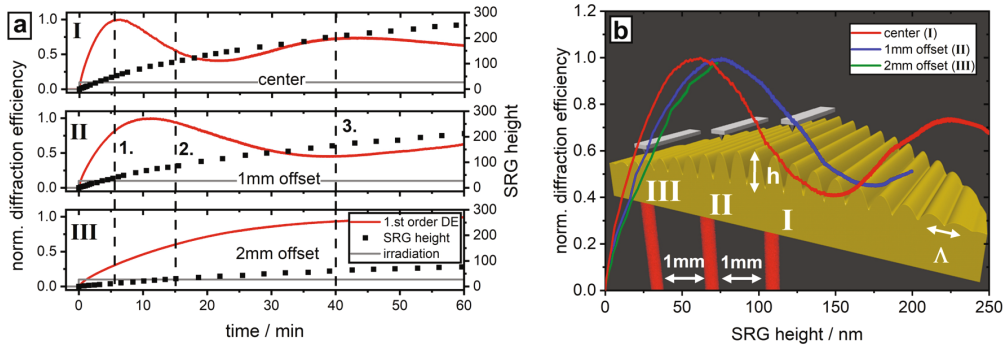

Fig. 4 **a** In situ-recorded SRG height and normalized diffraction efficiency for the ±45° interference pattern for different distances away from the center (center (I), 1 mm (II) and 2 mm (III) offset from center). The probe beam is focused to a four times smaller radius than the writing beam. The black dashed lines mark the moments where the fine structure of the 1st order diffracted beam is (1) Gaussian, (2) ring shaped (donut), and (3) ring shaped with a bright center. **b** Plot of DE vs. SRG amplitude (from **a**) measured at three different positions. A scheme is shown in the background for illustration. (Irradiation at $\lambda = 491$ nm with $I = 200$ mW/cm^2, $\Lambda = 2$ µm, $d_{\text{Pazo}} = 1$ µm)

$$I_n(\boldsymbol{r}) = |R|^2 I_{\text{in}} \left| J_n(u(\boldsymbol{r})) \right|^2 \exp\left(-\boldsymbol{r}^2/\sigma^2\right) \quad (1)$$

Here, $\boldsymbol{r}$ are two-dimensional coordinates in the plane perpendicular to the diffracted beam, $|R|^2 I_{\text{in}}$ is the total reflected intensity (typically only a few percent of I_{in}), J_n is the nth-order Bessel function, the function $u(\boldsymbol{r})$ is proportional to the phase front modulation amplitude imprinted at position $\boldsymbol{r}$ by the film, and $\exp\left(-\boldsymbol{r}^2/\sigma^2\right)$ gives the intensity profile of the probe beam. The diffraction efficiency η_n is obtained by integrating Eq. (1) over $\boldsymbol{r}$ followed by normalization. The results of this calculation are illustrated in Fig. 3. The angular profile of the diffraction spot is shown in Fig. 3a, assuming that the probe beam diameter (σ) is similar in size to the SRG-inscribed area ($w = \sigma$). As the grating amplitude grows (from bottom to top), a "dark ring" appears in the spot profile starting at black curve, $u = 3.5$, in Fig. 3a).

This happens when the total diffracted intensity is beyond its maximum, as shown in Fig. 3b (dots on the red curve). There, we also show the influence of the probe beam size: a narrow beam ($\sigma = 0.5w$) diffracts similar to a homogeneous grating, with an efficiency related to the Bessel function $\left|J_1\right|^2$ that oscillates beyond its first the maximum. For a much wider beam, the diffraction efficiency increases monotonously.

We finally estimate the SRG height that corresponds to the first maximum of the first-order DE. In the reflection screen model, the optical path length permits to estimate the phase as $2\pi n' L/\lambda$, where n' is the (real) refractive index at the probe wavelength. The probe beam passes from the substrate to the polymer–air interface and back. The relevant modulation depth of the path length L is, therefore, twice the SRG height δh. This gives a phase modulation depth

$$u = \frac{4\pi n' \delta h}{\lambda} \quad (2)$$

The maximum of the Bessel function J_1 appears at $u_{\max} \approx 1.84$ so that we get a peak-to-bottom amplitude $2\delta h_{\max} \approx 108$ nm in reasonable agreement with the experimental value 100 ± 10 nm ($n'_{633\,\text{nm}} = 1.7$). The agreement would become better (smaller value for $\delta h_{\max}$) if we took into account a volume grating in the film which also contributes to the optical DE. Such an analysis will be presented in another paper.

We confirm experimentally the theoretical predictions shown in Fig. 3. The spot size of the probe beam is reduced to 1 mm and the DE signal, as well as the SRG amplitude, is recorded during irradiation at different position along the irradiated area (Fig. 4b): at the center of the irradiated area (red curve in Fig. 4aI), 1 mm and 2 mm away (red curves in Fig. 4aII, III). Here, the probe beam is still centered with respect to the AFM probe, but the center of the pump beam is shifted stepwise with respect to the AFM cantilever. As can be seen from Fig. 4a with increasing the distance from the center, the height of the SRG decreases due to the Gaussian envelope of the writing beam intensity. The DE signal recorded in the center (I) has similar shape as in the case presented in Fig. 1, but the extrema of curve (maxima and minima) are shifted to smaller SRG height as predicted in Fig. 3b. At 1 mm off center, the SRG height is smaller and the DE curve shifts to later times (red curve in Fig. 4aII). The last measurement is performed 2 mm away from the center at the edge of the illumination spot (see Fig. 4aIII); here, the intensity is weak, and thus the maximal SRG height is 70 nm, so that no drop in the DE became noticeable.

4 Conclusions

We demonstrated that during continuous irradiation of a photosensitive polymer film with an interference pattern, the diffraction efficiency (DE) of a probe beam changes in a non-monotonous way, showing several maxima and minima; while the amplitude of the surface relief grating (SRG) is monotonously increasing. We used the Raman–Nath theory to compute the fine structure in the spatial profile of the diffraction spot that appears clearly when the DE goes through its maximum. The reason for this fine structure is that the spatial profile of the inscribed grating differs from an infinitely extended grating because of the Gaussian envelope of the irradiation pattern. Using a probe beam which matches the irradiated area in size, the profile of the diffraction spot changes as a function of the SRG height from a Gaussian through a hollow beam ("donut") to a ring structure with a bright center. For a narrow probe beam, the DE follows the theory for an infinite grating (squared n'th oder Bessel function), with a maximum first-order DE appearing for SRG heights around ~ 100 nm. In deeper reliefs, the DE is distinctly different from the Bessel function when the probe beam size is not much narrower than the irradiated area. These results are based on a simple reflecting phase screen model that combines the SRG and the birefringence grating in the bulk of the film into one complex reflection function [39]. These findings are confirmed in the experiment by probing the DE with a probe beam diameter much smaller than the inscribed area and aiming the probe at different positions of the SRG, while measuring the SRG amplitude simultaneously with an AFM. Only probe beams with sizes as narrow as half the waist of the writing beams ($\sigma = 0.5\ w$) diffract similar to an infinite grating with homogenous modulation depth. The Raman–Nath-based model we propose also comprehensively explains the fine structure within the diffraction spot.

Acknowledgements This research is supported by the Helmholtz Graduate School on Macromolecular Bioscience (Teltow, Germany). We thank Burkhard Stiller and Andreas Pucher for the fruitful discussions.

Appendix

We get a tractable calculation of the diffraction efficiency and the spot profile, when the sample is modeled as a reflecting phase screen. This means that the light wave, after (partial) reflection from the sample, is given by a complex reflection function that contains a spatially modulated phase [39]

$$\psi_{\text{out}}(\boldsymbol{r}) = R\exp\left[i\varphi(x,y)\right]\psi_{\text{in}}(\boldsymbol{r}) \tag{3}$$

where R is the overall reflection amplitude and x, y are coordinates parallel to the screen [we write $R\psi_{\text{in}}(\boldsymbol{r})$ although this wave has actually a reversed propagation direction due to reflection from the non-modulated screen (specular order)]. We first compute the diffraction pattern in the far field: it is given in the Fraunhofer–Kirchhoff approximation, by

$$I(\boldsymbol{q}) = \left|\tilde{\psi}_{\text{out}}(\boldsymbol{q})\right|^2 \tag{4}$$

where $\tilde{\psi}_{\text{out}}(\boldsymbol{q})$ is the the 2D Fourier transform of $\psi_{\text{out}}(\boldsymbol{r})$. We consider first the simple case of an infinitely extended phase grating where $\varphi(x,y) = u\sin(\boldsymbol{G}\cdot\boldsymbol{r})$ and $\boldsymbol{G}$ is the grating vector. Then, the outgoing wave is

$$\psi_{\text{out}}(\boldsymbol{r}) = R\exp[iu\sin(\boldsymbol{G}\cdot\boldsymbol{r})]\psi_{\text{in}}(\boldsymbol{r}) \tag{5}$$

The first factor (the phase modulation) is periodic in $\boldsymbol{r}$ along the direction $\boldsymbol{G}$ with period $\Lambda = 2\pi/G$. It can be expanded in a Fourier series

$$\exp[iu\sin(\boldsymbol{G}\cdot\boldsymbol{r})] = \sum_n J_n(u)\exp(in\boldsymbol{G}\cdot\boldsymbol{r}) \tag{6}$$

with coefficients $J_n(u)$ given by Bessel functions (Jacobi-Anger expansion). If the incoming wave is a plane wave, $\psi_{\text{in}}(\boldsymbol{r}) = \sqrt{I_{\text{in}}}\exp\left(i\boldsymbol{k}_{\text{in}}\cdot\boldsymbol{r}\right)$, the outgoing wave contains the wave vectors

$$\boldsymbol{k}_n = \boldsymbol{k}_0 + n\boldsymbol{G} \tag{7}$$

We may choose the x-axis along $\boldsymbol{G}$ and introduce the diffraction angle θ_n via $k_{nx} = k\sin\theta_n$ with the wavenumber $k = 2\pi/\lambda$. The discrete diffraction orders appear under the angles (Bragg–Laue condition)

$$\sin\theta_n - \sin\theta_0 = \frac{nG\lambda}{2\pi} \tag{8}$$

where λ is the wavelength of the wave. For an infinite grating, the diffraction efficiencies are thus given by the squared coefficients in Eq. (6):

$$\eta_n = \frac{I_n}{I_{\text{in}}} = |R|^2\left|J_n(u)\right|^2 \tag{9}$$

In the experiment, the grating does not have a constant modulation amplitude u, but rather a circular shape set by the profile of the writing beams. We assume here a Gaussian grating profile

$$\varphi(x,y) = u(\rho)\sin Gx \quad u(\rho) = ue^{-\rho^2/2w^2} \tag{10}$$

with $\rho^2 = x^2 + y^2$. The width w is much larger than the grating period Λ. This motivates an approximate evaluation of the Fourier transform $\tilde{\psi}_{\text{out}}(\boldsymbol{q})$ (the far field)

$$\tilde{\psi}_{\text{out}}(\boldsymbol{q}) = R\sqrt{I_{\text{in}}}\int \mathrm{d}x\,\mathrm{d}y\; \mathrm{e}^{iu(\rho)\sin Gx}\exp\left[i\left(\boldsymbol{k}_{\text{in}} - \boldsymbol{q}\right)\cdot\boldsymbol{r}\right] \tag{11}$$

that we explain in the following. We split the integral along x into periods of size Λ centered in $x_l = l\Lambda$ and replace $x \to x_l + x$ with $-\Lambda/2 \le x \le \Lambda/2$ and $l = 0, \pm1, \pm2, \cdots$. We also focus on a far-field direction close to the n'th order and set $q_x = k_{\text{in}x} + nG + \delta q$ with $\delta q \ll G$ (angular fine structure of the diffraction spot). Observe that $\left(q_x - k_{\text{in}x}\right)\left(x_l + x\right) \equiv \delta q x_l + (nG + \delta q)x \bmod 2\pi$. We apply a multiple-scale approximation and assume that the grating modulation $u(\rho)$ varies slowly across the grating period Λ. This means that we can set

$$u(\rho) \approx u\left(\rho_l\right), \quad \rho_l^2 = x_l^2 + y^2 \tag{12}$$

The integral along x over one grating period then gives

$$\int_{-\Lambda/2}^{\Lambda/2} \mathrm{d}x e^{iu(\rho_l)\sin Gx}\exp\left[-i(nG + \delta q)x\right] \approx \Lambda J_n\left(u\left(\rho_l\right)\right) \tag{13}$$

where a small phase ($|x\delta q| \le \Lambda\delta q$) was neglected. (This will be justified from the end result Eq. (15) below.) The sum over the grating periods is replaced back by an integral

$$\begin{aligned}\tilde{\psi}_{\text{out}}(\boldsymbol{q}) &\approx R\sqrt{I_{\text{in}}}\sum_l \Lambda\int \mathrm{d}y\; J_n\left(u\left(\rho_l\right)\right)e^{-i\delta\boldsymbol{q}\cdot\boldsymbol{r}_l} \\ &\approx R\sqrt{I_{\text{in}}}\int d^2r\; J_n(u(\rho))e^{-i\delta\boldsymbol{q}\cdot\boldsymbol{r}}\end{aligned} \tag{14}$$

This is the key result of the calculation: the shape of the diffracted beam (as measured by the angular deviation δq from the n'th order) is the Fourier transform of the *local* diffraction amplitude (the Bessel function $J_n(u(\rho))$).

We finally compute the near-field profile of the diffraction spot. It is easy to read off the back Fourier transform from Eq. (14). We get for the beam shape in the n'th order:

$$\psi_n(\boldsymbol{r}) = R\sqrt{I_{\text{in}}}J_n(u(\rho)) \tag{15}$$

This proves Eq. (1) in the main text.

To evaluate Eq. (14), one simplification is possible by switching to polar coordinates: $\exp(-i\delta\boldsymbol{q}\cdot\boldsymbol{r}) = \exp(-i\rho\delta q\cos\phi)$. The ϕ integral gives $2\pi J_0(\rho\delta q)$, and we finally get

$$\tilde{\psi}_{\text{out}}(\boldsymbol{q}) \approx 2\pi R\sqrt{I_{\text{in}}}\int_0^\infty \rho d\rho J_n\left(ue^{-\rho^2/2w^2}\right)J_0(\rho\delta q) \tag{16}$$

For large $\rho \gg w$, the Bessel function J_n becomes proportional to $e^{-n\rho^2/2w^2}$ so that the integral converges for $n > 0$. Its numerical evaluation presents no difficulties. We can estimate its typical width as a function of the scattering wave vector as $\delta q \sim 1/w$. Since we assumed a scale w for the grating profile much wider than the period Λ, the phase neglected in Eq. (13) is at most $\mathcal{O}(\Lambda/w) \ll 1$.

Finally, we consider the case that incident and specular beams have a Gaussian profile

$$\psi_{\text{in}}(\boldsymbol{r}) = R\sqrt{I_{\text{in}}}e^{i\boldsymbol{k}_{\text{in}}\cdot\boldsymbol{r}}\exp\left(-\rho^2/2\sigma^2\right) \tag{17}$$

We assume that the waist of the probe beam σ is also larger than the grating period. The preceding calculation can be carried through, and we get Eq. (16) with an additional factor $\exp\left(-\rho^2/2\sigma^2\right)$ under the integral. The predictions of this theory are illustrated in Fig. 3. The angular profile of the diffraction spot is shown in Fig. 3a, assuming that the probe beam is matched in size to the grating covered area ($\sigma = w$). As the grating amplitude grows (from bottom to top), a "dark ring" enters the spot profile (top curves). This happens when the total diffracted intensity is beyond its maximum, as shown in Fig. 3b (dots on the red curve). There, we also show the influence of the probe beam size: a narrow beam ($\sigma = w/2$) diffracts similar to an infinite grating, with an efficiency related to the Bessel function $\left|J_1(u)\right|^2$ that oscillates beyond the maximum efficiency. For a much wider beam ($\sigma \gg w$), the diffraction efficiency increases monotonously. An analytical proof of this property is given in the Supporting Information.

References

1. N.S. Yadavalli, F. Linde, A. Kopyshev, S. Santer, ACS Appl. Mater. Interfaces. **5**, 7743 (2013)
2. G. Di Florio, E. Bründermann, N.S. Yadavalli, S. Santer, M. Havenith, Soft Mater. **12**, 98 (2014)
3. S. Loebner, N. Lomadze, A. Kopyshev, M. Koch, O. Guskova, M.G. Saphiannikova, S.A. Santer, J. Phys. Chem. B **122**, 2001 (2018)
4. A. Ambrosio, L. Marrucci, F. Borbone, A. Roviello, P. Maddalena, Nat. Commun. **3**, 989 (2012)
5. T. Grosjean, D. Courjon, Opt. Express **14**, 2203 (2006)
6. J.P. Vernon, S.V. Serak, R.S. Hakobyan, A.K. Aleksanyan, V.P. Tondiglia, T.J. White, T.J. Bunning, N.V. Tabiryan, Appl. Phys. Lett. **103**, 201101 (2013)
7. P. Rochon, E. Batalla, A. Natansohn, Appl. Phys. Lett. **66**, 136 (1995)
8. D.Y. Kim, S.K. Tripathy, L. Li, J. Kumar, Appl. Phys. Lett. **66**, 1166 (1995)
9. A. Emoto, E. Uchida, T. Fukuda, Polymers **4**, 150 (2012)
10. J. Vapaavuori, A. Goulet-Hanssens, I.T.S. Heikkinen, C.J. Barrett, A. Priimagi, Chem. Mater. **26**, 5089 (2014)
11. J.E. Koskela, J. Vapaavuori, R.H.A. Ras, A. Priimagi, ACS Macro Lett. **3**, 1196 (2014)
12. M. Saccone, V. Dichiarante, A. Forni, A. Goulet-Hanssens, G. Cavallo, J. Vapaavuori, G. Terraneo, C.J. Barrett, G. Resnati, P. Metrangolo, A. Priimagi, J. Mater. Chem. C **3**, 759 (2015)
13. N.S. Yadavalli, M. Saphiannikova, S. Santer, Appl. Phys. Lett. **105**, 051601 (2014)
14. N.S. Yadavalli, M. Saphiannikova, N. Lomadze, L.M. Goldenberg, S. Santer, Appl. Phys. A **113**, 263 (2013)
15. N.S. Yadavalli, S. Santer, J. Appl. Phys. **113**, 224304 (2013)
16. M. Saphiannikova, V. Toshchevikov, J. Soc. Inf. Disp. **23**, 146 (2015)
17. V. Toshchevikov, J. Ilnytskyi, M. Saphiannikova, J. Phys. Chem. Lett. **8**, 1094 (2017)
18. M. Dumont, A. El Osman, Chem. Phys. **245**, 437 (1999)
19. B. Yadav, J. Domurath, K. Kim, S. Lee, M. Saphiannikova, J. Phys. Chem. B **123**, 3337 (2019)
20. G. Di Florio, E. Brundermann, N.S. Yadavalli, S.A. Santer, M. Havenith, Nano Lett. **14**, 5754 (2014)
21. N.S. Yadavalli, D. Korolkov, J. Moulin, M. Krutyeva, S. Santer, ACS Appl. Mater. Interfaces. **6**, 11333 (2014)
22. V. Toshchevikov, M. Saphiannikova, G. Heinrich, J. Phys. Chem. B **116**, 913 (2012)
23. V. Toshchevikov, M. Saphiannikova, J. Phys. Chem. B **118**, 12297 (2014)
24. M. Saphiannikova, D. Neher, J. Phys. Chem. B **109**, 19428 (2005)
25. V. Toshchevikov, M. Saphiannikova, G. Heinrich, J. Phys. Chem. B **113**, 5032 (2009)
26. H.J. Eichler, P. Günther, D.W. Pohl, *Laser-induced Dynamic Gratings* (Springer, Berlin, 1986)
27. X.L. Jiang, L. Li, D.Y. Kim, V. Shivshankar, S.K. Tripathy, Appl. Phys. Lett. **68**, 2618 (1996)
28. J. Mysliwiec, A. Miniewicz, S. Nespurek, M. Studenovsky, Z. Sedlakova, Opt. Mater. **29**, 1756 (2007)
29. H. Taunaumang, M. Solyga, M.O. Tija, A. Miniewicz, Thin Solid Films **461**, 316 (2004)
30. O. Kulikovska, L.M. Goldenberg, J. Stumpe, Chem. Mater. **19**, 3343 (2007)
31. L. Kulikovsky, O. Kulikovska, L.M. Goldenberg, J. Stumpe, ACS Appl. Mater. Interfaces. **1**(8), 1739 (2009)
32. L.M. Goldenberg, L. Kulikovsky, O. Kulikovska, J. Stumpe, J. Mater. Chem. **19**, 8068 (2009)
33. F.L. Labarthet, T. Buffeteau, C. Sourisseau, J. Phys. Chem. B **103**, 6690 (1999)
34. F.L. Labarthet, T. Buffeteau, C. Sourisseau, J. Phys. Chem. B **102**, 2654 (1998)
35. F.L. Labarthet, T. Buffeteau, C. Sourisseau, Appl. Phys. B **74**, 129 (2002)
36. F.L. Labarthet, P. Rochon, A. Natansohn, Appl. Phys. Lett. **75**, 1377 (1999)
37. J. Jelken, S. Santer, RSC Adv. **9**, 20295 (2019)
38. L. Frey, J.M. Jonathan, A. Villing, G. Roosen, Opt. Commun. **165**, 153 (1999)
39. M. Born, E. Wolf, *Principles of optics*, 6th edn. (Pergamon Press, Oxford, 1980)

Affiliations

Joachim Jelken[1] · Carsten Henkel[1] · Svetlana Santer[1]

✉ Carsten Henkel
henkel@uni-potsdam.de

[1] Institute of Physics and Astronomy, University of Potsdam, 14476 Potsdam, Germany

Supporting Information

Solving an old puzzle: Fine structure of diffraction spots from an azo-polymer surface relief grating

Joachim Jelken, Carsten Henkel*, Svetlana Santer

Institute of Physics and Astronomy, University of Potsdam, 14476 Potsdam, Germany

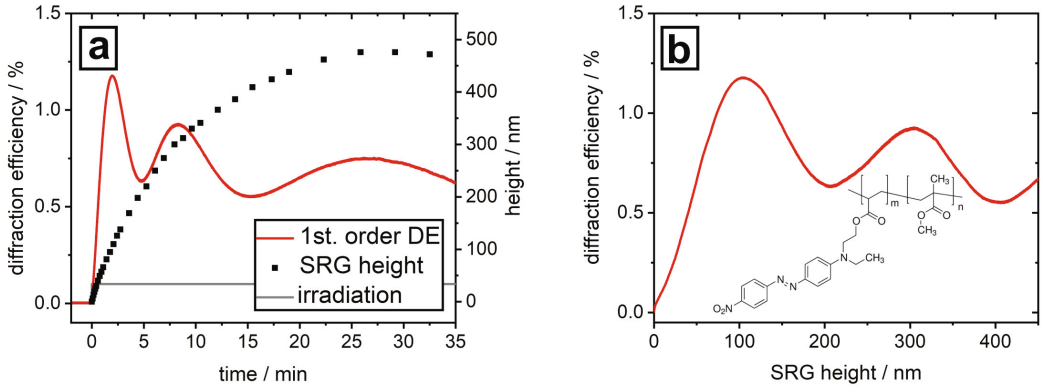

Figure S1. (a) *In-situ* recorded SRG height and 1st. order diffraction efficiency (DE) of the poly(MMA-co-DR1A) polymer film during irradiation with a $\pm 45°$ interference pattern. (b) Dependence of the DE signal on SRG height. The chemical structure of the polymer is shown in the inset. ($\lambda = 491\text{nm}$, $I = 200\text{mW/cm}^2$, $\Lambda = 2\mu\text{m}$, $d = 600\text{nm}$)

* Corresponding author: henkel@uni-potsdam.de

video file name (separate file, not embedded in this document):

340_2019_7331_MOESM2_ESM.mp4

Figure S2. Video (accelerated) showing the spatial fine structure of the 1st order diffraction spot as a function of time while irradiation with a $\pm 45°$ interference pattern (IP) of $\lambda = 491\text{nm}$ light ($I = 200\text{mW/cm}^2, \Lambda = 2\mu\text{m}$ grating period, Pazo film, thickness $1\mu\text{m}$). The spatial profile is changing with time from a Gaussian to a ring-shaped intensity distribution ("donut") and finally to a ring structure with a bright center.

We derive here a property mentioned in the Appendix, namely that the diffraction efficiency increases monotonously with grating amplitude for a wide probe beam. We compute the integral of the diffracted intensity over the spot profile (the q-integral is restricted to the nth diffraction order)

$$I_n = \int \frac{d^2q}{(2\pi)^2} \left|\tilde{\psi}_{out}(\boldsymbol{q})\right|^2 \tag{A.16}$$

Inserting Eq. (A.12) (with $\sigma = \infty$) and performing the $\boldsymbol{q}$-integral first, we get (Parseval-Plancherel formula)

$$I_n = I_{\text{in}}|R|^2 \int d^2r\, J_n\big(u(\rho)\big)^2 \tag{A.17}$$

Using $u(\rho) = u\, e^{-\rho^2/2w^2}$ of Eq.(A.8), the derivative with respect to the modulation amplitude u in the center of the grating is

$$\frac{\partial I_n}{\partial u} = 2I_{\text{in}}|R|^2 \int d^2r\, e^{-\rho^2/2w^2} J_n'\big(u(\rho)\big)\, J_n\big(u(\rho)\big) \tag{A.18}$$

where J_n' is the derivative of the Bessel function. We now show that this quantity is positive. In polar coordinates, the angular integral is trivial, and the substitution $z = u(\rho)$ permits to evaluate the radial integral in closed form:

$$\begin{aligned}
\frac{\partial I_n}{\partial u} &= \frac{4\pi}{u} I_{\text{in}}|R|^2 \int_0^\infty \rho d\rho\, u(\rho)\, J_n'\big(u(\rho)\big)\, J_n\big(u(\rho)\big) \\
&= \frac{4\pi w^2}{u} I_{\text{in}}|R|^2 \int_0^u dz\; J_n'(z)\, J_n(z) \\
&= \frac{2\pi w^2}{u} I_{\text{in}}|R|^2 J_n(u)^2 \geq 0
\end{aligned} \tag{A.19}$$

which is always a positive quantity.

4.2. Publication II: Polarization controlled fine structure of diffraction spots from an optically induced grating

DOI: https://doi.org/10.1063/1.5140067

Polarization controlled fine structure of diffraction spots from an optically induced grating

Joachim Jelken, Carsten Henkel, Svetlana Santer*

Institute of Physics and Astronomy, University of Potsdam, 14476 Potsdam, Germany

RECEIVED DATE

Keywords: azobenzene containing material, surface relief grating, photorefractive holograms, photonic materials

ABSTRACT

We report on the remote control of the fine structure of a diffraction spot from optically induced dual gratings within a photosensitive polymer film. The material contains azobenzene in the polymer side chains and develops a surface relief under two-beam holographic irradiation. The diffraction of a polarized probe beam is sensitive to the orientation of the azobenzenes forming a permanently stored birefringence grating within the film. We demonstrate that the fine structure of the probe diffraction spot switches from Gaussian to hollow or hollow to "Saturn"-like structure by a change in polarization. This makes it potentially useful in photonic devices, because the beam shape can be easily inverted by an external stimulus.

* santer@uni-potsdam.de

Photosensitive polymer films containing azobenzene have gained considerable interest during the last two decades due to their multiple applications, e.g. as a photoresist,[1] for optical data storage,[2] as cell culture platforms,[3] optical polarizers,[4] wavelength filters,[5] or polymeric lasers with a tunable wavelength.[6]

When these films are exposed to irradiation with an interference pattern (IP), the result is a deformation of the surface fixed by the spatial modulation of the light field (in intensity or polarization).[7] Key ingredients for the macroscopic deformation of the polymer surface are the cyclic photo-isomerization and re-orientation of the azobenzene side chains attached to the polymer backbone.[8] The photo-isomerization from the azobenzene *trans*- to *cis*-states takes place in both directions and on molecular time and length scales, i.e. fs and Å range. Multiple *trans*-*cis* switches are accompanied by the rotation of the azobenzene molecule as a whole and result in its alignment perpendicular to the polarization of the incident light, generating a birefringence grating. The orientation process occurs on larger time ($\sim$ 1s) and length ($\sim$ nm) scales. Gradients in azobenzene alignment induce opto-mechanical stresses[8,9] and the corresponding visco-plastic deformation of the polymer film drives the surface relief grating (SRG). This process is slow and requires several tens of minutes over which a structured surface with µm-period expands over a macroscopic area. The SRG growth kinetics depend on the interplay of these processes and is usually recorded by measuring the diffraction efficiency (DE) of the sample as a function of irradiation time. Using this method, one records a sum signal of the birefringence and surface grating.[10,11] Other approaches to characterize SRG growth are to measure *in situ* the change in the surface profile with atomic force microscopy (AFM)[12] or scanning near-field optical microscopy (SNOM).[13] Here, only information about the surface structure is obtained and the bulk orientation is not probed.

Recently, we have proposed a set-up which combines the AFM technique with DE measurements and acquires simultaneously information about the growth of surface and

birefringence gratings (**Fig. S1**, **SM**). It has been reported that the DE is not continuously increasing as a function of the SRG height,[14] but exhibits maxima and minima.[15,16] When the DE is recorded with a probe beam whose diameter is similar to the SRG size, one also observes a change in the spatial profile of the 1st order diffraction spot.[15] Three different spatial profiles (Gaussian, "donut" and "Saturn") are generated while the modulation depth increases. The "donut" structure consists of a bright ring with a dark hole in the center, while the "Saturn"-like structure has the shape of a bright ring with a bright center (inset of **Fig. 1a**).

In this letter we report on the remote control of the fine structure of the diffraction spot, where one can switch reversibly on a sub-second time scale the spatial intensity profile between "Gaussian" and "donut" or "donut" and "Saturn" shape by simply changing the polarization of the probe beam. The explanation is based on the combined contribution of the birefringence and surface relief gratings to the DE: a polarized probe beam is predominantly phase-shifted by those azobenzene groups that are aligned parallel to its electric field vector. By modelling the phase shift from bulk and surface[17,18], we show that the "hills" ("valleys") of the SRG coincide with domains where azobenzenes align parallel (perpendicular) to the grating vector (**Fig. 3b**). The fact that the spatial profile of the diffraction spot depends on the polarization of the probe beam, makes the photo-sensitive film a meta-surface.[19,20] This beam shaping property of the SRG can be used in photonic devices where the control of the spatial profile is important, e.g. in STED microscopy, ultrathin lenses or optical tweezers. Together with the feature that the spatial profile can be inverted by an external stimulus (change in the polarization of the probe beam) this may lead to unforeseen applications.

Fig. 1 shows the 1st order DE signal, recorded *in situ* with a P-polarized probe beam, and the SRG amplitude during irradiation with ±45°-IP (for more information see **Materials and Methods, SM**). In this IP, the electric field changes spatially in a continuous way between linear and circular polarization, while the intensity is constant over one grating period. For the

DE, we show the spatial intensity distribution within the diffracted spot (**Fig. 1a**) as well as the integrated signal (red curve).

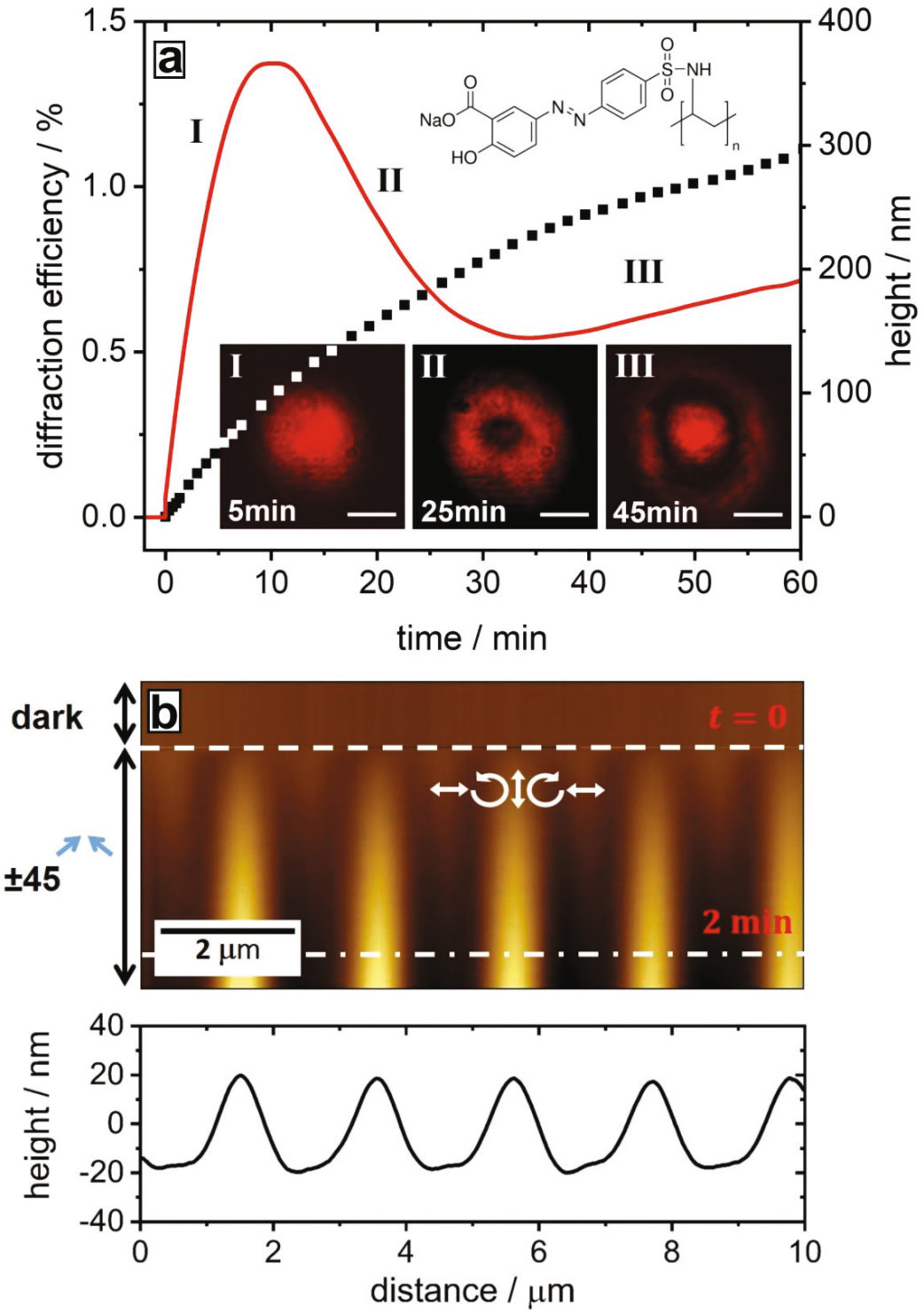

Figure 1. (a) *In situ* recorded SRG amplitude (black dots) and 1st order DE (red curve) under irradiation with $\pm 45°$-IP ($\lambda = 491\text{nm}$, $I = 200\text{mW/cm}^2$, $\Lambda = 2\mu\text{m}$ grating period, film thickness $d = 1\mu\text{m}$), probed by a P-polarized beam ($\lambda = 633\text{nm}$). The inset shows the chemical structure of the photosensitive polymer (Pazo) and the spatial profile of the 1st order diffraction spot as a function of the SRG height recorded at time I (Gaussian profile), II ("donut" structure) and III ("Saturn"-like structure). The scale bar is 1mm. (b) The *in-situ* recorded AFM micrograph: scanning starts from top, at the position marked by the dashed white line, the irradiation is applied. The white arrows depict the local distribution of the electrical field vector relative to the topography. The cross-section after 2min of irradiation (white dot dashed line) is shown underneath. The corresponding videos are provided in **Multimedia view**, **Figures 1-I, 1-II, 1-III**.

For low modulations of surface and bulk gratings, the 1st order DE increases steeply, and the diffraction spot has a Gaussian shape (inset I). For a 100nm SRG height, the DE goes through a maximum, and the spot profile changes to a "donut" structure (inset II). Under further irradiation one observes a minimum DE and the transformation of the spot profile to a "Saturn" structure (inset III), while the SRG continues growing. There are two reasons for this peculiar shape of the DE dynamics in our setup: the ±45°-IP is efficient in generating deep SRGs, and the DE is taken in reflection so that the relevant optical path length is proportional to twice the film thickness. Both effects lead to an unusually deep phase modulation compared to a transmission probe. The change in the spatial profile of the diffraction spot arises from the averaging along an inhomogeneous grating, recorded with a ±45 IP (polarization interference pattern).

The DE signal depends strongly on the probe beam polarization since it is sensitive to the orientation (phase grating) of the azobenzene groups in the bulk. This is demonstrated in **Fig. 2** where two *in situ* recorded DE curves with P- and S-polarized probe beams are shown. The curves are acquired simultaneously by switching the polarization of the probe beam every second with a Pockels cell (**Methods**, **SM**). At the beginning of SRG writing, the two signals behave similarly. After one minute of irradiation, when the SRG height grows to 10nm, the DE signal in S-polarization decreases and reaches a minimum after 5 minutes (~45nm SRG height).

During further irradiation, it increases again until a maximum signal is achieved after 25 min (170nm SRG height), followed by a drop in the DE signal. The first minimum is absent for the P-polarized probe, and the maximum appears earlier (100nm SRG height, 10 minutes of irradiation). The 1st order diffraction spot for the S-polarized beam shows a similar change in the spatial profile as for the P-polarized probe beam, but with a temporal delay, so that similar features emerge at larger SRG amplitudes. This shift in the DE signal allows for switching between the "donut" and "Saturn" structure of the diffraction spot by simply flipping the polarization of the probe beam from S to P (Multimedia view, Figure 2). The S-polarized diffraction spot still shows the "donut" structure, while for the P-polarized beam one already obtains the "Saturn"-like structure (insets in **Fig. 2**). After the irradiation is switched off, this property is stored permanently within the material. The "donut" structure can be inverted rapidly by switching the polarization of the probe beam, which is reproducible many times (Multimedia view, Figure 2). In case the beam shaping property is not required anymore, the polymer film can be irradiated with a single pump beam (circularly polarized) which will modify or erase the surface and birefringence gratings. A faster erasure with a phase-shifted two-beam irradiation has been demonstrated recently in Ref. 14.

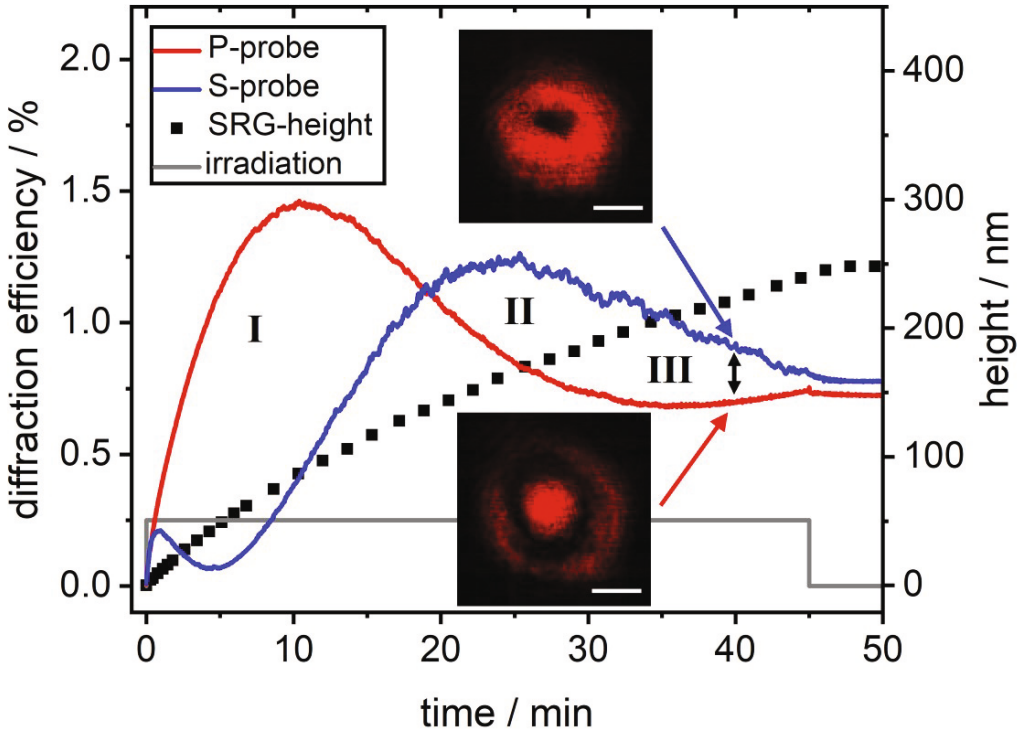

Figure 2. *In situ* recorded SRG amplitude (black dots) and 1st order diffraction efficiency for a probe beam with P- (red) and S-polarization (blue). The polarizations are switched every second using a Pockels cell. The corresponding videos are provided in **Multimedia view**, **Figure 2**. The scale bar is 1mm.

The dynamics of the DE signals can be modelled as follows.[11] The relief grating is described by the top surface:

$$z(x,t) = d + \frac{h(t)}{2}\cos(2\pi x/\Lambda) \qquad (1)$$

where d is the thickness before irradiation, $h(t)$ the (time-dependent) peak-to-valley amplitude of the SRG, and Λ its period. Upon reflection from below, a probe beam at normal incidence acquires a phase modulation proportional to the double optical path $2n\,z(x,t)$. Note that for a probe in transmission, $h(t)$ is weighted with an effective index $n_{\text{eff}} < n$. A simple model for

the birefringence grating in the bulk is sketched in **Fig. 3b**: a writing field with a locally linear polarization makes the molecules orient perpendicular to this direction. In regions of circular polarization, molecules orient most probably perpendicular to the film plane, but this is invisible for the probe beams used here. As shown in **Fig. 3b**, below the "hills" of the SRG, the molecules orient parallel to the P-polarization. The optical path length (excluding the surface region) thus depends on polarization and can be modeled as:

$$L_{p,s}(x,t) = n\,d \pm \frac{\Delta n(t)}{2}\,d\,\cos(2\pi x/\Lambda) \tag{2}$$

where n is the equilibrium refractive index and $\Delta n(t)$ the amplitude of the birefringence. Note the shift between the maxima by half the grating period. We get the DE of a polarized probe from its phase modulation: $\Delta\phi_{p,s}(x,t) = u_{p,s}(t)\cos(2\pi x/\Lambda)$ with amplitudes $u_{p,s}(t)$

$$u_{p,s}(t) = \frac{2\pi}{\lambda\cos\theta}(n\,h(t) \pm \Delta n(t)\,d) \tag{3}$$

The standard theory of phase modulation (in the Raman-Nath approximation)[21,22] gives for the n'th order diffraction efficiency:

$$\eta^{(n)}_{Rp,s}(t) = R_0^2\,J_n^2\big(u_{p,s}(t)\big) \tag{4}$$

where R_0^2 is the film reflectivity (in intensity) in the specular order, typically a few percent, and J_n the n'th order Bessel function. The last ingredient for the diffraction curves is to adapt the model of Ref.[17] with exponentially saturated growth and take:

$$\Delta n(t) = \Delta n_\infty\left(1 - \exp\left(-\frac{t}{\tau_1}\right)\right), \qquad h(t) = h_\infty\left(1 - \exp\left(-\frac{t}{\tau_2}\right)\right) \tag{5}$$

Typical data are: $\tau_1 = 10$ sec, $\Delta n_\infty = 0.058$, $\tau_2 = 27$ min, $h_\infty/\tau_2 = 11$ nm/min, $\sigma/w = 0.8$, consistent with our measurements. The refractive index $n_{633nm} = 1.7$ and the film thickness of $d = 1\mu$m were measured separately.

The results of this model are shown in **Fig. 3a**. The fast initial rise of the S-polarized signal, followed by a dip nearly down to zero, is explained by the contribution of the SRG that is growing with a temporal delay and that interferes destructively with the birefringence grating (minus sign in **Eq. 3**). Although the SRG eventually takes over, the delay with respect to the P-polarized probe remains visible. The solid curves (**Fig. 3a**) differ from the dashed ones by an average over the (Gaussian) intensity profiles of probe and writing beams, as explained in **Section 1**, **SM**. This approach also provides a prediction for the ring structure of the diffraction spot: it appears when the phase modulation parameter $u_{p,s}(t)$ is beyond the first maximum of J_1 in the center of the SRG and smaller towards its rim.[15] By averaging over this inhomogeneous SRG, the maxima of the diffraction curves move to later times and the signal in the minima increases significantly. A fit of the experimental data of **Fig. 2** with the model predicted by **Eq. 4** is presented in **Fig. S2**, **SM** and shows a more than qualitative agreement. The same behavior is observed in RL irradiation (right- and left-handed circular polarizations, **Fig. S3, SM**), but it does not appear for all inscribing IP: for instance, in the case of the SP-IP, SRG and birefringence grating do not interfere because the polymer topography responds at half the period Λ.[23]

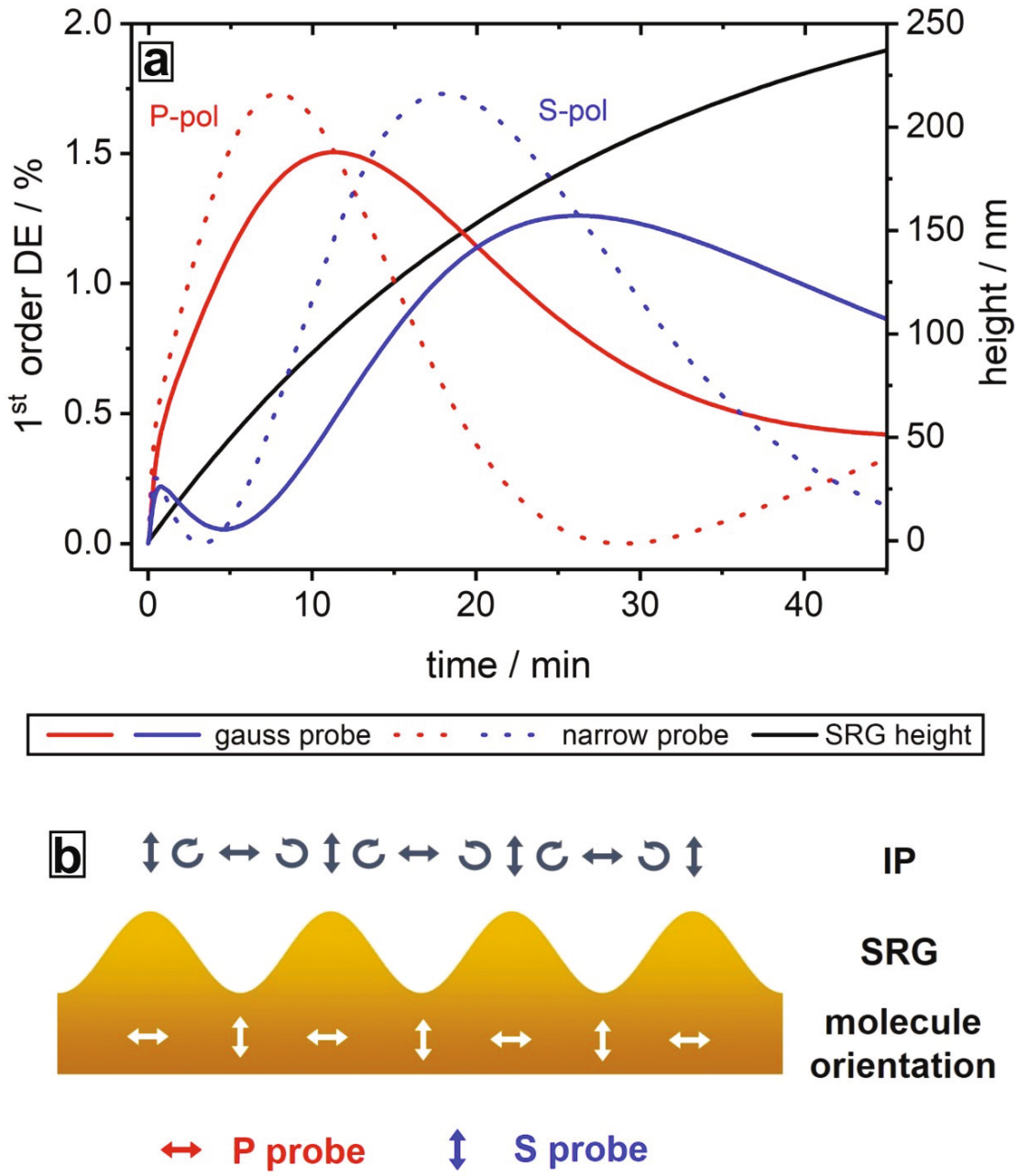

Figure 3. (a) Theoretical modelling of the SRG height (black curve) and DE signal for P- (red) and S-polarized (blue) probe beams. Dashed curves are based on **Eq. 4**. The thick solid curves take into account the average over the Gaussian intensity distribution of the probe beam and the spatially inhomogeneous intensity of the writing beams. The ratio between probe and pump beam diameters is $\sigma/w = 0.8$. (b) Scheme of the SRG with distribution of electrical field vector (arrows on the top) for the ±45°-IP. White arrows within the SRG depict the photo-stationary orientation of the azobenzene molecules in the bulk during irradiation. Polarizations and orientations are projected onto the film plane.

In conclusion, the polarization-dependent diffraction of a probe beam by an optically inscribed grating is discussed. For all polarizations, the DE signal acquired during the irradiation, i.e. under simultaneous development of birefringence (bulk) and surface relief gratings, shows complex behavior with several maxima and minima. The DE dynamics strongly depend on the polarization of the probe beam and are well explained by the interplay of two growing gratings, i.e. birefringence and topography. They are phase-shifted depending on the mutual orientation of the polarization distribution in the inscribing interference pattern and the probe beam. The orientation of the azobenzene with respect to the position of the SRG maximum and minimum decides about constructive or destructive interference in the recorded DE. We demonstrate that by changing the polarization between S- and P-state one can control the fine structure of the intensity distribution within the diffraction spot between either Gaussian to "donut" shape, or "donut" to "Saturn"-like shape, which makes it of interest to use in photonic devices, because the structure can be easily inverted by an external stimulus.

Supplementary Material. Figure S1 shows a home-made set-up. Section **Materials and Methods** describes the experimental part of the paper. **Section 1** represents the details of calculation of the diffraction efficiency for Gaussian pump and probe beams. **Figure S2** depicts fit of the experimental data of **Fig. 2** with the model predicted by **Eq.(4)**. **Figure S3** depicts *in situ* recorded SRG amplitude (black dots) and $1^{st.}$ order diffraction efficiency for RL irradiation, using S- (a) and P-polarized (b) probe beams.

ACKNOWLEDGMENTS: This research is supported by the Helmholtz Graduate School on Macromolecular Bioscience (Teltow, Germany). We thank Pooja Arya, Burkhard Stiller and Andreas Pucher for fruitful discussions.

References

1 T. Papke, N. S. Yadavalli, C. Henkel, and S. Santer, ACS Appl. Mater. Interf. **6**, 14174–80 (2014).

2 S. Hvilsted, C. Sánchez, and R. Alcalá, J. Mater. Chem. **19**, 6641–48 (2009).

3 C. Fedele, P. A. Netti, and S. Cavalli, Biomater. Sci. **6**, 990–95 (2018).

4 S. K. Tripathy, N. K. Viswanathan, S. Balasubramanian, and J. Kumar, Polym. Adv. Technol. **11**, 570–74 (2000).

5 R. J. Stockermans and P. L. Rochon, Appl. Opt. **38**, 3714–19 (1999).

6 T. Ubukata, T. Isoshima, and M. Hara, Adv. Mater. **17**, 1630–33 (2005).

7 N. S. Yadavalli, M. Saphiannikova, and S. Santer, Appl. Phys. Lett. **105**, 051601 (2014).

8 V. Toshchevikov, J. Ilnytskyi, and M. Saphiannikova, J. Phys. Chem. Lett. **8**, 1094 (2017).

9 G. Di Florio, E. Bründermann, N. S. Yadavalli, S. Santer, and M. Havenith, Nano Lett. **14**, 5754–60 (2014).

10 F. Lagugné Labarthet, T. Buffeteau, and C. Sourisseau, Appl. Phys. B **74**, 129 (2002).

11 F. Lagugné Labarthet, P. Rochon, and A. Natansohn, Appl. Phys. Lett. **75**, 1377–79 (1999).

12 N. S. Yadavalli and S. Santer, J Appl. Phys. **113**, 224304 (2013).

13 A. D. Vu, F. Fabbri, N. Desboeufs, J. P. Boilot, T. Gacoin, K. Lahlil, Y. Lassailly, L. Martinelli, and J. Peretti, Proc. of SPIE **9236**, 923611-1 (2014).

14 J. Jelken and S. Santer, RSC Advances **9**, 20295–305 (2019).

15 J. Jelken, C. Henkel, and S. Santer, Appl. Phys. B **125**, 218 (2019).

16 O. Sakhno, L.M. Goldenberg, M. Wegner, and J. Stumpe, Opt. Mater. X **1**, 100006 (2019).

17 N. Reinke, A. Draude, T. Fuhrmann, H. Franke, and R. A. Lessard, Appl. Phys. B **78**, 205–09 (2004).

18 A. Sobolewska and A. Miniewicz, J. Phys. Chem. B **111,** 1536–44 (2007).

19 K. Wu, P. Coquet, Q. J. Wang, and P. Genevet, Nature Commun. **9**, 3494 (2018).

20 Y Llu, Y. Ke, H. Luo, and S. Wen, Nanophotonics **6**, 51–70 (2017).

21 M. Born, and E. Wolf: Principles of Optics (Pergamon Press, Oxford 1980, 6th ed.)

22 H. J. Eichler, P. Günther, and D. W. Pohl: Laser-induced Dynamic Gratings (Springer, Berlin/Heidelberg 1986)

23 N. S. Yadavalli, M. Saphiannikova, N. Lomadze, L. M. Goldenberg, and S. Santer, Appl. Phys. A **113**, 263–72 (2013).

Supplementary Materials

Polarization controlled fine structure of diffraction spots from an optically induced grating

Joachim Jelken, Carsten Henkel, Svetlana Santer*

Institute of Physics and Astronomy, University of Potsdam, 14476 Potsdam, Germany

Keywords: azobenzene containing material, surface relief grating, photorefractive hologram, photonic materials

Experimental Part

Materials and Methods

Photosensitive polymer. Poly[1-[4-(3-carboxy-4-hydroxyphenylazo)benzenesulfonamido]-1,2-ethanediyl, sodium salt] (Pazo) is purchased from Sigma-Aldrich. The polymer solution is prepared by dissolving 170mg Pazo in 1ml solvent containing a mixture of 95% methoxyethanol and 5% ethylene glycol.

* Corresponding author: santer@uni-potsdam.de

Sample preparation. The polymer films are prepared by spin casting 100µl of the polymer solution on thin glass slides at 3000rpm for one minute. In this way one gets a fixed film thickness of 1µm, which is measured using an atomic force microscope (AFM) by scanning across a scratch within the polymer film.

Methods

Home-made set-up for studying SRG formation in situ. The set-up is described in details elsewhere.[1] In short, it consists of three parts: (1) two beam interference irradiation, (2) atomic force microscopy (AFM) and (3) diffraction efficiency (DE) measurement (**Figure S1**). The two-beam interference irradiation with a continuous-wave diode-pumped solid-state laser (Cobolt Calypso, λ=491nm) allows for generating well-defined spatial interference patterns (either intensity or polarization). The beam diameter is set to 4mm for the pump beams ($1/e^2$ diameter). The intensity is set initially to 200mW/cm^2 and a 50:50 beam splitter is added to generate two beams of same intensity. These two beams are polarized at $\pm 45°$ (relative to the vertical direction = optical axis) and their interference pattern (called $\pm 45°$ IP in the paper) creates an electric field distribution where the field vector changes spatially in a continuous way between linear and circular polarization, while the intensity is constant over a period. The polarization pattern is sketched by the arrows in **Fig. 1b** and **Fig. 3b**.

The second part of the set-up is an atomic force microscope (AFM) from PicoScan (Molecular Imaging) operating in intermittent contact mode. The scan-speed of the AFM is set to one line per second with a scan area of 10x10µm and a resolution of 512x512 pixel. Commercial tips (Nanoworld-Point probe) with a resonance frequency of 130 kHz and a spring constant of 15 N/m are used for measurements. The sample is oriented with the polymer surface pointing towards the AFM tip, such that irradiation is “from below”, i.e., through the glass substrate (**Figure S1**). The SRG amplitude is determined from the AFM scan by measuring the difference

in height between topographical maximum and minimum. A plot of this value as a function of time gives the growth kinetics of the SRG. To obtain at the same time information about the alignment of the azobenzene side chains in the polymer film, a red probe laser beam (Uniphase, HeNe, 633nm) with a beam diameter of 3mm (intensity 30mW/cm^2) is integrated into the set-up. The wavelength of 633nm falls outside the absorption bands of photosensitive polymer studied in this work. In a series of different experiments, including temperature measurements and AFM analysis of the polymer film during irradiation with the probe beam, we proved that irradiation at this wavelength does not alter the polymer film. The diffraction efficiency is defined as the ratio of the intensity of diffraction order (I_n) and the intensity of the incoming light (I_0): $\eta_n = I_n / I_0$, where I_0 is 90% of the total intensity of the probe beam. The DE set-up includes a Pockels cell (Thorlabs, EO-PC-550) in order to switch between the S- and P-polarizations by applying the half-wave-plate-voltage. The voltage is supplied by a high voltage amplifier (Trek 610D) and can be switched every second between zero and the half wave plate voltage in order to probe the DE of S- and P-polarized probe beams simultaneously. The detector D_2 measures the intensity in the –1 diffraction order as a function of time, while the integrated CMOS camera is detecting the temporal change in the spatial profile of the +1 diffraction order. The three different set-ups: two beam interference, AFM and DE equipment are controlled and operated with a software (Profilab-Expert, Abacom) designed in the laboratory to record signals of the photodiodes, control the irradiation shutter and the Pockels cell voltage. In order to synchronize the DE set-up and the AFM, a computer-generated signal is regulating the irradiation and the applied Pockels cell voltage with the help of an AD/DA converter (Kolter Electronic, PCI-AD12N-DAC2).

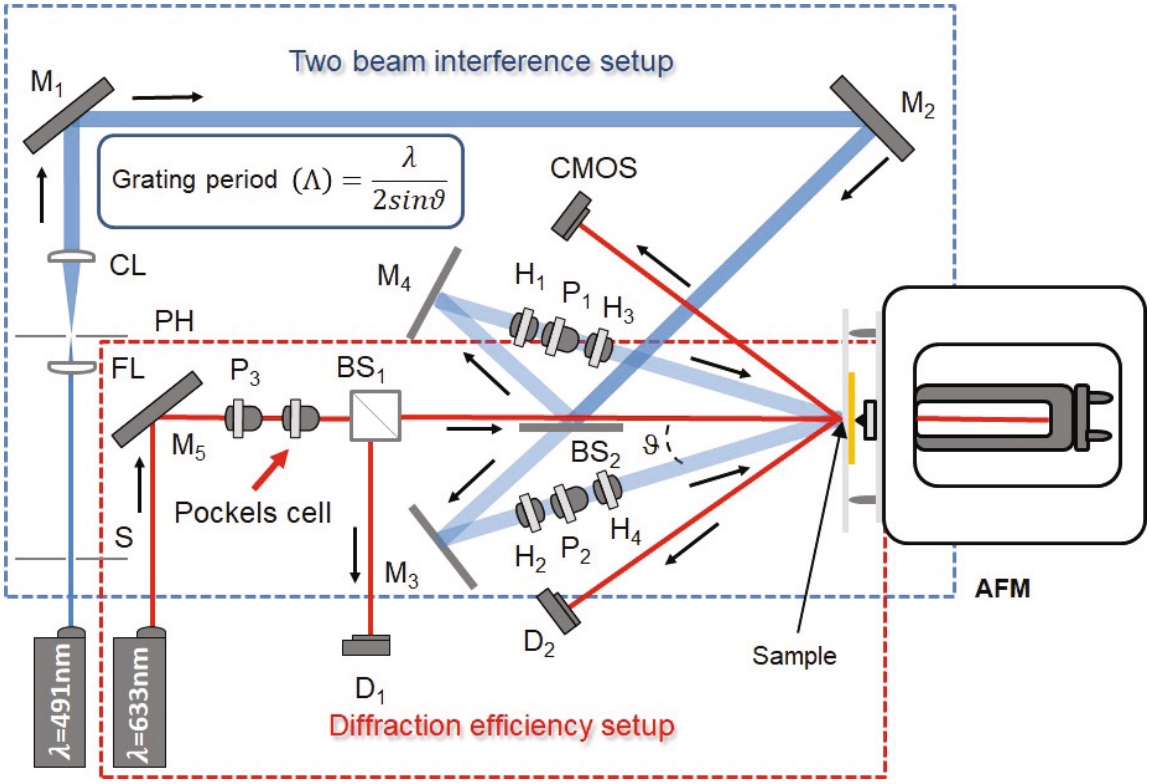

Figure S1. Scheme of the experimental set-up consisting of three parts: (1) a two-beam interference part for generation of the interference pattern (blue laser line), (2) an atomic force microscope (AFM) for *in situ* (during irradiation) recording of the surface morphology and (3) a diffraction efficiency (DE) set-up (red laser line) enabling the collection of information about the birefringence grating *in situ*. The DE setup contains additionally a Pockels cell in order to change the polarization of the probe beam. The –1 diffraction order is used in order to determine the DE (detector D_2) and the +1 order for recording the beam profile in time with the help of a CMOS camera. (S: shutter, M: mirror, D: detector, P: polarizer, H: half-wave-plate, BS: beam splitter, CL: collimating lens, FL: focusing lens, PH: pin hole).

Silicon detectors (Thorlabs DET 100A/M) are used to measure the intensity of the diffracted probe beam. A 600nm longpass filter is placed in front of each photodiode in order to be only sensitive to the probe beam. The intensity of the diffracted light is recorded every 200ms.

The change in the beam profile of the first order diffraction spot is recorded with a CMOS Camera (Thorlabs DCC1545M) with a sensor size of 6.7 x 5.3 mm and resolution of 1280 x 1024 pixel (pixel size 5.2 µm).

All experiments are carried out under yellow light in the laboratory (to avoid undesirable photo-isomerization) and under ambient conditions, *i.e.*, at room temperature with a relative humidity of 55%. The whole set-up is covered with a non-transparent encapsulation in order to avoid any influence of the environment on the measurement (parasitic light, air circulation and vibration).

Section 1. Calculation of the diffraction efficiency for Gaussian pump and probe beams

In Ref.[2], we have introduced a theoretical framework to deal with the diffraction of a probe beam with a spatially inhomogeneous profile. Using the results derived there [Eqs.(14, 17)], one gets for the diffraction amplitude $A_{\mathrm{n}}(\delta\boldsymbol{q})$ in reciprocal space near the *n*'th diffraction maximum

$$A_{\mathrm{n}}(\delta\boldsymbol{q}, t) = R_0 \int d^2r\, e^{-i\delta\boldsymbol{q}\cdot\boldsymbol{r}}\, J_n\left(u_{p,s}(\boldsymbol{r}, t)\right) N_\sigma\, e^{-r^2/\sigma^2}, \tag{S1}$$

where σ is the e^{-2} radius of the probe beam, $N_\sigma = (\pi\sigma^2/2)^{-1/2}$ is a normalization factor, $u_{p,s}(\boldsymbol{r}, t)$ the phase modulation amplitude at a position $\boldsymbol{r}$ in the grating, J_n the *n*'th order Bessel function, and R_0 the specular reflection amplitude of the film. This formula assumes that σ and the waist *w* of the pump beams are much larger than the grating period, an approximation well satisfied in the experiment.

The optical parameters of our setup are such that the ring structure of the diffraction spot is determined by the near field intensity which is given by[2]

$$I_{\mathrm{n}}(\boldsymbol{r}, t) = R_0^2\, J_{\mathrm{n}}^2\left(u_{p,s}(\boldsymbol{r}, t)\right) N_\sigma^2\, e^{-2r^2/\sigma^2}. \tag{S2}$$

The integral of this over $\boldsymbol{r}$ gives the 1st order diffraction efficiency

$$\eta_1(t) = R_0^2\, N_\sigma^2 \int d^2r\; J_1\big(u_{p,s}(\boldsymbol{r}, t)\big)^2 e^{-2r^2/\sigma^2}. \tag{S3}$$

The profile of the pump beams appears in the model for the growth of the birefringence and the relief gratings that we adapt from Ref. 3 (see main paper for the definition of symbols). The time-dependent amplitude of phase modulation is given by [Eqs.(3, 5) of the main paper]

$$u_{p,s}(\boldsymbol{r}, t) = \frac{2\pi}{\lambda}\left[\pm d\,\Delta n_\infty\left(1 - \exp\left(-\frac{t}{\tau_1(\boldsymbol{r})}\right)\right) + n\, h_\infty\left(1 - \exp\left(-\frac{t}{\tau_2(\boldsymbol{r})}\right)\right)\right] \tag{S4}$$

We assume that the growth rates $1/\tau_{1,2}(\boldsymbol{r})$ of the two gratings are proportional to the local intensity of the pump beams

$$\frac{1}{\tau_{1,2}(\boldsymbol{r})} = \frac{e^{-2r^2/w^2}}{\tau_{1,2}} \tag{S5}$$

where $\tau_{1,2}$ are the time constants in the center of the pump beams whose gaussian profiles overlap. This assumption can be checked experimentally by overlaying the growth curves obtained for different intensities I as a function of the dose $I \cdot t$. The integral (S3) can be evaluated in polar coordinates because the integrand only depends on the distance r from the grating center. With the substitution $z = e^{-2r^2/w^2}$, we get the convenient form ($dz = -4r\, dr\, z/w^2$)

$$\begin{aligned} \eta_{1p,s}(t) &= R_0^2 \tfrac{4}{\sigma^2} \int r\, dr\, J_1\left(u_{p,s}(r,t)\right)^2 e^{-2r^2/\sigma^2} \\ &= R_0^2 \tfrac{w^2}{\sigma^2} \int_0^1 \tfrac{dz}{z} J_1\left(u_{p,s}(r(z),t)\right)^2 z^{w^2/\sigma^2} \end{aligned} \tag{S6}$$

The result of this averaging is that zeros and maxima of $\eta_{1p,s}(t)$ appear at later times compared to those of $J_1^2(u_{p,s}(0,t))$. (These would be obtained with a very narrow probe beam centered on the SRG.) The zeros turn into minima with a nonzero signal. This can be seen in **Fig. S2** where the dash-dotted lines represent **Eq.(S6)**, while the dotted lines give $J_1^2(u_{p,s}(0,t))$. A satisfactory agreement is obtained for all three sets of experimental data and over a large irradiation period, by adjusting the parameters to the following values: $\tau_1 = 10$ sec, $\Delta n_\infty = 0.058$, $\tau_2 = 27$ min, $h_\infty/\tau_2 = 11$ nm/min, $\sigma/w = 0.8$. (The DE data were scaled by an overall scale factor.)

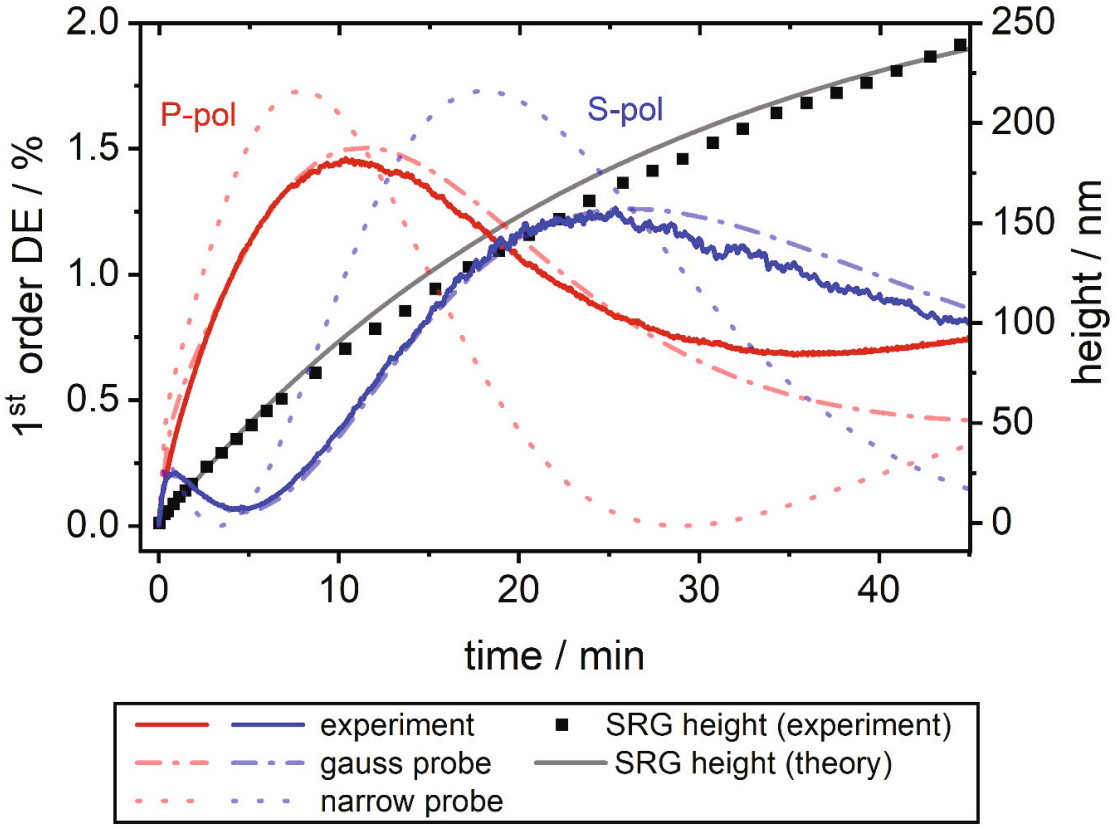

Figure S2. Fit of the experimental data of **Fig. 2** with the model predicted by **Eq.(4)** of the manuscript (see also **Fig. 3a** of the manuscript). The solid curve is showing the *in situ* recorded 1st order DE for an P- (red curve) and S-polarized probe beam (blue curve). The dotted line is showing the predicted DE for a narrow probe beam, while the dash dot line gives the DE obtained with a gaussian profile of the probe beam (**Eq. 4**). The ratio between probe and pump beam diameters is $\sigma/w = 0.8$. The black dots are showing the *in situ* recorded SRG height, while the solid black line is the predicted SRG amplitude. Comparing the experimental results with the model shows a very good matching.

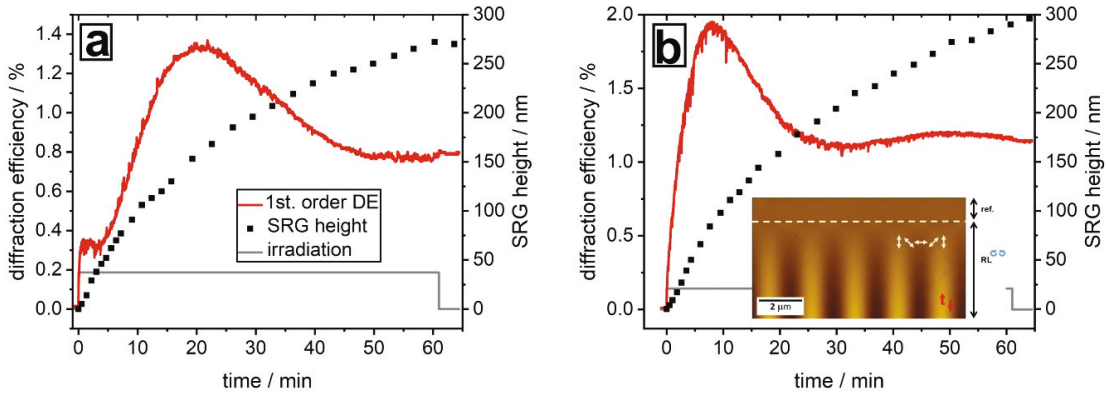

Figure S3. *In situ* recorded SRG amplitude (black dots) and 1st. order diffraction efficiency for a S- (a) and P-polarized (b) probe beam ($\lambda = 633\text{nm}$) under irradiation with RL circular interference pattern ($\lambda = 491\text{nm}$, $I = 200\text{mW/cm}^2$, $\Lambda = 2\mu\text{m}$ grating period, film thickness $d_{Pazo} = 1\mu\text{m}$). Inset: AFM micrograph showing (from top to bottom) the growth of the SRG in time. Irradiation starts at the dashed line. The white arrows illustrate the local polarization projected onto the film plane (the electric field vector rotates along the grating coordinate): the S- (P-) polarization is marked ↕ (↔), respectively.

1 J. Jelken, and S. Santer, RSC Adv. **9**, 20295-20305 (2019).
2 J. Jelken, C. Henkel, and S. Santer, Appl. Phys. B **125**, 218 (2019).
3 N. Reinke, A. Draude, T. Fuhrmann, H. Franke, and R. A. Lessard Appl. Phys. B **78**, 205 (2004).

4.3. Publication III: Light induced reversible structuring of photosensitive polymer films

DOI: https://doi.org/10.1039/C9RA02571E

RSC Advances

PAPER

View Article Online
View Journal | View Issue

Cite this: *RSC Adv.*, 2019, **9**, 20295

Light induced reversible structuring of photosensitive polymer films†

Joachim Jelken and Svetlana Santer *

In this paper we report on photoswitchable polymer surfaces with dynamically and reversibly fluctuating topographies. It is well known that when azobenzene containing polymer films are irradiated with optical interference patterns the film topography changes to form a surface relief grating. In the simplest case, the film shape mimics the intensity distribution and deforms into a wave like, sinusoidal manner with amplitude that may be as large as the film thickness. This process takes place in the glassy state without photo-induced softening. Here we report on an intriguing discovery regarding the formation of reliefs under special illumination conditions. We have developed a novel setup combining the optical part for creating interference patterns, an AFM for *in situ* acquisition of topography changes and diffraction efficiency signal measurements. In this way we demonstrate that these gratings can be "set in motion" like water waves or dunes in the desert. We achieve this by applying repetitive polarization changes to the incoming interference pattern. Such light responsive surfaces represent the prerequisite for providing practical applications ranging from conveyer or transport systems for adsorbed liquid objects and colloidal particles to generation of adaptive and dynamic optical devices.

Received 5th April 2019
Accepted 12th June 2019

DOI: 10.1039/c9ra02571e

rsc.li/rsc-advances

Introduction

Designing programmable polymer substrates is an active and growing field of research, continuously pushed by many branches of nanotechnology seeking unprecedented and ever more efficient solutions for developing novel types of sensors, strategies for self-healing integrated structures, optical information storage, solutions for creating adaptable and dynamic optical devices (auto focusing lenses, DFB lasers, diffractive thin films, diffusers and directional reflectors) or hybrid bio-electro-mechanical systems.[1–11] In even more exotic applications one utilizes dynamically switchable surfaces for controlling the adhesion and thus the position of adsorbed particles (a gecko "in reverse"), or for moving and handling small amounts of liquid within micrometer dimensions such as microfluidic chambers, channels or surfaces that act as microarrays for droplet deposition and screening.[1,12–15] In a general sense, programmable polymer substrates may be defined as systems the surface topography and morphology of which, including local surface energy and ordering, can be switched between distinct states by applying external stimuli such as electrical fields, temperature or light.[16–18] Photo-switchable surfaces offer greater simplicity and convenience in manipulation, since light as an external stimulus can be tuned and controlled spatio-temporally without undesired contact with electrodes, wires or heating elements.[19–23] One of the strategies to render a polymer photo-responsive is to modify it with photo-reactive groups among which azobenzenes are the most common. Azobenzene containing polymers belong to a class of functional materials exhibiting a strong mechanical response upon applying external radiation fields. Although the radiation only acts on the photosensitive azobenzene moieties by inducing *trans–cis* isomerization and thus configurational changes, as side groups in a polymer chains they can affect the system as a whole. Such materials have extensively been studied and were proposed for the construction of holographic gratings and optical data storage devices.[10] Very peculiar phenomena are obtained when azobenzene modified physisorbed polymer films or the even more exotic polymer brushes are exposed to irradiation exhibiting interference patterns (IP).[24–32] Following the IP's periodicity either with respect to intensity or polarization distribution, the polymer topography is modulated into a wave like form with period equal to optical one.[33–36] The mechanism of SRG formation is related to the generation of strong, internal opto-mechanical stresses. Since the polymer material is in a glassy state, the opto-mechanical stresses needed for the deformation of mechanically stable polymer films (Young modulus of several GPa) must be quite high of 100 MPa up to ~1 GPa, as was recently shown.[37–40] The process can be viewed as follows: under irradiation inducing cyclic *trans–cis–trans* isomerization,[41] the azobenzene molecules rotate and re-orient perpendicularly to the electrical field vector (formation of bulk birefringence grating) causing a re-orientation of the polymer backbones to

Institute of Physics and Astronomy, University of Potsdam, 14476 Potsdam, Germany. E-mail: santer@uni-potsdam.de

† Electronic supplementary information (ESI) available. See DOI: 10.1039/c9ra02571e

which they are attached. This creates local gradients in internal stresses within the polymer material, varying with the distribution of the interference pattern and thus induces a viscoplastic deformations of the solid material (formation of topographical grating).[42–47] In fact, the inscribed SRG topography is stable over years at room temperature and can be erased only by further intense treatment such as either irradiation with a circularly polarized beam[48] or by heating[49] the polymer sample above the glass transition temperature.

Usually the dynamics of the SRG formation is probed by measuring the changing diffraction efficiency of the formed grating. Here a probe beam not affecting the azobenzene moieties is focused on the relief structure and the change in intensity of the first order diffraction peak is recorded as a function of time. The surface grating and the birefringent grating contribute to the signal and it is hard to separate these two components.[50–52] Another approach is to directly measure the change in the SRG using an atomic force microscope (AFM).[39,53–55] The drawback of the latter methodology is that there will be no information obtained about the orientation process in the bulk polymer. Here we present a novel set-up which combines these two approaches.

An AFM is integrated into a two beam interference set-up generating the interference pattern. This allows the *in situ* acquisition of surface topography changes. At the same time the diffraction efficiency (DE) signal is measured to obtain information about the bulk birefringence. Integrating a delay stage into the two beam setup allows controllable spatio-temporal shifts of the interference pattern, which locally appears as a redistribution of the electrical field vector. In this way gradual shifts or even more dynamic fluctuations in the polymer topography and the bulk birefringence can be generated, for instance, mimicking a passing wave train the speed of which can be adjusted. One may, for instance, stop migration at some point and resume at a desired later time just by switching light on and off. Additionally, we introduce a fast method of optically erasing SRGs by manipulating the illumination pattern in a particular way. One may either completely erase the topography and bulk birefringence grating or erase the primary topography grating. The time needed for erasure (only a few seconds) is much shorter than that needed for single beam irradiation (several minutes to hours) and heating (several tens of seconds during direct heating by laser irradiation[49] to several minutes and hours under external temperature increase) to achieve a comparably flattening.

Experimental part

Materials and methods

Photosensitive polymers. Poly[1-[4-(3-carboxy-4-hydroxyphenylazo)benzenesulfonamido]-1,2-ethanediyl, sodium salt] (Pazo) and poly[(methyl methacrylate)-*co*-(disperse red 1 acrylate)] (poly(MMA-*co*-DR1A)) were purchased from Sigma-Aldrich. The chemical structures of Pazo and poly(MMA-*co*-DR1A) are shown in the inset of Fig. 2a and b. The Pazo polymer solution was prepared by dissolving 170 mg Pazo in 1 ml solution containing a mixture of 95% methoxyethanol and 5% ethylene glycol. The poly(MMA-*co*-DR1A) polymer was dissolved in chloroform to achieve a concentration of 60 mg ml^{-1}. The polymers were chosen to represent two extrema, *i.e.* Pazo-polymer does not have T_g and cannot be flattened by arising temperature (as discussed in the paper), poly(MMA-*co*-DR1A) has T_g around 100 °C, and can be flattened thermally.

Sample preparation. The polymer films were prepared by spin casting 100 μl of the polymer solution on thin glass slides at 3000 rpm for one minute. This results in a film thickness of 1 μm in the case of the Pazo polymer and of 600 nm for the poly(MMA-*co*-DR1A). The film thickness was directly obtained with the help of an atomic force microscope and the cross-section analysis of a scratch within the polymer film.

Methods

The interference pattern is generated using a homemade two-beam interferometer with a continuous wave diode pumped solid state laser of the wavelength 491 nm (Cobolt Calypso). The beam diameter is set to 4 mm and the total intensity to 200 mW cm^{-2}. To probe the diffraction efficiency a 633 nm HeNe-Laser (Uniphase) with a beam diameter of 3 mm and an intensity of 30 mW cm^{-2} is focused on the sample.

The *in situ* atomic force microscope (AFM) measurements are performed using a PicoScan (Molecular Imaging) AFM working in intermittent contact mode. The scan-speed of the AFM is set to 1 Hz with a scan-area of 10 × 10 μm and a resolution of 512 × 512 pixel. Commercial tips (Nanoworld-Point probe) with a resonance frequency of 130 kHz, and a spring constant of 15 N m^{-1} are used for measurements.

Commercially available Si-Detectors (Thorlabs DET 100A/M) are used in the diffraction efficiency (DE) set-up to measure the intensity of the diffracted probe beam. A longpass filter (600 nm) was placed in front of each photodiode in order to be only sensitive to the probe beam. The set-up is controlled and the signals are recorded by an AD/DA converter (Kolter Electronic, PCI-AD12N-DAC2). The software Profilab-Expert (Abacom) for visual programming is used to synchronize the DE and two-beam-interference set-up. The intensity of the diffracted light is recorded every 200 ms.

In order to change the position of one mirror in the two-beam-interference set-up to introduce a phase delay between the two interfering beams, a piezo stack actuator (PiezoSystemJena, PA8-14 SG) with a closed loop feedback system and a travel maximum of 9.5 μm, controlled by a piezo-controller (Piezo System Jena, 12V40SG), is used. Additionally a Pockels cell (Thorlabs, EO-PC-550) acting as an optical switch is integrated into the system for fast switching between the two-beam-interference lithography and single beam erasure experiment. The voltage is supplied by a high voltage amplifier (Trek 610D) which also allows driving the Pockels cell as a lambda quarter or lambda half wave plate depending on the applied voltage.

The AFM measurements performed *ex situ* (measurements of film thickness and SRG height before and after thermal treatment) are carried out using an NTEGRA (NT-MDT) AFM operating in intermittent contact mode. Commercial tips (Nanoworld-Point probe) with a resonance frequency of 320

kHz, and a spring constant of 42 N m^{-1} are used for these measurements. All experiments are carried out under yellow light in the laboratory (to avoid undesirable photo-isomerization) and under ambient conditions, *i.e.*, at room temperature with a relative humidity of 55%. The whole set-up (see Fig. 1) was covered with a non-transparent encapsulation in order to avoid any influence of the environment on the measurement (room light, air circulation).

Results and discussion

In order to study the surface relief grating (SRG) formation a novel set-up consisting of three parts is designed enabling *in situ* recording the change of the SRG-height and diffraction efficiency (DE) as a function of irradiation time (Fig. 1). The first part contains a two beam interference set-up that permits to generate well-defined spatiotemporal intensity or polarization interference patterns by changing polarization of two interfering beams in a controlled manner. In this part of the set-up the laser beam (λ = 491 nm) is spatially expanded and then collimated with a pair of focusing and collimating lenses and a pinhole (Fig. 1). Additionally, a 50 : 50 beam splitter is added in order to separate the initially single beam into two beams of the same intensity. These two beams then pass through a set of wave plates and polarizers allowing independent control of intensity and polarization. For instance, adding a lambda quarter plate to each of the beam paths of the interference set-up, one with an angle of +45° and the second with an angle of −45° with respect to the optical axis, results in the right-left-circular interference pattern (RL). The second part of the home made set-up is an atomic force microscope (AFM) enabling measurements of the polymer topography changes *in situ*, *i.e.* even while irradiation conditions are varying. The sample is orientated with the polymer surface pointing towards the AFM tip, such that irradiation is "from below", *i.e.*, through the glass surface (Fig. 1).

To obtain at the same time information about the alignment of the azobenzene side chains in the polymer film, a red probe laser beam (HeNe, 633 nm) is integrated into the set-up. Its wave length of 633 nm falls out of the absorption bands of both polymers studied in this work and does not affect the polymer film, so that diffraction efficiency (DE) of the formed SRG can be recorded simultaneously. With our set-up we can acquire the intensity of the diffraction pattern in reflection mode in order to determine the DE of the first order diffraction (Fig. 1). To calibrate the DE, a beam splitter with the ratio of (T90/R10) is used in the DE set-up, such that 90% of the light arrives on the sample and 10% on a photodiode. The signal of this photodiode is recorded during the whole measurement for controlling the stability of the probe beam (and its intensity I_0 prior to arrival at the sample) during the experiment. The diffraction efficiency is defined as the ratio of the intensity of diffraction order (I_{DO}) and the intensity of the incoming light (I_0): $\eta = \frac{I_{DO}}{I_0}$, where I_0 is 90% of the total intensity of the probe beam. The DE set-up additionally includes a lambda quarter wave plate converting the polarization of the probe beam from linear to circular. By adding a polarizer one can deliberately set the polarization state of the probe beam (*e.g.* S- or P-polarization). By adding

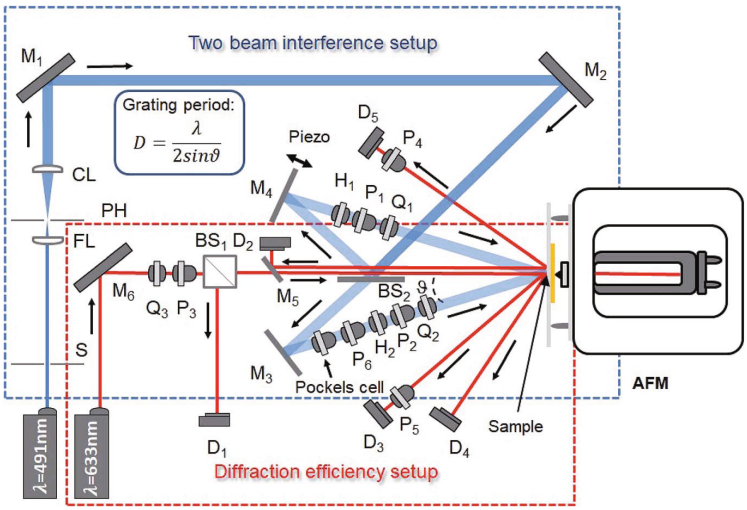

Fig. 1 Sketch of the experimental set-up consisting of three parts: (i) a two beam interference part for generation of the interference pattern (blue laser line), (ii) an atomic force microscope (AFM) for *in situ* (during irradiation) recording of the surface morphology and (iii) a diffraction efficiency (DE) set-up (red laser line) enabling the collection of information about the birefringence grating *in situ*. The mirror M_4 is combined with a piezo actuator to shift the position of the mirror and thereby to introduce a phase delay between the two interfering beams resulting in a lateral shift of the whole interference pattern along the polymer film. In order to erase the SRG by irradiation, a Pockels cell is placed in one of the two interfering beam lines (S = shutter, M = mirror, D = detector, P = polarizer, H = half-wave-plate, BS = beam splitter, Q = quarter-wave-plate, CL = collimating lens, FL = focusing lens, PH = pin hole).

a polarizer in front of the photodetector, one can measure both components of the diffracted light: polarized in plane (further denote as 1st order DE (P), measured by photodiode D_3) and out of plane (cross-polarized, further denote as 1st order DE (S), measured by photodiode D_5) with the probe beam. From the cross-polarized component one can directly obtain information about the birefringent grating, *i.e.* alignment of the azobenzene side chains within the polymer film. The set-up allows also to record the 2nd order DE (photodiode D_4) and the directly reflected light (0th order of diffraction, photodiode D_2). Adding a piezo actuator to the set up permits nanometer sized position control of mirror M_4 (see Fig. 1) for shifting the interference pattern across the polymer film plane in a defined way. Repositioning the mirror simply introduces a phase delay between the two interfering beams, resulting in a change of the local distribution of the polarization vector within interference pattern. A Pockels cell and a polarizer are further placed in the second beam line acting as a fast optical switch. Applying the "lambda half" voltage periodically to the Pockels cell one can rotate the polarization of the writing beam by 90° such that the light either passes the polarizer or is blocked. In this way, we are able to switch rapidly between two-beam interference and the single beam "erase" configuration of the set-up. The three different set-ups: two beam interference, AFM and DE acquisition are controlled and operated with software specifically designed by us to record signals of the photodiodes, control the irradiation shutter, position the mirror and apply voltage on the Pockels cell. The computer generated signals regulate, with the help of an AD/DA converter, the irradiation, the voltage send to the piezo-controller and the high-voltage-amplifier used for driving the Pockels cell. These signals are recorded in the diffraction efficiency set-up as well as with the AFM by sending the signals to the aux-input of the AFM controller.

Fig. 2 shows the *in situ* recorded SRG height and DE signal for the Pazo and poly(MMA-*co*-DR1A) polymer films as a function of irradiation time. The probe beam is p-polarized for all results discussed in this paper, while one photodiode measures the intensity of the first order diffraction in-plane (1st order DE

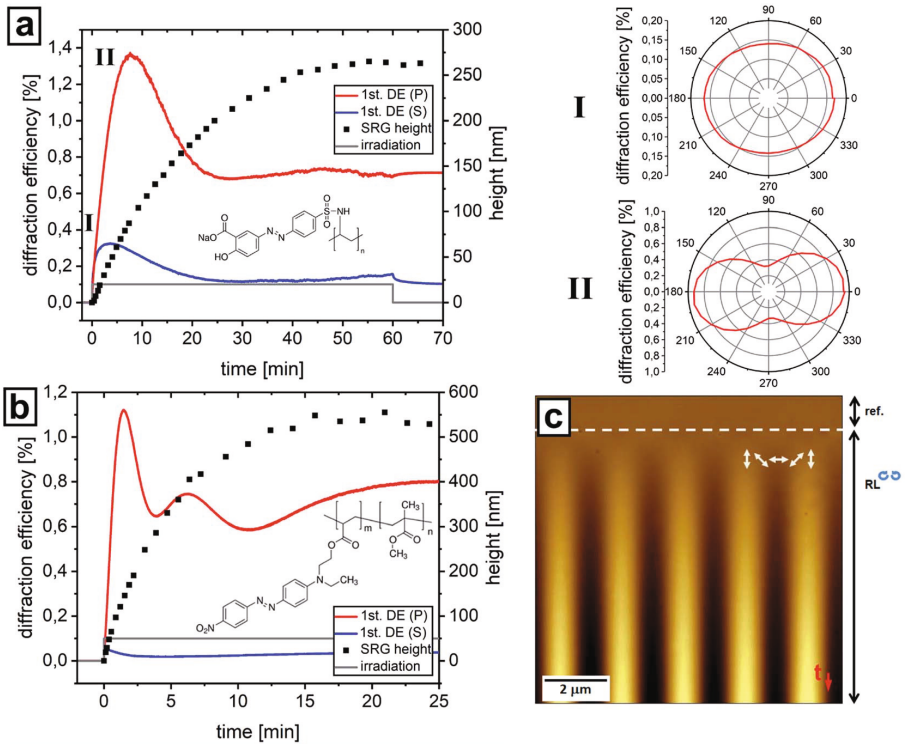

Fig. 2 (a) *In situ* recorded SRG height and diffraction efficiency of the 1st order of the Pazo polymer film (h_{Pazo} = 1 µm) irradiated with RL interference pattern as a function of time. The polarization analysis of the 1st order DE signal is shown for two different irradiation times (I = 30 s, II = 3 min) on the right. At the beginning the diffracted light is circularly polarized, but with time the component pointing along the polarization of the probe beam dominates. (b) *In situ* recorded SRG height and 1st order DE of the poly(MMA-*co*-DR1A) polymer film ($h_{poly(MMA\text{-}co\text{-}DR1A)}$ = 600 nm) irradiated with RL IP as a function of irradiation time. (c) AFM micrograph of the Pazo polymer film during irradiation, the direction of scanning is from top to bottom documenting the temporal evolution of polymer topography (the direction of scanning is indicated by the red arrow at the bottom right corner) as a function of irradiation time. The AFM scanning starts without irradiation (flat topography), at the position marked by the dashed white line the irradiation with RL interference pattern (λ = 491 nm, I = 200 mW cm^2; Λ = 2 µm) is switched on. The distribution of the electric field vector relative to the topography maxima and minima is shown by white arrows.

(P)), and the second one measures first order diffraction out-of-plane (1st order DE (S)). The presence of the out-of-plane component of the signal indicates that due to the interaction with the sample the polarization of the p-probe beam is rotated. In the case of the Pazo polymer, the DE signal of the first order diffraction on both photodiodes (red and blue curves in Fig. 2a) continuously increases during irradiation with a RL interference pattern (IP). The DE signals in-plane (red curve, 1st DE (P)) and out of plane (blue curve, 1st DE (S)) start to decrease when the SRG height reaches 120 nm and 60 nm, respectively. This behavior follows directly from the Raman–Nath theory[56,57] and gives rise to describe intensity variation as a function of SRG height by Bessel function first kind of order. The ratio of the in-plane and out-of-plane component of the 1st order DE is changing with time. At the beginning (after 30 s of irradiation) the first order diffraction is circularly polarized (Fig. 2a(I)), while for longer irradiation times (more than 3 min) the in-plane component is dominating (Fig. 2a(II)). The polar plot in Fig. 2a(I and II) is measured by switching off the pump beam and recording the intensity of the first order diffraction as a function of rotation angle by rotating the polarizer in front of photodiode D_3 (in plane component). After 1 hour irradiation the SRG height is 260 nm. The saturation in the SRG growth under irradiation with RL interference patterns for a 1 μm thick film is achieved after *ca.* 10 hours of irradiation at which the height is around 900 nm.

In the case of the second polymer studied here (poly(MMA-*co*-DR1A)), the saturation of the SRG height is already achieved after 15 minutes of irradiation with the final value of 550 nm (total film thickness of 600 nm). The DE is showing similar behavior as in the case of the Pazo polymer film, but due to the rapid evolution of the grating, the characteristic 1st order DE (P) peak is reached faster, *i.e.* after 86 seconds of irradiation, at which the SRG height is again 120 nm (Fig. 2b). There is also no significant out of plane component in the first order DE noticeable (see blue curve 1st DE (S) in Fig. 2b).

With the above described set-up we are able to generate a reversible switching of the polymer topography between a structured and a flat state utilizing irradiation with changing interference patterns. This was achieved by changing the position of the mirror M4 (see Fig. 1) during irradiation which results in a lateral shift of the whole interference pattern along the polymer topography. Fig. 3 shows the results of shifting the interference pattern by half of the optical period for Pazo polymer film. The experiment is performed as follows: first the sample is irradiated for 180 seconds with RL polarization IP (onset of irradiation is shown by 1st dashed white line at the top of Fig. 3a). Polarization IP means that the intensity along the sample is constant, while the orientation of the electric field vector (see white arrows in Fig. 2c and 3a) varies locally with a certain period (optical period, Λ). This first irradiation step generates a grating height of 40 nm (Fig. 3a). Afterwards the local distribution of the electrical field vector is shifted by half of the optical period, which corresponds to 90° rotation of local electrical field vector (see white arrows in Fig. 3a). After the shift the SRG height continuously decreases till a flat topography is reached (dashed white line at the bottom of Fig. 3a). At this point the irradiation is stopped. This erase process is slightly faster (160 s, *i.e.* 0.29 nm s^{-1} of topography flattening) compared to SRG inscription (180 s, 0.20 nm s^{-1} of topography increase). A possible explanation is that the initial state of both processes is different. During irradiation with IP and corresponding cyclic *trans–cis* photoisomerization the azobenzene groups rotate to align perpendicularly with their main axis to the electrical field vector resulting in locally ordered domains. Since in the case of the SRG formation the azobenzene molecules are initially randomly orientated within the polymer film, the time needed for local azobenzene alignment is larger than

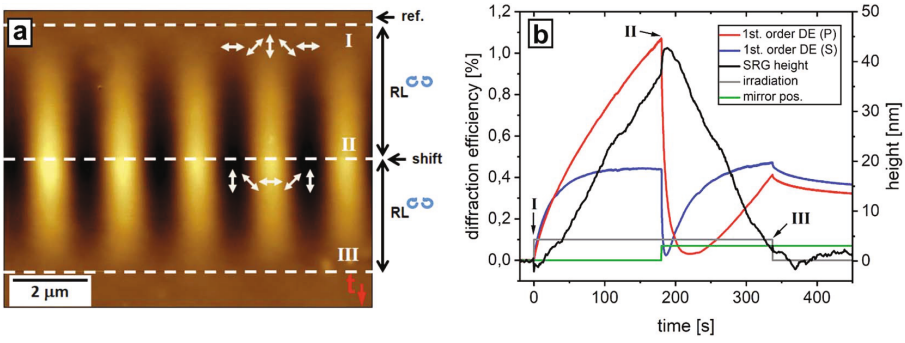

Fig. 3 (a) *In situ* recorded AFM micrograph of the Pazo polymer film during irradiation with RL IP ($\lambda = 491$ nm, $I = 200$ mW cm^{-2}; $\Lambda = 2$ μm), the local distribution of polarization is indicated by white arrows. AFM scanning starts at the top in dark with flat topography; at the point marked by the 1st (I) white dashed line, the irradiation with IP is switched on for 180 s; at the point marked by "shift" at the 2nd (II) dashed white line, the interference pattern is shifted by half an optical period. The new distribution of the electrical field vector relative to the polymer topography is shown as above. The shifting of the interference pattern is equivalent to a rotation of the local electric field vectors by 90°. At the bottom of the micrograph marked by 3rd (III) dashed white line, the irradiation is switched off. (b) *In situ* recorded SRG height and diffraction efficiency as a function of irradiation time. At the point where the interference pattern is shifted, the increase in the SRG height becomes noticeable (black curve), while the diffraction efficiency decreases (red and blue curves). The SRG is erased with time accompanied by the formation of a new birefringent grating in the bulk.

in the case of irradiation with shifted interference patterns. In this case, due to local rotation of the electric field vector by 90°, the probability to absorb light by the aligned azobenzene molecules is larger thus resulting in a faster kinetics of topography response. At the point where the interference pattern is shifted, a fast jump in the SRG height of 5 nm became noticeable followed by a linear decrease (Fig. 3b, black curve). The explanation for this behavior is based again on local preorientation of the azobenzene molecules during the first step of irradiation. At the point of IP shifting all the aligned molecules are able to absorb incoming light resulting in noticeable increase of the free volume in polymer film and as a consequence its height increases.

The in-plane component of the diffraction efficiency of the first order diffraction (red curve, 1st order DE (P), in Fig. 3b) continuously increases with SRG height. The out of plane component (blue curve, 1st order DE (S), in Fig. 3b) saturates after a certain time. At the point where the interference pattern is shifted, there is fast drop (within 6 seconds) of out-of-plane component (blue curve in Fig. 3b), at this point the SRG height and the out-of-plane component contribute to the overall DE signal. After 37 seconds the in-plane component (red curve in Fig. 3b) settles to zero, while the increasing 1st order DE (S) component and the left SRG result in DE signal of 0.4%.

A short time after shifting of the IP, both components of the DE, *i.e.* in- and out-of-plane, start to increase, while the SRG height decreases. At the point where the topography becomes flat there is nevertheless still significant DE signal indicating the formation of a new birefringent grating from alignment of azobenzene groups in the bulk. In this case the erase process with shifting the interference pattern can be understood as erasing the primary, topographical SRG and forming a new birefringent grating in the bulk. Further irradiation will create a new SRG but shifted by half an optical period as described below (see Fig. 5).

A similar behavior is also observed in case of poly(MMA-*co*-DR1A) polymer films (Fig. 4). Since the response of this polymer on irradiation is faster, the first exposure to RL IP lasts for only 48 seconds resulting in a grating height of 80 nm (speed of grating increase is 1.7 nm s^{-1}). After shifting the interference pattern by half a period, the topography is flattened within only 34 seconds (speed of grating decrease is 2.1 nm s^{-1}) (Fig. 4). At the point where the topography is flat again, there is a small signal in the 1st order DE indicating the formation of new bulk phase grating. The out-of-plane component in the DE (blue curve, 1st order DE (S), in Fig. 4b) is negligible. In contrast to the Pazo polymer film there is no jump in the SRG height detected at the point where the interference pattern is shifted. One possible explanation for this is that due to the fast response on irradiation, the topography jump is completed within a time too short for the AFM to detect it.

In the previous experiments the irradiation is stopped when the surface is flattened, but in case of further irradiation after IP shifting, the formation of a new SRG is observed with positions of maxima and minima interchanged (Fig. 5). Moreover, when the IP is shifted back to its initial distribution, the primary SRG is recovered. This procedure can be conducted repeatedly, as shown in Fig. 5, where the continuous scan with repeated shifts leads to a checkerboard pattern in the AFM recording. For the Pazo polymer, the irradiation is stopped after 4 cycles of IP shifting, at a point where the surface has just been rendered flat again (Fig. 5a).

The presence of the diffraction efficiency signal (red and blue curves in Fig. 5b) indicates the existence of bulk birefringent grating due to local alignment of the azobenzene side groups. This phase grating decreases in the dark indicating orientation relaxation of the azobenzenes with time. A similar experiment is performed in the case of poly(MMA-*co*-DR1A) polymer films that permits the same reversible surface structuring (Fig. 5c and d). In this case, the shifting is carried out seven times as indicated in Fig. 5c. Here, the irradiation time for each step is increased

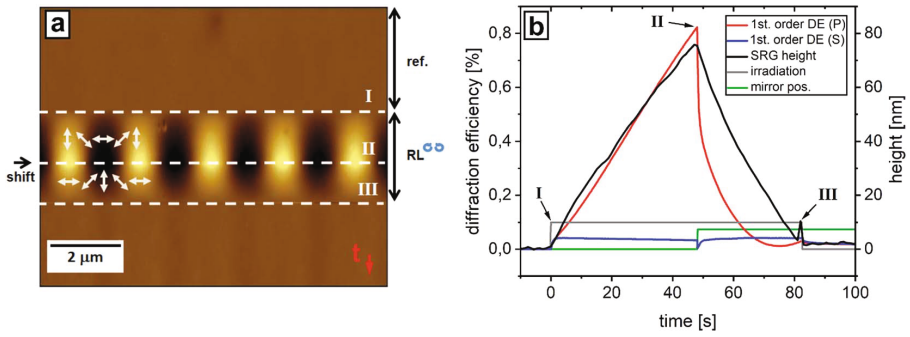

Fig. 4 (a) *In situ* recorded AFM micrograph of the SRG formation and erasure within the poly(MMA-*co*-DR1A) polymer film ($h_{poly(MMA\text{-}co\text{-}DR1A)}$ = 600 nm) during irradiation with a RL interference pattern (λ = 491 nm, I = 200 mW cm^{-2}; Λ = 2 µm). The AFM scanning proceeds from top to bottom (the direction is indicated by red arrow in the lower right corner), during scanning in dark, the topography is flat. At the position marked with the 1st (I) dashed white line the irradiation with RL IP is switched on for 48 seconds. At the second dashed line (II) the interference pattern is shifted by $\lambda/2$ (half of the optical period). The local distribution of the electric field vector relative to the topography extrema is shown by white arrows for both cases. After erasing of the polymer grating (34 seconds of irradiation), the laser is switched off (at the point marked by the 3rd (III) dashed white line). (b) *In situ* recorded SRG height (black line) and 1st order diffraction efficiency in plane (red line, 1st order DE (P)) and out of plane (blue line, 1st order DE (S)) as a function of time.

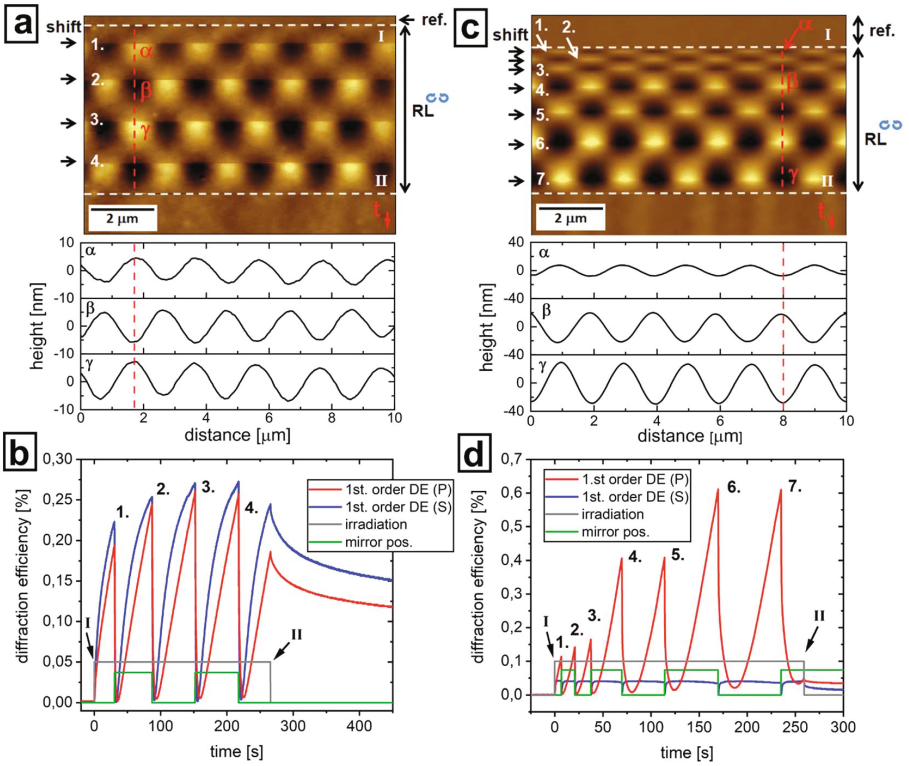

Fig. 5 (a) *In situ* recorded AFM micrograph of the Pazo polymer film ($h_{Pazo} = 1$ μm) during irradiation with RL IP ($\lambda = 491$ nm, $I = 200$ mW cm^{-2}; $\Lambda = 2$ μm). The interference pattern is shifted four times by $\lambda/2$ of the optical period each after 60 s of irradiation. After each shifting of the IP the initial SRG is erased and a new SRG is formed with interchanged position of topography maxima and minima. The irradiation was stopped at the point where the surface was flat again, marked by dashed white line (II). (b) The evaluation of the 1st order DE recorded in plane (red curve) and out-of-plane (blue curve) is presented as a function of time for four successive IP shifts. A drastic drop in the diffraction efficiency became noticeable whenever the interference pattern is shifted. (c) AFM micrograph of poly(MMA-*co*-DR1A) film topography ($h_{poly(MMA\text{-}co\text{-}DR1A)} = 600$ nm) irradiated with periodically shifted RL IP with continuously increasing irradiation time: 7 s, 14 s, 17 s, 32 s, 44 s, 56 s, 65 s. (d) The corresponding 1st order DE recorded simultaneously with the topography change in (c). Red line in (a) and (c) indicates the direction along which the cross-section was recorded as indicated in the corresponding plots below (a) and (c).

between successive shifting events resulting in a continuous increase in SRG height showing also here the independency of the erase process from the SRG height. By continuously shifting the interference pattern, *e.g.* by applying a saw-tooth signal to the piezo, one can shift the SRG over several micrometers (Fig. 6).

In this way, we are able to induce fluctuations in the polymer topography resembling propagation of the water wave (Fig. 6b). To achieve continuous change in the polymer topography without intermittent flat state, we shift the IP in each subsequent step by fourth of the optical period which results in propagation of the primary topography maxima/minima over 14 μm to the right (see Fig. 6b). The corresponding changes in the DE signal are shown in Fig. S2 (see ESI†).

Summarizing this part we can state that the erasure of the polymer topography by applying shifts to the interference patterns (*i.e.* rotating the local distribution of the electric field vector by 90°) is an efficient and fast process which proceeds by overwriting the initial SRG by a new bulk birefringent grating. In order to estimate the efficiency of this erase mechanism, we compare in the following how erasure can be achieved alternatively by applying a single beam or by thermal treatment.

Erasing a SRG pattern with a single laser beam

A fast optical switch is integrated into the set-up in order to turn off one of the two interfering beams. This is achieved by employing a Pockels cell and an additional polarizer (see Fig. 1). By applying the lambda-half voltage on the Pockels cell the polarization of the writing beam is rotated by 90° so that the light will be blocked by the subsequent polarizer. This established a very fast switching between two-beam and single beam erasure. Due to the two integrated lambda quarter plates of the RL interference pattern, the single beam is also circularly polarized, which can be expected to induce an effective erasure process.[48] Fig. 7 shows the results of the single beam experiment performed with a poly(MMA-*co*-DR1A) structured polymer film.

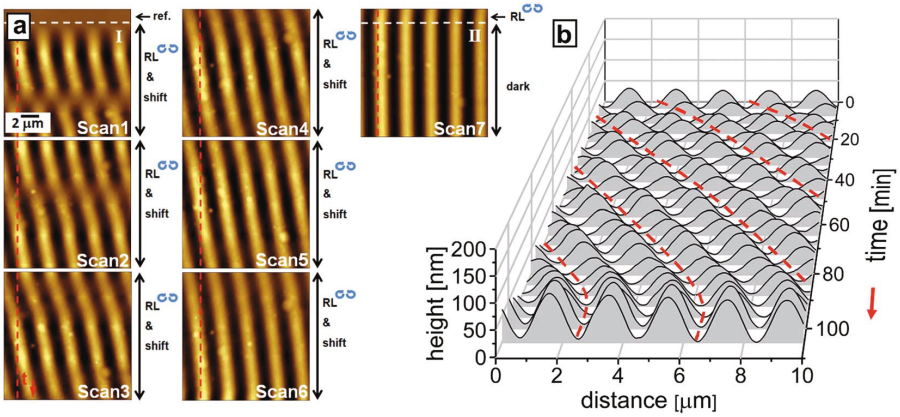

Fig. 6 (a) AFM micrographs of the Pazo polymer irradiated by shifting the RL IP 26× times by $\lambda/4$, which corresponds with a total shift of *ca.* 7 periods of the optical grating, *i.e.* over 14 µm distance. The dashed red vertical line indicates the position of one of the primary topography maxima. With the IP shifting the SRG propagates to the right resembling a traveling wave schematically shown in (b).

The film was first irradiated with RL IP for 1 minute resulting in 80 nm SRG height. Afterwards the writing beam is switched off for 10 minutes. During this time the in-plane component of the 1st order DE drops exponentially while the SRG height stays constant (Fig. 7). In the following step switching on the erase beam results in fast decrease of the DE signal and SRG height. The irradiation is stopped after 400 min when no diffraction efficiency signal could be detected. At this point the polymer film is found to be atomically smooth (see Fig. 7c). In the case of Pazo polymer the erasure with the circularly polarized beam does not result in a complete flattening of the polymer topography as well as vanishing of DE signal even after 20 h of irradiation (see ESI, Fig. S1†). Comparing these results with those obtained by the shifting procedure (Fig. 3 and 4) shows that erasure *via* shifting is indeed much faster for both polymers, but the final state of the flattened polymer film is different. In the case of single beam erasure, the alignment of azobenzene molecules introduced by the IP irradiation is getting destroyed and transformed to a random orientation indicated by decreasing of DE signal. Shifting the interference pattern eliminates the grating topography by overwriting the initial birefringent grating with a new one. At the point of a flat surface the bulk is already reoriented with a pure phase grating which can directly be seen in the DE (red and blue curves in Fig. 3b).

To compare the optically induced SRG erasure process to the thermal one, we employed another home-made set-up consisting of a hot plate with a temperature sensor onto which the sample is placed, and an optical part facilitating red laser beam

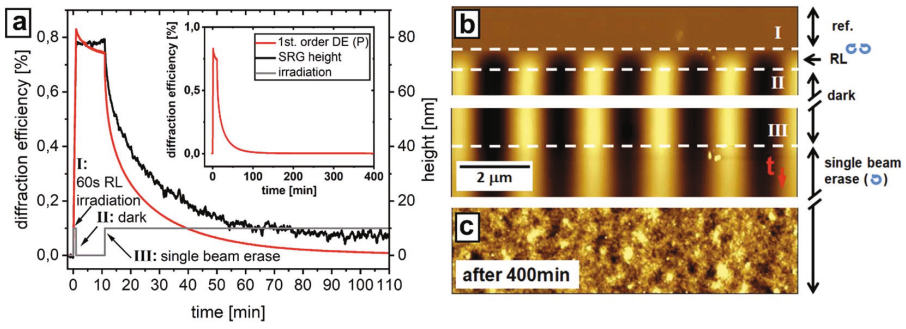

Fig. 7 Single beam erasure experiment of the SRG in a poly(MMA-*co*-DR1A) film. (a) *In situ* recorded SRG height (black curve) and in plane component of the 1st order DE signal (red curve) as a function of time. The gray curve indicates irradiation steps. The polymer film is illuminated with RL interference pattern for 1 min resulting in 80 nm SRG height (see AFM topography in "b"). Afterwards the irradiation is switched off for 10 min. The 1st order DE signal decreases with time, while the SRG height is constant. In the following step, the circularly polarized erase beam is switched on resulting in a decay of the SRG height and DE signal. (b) *In situ* recorded AFM micrograph showing the change in the SRG height as a function of time. The scanning is started at the top in dark where the topography is flat followed by 1 min irradiation with RL IP started at point marked by 1st (I) and stopped at 2nd (II) dashed white line, after 10 minutes scanning in dark, the circular polarized erasure beam is switched on (3rd white dashed line (III)). (c) Polymer film surface after 400 min of single beam irradiation. The SRG (80 nm) is completely erased and the DE reached its initial value of zero ($I_{RL} = 200$ mW cm^2; $I_{single\ beam} = 100$ mW cm^2; $\Lambda = 2$ µm; $h_{poly(MMA\text{-}co\text{-}DR1A)} = 600$ nm).

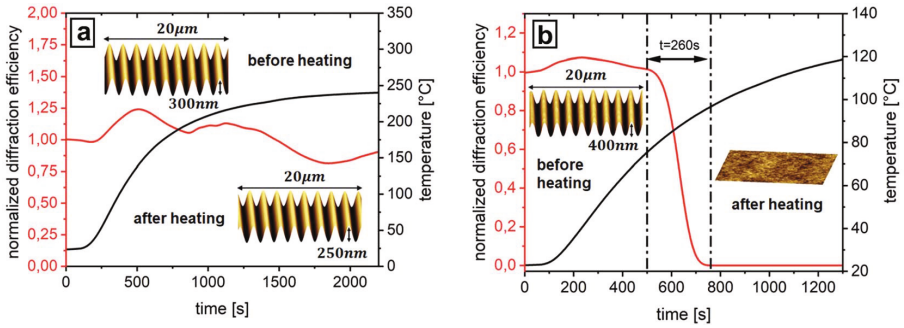

Fig. 8 Thermal treatment of the surface relief grating: diffraction efficiency (red curves) of the Pazo (a) and poly(MMA-*co*-DR1A) film (b) as a function of time during temperature increase. The Pazo film shows no significant drop in the DE as well as in grating height under heating up to 250 °C. The poly(MMA-*co*-DR1A) film shows a fast drop in the DE down to zero within 260 seconds initiated at 80 °C. The *ex situ* acquired AFM micrographs show that the 400 nm SRG was completely erased ($I = 200$ mW cm^2; $\Lambda = 2$ μm; $h_{\text{poly(MMA-co-DR1A)}} = 600$ nm; $h_{\text{Pazo}} = 1$ μm).

for measurements of diffraction efficiency to be directed at the polymer sample. As can be seen from Fig. 8 the erasure of a 400 nm high grating of poly(MMA-*co*-DR1A) sets in at *ca.* 80 °C ($T_g \sim 102$ °C)[58] and after *ca.* 260 seconds the diffraction efficiency signal drops to zero (Fig. 8b). So, the thermal erasure needs around 5 minutes and heating up to 100 °C, while optical erasure by IP shifting takes place within 34 seconds at room temperature. Single beam erasure requires the most time (400 min). In contrast, it was not possible to flatten Pazo film thermally. Indeed, heating up to 250 °C, at which the decomposition of the polymer materials sets in (see TGA measurement in ESI, Fig. S3a†), does not result in decrease of the diffraction efficiency signal (red curve in Fig. 8a), the SRG height is also only slightly affected: it drops from 300 to 250 nm within 30 minutes of heating at 250 °C. As can be seen from DSC measurements (ESI, Fig. S3b†), there is no clear indication of the glass transition temperature. This result is in contrast to the work published by Ferreira *et al.*, who measured 95 °C as T_g for this polymer,[59] but in a good agreement with the results of Stumpe *et al.*[60] where it was reported that the SRG inscribed in Pazo could not be erased by heating at 200° over 6 hours. This is explained by the presence of ionic interactions in the side chains of the Pazo (see chemical structure in Fig. 2a).[61,62] Thus with these results, we can state that the erasure of the surface relief grating of Pazo polymer can be done quite easily and fast (160 seconds of irradiation at room temperature) using the IP shifting method (Fig. 3), with single beam the procedure takes 20 hours and does not result in complete elimination of the grating, while the thermal erasure is not possible at all. These experiments show that the temperature stability of the SRG depends on the polymer structure itself.

Conclusions

Here we have reported on the reversible surface structuring of photosensitive polymer films using a novel method of fast SRG erasure simply by shifting the interference pattern by half an optical period. This is achieved by utilizing a home-made set-up to record the changes in the surface relief grating (SRG) and the diffraction efficiency (DE) signal upon irradiation with varying interference patterns *in situ*. Our setup also permits to separate the SRG part from the birefringent grating component in the DE, so that we can directly probe the molecular orientation of the azobenzene moieties in the bulk. Integrating a phase delay stage into the two beam interference set-up allows for shifting the interference patterns along the sample plane; in this way the polymer surface can be rendered "dynamic". A shift of half of the optical period leads to erasure of the just created surface grating by inscribing a new birefringent grating in the bulk. Depending on the polymer material this leads to the generation of a pure phase grating without any surface structure (with the interesting example of the Pazo polymer studied here). The reversibility of the surface structuring is demonstrated for two different polymers. Attempts to erase the SRG by single beam irradiation and a change in the temperature required significantly more effort than optical shifting method. In the case of thermal erasure, the Pazo polymer is found to be stable such that both gratings, topographical and the bulk birefringence withstand temperatures up to 250 °C over hours of heating, while in the poly(MMA-*co*-DR1A) film the SRG is erased completely with heating at the glass transition temperature T_g during 5 minutes. Erasing SRGs with a single circularly polarized beam is feasible, but requires 400 minutes of irradiation time for poly(MMA-*co*-DR1A), while the more rigid polymer Pazo takes more than 20 hours of irradiation. In contrast, the optical shift method reduces these times to only 160 seconds and 34 seconds irradiation time for Pazo and poly(MMA-*co*-DR1A) polymers, respectively. This phenomenon is simply related to the fact that shifting the interference pattern produces a pure phase grating with a flat topography, while erasing with a single beam completely destroy the grating restoring the initial amorphous state of the polymer film and thus requires more time. The method proposed here bears one decisive advantage: patterns in topography and other optical properties such as birefringence are inscribed at the same time. By using the peculiar dynamics and depending on the protocol of optical

settings we can end up with topographical and optical (birefringence) patterns, or combinations thereof. This might lead to hitherto unprecedented applications as indicated in the introduction.

Conflicts of interest

There are no conflicts to declare.

Acknowledgements

This research is supported by the Helmholtz Graduate School on Macromolecular Bioscience (Teltow, Germany) and German-Russian Interdisciplinary Science Center (G-RISC). We thank Prof. Dr Carsten Henkel and Burkhard Stiller for the fruitful discussions. We thank Prof. I. Zvereva (Centre of Thermal Analysis and Calorimetry, St. Petersburg State University) for the support in measurements and interpretation of TGA and DSC results.

References

1 D. Liu and D. J. Broer, *Responsive Polymer Surfaces: Dynamics in Surface Topography*, Wiley-VCH, Weinheim, Germany 2017.
2 L. Dong, A. K. Agarwal, D. J. Beebe and H. Jiang, *Nature*, 2006, **442**, 551.
3 T. M. de Jong, D. K. G. de Boer and C. W. M. Bastiaansen, *Opt. Express*, 2011, **19**, 15127–15142.
4 M. Yamada, M. Kondo, J. Mamiya, Y. Yu, M. Kinoshita, C. J. Barrett and T. Ikeda, *Angew. Chem., Int. Ed. Engl.*, 2008, **47**, 4986.
5 S. Hvilsted, C. Sanchez and R. Alcala, *J. Mater. Chem.*, 2009, **19**, 6641–6648.
6 M. Ibn-Elhaj and M. Schadt, *Nature*, 2001, **410**, 796.
7 T. S. Wong, S. H. Kang, S. K. Y. Tang, E. J. Smythe, B. D. Hatton, A. Grinthal and J. Aizenberg, *Nature*, 2011, **477**, 443.
8 L. M. Goldenberg, V. Lisinetskii, Y. Gritsai, J. Stumpe and S. Schrader, *Laser Phys. Lett.*, 2013, **10**, 085804.
9 L. M. Goldenberg, V. Lisinetskii, Y. Gritsai, J. Stumpe and S. Schrader, *Adv. Mater.*, 2012, **24**, 3339.
10 T. Alasaarela, D. Zheng, L. Huang, A. Priimagi, B. Bai, A. Tervonen, S. Honkanen, M. Kuittinen and J. Turunen, *Opt. Lett.*, 2011, **36**, 2411–2413.
11 R. H. Bishop, in *Mechatronics: An Introduction*, ed. T. Francis, Taylor and Francis Group, Oxfordshire, England, 2006, p. 312.
12 S. Loebner, J. Jelken, N. S. Yadavalli, E. Sava, N. Hurduc and S. Santer, *Molecules*, 2016, **21**, 1663.
13 S. L. Oscurato, F. Borbone, P. Maddalena and A. Ambrosio, *ACS Appl. Mater. Interfaces*, 2017, **9**, 30133–30142.
14 N. A. Malvadkar, M. J. Hancock, K. Sekeroglu, W. J. Dressick and M. C. Demirel, *Nat. Mater.*, 2010, **9**, 1023.
15 P. Zhang, H. Liu, J. Meng, G. Yang, X. Liu, S. Wang and L. Jiang, *Adv. Mater.*, 2014, **26**, 3131–3135.
16 X. Qiu, *J. Appl. Phys.*, 2010, **108**, 011101.
17 D. Liu, N. B. Tito and D. J. Broer, *Nat. Commun.*, 2017, **8**, 1526.
18 W. Feng, D. J. Broer and D. Liu, *Adv. Mater.*, 2018, **30**, 1704970.
19 A. H. Gelebart, D. J. Mulder, M. Varga, A. Konya, G. Vantomme, E. W. Meijer, R. L. B. Selinger and D. J. Broer, *Nature*, 2017, **546**, 632–636.
20 K. Kumar, A. P. H. J. Schenning, D. J. Broer and D. Liu, *Soft Matter*, 2016, **12**, 3196–3201.
21 A. J. J. Kragt, D. J. Broer and A. P. H. J. Schenning, *Adv. Funct. Mater.*, 2018, **28**, 1704756.
22 D. Liu, L. Liu, P. R. Onck and D. J. Broer, *Proc. Natl. Acad. Sci. U. S. A.*, 2015, **112**, 3880–3885.
23 A. Kopyshev, C. J. Galvin, R. R. Patil, J. Genzer, N. Lomadze, D. Feldmann, J. Zakrevski and S. Santer, *ACS Appl. Mater. Interfaces*, 2016, **8**, 19175.
24 P. Rochon, E. Batalla and A. Natansohn, *Appl. Phys. Lett.*, 1995, **66**, 136–138.
25 D. Y. Kim, S. K. Tripathy, L. Li and J. Kumar, *Appl. Phys. Lett.*, 1995, **66**, 1166–1168.
26 C. J. Barrett, P. Rochon and A. Natansohn, *J. Chem. Phys.*, 1998, **109**, 1505–1516.
27 K. G. Yager and C. J. Barrett, *Curr. Opin. Solid State Mater. Sci.*, 2001, **5**, 487–494.
28 T. König, N. S. Yadavalli and S. Santer, *J. Mater. Chem.*, 2012, **22**, 5945–5950.
29 T. König, V. V. Tsukruk and S. Santer, *ACS Appl. Mater. Interfaces*, 2013, **5**, 6009–6016.
30 Th. Papke, N. S. Yadavalli, C. Henkel and S. Santer, *ACS Appl. Mater. Interfaces*, 2014, **6**, 14174–14180.
31 A. Kopyshev, C. J. Galvin, J. Genzer, N. Lomadze and S. Santer, *Polymer*, 2016, **98**, 421–428.
32 A. Kopyshev, N. Lomadze, D. Feldmann, J. Genzer and S. Santer, *Polymer*, 2015, **79**, 65–72.
33 J. Vapaavuori, A. Goulet-Hanssens, I. T. S. Heikkinen, C. J. Barrett and A. Priimagi, *Chem. Mater.*, 2014, **26**, 5089–5096.
34 J. E. Koskela, J. Vapaavuori, R. H. A. Ras and A. Priimagi, *ACS Macro Lett.*, 2014, **3**, 1196–1200.
35 N. S. Yadavalli, T. König and S. Santer, *J. Soc. Inf. Disp.*, 2015, **23**, 154–162.
36 T. König, L. M. Goldenberg, O. Kulikovska, L. Kulikovsky, J. Stumpe and S. Santer, *Soft Matter*, 2011, **7**, 4174–4178.
37 V. Toshchevikov, J. Ilnytskyi and M. Saphiannikova, *J. Phys. Chem. Lett.*, 2017, **8**, 1094–1098.
38 N. S. Yadavalli, D. Korolkov, J. Moulin, M. Krutyeva and S. Santer, *ACS Appl. Mater. Interfaces*, 2014, **6**, 11333–11340.
39 N. S. Yadavalli, F. Linde, A. Kopyshev and S. Santer, *ACS Appl. Mater. Interfaces*, 2013, **5**, 7743–7747.
40 G. Di Florio, E. Bründermann, N. S. Yadavalli, S. Santer and M. Havenith, *Nano Lett.*, 2014, **14**, 5754–5760.
41 J. Ilnytskyi and M. Saphiannikova, *ChemPhysChem*, 2015, **16**, 3180–3189.
42 J. M. Ilnytskyi, D. Neher and M. Saphiannikova, *J. Chem. Phys.*, 2011, **135**, 044901.
43 V. Toshchevikov, M. Saphiannikova and G. Heinrich, *J. Phys. Chem. B*, 2012, **116**, 913–924.

44 V. Toshchevikov and M. Saphiannikova, *J. Phys. Chem. B*, 2014, **118**, 12297–12309.
45 V. Toshchevikov, M. Saphiannikova and G. Heinrich, *J. Phys. Chem. B*, 2009, **113**, 5032–5045.
46 K. G. Yager and C. J. Barrett, *J. Chem. Phys.*, 2007, **126**, 094908.
47 T. M. Geue, M. G. Saphiannikova, O. Henneberg, U. Pietsch, P. L. Rochon and A. L. Natansohn, *Phys. Rev. E: Stat., Nonlinear, Soft Matter Phys.*, 2002, **65**, 052801.
48 J. Vapaavuori, R. H. A. Ras, M. Kaivola, C. G. Bazuin and A. Priimagi, *J. Mater. Chem. C*, 2015, **3**, 11011–11016.
49 A. Tofini, L. Levesque, O. Lebel and R. G. Sabat, *J. Mater. Chem. C*, 2018, **6**, 1083–1091.
50 F. L. Labarthet, T. Buffeteau and C. Sourisseau, *J. Phys. Chem. B*, 1998, **102**, 2654–2662.
51 F. L. Labarthet, P. Rochon and A. Natansohn, *Appl. Phys. Lett.*, 1999, **75**, 1377–1379.
52 F. L. Labarthet, J. L. Bruneel, T. Buffeteau and C. Sourisseau, *J. Phys. Chem. B*, 2004, **108**, 6949–6960.
53 N. S. Yadavalli and S. Santer, *J. Appl. Phys.*, 2013, **113**, 224304.
54 N. S. Yadavalli, M. Saphiannikova, N. Lomadze, L. M. Goldenberg and S. Santer, *Appl. Phys. A*, 2013, **113**, 263–272.
55 N. S. Yadavalli, M. Saphiannikova and S. Santer, *Appl. Phys. Lett.*, 2014, **105**, 051601.
56 A. Emoto, S. B. Baharim, T. Sasaki, T. Shioda, A. Ogiwara and H. Ono, *Jpn. J. Appl. Phys.*, 2010, **49**, 122502.
57 C. V. Raman and N. S. Nagendra Nathe, *Proc. Indian Acad. Sci. Sect. A*, 1935, **2**, 406–412.
58 As provided by Sigma Aldrich.
59 Q. Ferreira, P. A. Ribeiro, O. N. Oliveira and M. Raposo, *ACS Appl. Mater. Interfaces*, 2012, **4**, 1470–1477.
60 L. M. Goldenberg, O. Kulikovska and J. Stumpe, *Langmuir*, 2005, **21**, 4794.
61 Q. Zhang, X. Wang, C. J. Barrett and C. G. Bazuin, *Chem. Mater.*, 2009, **21**, 3216.
62 J. Vapaavuori, C. G. Bazuin and A. Priimagi, *J. Mater. Chem. C*, 2018, **6**, 2168.

Supporting Information

Light Induced Reversible Structuring of Photosensitive Polymer Films

Joachim Jelken, Svetlana Santer*

Institute of Physics and Astronomy, University of Potsdam, 14476 Potsdam, Germany

AUTHOR EMAIL ADDRESS: santer@uni-potsdam.de

RECEIVED DATE

* Corresponding author: santer@uni-potsdam.de

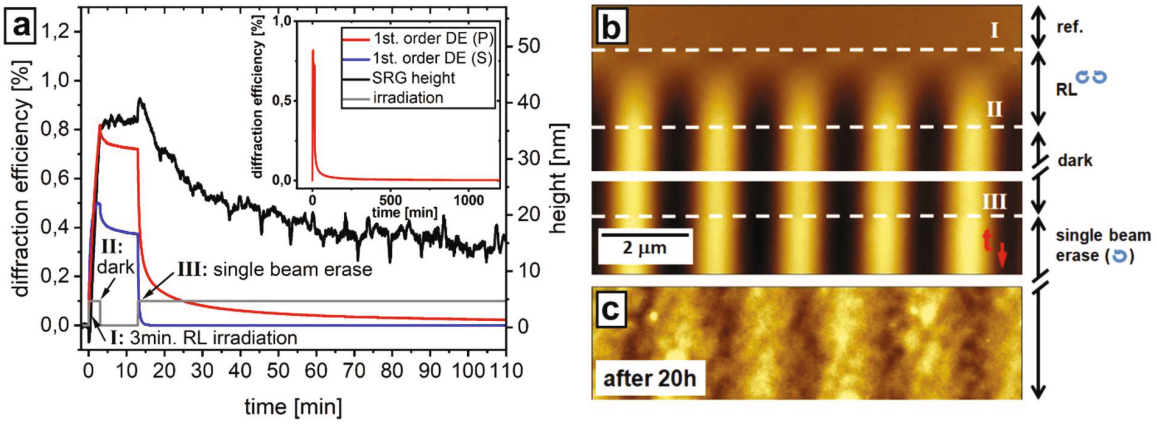

Figure S1. Single beam erasure experiment of the SRG in Pazo film. (a) *In-situ* recorded SRG height (black curve) and in- (red curve) and out- (blue curve) of plane components of the 1st diffraction order DE signal as a function of time. Gray line depicts illumination steps. The polymer film was irradiated with RL interference pattern for 3 min resulting in 40nm SRG height (see AFM topography in "b"). Afterwards the irradiation was switched off for 10min. The DE signals decrease with time, while the SRG height is constant. In the following step, the circular polarized erase beam was switched on resulting in drop of the SRG height and DE signal. (b) *In-situ* recorded AFM micrograph showing the change in the SRG height as a function of time. The scanning is started at the top in dark where the topography is flat followed by 3min irradiation with RL IP started at point marked by I^{st} and stopped at II^{d} dashed white line, after 10 minutes scanning in dark, the circular polarized erasure beam is switched on (III^{d} dashed white line). (c) Polymer film surface after 20 hours of single beam irradiation. The SRG height is 4 nm and the DE has residual value indicating still the presence of birefringent phase grating. ($I_{RL} = 200mW/cm^2$; $I_{single\ beam} = 100mW/cm^2$; $\Lambda = 2\mu m$; $h_{\mathrm{Pazo}} = 1000nm$).

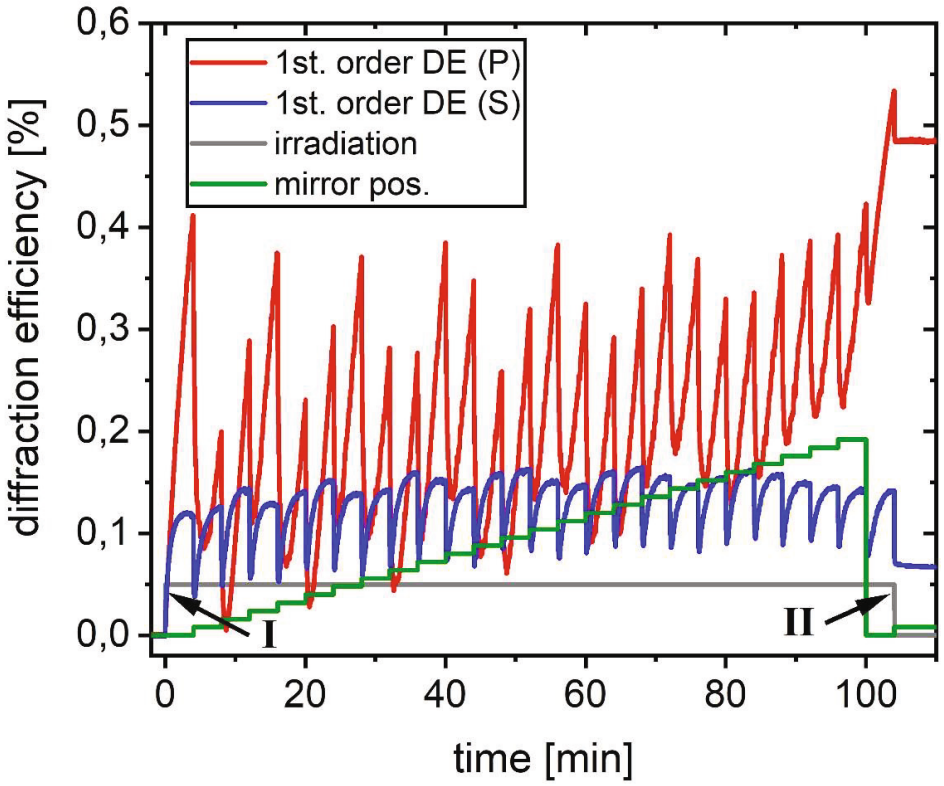

Figure S2. Diffraction efficiency corresponding to the *in-situ* AFM micrograph of the continuously shifting experiment in **Figure 6**. The RL IP is shifted 26 times with a saw-tooth pulse by $\approx \lambda/4$ every 4min. In total this is a shift of ≈ 7 periods of the interference pattern. By applying this pulse the SRG is shifted by $\approx 14\mu m$. At the point of IP shift the in- and out-of-plane component of the DE is decreasing followed by fast recovering to the initial state. ($I_{RL} = 200mW/cm^2$; $\Lambda = 2\mu m$; $h_{\mathrm{Pazo}} = 1000nm$).

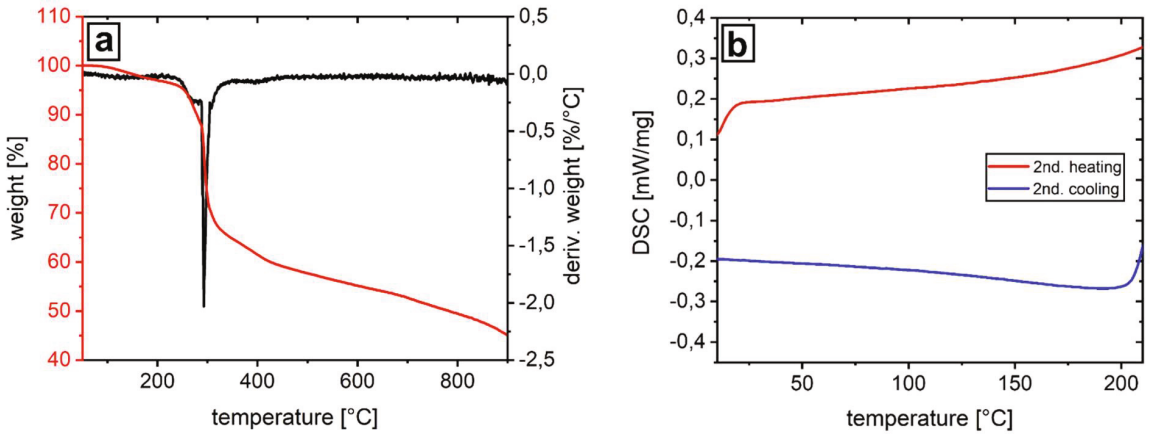

Figure S3. Thermogravimetric analysis (a) and differential scanning calorimetry (b) of the Pazo polymer. At the temperature of 250°C a significant mass loss became noticeable indicating the thermal decomposition. In (b) the second heating and cooling of the sample from 0°C till 200°C with a heating/cooling rate of 10K/min is displayed. The measurement doesn't show any characteristic feature like a glass transition or melting point.

4.4. Publication IV: Rapid optical erasure of surface relief and bulk birefringence gratings in azo-polymer thin films

PROCEEDINGS OF SPIE

SPIEDigitalLibrary.org/conference-proceedings-of-spie

Rapid optical erasure of surface relief and bulk birefringence gratings in azo-polymer thin films

Jelken, Joachim, Brinkjans, Marius, Henkel, Carsten, Santer, Svetlana

Joachim Jelken, Marius Brinkjans, Carsten Henkel, Svetlana Santer, "Rapid optical erasure of surface relief and bulk birefringence gratings in azo-polymer thin films," Proc. SPIE 11367, Photosensitive Materials and their Applications, 1136710 (1 April 2020); doi: 10.1117/12.2555447

SPIE.

Event: SPIE Photonics Europe, 2020, Online Only, France

Rapid Optical Erasure of Surface Relief and Bulk Birefringence Gratings in Azo-Polymer Thin Films

Joachim Jelken, Marius Brinkjans, Carsten Henkel, Svetlana Santer[*]

Institute of Physics and Astronomy, University of Potsdam, 14476 Potsdam, Germany

AUTHOR EMAIL ADDRESS: santer@uni-potsdam.de

RECEIVED DATE

Keywords: Photosensitive polymers, azobenzene containing molecules, surface relief grating formation, reversible structuring of polymer films

[*] santer@uni-potsdam.de

ABSTRACT

We report on light induced reversible structuring of azobenzene containing polymer films under dynamic changes of the local distribution of the electrical field in the irradiating interference pattern. This is achieved utilizing a homemade setup which consists of three parts: a two-beam interference lithography for topography structuring, an atomic force microscope for *in-situ* recording (during irradiation) of surface morphology and a diffraction efficiency setup which enables to obtain information about the birefringence grating development simultaneously. Introducing a phase delay between the two interfering beams results in a shift of the whole interference pattern along the sample plane and subsequent change in topographical grating. In this way one can reversibly structure the surface topography in a controlled way and quite fast. On the other hand, this allows to erase the surface grating by just performing half period shift. Combining this method with a single beam exposure creates a very efficient way of completely erasing the birefringence and surface grating.

Introduction

Under irradiation of thin polymer films containing azobenzene molecules with spatially modulated light such as an interference pattern (IP), two gratings are formed: a surface relief grating (SRG), i.e. sinusoidal topography variations, and a bulk birefringence grating (BBG), where a periodic pattern of locally ordered azobenzene groups mimics the distribution of the electrical field vector in the applied light.[1,2,3] The BBG is generated during multiple photo- isomerization cycles of the azobenzene chromophore from *trans* to *cis* states and back, at which the azobenzene rotates to align perpendicular to the local electric field vector ("angular hole burning"). The light-induced orientation leads to mechanical stresses which are the driving force behind a macroscopic deformation manifested in SRG

formation.[4,5] Once inscribed, both gratings are stable and at ambient conditions are stored within the polymer film over many years. However, since the polymer film deformation is a non-destructive and reversible process, the gratings can be re-written many times. The fast recording and rewriting of the SRG in an amorphous azobenzene containing polymer films is usually a challenging task because of the slow erase process. There are two well established procedures to flatten the SRG: heating above the glass transition temperature T_g of the polymer[6] or exposure to single beam irradiation.[7] Both techniques show certain disadvantages limiting the possible fields of application. In the case of thermal erase, the sample has to be heated up to high temperatures, which is not suitable, for instance, for biological applications,[8,9,10,11] where e.g., cell adhesion is guided by a surface grating. On the other hand, the erase process by single beam exposure is slow (one hour or more). The erase kinetic can be accelerated by increasing the intensity which, however, also leads to an increase in temperature. Therefore, there is a need for a fast light-driven erase protocol in order to create a dynamic surface that can be reconfigured on the minute scale, and this is what we describe in this paper.

Recently, we presented a set-up that combines the DE probe beam with *in situ* surface analysis based on an atomic force microscope (AFM).[12] It enables to track at the same time and independently the growth kinetics of both the SRG and the BBG.[13] This is very important for the understanding of the optical erasure of the two gratings which are typically forming on two different time scales, in particular under IPs with polarization gradients. Using a single-beam illumination with circular polarization will erase the BBG and create an isotropic chromophore orientation in the bulk (except for an alignment parallel to the beam axis). The erasure of the SRG is rather slow, however, because it is limited by the material deformation rather than by the photo-orientation.

In a previous publication, we presented an optical erase technique by a precise translation of the IP by half the optical period, where the SRG is flattened by a shifted birefringence grating.[14] In this paper we introduce a fast optical erase process enabling the generation of a dynamic fluctuating surface. We report that the leftover birefringence grating can be erased by a single beam illumination afterwards. These combined methods erase both SRG and BBG 600 times faster compared to the single beam illumination, so that it will take the same time as grating inscription. The relief is flattened by taking advantage of the mechanical stress due to the BBG that is re-oriented by the shifted polarization pattern. In this contribution, we show that the leftover BBG can be eliminated by a last step of single-beam irradiation. The proposed approach is especially interesting for the polymer discussed in the paper, since the inscribed SRG cannot be flattened thermally (see Supporting Information, **Figure S2**),[15] indicating a significant difference between the two erasing techniques discussed here.

Experimental Part

Materials and Methods

The *Poly[1-[4-(3-carboxy-4-hydroxyphenylazo)benzenesulfonamido]-1,2-ethanediyl, sodium salt]* (Pazo) is purchased from Sigma-Aldrich. The polymer solution is prepared by dissolving 170mg Pazo in 1ml solvent containing a mixture of 95% methoxyethanol and 5% ethylene glycol.

Sample preparation. Polymer films of a thickness 1μm are prepared by spin casting 100μl of the polymer solution at 3000 rpm for one minute on thin glass slides. The thickness is measured using an AFM profile acquired across a scratch through the polymer film.

Methods

Home-made set-up for studying SRG formation in situ. This set-up has been described elsewhere[14] and consists of three parts (**Scheme 1**): (1) irradiation with two-beam interference, (2) atomic force microscopy (AFM) and (3) probe beam diffraction. The irradiating beams are split from an initial laser (λ=491nm, 200mW/cm^2) by a 50:50 beam splitter into two parts of same intensity. The two beams pass through a set of wave plates and polarizers allowing independent control of intensity and polarization. By overlapping two Gaussian spots on the polymer sample, we generate well-defined intensity or polarization interference patterns (IIP or PIP). The beam diameters are set to 4mm using a beam expander and spatial filter. For instance, adding quarter-wave plates Q_1, Q_2 in the two beam paths, one with an angle of $+45°$ and another with an angle of $-45°$ with respect to the vertical axis, results in a right-left-circular interference pattern (RL-IP). This is a PIP with a constant intensity across one grating period.

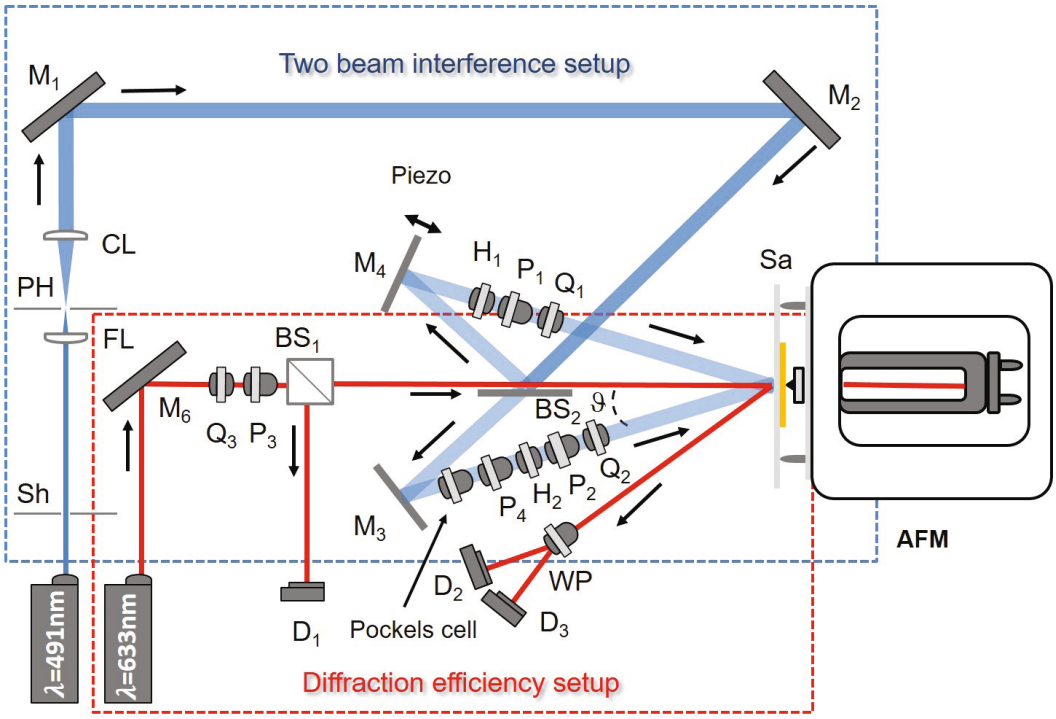

Scheme 1. Scheme of the experimental setup consisting of three parts: (1) a blue laser split in two beams with polarization control for irradiating the sample with an interference pattern, (2) an atomic force microscope (AFM) for recording *in situ* (during irradiation) the surface morphology and (3) a red laser used as a diffraction probe with polarization control in preparation and detection, collecting information about both birefringence and relief gratings in real time. The two-beam setup contains a Pockels cell to switch to the single-beam erase configuration. The interference pattern is shifted by mounting mirror M_4 on a piezo stack. (Sh=shutter, Sa=sample, M=mirror, D=detector, P=polarizer, H=half-wave plate, Q=quarter-wave plate, BS=beam splitter, CL=collimating lens, FL=focusing lens, PH=pin hole, WP=Wollaston prism).

The second part of the set-up is an *in situ* atomic force microscope (AFM) measurement of the polymer topography, using a PicoScan (Molecular Imaging) instrument working in intermittent contact mode. This can be done in real time, e.g., while the irradiation conditions are switched. The scan speed of the AFM is set to 1Hz with a scan area of 10x10µm and a resolution of 512x512 pixel (from top to bottom, each image corresponds to 512sec of elapsed time). The sample is mounted with the polymer surface

facing the AFM tip, such that the irradiation is “from below”, i.e., through the glass substrate (**Scheme 1**). The SRG amplitude is determined from the difference in height between maximum and minimum of the AFM scan. A plot of this value as a function of time represents the growth kinetics of the SRG.

We obtain real-time information about the molecular alignment in the polymer film from the diffraction efficiency (DE) of a red probe laser beam (λ=633nm, beam diameter 3mm, 30mW/cm^2). Its wavelength falls outside the absorption band of the polymer studied in this work and thus does not drive any photo-isomerization processes. The DE is defined as the ratio of the intensity in a given diffraction order and the intensity of the incoming light. Using a Wollaston prism (**Scheme 1**), detector D2 measures the S-polarized and detector D3 the P-polarized component of the first diffraction order reflected from the sample (typically a few percent only).

The irradiation set-up includes a Pockels cell (Thorlabs, EO-PC-550), which acts as an optical switch in order to block one of the two pump beams. This enables to flip the set-up fast between two-beam and single-beam irradiation. The voltage is supplied by a high voltage amplifier (Trek 610D) which also permits to drive the Pockels cell as a quarter-wave or half-wave plate. In order to introduce a phase delay between the two irradiation beams and to shift the interference pattern across the sample, one mirror of the interference set-up is mounted on a piezo stack actuator (PiezoSystemJena, PA8-14 SG). It is operated with a closed-loop feedback system and a travel maximum of 9.5 μm, controlled by a piezo-controller (PiezoSystemJena, 12V40SG). A half-period shift of the IP can be achieved within less than a second, much faster than the response time of the polymer material.

The three different set-ups are aligned in such a way that the AFM probe is in the center of each of the two interfering beams. This can be done with the help of the red reading laser of the AFM. Afterwards

the probe beam is aligned to the center of the IP and AFM probe. The AFM scanning tip is small enough so that it does not introduce any noticeable perturbation of the IP.

Silicon detectors (Thorlabs DET 100A/M) are used in the DE set-up to measure the intensity of the diffracted probe beam in two polarization channels. A 600nm longpass filter is placed in front of each photodiode in order to sense only the probe beam. The intensity of the diffracted light is recorded every 200ms, allowing to resolve fully the time scales for photo-alignment and SRG growth. (A much faster detection rate is just a matter of signal-to-noise ratio.)

We also carry out *ex-situ* AFM measurements (of film thickness and SRG height before and after thermal treatment) using an NTEGRA (NT-MDT) AFM operating in intermittent contact mode.

Results and Discussion

Figures 1a, b shows the *in situ* recorded surface relief amplitude (SRG, black dots) and diffraction efficiency (DE, red lines) during the irradiation with the RL-IP. This is a polarization interference pattern (PIP), where the intensity along the sample is constant, while the orientation of the local electric field rotates once over an optical period Λ (see **Figure 1c**). The AFM scans show a monotonous growth in SRG amplitude, reaching ≈ 300 nm after 60 min of irradiation. The 1st-order DEs of P- and S-polarized probe beams show a strikingly different behavior, although they probe regions that are just shifted by a half-period within the PIP. (Note that in **Fig.1**, the DE is not resolved in polarization.)

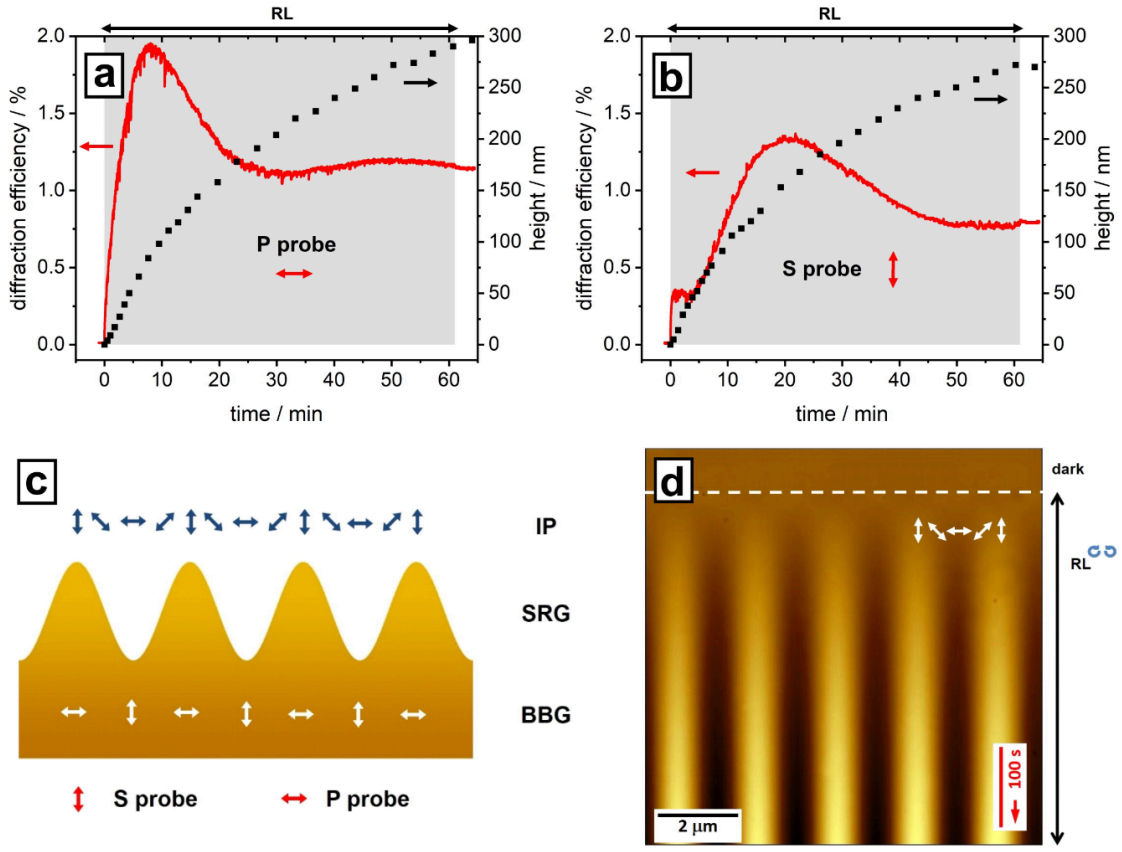

Figure 1. *In situ* recorded surface relief (SRG) amplitude (black dots) and 1st order diffraction efficiency (DE) for P- (a) and S- (b) polarized probe beams. The grey zone marks the irradiation time, using a polarization interference pattern formed by two beams with right- and left-handed circular polarization (RL-IP). While the DE in the P-polarization increases rapidly and then levels off, the S-polarized probe beam shows a plateau in the first few minutes of SRG inscription. (c) Scheme explaining the surface relief grating (SRG) and bulk birefringence grating (BBG). The distribution of the electrical field vector (blue arrows, seen from above) is shown relative to the topography variation (orange color, seen from the side). The orientation of the chromophores within the polymer film is shown with white arrows (seen from above). In the photo-stationary state, the chromophores are oriented perpendicular to the electrical field vector, forming the BBG. For a P- or S-polarized probe beam, the two gratings interfere constructively or destructively. (d) *In situ* recorded AFM micrograph during scanning in dark (top of the image) and under irradiation with RL-IP (starts at the dashed line). The scan direction is from top to bottom. (Writing wavelength 491nm, probe wavelength 633nm, total writing intensity $I = 200\text{mW/cm}^2$, grating period $\Lambda = 2\mu\text{m}$, film thickness $d = 1\mu\text{m}$.)

The P-polarization shows rapid growth in DE, followed by a decline when the SRG height exceeds ≈ 100 nm (**Figure 1a**). This conforms with earlier work where the modulated phase fronts of the reflected beam were modelled with Raman-Nath theory.[12,13] One finds a DE described by the square of a first-order Bessel function that goes through a maximum at a certain value of the phase modulation depth. In the case of an S-polarized probe beam (**Figure 1b**), the DE shows an additional peak or plateau in the first few minutes of irradiation, which is not visible for the P-polarized probe beam. The following maximum appears later and with a reduced amplitude. **Figure 1d** shows the *in situ* recorded topography change. The scan starts at the top where a flat surface is visible before irradiation. The direction of scanning (time axis) is indicated by the red time bar in the lower right corner. At the white dashed line, the irradiation with the RL-IP is started. The SRG amplitude becomes noticeable after one or two minutes and continues to grow steadily (the AFM scan shows approx. 8 min of irradiation only).

The origin of the first feature in the S-polarized DE is the offset between SRG and bulk birefringence grating (BBG) of half the grating period (see Scheme in **Figure 1c**). The optical path length (the refractive index) for the probe beam is larger at the SRG peaks, on the one hand, and where its polarization is parallel to the orientation of the azobenzene chromophores within the polymer film (positive birefringence), on the other. In the S-polarization, the maximum path length from the BBG coincides with the SRG minimum so that the two contributions to the phase modulation partly cancel. In other words, the two gratings, SRG and BBG, interfere destructively. The opposite situation happens for the P-polarization where the optical path modulations due to BBG and SRG occur in phase.

Now we take into account the different time scales for forming the two gratings. The faster process at the onset of irradiation is the orientation of the azo-chromophores in the bulk and hence, only the BBG contributes to the DE signal. After a few minutes, it saturates into a stationary state. The SRG amplitude is developing more slowly, but it continuously outgrows the phase modulation of the BBG. The total DE for the S-polarized probe goes through a minimum when the SRG and BBG interfere destructively. It does not go to zero because of a cross-polarized contribution (shown separately in **Figure 2**) and because of spatial inhomogeneities in the grating on the scale of the beam radius.[12] Eventually, the SRG takes over, and the diffraction efficiency rises again to a pronounced maximum, followed by another drop at deep phase modulations.

In order to erase the inscribed grating and flatten the film, one has to reduce the local mechanical stresses generated during photo-alignment by, for instance, creating an isotropic orientation of the azo-chromophores in the bulk. This can be achieved by heating up the sample above the glass transition or by irradiating it with a circularly polarized beam. The disadvantages of these relatively slow techniques have been mentioned in the introduction. As an alternative approach, we can also perform a half-period shift of the interference pattern[14] and take advantage of the mechanical stress in a photo-oriented material.

Figure 2a shows the *in situ* recorded topography during such a shift of the interference pattern. The scan starts with a flat surface, and at the dashed line marked I, the irradiation with the RL-IP is switched on. The SRG amplitude grows roughly linearly, up to the moment marked by the line II where the IP is shifted by half the optical period (using the piezo actuator at mirror M_4, see **Scheme 1**). This is equivalent to a sudden rotation of the local electric field by 90° (as indicated in **Figure 2a**). The surface

modulation jumps up immediately, but after a few tens of seconds, it decreases steadily with irradiation time. We stop the irradiation when the surface structure is completely flattened (dashed line III).

In **Figure 2c** the results of an *in situ* performed AFM and DE measurement are shown for a P-polarized probe beam, providing both the co- and the cross-polarized components of the 1st diffraction order. At the onset of irradiation, the SRG amplitude (black line) and both components of the DE signal increase. The cross-polarized component (blue curve) saturates fast, while the co-polarized component (red curve) continuously increases. The IP is shifted by half a period when the SRG height is about 40nm. Immediately after the shift, the DE drops almost down to zero and recovers fast, while the SRG amplitude decreases slowly. The cross-polarized component shows nearly the same behavior as during the first irradiation period. When a flat surface is reached (as seen from the AFM scan) the irradiation is switched off. The DE still shows a signal, which is due to the re-written birefringence grating that is quite stable and relaxes only slightly (probably due to the decay of the *cis* isomer).

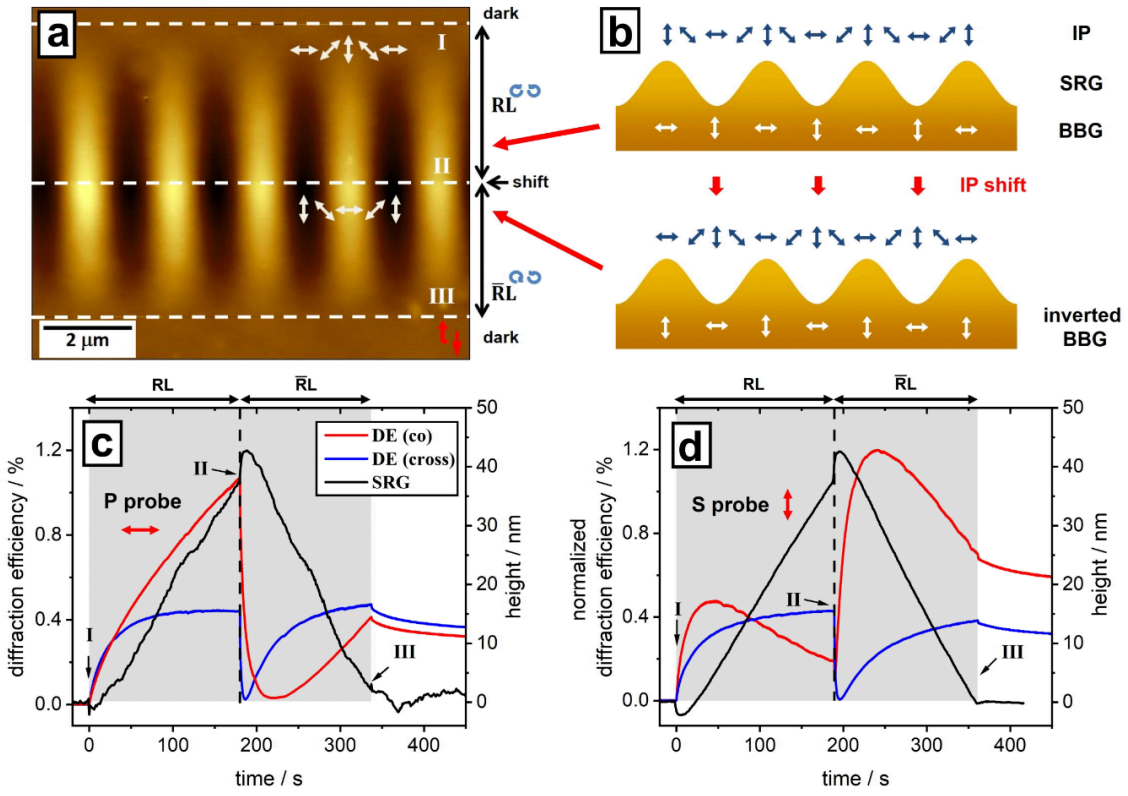

Figure 2. *In situ* recorded SRG amplitude and polarization-resolved DE recorded for a sequence of two irradiations, separated by a half-period shift of the RL-IP. Note the difference in time scale compared to **Fig.1**. (a) *In situ* recorded AFM micrograph. The scan starts with a flat surface (top). At the moment of the dashed line I, the irradiation is started. The interference pattern is shifted at dashed line II. This shift corresponds to a rotation of the local electric field vector by 90° and initiates the erasure of the SRG amplitude. The irradiation is switched off at dashed line III. (b) Scheme of the IP before and after the phase shift. In the case of a P-polarized probe beam (↔), the SRG grows in phase with the bulk birefringence grating (BBG). After the IP shift, the chromophores reorient in the bulk and a π phase shift appears between the two gratings. In the DE, two gratings now interfere destructively. In the case of the S-polarized probe beam (↕), one starts with destructive interference (declining plateau) which is converted into constructive interference by the IP shift. (c) *In situ* recorded SRG amplitude (black dots) and DE for a P-polarized probe beam (co-polarized component in red, cross- polarized in blue). The grey zone marks the irradiation sequence, the vertical dashed line the shift of the IP. (d) Same experiment as in (c), but with an S-polarized probe beam (red curve: co-(S)-, blue curve: cross-(P)-polarized components of the diffracted beam). The cross-polarized DE signal is only sensitive to the build-up of the BBG and behaves very similar in both cases, initially and after the IP shift. The DEs are normalized by a global calibration factor so that the cross-polarized DE reaches the same level at the moment of shifting the IP for both P- and S-polarized probe beams. Same parameters as **Figure 1**.

To explain this behavior, we recall that only the material anisotropy (BBG) can lead to a cross-polarized diffracted intensity. We consider again the orientation of the chromophores with respect to the SRG (**Figure 2b**). In the case of the P-polarized probe, there is no phase shift between SRG and BBG, resulting in constructive interference of the two gratings. When the IP is shifted by half a period, it is aligned with the molecular orientation. The *trans* to *cis* isomerization rate jumps up, explaining the brief increase in SRG amplitude.[16] After one or two minutes, the chromophores have changed their orientation by 90°, so that the BBG is shifted by half a period, while the large SRG amplitude is still in place. Now the two gratings interfere destructively in the DE signal (as it happened at the start of **Fig.1b** for the S-polarized probe). This is the explanation for the drastic drop in both DE signals after the shift of the IP. When the orientation-induced stresses are setting in with an opposite sign, the surface grating amplitude starts to decrease and with it the contribution to the DE. When the amplitude of the SRG crosses zero, only the birefringence grating is left. The SRG would continue to grow with the same phase shift as the BBG if the two-beam irradiation were kept on.

The same experiment has been repeated with an S-polarized probe beam (**Figure 2d**). Here, the SRG amplitude behaves in the same way, but the DE differs significantly. Now, one starts with a destructive interference between birefringence and surface gratings (as in **Figure 1b**), which results in a plateau of the co-(S)-polarized signal (blue curve, note the different scales in **Figure 1b**). When the IP is shifted and the new BBG has been established, constructive interference results and therefore the DE signal increases: there is no offset between SRG and BBG anymore. The DE starts to decrease after a certain time because the SRG drops in height. Summarizing, the initial surface relief can be erased rapidly by forming a new birefringence pattern in the bulk, shifted in position, the result being a reversal of the opto-mechanical stresses in the polymer film.

In the above described optical erase method, a birefringence grating remains in the polymer film which is not in a completely isotropic state. This can be achieved (except for a certain orientation perpendicular to the film) by irradiating with a circularly polarized pump beam (see **Figure S1** in Supporting Information). The SRG amplitude and the 1st order DE start to decrease as soon as the sample is illuminated by only one beam. The erasing of the SRG is rather slow compared with the scheme based on shifting the IP. The sample has to be irradiated for 20h for the complete erase of the surface as well as the birefringence grating.

We have found that by combining these two optical methods it is possible to erase both gratings quite fast. **Figure 3** shows the result of such a combined experiment. First the grating is inscribed (3min, 45nm SRG height), then the IP is shifted to erase the topography grating and afterwards, at the point of a flat surface, the sample is additionally irradiated with a circularly polarized beam. This removes the remaining BBG. This combined protocol results in the complete elimination of both gratings within 3min, which is approx. 600 times faster than with a single-beam and ends up in the same final state (isotropic orientation parallel to the surface, not considering a certain orientation perpendicular to the film). The erase time is now comparable with the grating recording time.

Irradiating with another IP will again generate an SRG within the polymer film, thus allowing for the generation of a dynamically reconfigurable polymer film.

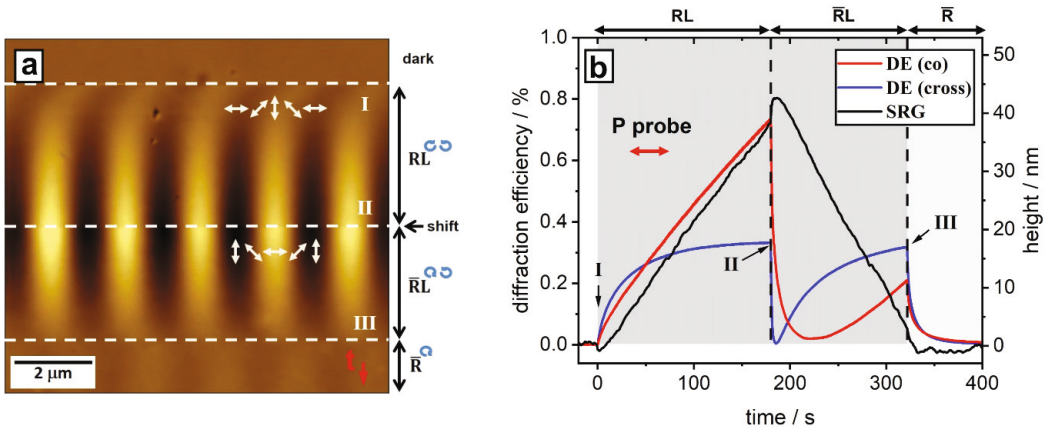

Figure 3. (a) *In situ* recorded AFM micrograph of a combined erasing protocol: shifting the interference pattern (IP), followed by single-beam exposure. The irradiation with the RL-IP is started at the dashed line I. At line II, the IP is shifted by 1µm, i.e. half its period. The single-beam irradiation (circular polarization) is applied at line III. (b) *In situ* recorded relief height (SRG, black dots) and 1st order diffraction efficiency (DE, both co-(P)- and cross-(S)-polarized components are shown). The grey rectangles mark the irradiation sequence with RL-IP and single beam. First the SRG is erased by the shift in the IP, then the remaining bulk birefringence grating is removed by ~1min of single-beam irradiation. (P-polarized probe beam, other parameters as in **Fig. 2**.)

Conclusions

We report on a protocol for a rapidly reconfigurable surface by illuminating a photosensitive polymer film with light. Within the sample, gratings (SRG and BBG) are generated by the irradiation with an interference pattern (IP) and erased by the combination of a shift of the IP and subsequent single-beam illumination. The IP shift is a quite fast and efficient way of flattening the surface grating, while the remaining birefringence grating is removed by the single-beam irradiation, resulting in an isotropic distribution of the azobenzene side chains in the film plane. Comparison with a single-beam illumination reveals a significant increase in erasing speed (600 times faster). In contrast, it is not possible to erase the gratings in these materials by thermal treatment of the sample (**Figure S2** in Supplementary Information). These findings are important for the development of a dynamically

reconfigurable surface: for example, the transport of adsorbed objects along the surface can be significant sped up because of the demonstrated reduction in cycle (response) time. Moreover, utilizing the optical method makes external stimuli for polymer reconfiguration compatible with biological applications, e.g. cell seeding.

ACKNOWLEDGMENTS: This research is supported by the Helmholtz Graduate School on Macromolecular Bioscience (Teltow, Germany). We thank Burkhard Stiller, Andreas Pucher and Pooja Arya for the fruitful discussions.

References

1 Seki, T. “Light-directed alignment, surface morphing and related processes: recent trends” J. Mater. Chem. C 4, 7895 (2016).

2 Kim, K.; Park, H.; Park, K. J.; Park, S. H.; Kim, H. H and Lee, S. “Light-Directed Soft Mass Migration for Micro/Nanophotonics” Adv.Optical Mater. 7, 1900074 (2019).

3 Yadavalli, N. S.; Saphiannikova, M. and Santer, S. “Photosensitive response of azobenzene containing films towards pure intensity or polarization interference patterns” Applied Physics Letters 105 (5), 051601 (2014).

4 Toshchevikov, V., Ilnytskyi, J. and Saphiannikova, M., “Photoisomerization Kinetics and mechanical stress in azobenzene containing materials.” J. Phys. Chem. Lett. 8, 1094–98 (2017).

5 Toshchevikov, V., Saphiannikova, M. and Heinrich, G., “Microscopic theory of light-induced deformation in amorphous side-chain azobenzene.” J. Phys. Chem. B 113, 5032–45 (2009).

6 Tofini, A., Levesque, L., Lebel, O. and Sabat, R. G., “Erasure of surface relief gratings in azobenzene molecular glasses by localized heating using a CO_2 laser.” J. Mater. Chem. C 6, 1083-1091 (2018).

7 Vapaavuori, J., Ras, R. H. A., Kaivola, M., Bazuin, C. G. and Priimagi, A., “From partial to complete optical erasure of azobenzene polymer gratings: effect of molecular weight.” J. Mater Chem. C 3, 11011-11016 (2015).

8 Barillé, R., Janik, R., Kucharski, S., Eyer, J. and Letournel, F., “Photo-responsive polymer with erasable and reconfigurable micro- and nano-patterns: An in vitro study for neuron guidance.” Colloids Surf B Biointerfaces 88, 63-71 (2011).

9 Rocha, L., Păius, C. M., Luca-Raicu, A., Resmerita, E., Rusu, A., Moleavin, I. A., Hamel, M., Branza-Nichita, N. and Hurduc, N., “Azobenzene based polymers as photoactive supports and micellar structures for applications in biology.” J. Photochem. Photobiol. A Chem. 291, 16-25 (2014).

10 Rianna, C., Rossano, L., Kollarigowda, R. H., Formiggini, F., Cavalli, S., Ventre, M. and Netti, P. A., “Spatio-temporal control of dynamic topographic patterns on azopolymers for cell culture applications.” Adv. Funct. Mater. 26, 7572-80 (2016).

11 Fedele, C., Netti, P. and Cavalli, S., “Azobenzene-based polymers: emerging applications as cell culture platforms.” Biomater. Sci. 6, 990-5 (2018).

12 Jelken, J., Henkel, C. and Santer, S., “Solving an old puzzle: fine structure of diffraction spots from an azo-polymer surface relief grating.” Appl. Phys. B 125, 218 (2019).

13 Jelken, J., Henkel, C. and Santer, S., “Polarization controlled fine structure of diffraction spots from an optically induced grating.” Appl. Phys. Lett. 116, 051601 (2020).

14 Jelken, J. and Santer S., “Light induced reversible structuring of photosensitive polymer films.” RSC Adv. 35, 20295-20305 (2019).

15 Goldenberg, L. M., Kulikovska, O. and Stumpe, J.,“Thermally stable holographic surface relief gratings and switchable optical anisotropy in films of an azobenzene-containing polyelectrolyte.” Langmuir 21, 4794-4796 (2005).

16 Barrett, C. J., Natansohn, A. L. and Rochon, P. L., “Mechanism of optically inscribed high-efficiency diffraction gratings in azo polymer films.” J. Phys. Chem. 100, 8836–42 (1996).

Supplementary Materials

Rapid Optical Erasure of Surface Relief and Bulk Birefringence Grating in Azo-Polymer Thin Films

Joachim Jelken, Marius Brinkjans, Carsten Henkel, Svetlana Santer*

Institute of Physics and Astronomy, University of Potsdam, 14476 Potsdam, Germany

AUTHOR EMAIL ADDRESS: santer@uni-potsdam.de

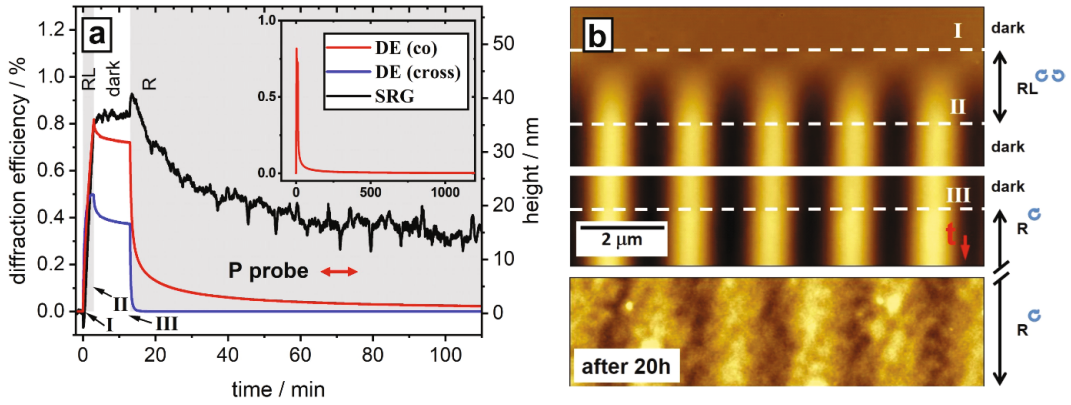

Figure S1. (a) *In situ* SRG (black line) and 1st. order DE signal recorded in two modes: co-(P)- (red curve) and cross-(S)-polarized components (blue curve). The probe beam is P-polarized. The sample is irradiated for 3min with an RL-IP, the SRG amplitude (peak to valley) is then 40nm. Changes in topography and DE signal are recorded for 10min (without irradiation), followed by switching on the erase beam (the grey rectangles mark the irradiation sequences). The moments marked I, II, III correspond to the dashed lines in the AFM scan (b). (b) *In situ* recorded AFM micrograph. At the dashed line I, the RL-IP is switched on till line II, when the SRG is recorded in the dark. The single beam irradiation is started at the moment marked by line III. After 20h of single beam exposure both the surface structure and the diffraction signal vanish. ($\lambda_{\mathrm{pump}} = 491\mathrm{nm}$, total pump intensity $I = 200\mathrm{mW/cm^2}$, SRG period $\Lambda = 2\mu\mathrm{m}$, $\lambda_{\mathrm{probe}} = 633\mathrm{nm}$, film thickness $d = 1\mu\mathrm{m}$.)

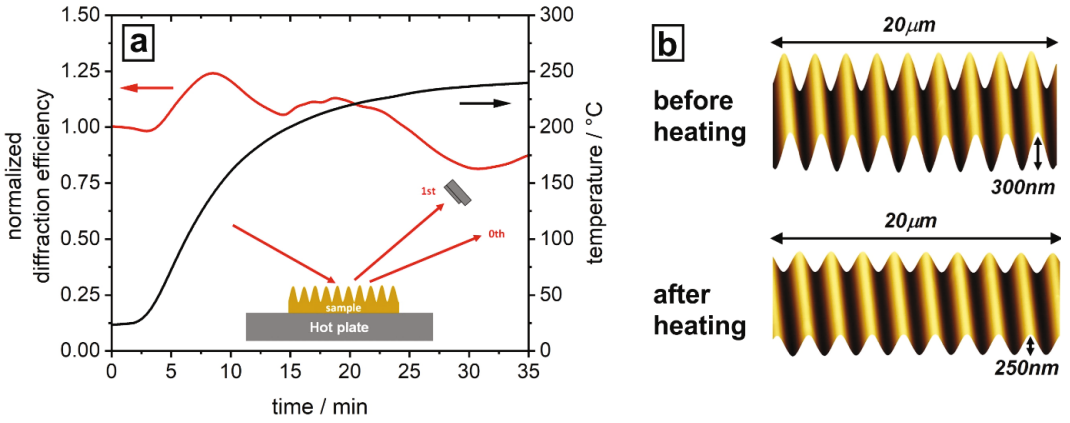

Figure S2. (a) Dependence of the 1st. order DE signal (red curve) on increase in temperature (black curve). The inset shows a scheme of the experimental setup. The sample is placed on a hot plate and the DE is recorded in reflection. Only small fluctuations in the DE signal are observed during the increase in temperature. (b) *Ex-situ* acquired AFM micrographs. The initial SRG height is 300nm, after heating over 30min at 250°C the height reduces to 250nm.

4.5. Publication V: Formation of half-period surface relief gratings in azobenzene containing polymer films

Formation of Half-Period Surface Relief Gratings in Azobenzene Containing Polymer Films

Joachim Jelken, Carsten Henkel and Svetlana Santer*

Institute of Physics and Astronomy, University of Potsdam, 14476 Potsdam, Germany

AUTHOR EMAIL ADDRESS: santer@uni-potsdam.de

RECEIVED DATE

KEYWORDS: Photo-sensitive polymers, azobenzene containing molecules, surface relief grating formation, sub-diffraction gratings, photo-structuring of polymer films

ABSTRACT

We study the peculiar response of photo-sensitive polymer films irradiated with a certain type of interference pattern where one interfering beam is S-polarized while the second one is P-polarized. The polymer film, although in a glassy state, deforms following the local polarization distribution of the incident light, and a surface relief grating (SRG) appears whose period is half the optical one. All other types of interference patterns result in the matching of both periods. The topographical response is triggered by the alignment of photo-responsive azobenzene containing polymer side chains orthogonal to the local electrical field, resulting in a bulk birefringence grating (BBG). We investigate the process of dual grating formation (SRG

* Corresponding author: santer@uni-potsdam.de

and BBG) in a polymer film utilizing a dedicated set-up that combines probe beam diffraction and atomic force microscopy (AFM) measurements and permits acquiring *in situ* and in real time information about changes in local topography and birefringence. We find that the SRG maxima appear at the positions of linearly polarized light (tilted by 45° relative to the grating vector), causing the formation of the half-period topography. This permits to inscribe symmetric and asymmetric topography gratings with sub-wavelength period, while changing only slightly the polarization of one of the interfering beams. We demonstrate an easy generation of sawtooth profiles (blazed gratings) with adjustable shape. With these results we have taken a significant step in understanding the photo-induced deformation of azo-polymer films.

Introduction

Polymer films with embedded azobenzene chromophores have attracted broad interest due to their ability to convert optical energy into mechanical deformations of large magnitude (up to few hundred nanometers).[1,2,3] One of the peculiar examples here is the formation of a surface relief grating (SRG) in thin polymer films irradiated with a holographic interference pattern (IP) of visible light.[4,5,6,7] Although the polymer film is in a solid, glassy state, it deforms following the intensity and/or polarization pattern of the incident light.[8] The mechanism of the SRG inscription involves internal, opto-mechanical stresses, which are quite high (100 MPa up to ~1 GPa) to deform a material of Young modulus up to several GPa.[3,9,10,11,12] The appearance of internal stresses is initiated by photo-induced isomerization cycles between the *trans* and *cis* states of the azobenzene chromophore. This drives a local re-orientation of azobenzene side chains perpendicular to the optical polarization (formation of a bulk birefringence grating, BBG),[13] which in turn results in the re-orientation of the polymer backbones. The subsequent generation of local gradients in the internal stresses within the material causes a viscoplastic

deformation of the film that manifests itself in the SRG (topographical grating).[14,15,16,17,18,19] Following this mechanism, one can state that the response of the polymer film to irradiation with an IP depends strongly on the local distribution of the optical polarization within one period of the pattern.[20] The IPs are usually generated by two-beam lithography, where two coherent laser beams interfere to form a holographic pattern. Their nominal period (called "optical period" in the following) depends on the angle between the two interfering beams and the irradiation wavelength. One distinguishes between intensity interference pattern (IIP), where the polarization of the light stays constant across the irradiated spot, while the intensity varies between zero and maximal over one optical period. The examples here are so-called SS (two interfering beams with S-polarization), PP, and DD ("D" means a diagonal polarization at +45°). In the case of polarization interference patterns (PIP), the intensity of the incident light is constant over the period, but the local field polarization varies, e.g. Dd ("d" is the diagonal polarization at –45°), SP, and RL (right- and left-handed circular polarizations). It has been reported that the SP configuration (one beam is S-, the other one P-polarized) is quite peculiar because it inscribes a surface relief whose period is half the optical one (**Figure 1b**),[21,22,26,27] while all other configurations (SS, PP, DD, Dd, RL etc.) result in a 1:1 match between optical and topographical periods. In this way it is possible to structure a polymer film with topographical features smaller than the diffraction limit of the used light (usually in the visible range),[23] which is otherwise only possible by utilizing near fields (e.g., from surface plasmons).[24,25] In the SP configuration, the local distribution of the electric field vector represents linear and circular polarized components that alternate over a period, as shown in **Figure 1b**. One optical period has two linearly polarized regions at ±45° angle relative to the S-polarization, surrounded by alternating left- and right-circular polarizations.

In the few existing reports on structuring polymer films with the SP-IP, it was suggested that the half-period SRG arises from the interference between zeroth- and first-order irradiation

beams scattered on the bulk birefringence grating.[26,27] The half-period grating is then developing with time, but is not showing the same growth rate like the grating with the nominal period.

Here we present a comprehensive experimental investigation of the dual grating formation (SRG and BBG) in a polymer film under SP irradiation, utilizing a homemade set-up that combines *in situ* probe beam diffraction and atomic force microscopy (AFM) measurements (**Scheme 1**). The AFM is continuously scanning the polymer surface during irradiation and detects directly the change in the SRG height. The integrated diffraction efficiency (DE) set-up probes in parallel bulk and surface gratings. By including the AFM data in a model of the recorded DE, one obtains information about the birefringence grating. The writing part of the set-up performs the two-beam interference lithography. Here, intensity, polarization and relative phase of the interfering beams can be changed in a controlled way.

We find that the SRG maximum forms at the positions of linearly polarized light (with ±45° orientation), causing the formation of the half-period topography. A rotation by only ~±1° of the linear polarization in the interfering beams affects the amplitude of the half period grating significantly: this may explain why the half-period SRG was often missed experimentally. We observe by turning the polarization that one may easily generate a blazed grating with a "saw-tooth" profile.[28,29,30] Changing the IP from SP to PP finally results a grating whose period matches the optical one.

All in one, the structuring of the photo-sensitive polymer films with SP-IP makes it possible to initiate several unique processes not available with other types of IP, i.e. the formation of a sub-wavelength topographical grating, an easily tunable SRG period and the generation of sawtooth profiles (blazed gratings) with adjustable shape.

Experimental Part

Materials and Methods

Photosensitive polymer (Poly[1-[4-(3-carboxy-4-hydroxyphenylazo)benzenesulfonamido]-1,2-ethanediyl, sodium salt], (PAZO)) is purchased from Sigma-Aldrich. The polymer solution is prepared by dissolving 170mg PAZO in 1ml solvent containing a mixture of 95% methoxyethanol and 5% ethylene glycol.

Sample preparation. The polymer films of thickness 1μm are prepared by spin casting at 3000 rpm for one minute of 100μl polymer solution on thin glass slides. The thickness of the film is measured using an atomic force microscope (AFM) by scanning across a scratch within the polymer film.

Methods

Home-made set-up for studying SRG formation in situ. The set-up consists of three parts: (1) two beam interference irradiation, (2) atomic force microscopy (AFM) and (3) equipment for measuring the diffracting efficiency (DE) (**Scheme 1**). The two-beam irradiation with a continuous wave diode pumped solid state laser (Cobolt Calypso, $\lambda = 491$nm) permits the generation of well-defined spatial interference patterns (either intensity or polarization) by changing the polarization of two interfering beams in a controlled way. The beam diameter is set to 4mm by a beam expander and spatial filter. The intensity is set to 200mW/cm^2 and a 50:50 beam splitter is added in order to separate the initially single beam into two beams of equal intensity. These two beams then pass through a set of wave plates and polarizers allowing independent control of intensity and polarization. Adding a half-wave plate to each of the beam paths of the interference set-up (H_3, H_4 in **Scheme 1**), one with an angle of 0° and the second with $+45°$ with respect to the optical axis, results in the SP interference pattern (IP). A rotation

of the half-wave plates permits to rotate the linear polarization of the beams without introducing any additional phase shifts (provided there are no birefringent elements downstream). This is a convenient feature to check experimentally the assignment of the local polarization pattern relative to the SRG. In order to introduce a phase shift between the two interfering beams, one mirror in the two-beam-interference set-up is mounted on a piezo stack actuator (PiezoSystemJena, PA8-14 SG) with a closed-loop feedback system and a travel maximum of 9.5 μm, controlled by a piezo-controller (PiezoSystemJena, 12V40SG), is used.

The second part of the set-up is an AFM that measures the polymer topography changes *in situ*, i.e. under varying irradiation conditions. The *in situ* AFM measurements are performed using a PicoScan (Molecular Imaging) AFM working in intermittent contact mode. The scan-speed of the AFM is set to 1Hz with a scan-area of 10x10μm and a resolution of 512x512 pixel. Commercial tips (Nanoworld-Point probe) with a resonance frequency of 130 kHz and a spring constant of 15 N/m are used for measurements. The sample is oriented with the polymer surface pointing towards the AFM tip, such that irradiation takes place "from below", i.e., through the glass substrate (**Scheme 1**). The SRG amplitude is determined from the AFM surface profile by measuring the difference in height between topography maximum and minimum. A plot of this value as a function of time gives the SRG growth kinetic. Scanning profiles are analyzed to determine the relative amplitudes of half-period and nominal period gratings.

To obtain in real time information about the alignment of the azobenzene side chains in the polymer film, a red probe laser beam (Uniphase, HeNe, 633nm, I=30mW/cm^2, beam diameter 3mm) is integrated into the set-up. Its intensity is weak and its wavelength falls outside the absorption bands of the photosensitive polymer studied in this work. The probe beam is P-polarized for all experiments reported here, which is inclined to the molecular alignment in those areas within the sample that are irradiated with linearly polarized light (in the SP-IP,

these are polarized at $\pm 45°$ relative to the P-polarization). To calibrate the DE, a beam splitter with a ratio T:R = 90:10 is used in the DE set-up, such that 90% of the light arrives on the sample (intensity I_0) and 10% on a photodiode. The signal of this photodiode is recorded during the whole measurement for controlling the stability of the probe beam during the experiment. The diffraction efficiency is defined as the ratio of the intensity of the *n*th diffraction order (I_n) and the intensity of the incoming light (I_0). The 1st order diffracted beam passes through a Wollaston prism which splits the light into S- and P-polarized components. The detector D2 measures the S- while detector D3 records the P- polarized light.

The three different set-ups: two beam interference, AFM and DE equipments are controlled and operated with a software (Profilab-Expert, Abacom) designed in the laboratory to record signals of the photodiodes, control the irradiation shutter and mirror position. In order to synchronize DE set-up and the AFM, a computer-generated signal is regulating the irradiation with the help of an AD/DA converter (Kolter Electronic, PCI-AD12N-DAC2). These signals are sent to the diffraction efficiency set-up as well as to the AFM using the "aux" input of the AFM controller.

Silicon-detectors (Thorlabs DET 100A/M) are used in the DE set-up to measure the intensity of the diffracted probe beam. A 600nm long-pass filter is placed in front of each photodiode in order to be sensitive to the probe beam only. The intensity of the diffracted light is recorded every 200ms, limited by the signal-to-noise ratio.

All experiments are carried out under yellow light to avoid undesirable photo-isomerization and under ambient conditions, i.e. at room temperature with a relative humidity of 55%. The whole set-up is covered with a non-transparent encapsulation in order to avoid any influence of the environment on the measurement (parasitic light, air circulation and vibration).

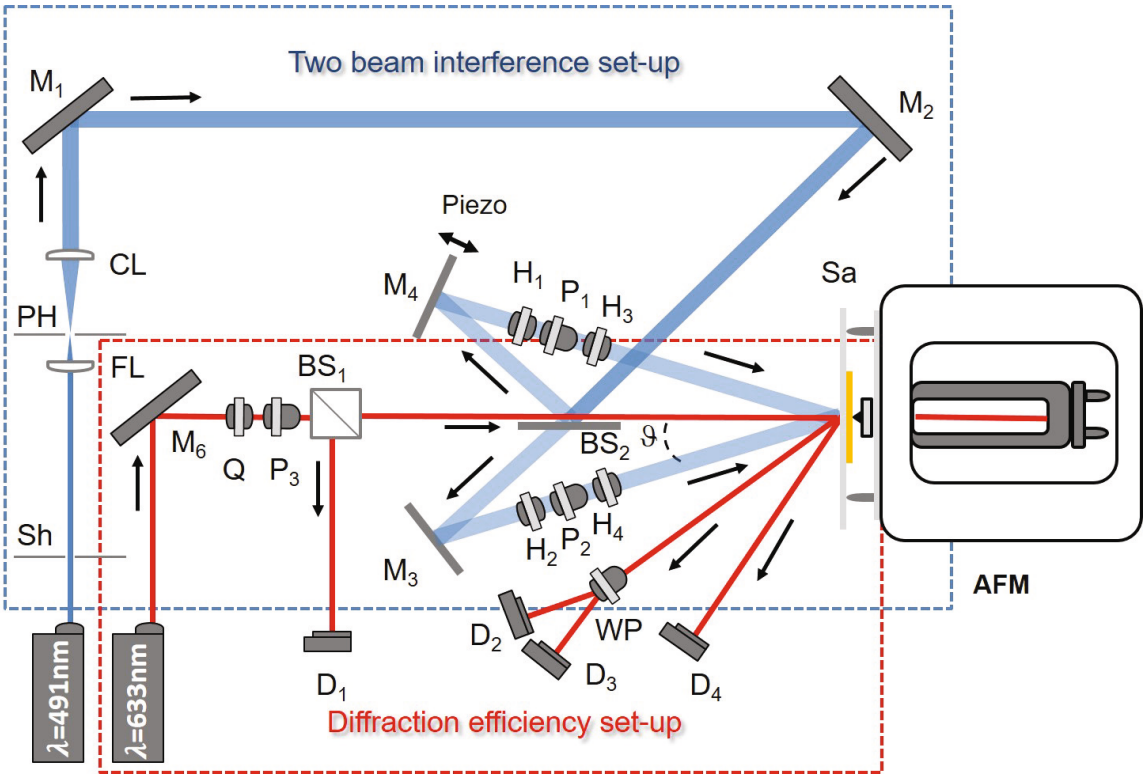

Scheme 1. Sketch of the experimental set-up consisting of three parts: (i) a two-beam interference part for generating the IP (blue laser line), (ii) AFM for *in situ* recording the surface morphology and (iii) DE set-up (red laser line) enabling information collection about surface and birefringence gratings in real time. The mirror M_4 is combined with a piezo actuator to shift its position, introduce a phase shift between the two interfering beams and thereby shifting laterally the whole interference pattern along the polymer film in a controlled way. The Wollaston prism (WP) is analyzing the light in the 1st diffraction order of S- (D_2) and P- (D_3) polarized components. Photodiode D_4 collects the 2nd order diffraction. (Sh: shutter, Sa: sample, M: mirror, D: detector, P: polarizer, H: half-wave-plate, BS: beam splitter, Q: quarter-wave-plate, CL: collimating lens, FL: focusing lens, PH: pin hole).

Results and Discussion

Figure 1a shows the *in situ* recorded SRG amplitude and diffraction efficiency during irradiation with the SP-IP. The 1st order diffraction signal (red curve) increases rapidly and saturates to a fraction of a percent within the first 5 minutes of irradiation. The 2nd order (blue curve) and the SRG amplitude (black dots) continuously increase and saturate only after hours of irradiation.[31] It seems that the 1st order DE is very little correlated with the SRG amplitude.

After switching off the irradiation, the 1st order DE partially relaxes, in contrast to the 2nd order DE and the SRG amplitude.

The polarization analysis of the P-polarized probe beam reveals that the 1st order DE signal is purely cross-(S-)polarized, while the 2nd order is purely co-(P)-polarized (**Figure 1c**). This means that the polarization of the probe beam is rotated, in the first order, by 90° (like in a wave plate) and indicates the existence of a birefringence grating in the bulk of the film (BBG for short). Indeed, the topographic relief cannot diffract into the crossed polarization because S and P are the principal polarizations in this geometry (they have distinct signatures with respect to the reflection symmetry in the plane of incidence). In **Figure S1** of the **Supporting Information**, the *in situ* recorded DE and SRG signals are shown for different polarizations of the probe beam, confirming the existence of the BBG. **Figure 1b** depicts the *in situ* recorded evolution of the polymer topography: the vertical scanning direction corresponds to the irradiation time (from top to bottom). The local distribution of the electrical field vector relative to the topography variation is assigned as described elsewhere:[23] the topography maxima develop at the positions of linearly polarized light ($\pm 45°$).

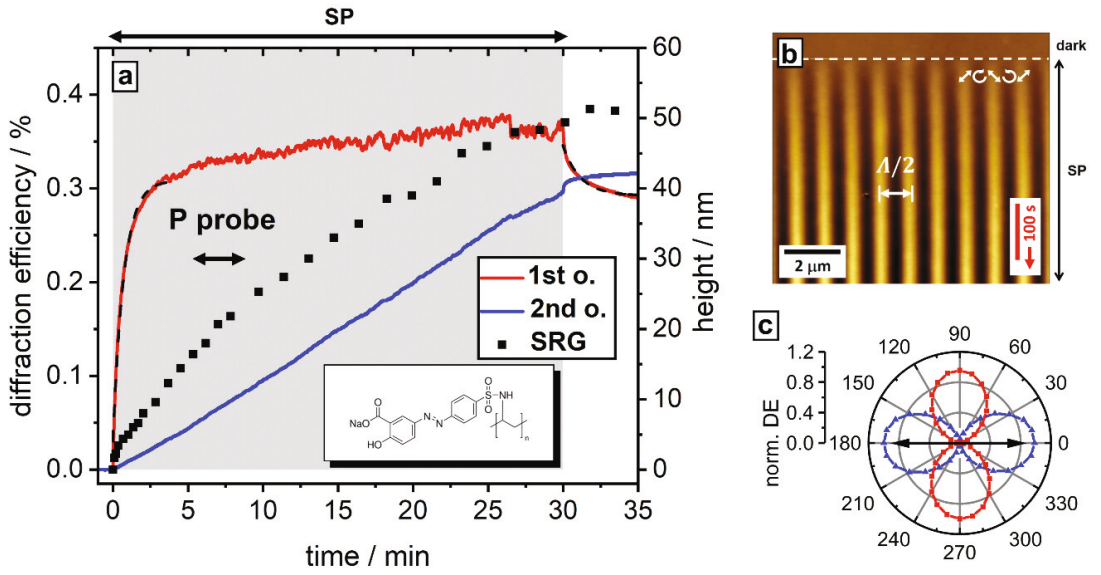

Figure 1. (a) *In situ* recorded SRG and DE signal (solid curves) of a PAZO polymer film under irradiation with SP-IP ($\lambda_{\mathrm{pump}} = 491\mathrm{nm}$, $I = 200\mathrm{mW/cm^2}$, optical grating pitch $\Lambda = 2\mu\mathrm{m}$, film thickness $d = 1\mu\mathrm{m}$). The grey rectangle marks the irradiation period with the SP-IP. The 1st order DE (red curve) increases first and saturates after a short time, while the 2nd order DE (blue curve) grows continuously. The SRG amplitude (black dots) increases also continuously. The increase and the relaxation of the 1st-order DE is fitted with an exponential function (dashed line) giving the time constant $\tau_{\mathrm{write}} = 43\mathrm{s}$ and $\tau_{\mathrm{relax}} = 70\mathrm{s}$. The inset shows the chemical structure of the PAZO polymer. (b) *In situ* recorded AFM micrograph of the polymer film topography during irradiation. Scanning is from top to bottom, showing the temporal evolution of the topography (red arrow at bottom right). The scanning starts without irradiation (flat film), and at the time marked by the dashed white line, the irradiation with the SP-IP is switched on. The local polarization of the electric field relative to the topography maxima and minima is shown by white arrows. The surface profile after irradiation displays a half-period relief ($\Lambda/2 = 1\mu\mathrm{m}$). (c) Polarization analysis of the 1st (red) and 2nd order (blue) diffraction spot. The 1st order is purely cross-(S-) polarized (90° rotated), while the 2nd order is polarized in the same direction as the probe beam (P-polarized, black arrow).

Information stored in the 1st and 2nd order DE. A straightforward evaluation of the Bragg-Laue equation for the diffraction of the probe beam ($\lambda_{\mathrm{probe}} = 633\mathrm{nm}$) with a grating of $\Lambda = 2\mu\mathrm{m}$ pitch (called "optical period") shows that the 1st and 2nd order diffraction spots appear at angles of 18° and 39°, respectively (**Scheme 2**). Since the polymer topography has half the optical period, $\Lambda/2 = 1\mu\mathrm{m}$, the diffraction by this relief grating results in a 1st diffraction order at an

angle of 39° (i.e., 2nd order for the optical grating), while the second order is already evanescent (**Scheme 2**). This means that the 1st order DE contains only the information about the birefringence grating, while the 2nd diffraction order carries information about both the SRG and the BBG. This is in contrast to, e.g. the ±45°-IP, where the topography responds at the optical period (Λ), although the pattern of the field polarization is just the same apart from a rotation by 45° (the linearly polarized regions are S- or P-polarized, see **Figure S2** of **Supporting Information**).

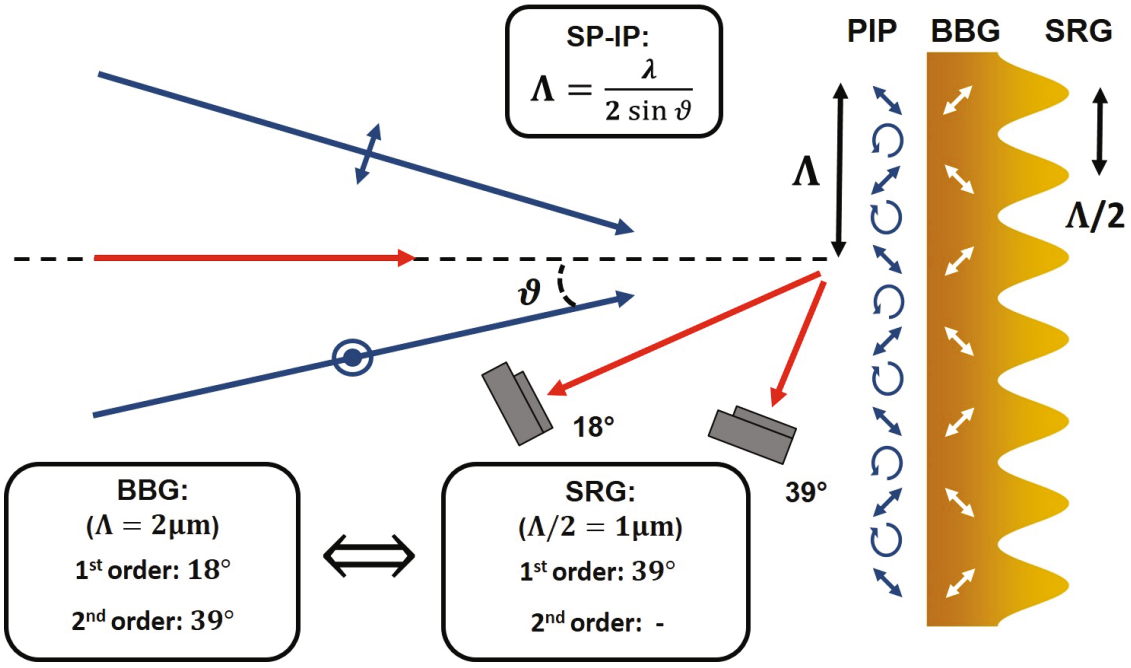

Scheme 2. Scheme highlighting different gratings: PIP, SRG and BBG together with paths of writing (blue) and recording beams (red). The SP-IP is a polarization pattern whose optical period Λ is set by the angle ϑ between the two interfering beams. The local polarization of the SP-IP relative to the topography variation is depicted as blue arrows (marked PIP). The molecular orientation in the polymer film (yellow) responds at the optical period (white arrows marked BBG). The film surface responds at half the optical period Λ/2 (SRG). The 1st order diffraction spot for a grating of period $\Lambda = 2\mu m$ is at an angle of 18°, while the 2nd order appears at 39°. Performing the same calculation for the relief grating ($\Lambda/2 = 1\mu m$ period) results in a 1st order scattering angle of 39°, while the 2nd order is evanescent.

In order to check the dual grating structure in the polymer film, we study how the DE signal in the 1st and 2nd order varies when the local polarization is switched, keeping the optical period constant. By adjusting the position of the mirror M_4 (**Scheme 1**), one introduces a phase shift between the two interfering beams, resulting in a shift of the whole interference pattern along the sample surface. **Figure 2a** shows the *in situ* recorded AFM micrographs for several shifting events. The start of the irradiation with the SP-IP is marked by the dashed line no. 1. At line no 2, the IP is shifted by *half* the optical period, i.e., by $\Lambda/2$, giving a configuration denoted $S\overline{P}$. This corresponds to a polarization rotation by 90° in the linearly polarized regions and a transformation of the circularly polarized regions from left to right and vice versa (compare white arrows in **Figure 2a**). The AFM micrographs demonstrate that the SRG is very little affected by this shift, nor is the 2nd order DE. The 1st order DE, however, drops down to zero and recovers on a time scale of 1–2min. At line no. 3 in **Figure 2a**, the IP is shifted back to its initial position. It appears again that this shift of the IP is neither affecting the SRG nor the 2nd order DE, but transiently eliminates the 1st order DE completely. At line no. 4 (**Figure 2a**), the IP is shifted by a *quarter* of the optical period (SP' configuration) which corresponds to swapping regions of linear and circular polarizations. This shift results in a drop of all signals followed by recovering in the course of further irradiation, albeit more slowly compared to the previous shifts. The AFM scan shows that the SRG "drifts" by half a period (500nm) while its amplitude goes through a minimum. Eventually, the topography maximum has moved again to the linearly polarized regions (**Figures 2a, 2c**). At line no. 5, the irradiation is switched off, and the 1st order DE decreases, indicating a certain relaxation of the molecular orientation (alignment), while no changes in SRG amplitude and 2nd order DE are observed. These results confirm the statement that the 1st order DE appears due to diffraction from the birefringence grating.

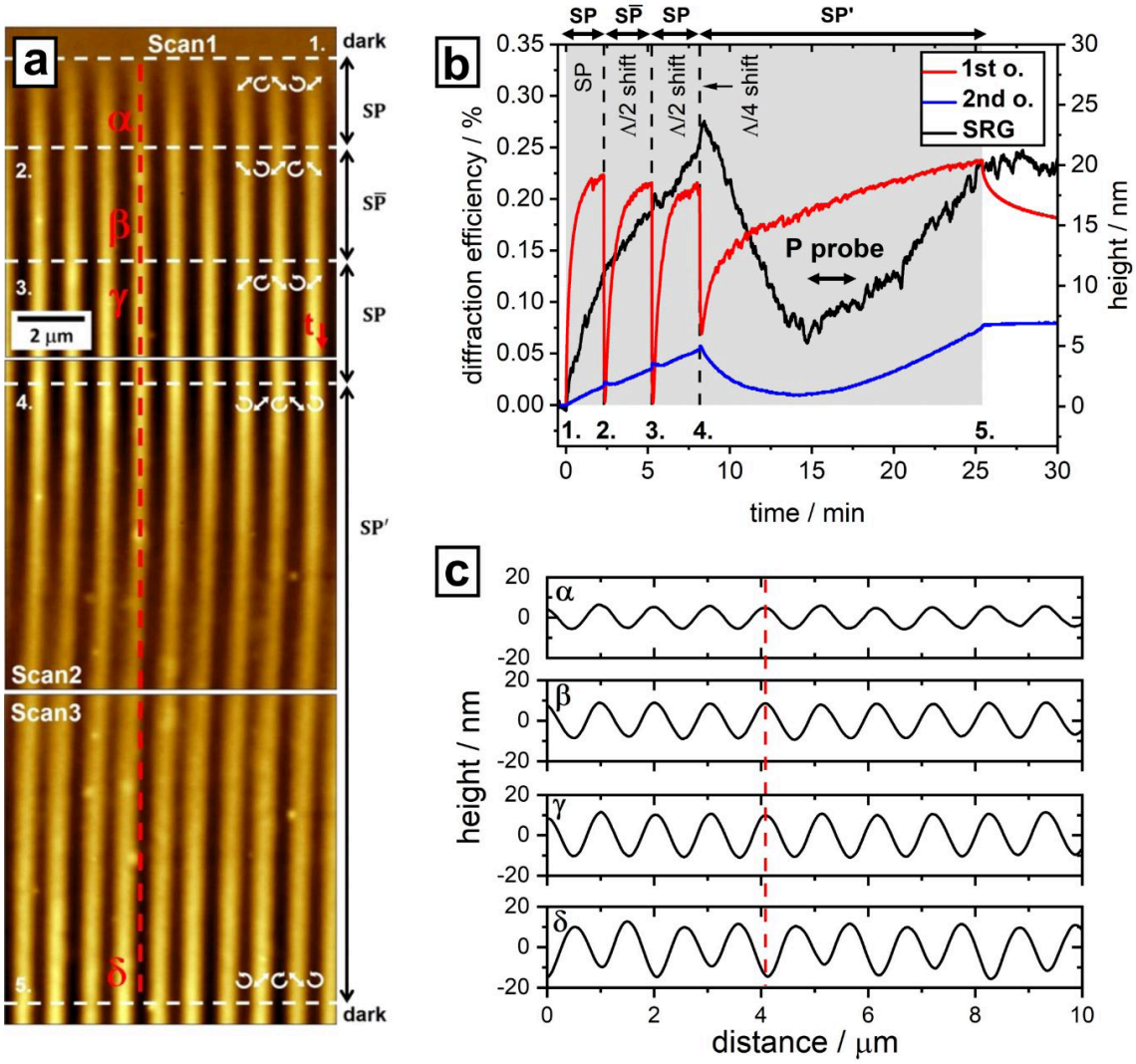

Figure 2. (a) AFM micrographs of the polymer film when shifting the SP-IP (same parameters as in **Fig. 1**). At each irradiation step, the local polarization pattern is indicated by white arrows. AFM scanning starts at the top in the dark (time direction indicated by the red arrow), at white line no. 1, the irradiation with the SP-IP is switched on. The topography responds with a half-period grating ($\Lambda/2 = 1\mu m$). At line 2, the IP is shifted by half its period (1μm), by displacing one mirror in the set-up. At line 3, the IP is shifted back by 1μm. At line 4, the IP is again shifted by 500nm ($\Lambda/4$). At line 5, the irradiation is switched off. (b) SRG height (black line) and diffraction efficiency in 1st (red) and 2nd order (blue) as a function of irradiation time (the grey rectangle marks the irradiation period with the SP-IP, the vertical dashed lines mark the switching). The 1st order shows significant changes, as the molecular orientation adapts to the new local polarization. (c) SRG profile recorded at four lines marked $\alpha - \delta$ in panel (a). The $\Lambda/2$ shift of the IP does not affect the surface grating, while the $\Lambda/4$ shift makes the SRG drift by $\Lambda/4$ (see red reference line in panel (a)).

Dependence of SRG and DE signal on optical period. In the following we investigate how the optical period of the IP alters the AFM and DE signals in amplitude and temporal evolution. **Figure 3a** shows the *in situ* recorded AFM micrograph for the irradiation of the polymer film with SP-IP of 500nm in period. This period of the interference pattern is far below the wavelength of the probe beam (633nm), which is the reason why no DE can be recorded. Nevertheless, the AFM is still sensitive to the surface grating and shows a half-period SRG (250nm) with a height amplitude of 3nm. When the period of the IP is set to 650nm, which is close to the diffraction limit of the probe beam, the 1st DE can be recorded and shows a fast increase at the beginning of irradiation followed by saturation (**Figure 3b**). The final SRG height is again 3nm and its period 325nm. With 1µm period of the IP, one gets a topography with a height of 15–20nm after 30min of irradiation. Changing the IP period to 2µm allows to record also the 2nd order DE (**Figure 3d**). Here, the SRG period is 1µm and the height is 50nm after 30min irradiation. At the IP of 3µm, one gets an efficient topographic deformation: after 30min of irradiation, the SRG height is 85nm with a period of 1.5µm. The intensity of the 2nd order diffraction spot overcomes that of the 1st order after 15min of irradiation. We conclude that the SRG development is more efficient for larger periods of the IP and that the optical probing method, i.e. the DE signal is unable to detect small periods of the SRG due to the diffraction limit. These gratings can only be probed with the AFM.

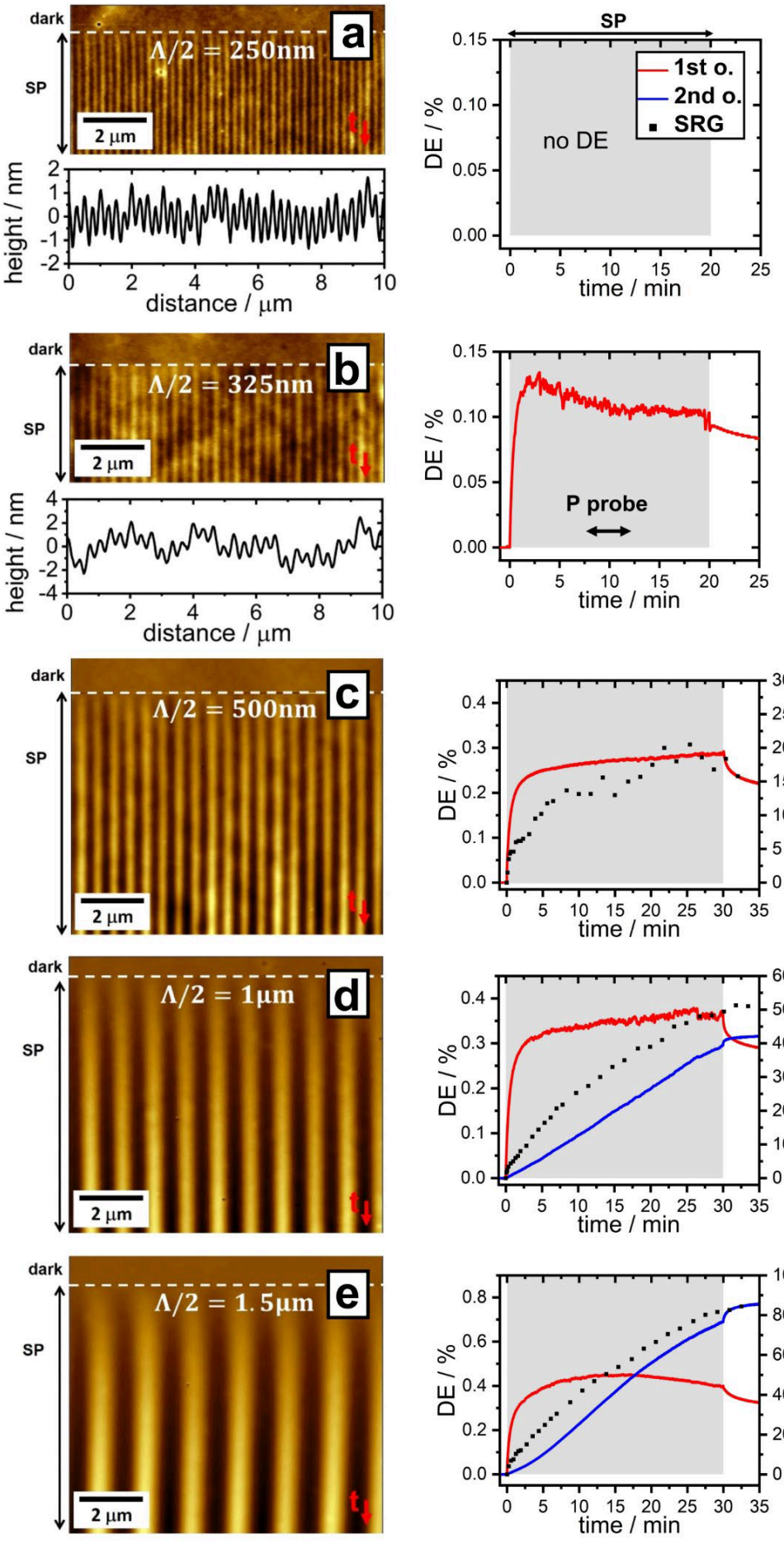
dark
SP
Λ/2 = 250nm
a
2 µm
height / nm
distance / µm
SP
1st o.
2nd o.
SRG
no DE
DE / %
time / min
Λ/2 = 325nm
b
P probe
Λ/2 = 500nm
c
height / nm
Λ/2 = 1µm
d
Λ/2 = 1.5µm
e

Figure 3. *In situ* performed AFM and DE data for different optical periods of the SP-IP: (a) $\Lambda = 500$nm, (b) 650nm, (c) 1μm, (d) 2μm, (e) 3μm. The grey color in the plots on the right marks the irradiation time. In all cases, the polymer film responds with a SRG of period $\Lambda/2$. (a) The period of the SRG is well below the diffraction limit of the probe beam ($\lambda_{\text{probe}} = 633$nm). (b) The optical period is large enough to see the 1st order of the probe beam (red curve) at the BBG. (c) For a 1μm optical period, one observes only the 1st order DE (red curve). In the AFM data, the SRG amplitude appears to saturate around 20nm. (d) One can record both the 1st order (red curve) and the 2nd order (blue curve) in diffraction. The 2nd order DE shows a growth kinetics similar to the SRG amplitude. After 30min of irradiation the SRG height has increased to 50nm. (e) At the optical period of 3μm, the SRG growth is most pronounced. The 1st diffraction order shows some decline at large times, while the 2nd order steadily increases.

Topography response at slight polarization mismatch. Under irradiation with the SP-IP, the topographic response strongly depends on the exact alignment of the interfering beams. **Figure 4** shows *in situ* recorded AFM micrographs and DE for different angles between the polarizations of the two beams ($\Lambda = 2\mu$m). In **Figure 4a** the SP-IP is well aligned so that the SRG shows a half-period grating of constant amplitude. Rotating the polarization of the S-polarized beam by only 1° results in asymmetric peaks of the SRG: its period doubles and now coincides with the optical one (**Figure 4b**). The height of the surface grating after 30min of irradiation is not affected by this change in the PIP. Like in the case of a perfect aligned SP-IP, the 1st order DE is still cross-(S-) polarized (blue curve in **Figure 4**, left column, the probe beam is P-polarized), but shows also a slowly increasing co-(P)-polarized component (red curve in **Figure 4**, left column). This is to be expected, since now also the topographic relief (which diffracts in the polarization-preserving channel) shows a periodic structure at the optical period Λ. Further rotation of the S-polarized beam by 6° causes a further decrease in the amplitude of the half-period relief, while the final SRG height of the grating with period Λ increases to 75nm (**Figure 4c**). The recorded DE now shows a strong increase of the co-(P)-polarized component which matches with the increase of the 2nd order DE, while there is no change in the cross-(S-) polarized component. For an +20°:P-IP the DE is mainly determined

by the co-(P)-polarized component (**Figure 4d**). The cross-(S-) polarized component shows the same behavior as for the other IP, but the absolute value is now decreased similar to the 2nd order DE (green curve in **Figure 4**). This can be explained by inspection of the surface profile, which now looks similar to a blazed grating (sawtooth profile in **Figure 5d**). The SRG height now is 130nm after 30min of irradiation. Further rotation in the polarization angle forms the +45°:P-IP. Here, the blazed structure vanishes and a smooth sinusoidal surface profile is recorded with period equal to the optical one (**Figure 4e**). The co-(P)-polarized component of the 1st order DE increases very fast until it starts to drop at the SRG height of 100nm, as expected from the Raman-Nath theory that predicts a first-order Bessel function.[32] The final SRG height is 190nm after 30min of irradiation. The 2nd order DE continuously increases and reaches a final value of one percent.

In the case of the P:P-IP, there is a sinusoidal surface profile whose period matches the optical one (**Figure 4f**). The 1st order DE is now purely co-(P)-polarized, indicating that also the SRG component contributes to the signal. The SRG shows a fast kinetic, i.e., within the first 150sec of irradiation, it has reached an amplitude of 100nm. At this height there is again a drop in the DE when passing through the maximum of the Bessel function. [33] After 30 min of irradiation the SRG amplitude has reached 210nm. The 2nd order DE develops to the same absolute value as in the case of the +45:P-IP, but shows a faster kinetic at the beginning.

The transition from the SP- to the PP- IP thus converts the 1st order DE from pure cross-(S-) to purely co-(P)-polarization. In the case of the SP-IP, the 1st order DE contains only the birefringence grating, as can be seen from its pure cross-polarization due to the ±45° orientation of the azo-chromophores in the bulk. For the PP-IP, the half-period structure is degraded so that the 1st order DE now also carries the SRG signal.

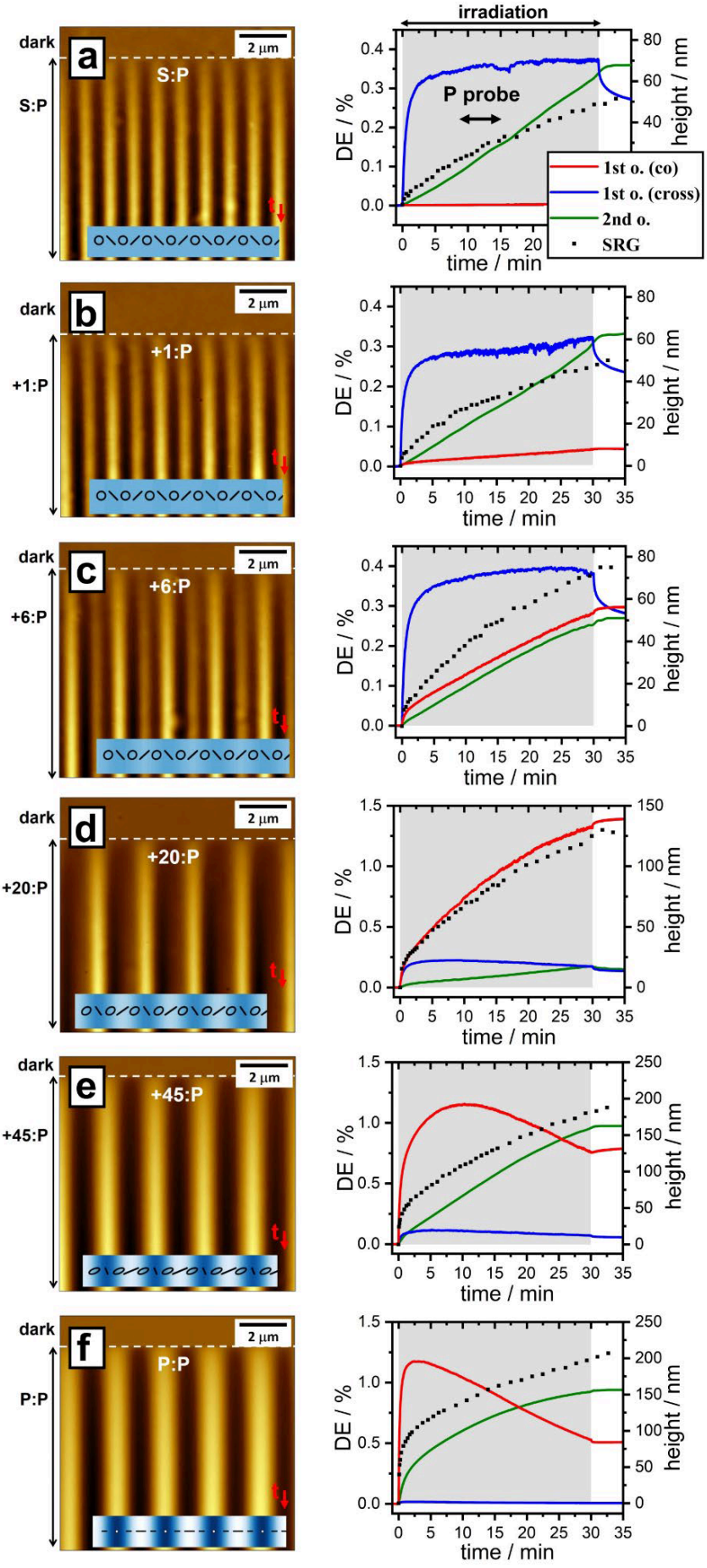
irradiation
dark
a
2 µm
S:P
S:P
P probe
DE / %
height / nm
time / min
1st o. (co)
1st o. (cross)
2nd o.
SRG
b
+1:P
+1:P
c
+6:P
+6:P
d
+20:P
+20:P
e
+45:P
+45:P
f
P:P
P:P

Figure 4. AFM micrographs (left column) and changes in topography and diffraction efficiency (right) for the transition of the interference pattern from SP to PP. The insets in AFM micrographs show a computed map of the IP intensity, with black lines and ellipses marking the local polarization. The shading in the inserts indicate the intensity modulation: dark – low, bright – high intensity. (a) SP configuration: the PIP is well aligned, the SRG is sinusoidal with $\Lambda/2$ period. On the right, the *in situ* recorded 1st (in blue the cross-(S-) and red the co-(P-) polarized component) and 2nd order DE (green) are shown. The grey rectangle marks the irradiation time. (b) Rotating the S-polarization by only 1° results in an asymmetric relief grating with period of Λ. The growth kinetics is unaffected, however. (c) The polarization is further rotated by 6° showing a stronger growth in SRG amplitude. The co-polarized 1st order DE grows to the same level as the cross-polarized one. (d) In the 20°:P-IP configuration, the half-period grating is nearly completely degraded. The co-polarized 1st order is now dominant. In **Figure 5d** the corresponding "sawtooth" cross-section is shown. (e) The 45°:P-IP generates a nearly sinusoidal surface grating with the nominal period Λ. (f) For the PP-IP, a sinusoidal surface profile of period $\Lambda = 2\mu m$ emerges. A quite fast growth of all signals appears right at the beginning of the irradiation.

Figure 5 shows the surface profile (black dots and line) for the same sequence of IPs [(a) SP, (b) +1:P, (c) +6:P, (d) +20:P, (e) +45:P, and (f) PP-IP] after 150s of illumination, together with the local intensity distribution (blue line) and the helicity (brown line). The blue ellipses and lines in the center illustrate the local polarization. The helicity is computed according to $|\mathrm{Im}(\boldsymbol{E}^* \times \boldsymbol{E})|$, it coincides with the intensity $|\boldsymbol{E}|^2$ for a purely circular polarization and vanishes for a linearly polarized field. The calculation takes into account the three-dimensional field which is tilted out of the film plane because of the finite angle of incidence ϑ in **Scheme 1**. In the case of the SP-IP, there is no intensity modulation and the SRG minimum appears at a local maximum of the helicity. The intensity modulation increases when the polarization of the S-polarized beam is rotated towards the P-polarization (**Figures 5b** and **5c**), although the local polarization is only slightly changing. The impact on the surface profile indicates the interplay between two processes: on the one hand, the photo-orientation due to the local polarization

gradients and the intensity modulation. On the other, the additional intensity modulation first reduces the amplitude of the half-period component of the SRG and finally suppresses it. For the PP-IP, the polarization is keeping a fixed direction and only intensity gradients occur, which results in a grating with period Λ.

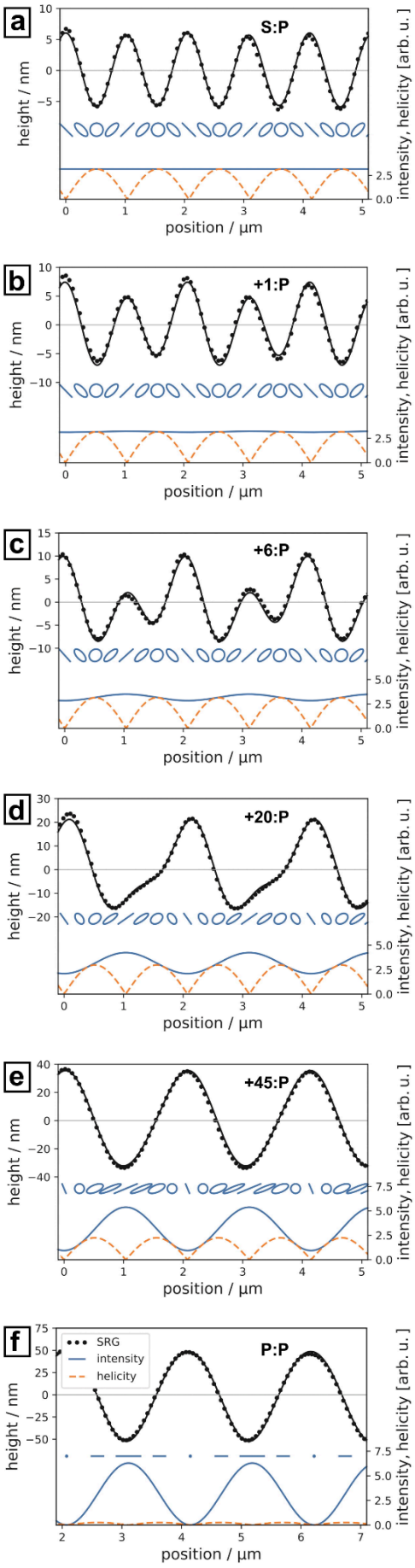
a
S:P
b
+1:P
c
+6:P
d
+20:P
e
+45:P
f
P:P
SRG
intensity
helicity
height / nm
intensity, helicity [arb. u.]
position / µm

Figure 5. SRG profile (black dots and line), the intensity (light blue line), the helicity (light brown line, see text for its definition) and the polarization (blue lines and ellipses) as a function of position for the same sequence of IPs as in **Figure 4**: (a) SP, (b) 1:P, (c) 6:P, (d) 20:P, (e) 45:P, (f) PP-IP. The surface profiles (black dots) are taken from **Figure 4** after 150s of illumination with optical period $\Lambda = 2\mu m$. The black solid lines are fits with two harmonics (periods Λ and $\Lambda/2$).

Concluding this part, we can state that when the polarizations between the two interfering beams are well adjusted, one gets a symmetric, sinusoidal SRG with period $\Lambda/2$, i.e. half the optical one. Changing the angle slightly results in an asymmetric SRG with harmonics at both Λ and $\Lambda/2$.

The change in polarization described above can also be applied during the irradiation, and its consequences studied in real time. This provides a way to ascertain the position of the optical polarization pattern relative to the surface relief. We used the results obtained here for the polarization pattern sketched in previous figures. **Figure 6a** shows the *in situ* recorded AFM micrographs for a direct switching from the SP- PIP to the PP-IIP and to a PP-IIP with a π phase shift (out-of-phase or $\overline{P}P$, similar to **Figure 2**, although with a different technique, see below). The irradiation with the SP-PIP is applied between the dashed lines 1 and 2. The topography shows a half-period grating and the SRG amplitude is continuously increasing. After a dark period of 2min follows an exposure (between lines 3 and 4) with the PP-IIP (see arrows in **Figure 6a** for the polarization pattern). This switch in IP results in the vanishing of the half-period grating. The irradiation with a PP out-of-phase pattern ($\overline{P}P$) is resumes between lines 5 and 6. Here the polarization of one of the beams is rotated by 180° resulting in a shift of the IIP by half a period, i.e. the intensity minima and maxima swap their positions (see white arrows). Responding to the IP shift, the SRG maxima are drifting over $1\mu m$ to adjust their positions to the low-intensity region.

We thus demonstrate that the local erasure of one of the topographic maxima inscribed during exposure to SP-IP can be selectively controlled by the change to the PP- or $\overline{P}$P-IP. In addition, one can now assign the topography maxima under SP-IP to the regions of linear polarization as follows: it is well-known from other experiments that in the PP-IIP, the minimum appears "in the bright" where the intensity is maximal (see dashed red line in **Figure 6a**).[34,35] This corresponds to a constructive interference of the two beams. The polarization rotation is performed in such a way (rotating half-wave plates) that no additional phase shifts appear. Hence at this position, also the S- and P-polarized beams interfere constructively, leading to a linear polarization. Indeed, at this position, an SRG maximum under the SP-PIP has developed (and is suppressed when we switch to the PP-IIP).

The kinetics of the probe beam diffraction (P-polarized) is shown in **Figure 6b** when switching the irradiation pattern. Similar to **Figure 4**, the polarization state of the 1st order changes from purely cross-(S)-polarized (PIP) to mostly co-(P)-polarized (IIP). The switch from PP to $\overline{P}$P forces the azobenzene molecules to re-orient, as manifested in a first drastic drop in the co-(P)-polarized component of the 1st order, followed by its recovery as the irradiation continues. This drop corresponds with a decrease of the SRG height and a slow drift of the relief by half a period of the IP. When the re-orientation of the azobenzene molecules is completed, the SRG height and DE signal increases again. The 1st order DE now contains contributions from both topography and birefringence gratings and thus shows continuous increase till the light is switched off (line no. 6).

The results of these changes in polarization are even more striking when we repeat the experiment with a switch from the SP- to the ±45°-IP. Both are polarization interference patterns and only differ by a local polarization rotation by 45°. The data in **Figure 7** show again the disappearance of the half-period grating. This time the SRG minimum develops at the position where the local electric field vector is P-polarized (destructive interference, i.e., taking

the difference between +45° and –45° polarized fields). At this position in the SP-PIP, a linear polarization prevails and has formed an SRG maximum. The change to a ±45° out-of-phase grating ($\pm 45_{\pi}$, by rotating the polarization of one beam by 180°) is again shifting the SRG by $\Lambda/2$ and corresponds to a rotation of the linearly polarized components by 90° and the conversion from left- to right-handed circular polarization. As in **Figure 6b**, the 1st order DE rapidly changes from pure cross-(S)-polarization to co-(P)-polarization, as soon as the PIP is switched from SP to ±45°. The change to the $\pm 45_{\pi}$-PIP (locally S- and P-polarized regions are swapped) results in a fast decrease of the DE which recovers somewhat faster (compare to **Figure 6b**). Here, the SRG does not drift to its new position, but the "old" hills are flattened "in place". If we switch from ±45° to the $\mp$45°-PIP (by rotating the polarization of both beams by 90°), no effect is seen in the SRG and birefringence grating. This switch just flips the helicity of the circularly polarized regions (between left- to right-handed, see **Figure S3**). From this observation, one may conclude that the irradiated polymer does not show any circular dichroism nor optical activity.

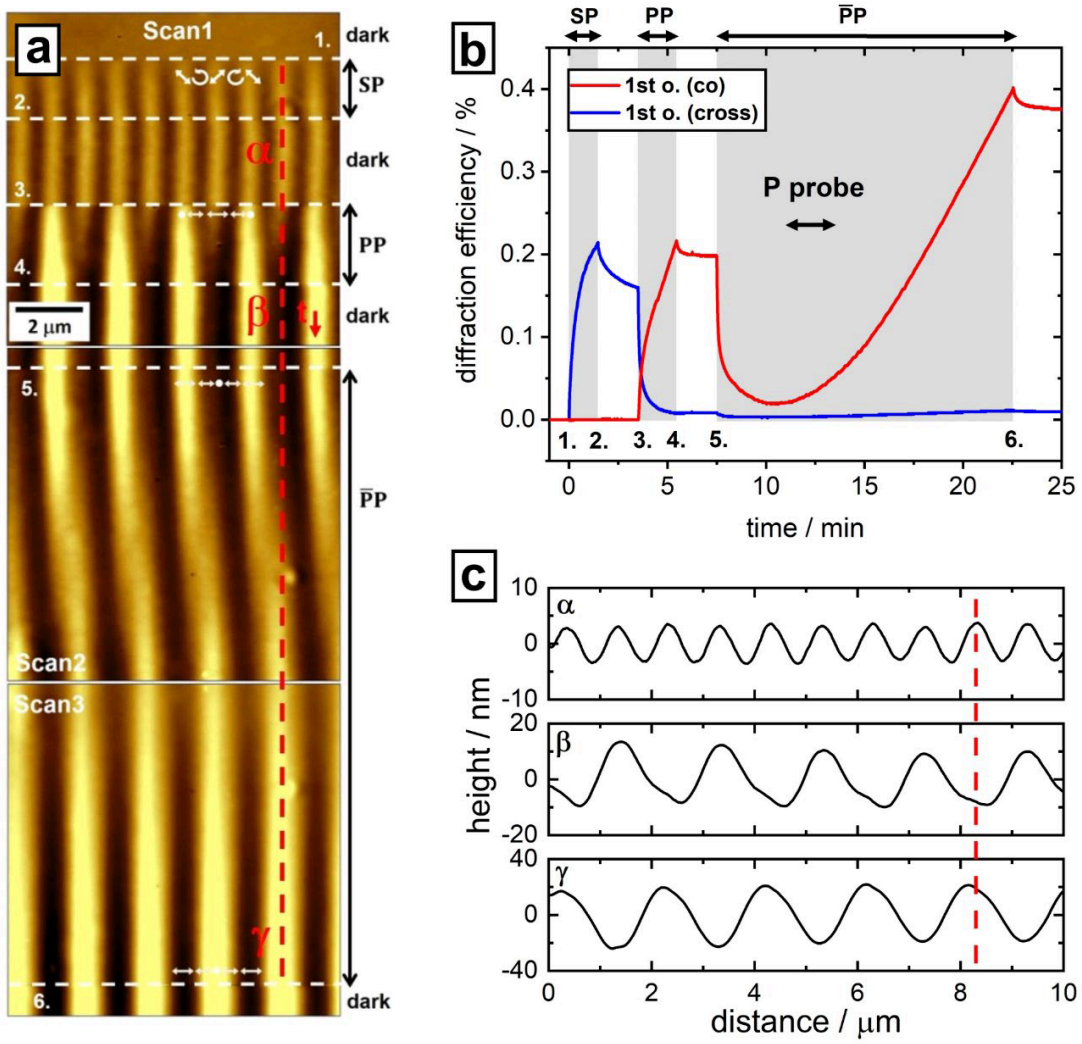

Figure 6. AFM micrograph (a) and kinetics of the DE (b) when switching from SP-PIP to PP-IIP (all other parameters as in **Figure 1**). AFM scanning is from top to bottom (red arrow). Between the dashed lines 1 and 2, the irradiation with SP-PIP is switched on (local distribution of polarization is indicated by white arrows). The topography responds with a half-period grating ($\Lambda/2 = 1\mu m$). Between the lines 3 and 4, the sample is irradiated with PP-IIP, which makes one SRG maximum out of two. Between lines 5 and 6, an PP out-of-phase ($\bar{P}P$) pattern is applied (the polarization of one beam is rotated by 180°). This results in a drift of the SRG maxima by half a period. (b) Kinetics of the 1st order DE: cross-(S)-polarized component in blue and co-(P)-polarized component in red, the grey rectangles mark the irradiation periods. (c) SRG profile recorded at lines marked by α–γ (see **Figure 6a**) after irradiation with SP- or PP-IP, respectively.

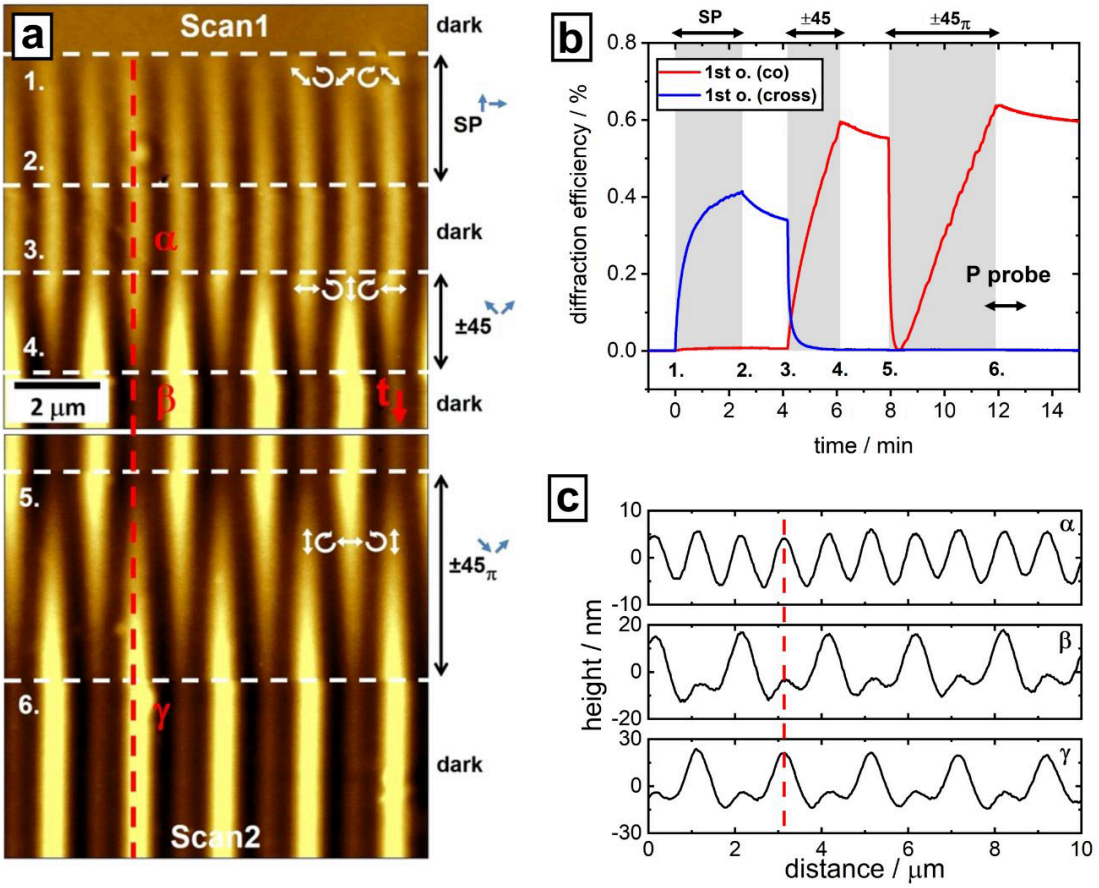

Figure 7. AFM micrograph (a) and DE kinetics (b) when switching the irradiation between two polarization interference patterns: SP-PIP to ±45°-PIP (all other parameters as in **Figure 6**, $\Lambda = 2\mu m$). (a) In the AFM scan, the SP-irradiation is applied between the dashed lines 1 and 2. The topography responds with a half-period grating ($\Lambda/2 = 1\mu m$, the local distribution of the polarization is indicated by white arrows). Between lines 3 and 4, the sample is irradiated with ±45°-PIP. The local polarization pattern relative to the surface grating is known from earlier work.[33] As a result of the change in the IP, the half-period structure is fading out and only the maximum located in the region of S-polarization remains. Between lines 5 and 6, irradiation with ±45° out-of-phase configuration ($\pm 45_\pi$) is applied. Here, the polarization of one beam is rotated by 180°. The SRG maximum is fading and a new one is formed but shifted in position. (b) Kinetics of the 1st order DE: cross-polarized component (S, blue curve) and co-polarized component (P, red curve) as a function of time, grey rectangles mark the irradiation. (c) SRG profile recorded at lines marked by α–γ (see **Figure 7a**) after irradiation with the SP- and ±45°-PIPs. The change of the polarization pattern from SP to ±45° results in the fading of the half-period grating, and the change from ±45° to $\pm 45_\pi$ re-builds the SRG at positions shifted by half its period.

Conclusions

We have studied the formation of two gratings, SRG and BBG, within photo-sensitive polymer films under exposure to light of spatially modulated intensity and polarization, i.e. interference patterns (IPs). For this we combine two-beam interference equipment with diffraction efficiency measurements and AFM. Special attention is paid to the SP-IP, where the response of topography differs from all other types of IPs, i.e. the SRG has half the optical period, while the BBG has the same period as IP. By simultaneously recording the topographical and DE signals, we understood how the topography variations correlate with the local distribution of the electrical field vector. We find that the SRG maximum appears at the positions of linearly polarized light, oriented at ±45° relative to the grating vector, which occurs twice per one period. This results in the formation of the half-period topography. Moreover, we demonstrate that a symmetric SRG can be inscribed by SP-IP, but only slight changes in the alignment of one of the interfere result in a blazed grating with a sawtooth profile and a period equal to the optical one.

Acknowledgements: This research is supported by the Helmholtz Graduate School on Macromolecular Bioscience (Teltow, Germany). We thank Burkhard Stiller, Andreas Pucher and Pooja Arya for the fruitful discussions.

References

1 Zhao, Y.; Ikeda, T. *Smart Light-Responsive Materials*; John Wiley & Sons, Inc., 2009.

2 Vapaavuori, J.; Bazuin, C. G.; Priimagi, A. Supramolecular Design Principles for Efficient Photoresponsive Polymer-Azobenzene Complexes. *J. Mater. Chem. C* **2018**, *6*, 2168-2188.

3 Di Florio, G.; Brundermann, E.; Yadavalli, N.S.; Santer, S.A.; Havenith, M. Graphene Multilayer as Nano-sized Optical Strain Gauge for Polymer Surface Relief Gratings. *Nano Lett.* **2014**, *14*, 5754-5760.

4 Rochon, P.; Batalla, E.; Natansohn, A. Optically Induced Surface Gratings on Azoaromatic Polymer Films. *Appl. Phys. Lett.* **1995**, *66*, 136.

5 Kim, D. Y.; Tripathy, S. K.; Li, L.; Kumar, J. Laser-induced Holographic Surface Relief Gratings on Nonlinear Optical Polymer Films. *Appl. Phys. Lett.* **1995**, *66*, 1166.

6 Barrett, C. J.; Rochon, P. L.; Natansohn, A. L. Model of Laser-Driven Mass Transport in Thin Films of Dye-Functionalized Polymers. *J. Chem. Phys.* **1998**, *109*, 1505.

7 Kumar, J.; Li, L.; Jiang, X. L.; Kim, D.; Lee, T. S.; Tripathy, S. Gradient force: The Mechanism for Surface Relief Grating Formation in Azobenzene Functionalized Polymers. *Appl. Phys. Lett.* **1998**, *72*, 2096.

8 Goulet-Hanssens, A.; Corkery, T. C.; Priimagi, A.; Barrett, C. J. Effect of Head Group Size on the Photoswitching Applications of Azobenzene Disperse Red 1 Analogues *J. Mater. Chem. C* **2014**, *2*, 7505-7512.

9 Saphiannikova, M.; Toshchevikov, V. Optical Deformations of Azobenzene Polymers: Orientation Approach vs. Photofluidization Concept. *J. Soc. Inf. Disp.* **2015**, *23*, 146.

10 Toshchevikov, V.; Ilnytskyi, J.; Saphiannikova, M. Photoisomerization Kinetics and Mechanical Stress in Azobenzene-Containing Materials. *J. Phys. Chem. Lett.* **2017**, *8*, 1094-1098.

11 Yadavalli, N. S.; Korolkov, D.; Moulin, J.; Krutyeva, M.; Santer, S. Probing Opto-Mechanical Stresses within Azobenzene-Containing Photosensitive Polymer Films by a Thin Metal Film Placed Above. *ACS Appl. Mater. Interfaces* **2014**, *6*, 11333-11340.

12 Yadavalli, N. S.; Linde, F.; Kopyshev, A.; Santer, S. Soft Matter Beats Hard Matter: Rupturing of Thin Metallic Films Induced by Mass Transport in Photosensitive Polymer Films. *ACS Appl. Mater. Interfaces* **2013**, *5*, 7743-7747.

13 Ilnytskyi, J.; Saphiannikova, M. Reorientation Dynamics of Chromophores in Photosensitive Polymers by Means of Coarse-Grained Modeling. *Chem. Phys. Chem.* **2015**, *16*, 3180-3189.

14 Ilnytskyi, J. M.; Neher, D.; Saphiannikova, M. Opposite Photo-Induced Deformations in Azobenzene-Containing Polymers with Different Molecular Architecture: Molecular Dynamics Study. *J. Chem. Phys.* **2011**, *135*, 044901.

15 Toshchevikov, V.; Saphiannikova, M.; Heinrich, G. Light-Induced Deformation of Azobenzene Elastomers: A Regular Cubic Network Model. *J. Phys. Chem. B* **2012**, *116*, 913-924.

16 Toshchevikov, V.; Saphiannikova, M. Theory of Light-Induced Deformation of Azobenzene Elastomers: Effect of the Liquid-Crystalline Interactions and Biaxiality. *J. Phys. Chem. B* **2014**, *118*, 12297-12309.

17 Toshchevikov, V.; Saphiannikova, M.; Heinrich, G. Microscopic Theory of Light-Induced Deformation in Amorphous Side-Chain Azobenzene Polymers. *J. Phys. Chem. B*, **2009**, *113*, 5032-5045.

18 Yager, K. G.; Barrett, C. J. Confinement of Surface Patterning in Azo-Polymer Thin Films. *J. Chem. Phys.* **2007**, *126*, 094908.

19 Geue, T. M.; Saphiannikova, M. G.; Henneberg, O.; Pietsch, U.; Rochon, P. L.; Natansohn, A. L. Formation Mechanism and Dynamics in Polymer Surface Gratings. *Phys. Rev. E* **2002**, *65*, 052801.

20 Yadavalli, N. S.; Loebner, S.; Papke, Th.; Sava, E.; Hurduc, N.; Santer, S. A Comparative Study of Photoinduced Deformation in Azobenzene containing Polymer Films. *Soft Matter* **2016**, *12*, 2593-2603.

21 Holme, N. C. R.; Nikolova, L.; Norris, T. B.; Hvilsted, S.; Pedersen, M.; Berg, R. H.; Rasmussen, P. H.; Ramanujam, P. S. Physical Processes in Azobenzene Polymers on Irradiation with Polarized Light. *Macromol. Symp.* **1999**, *137*, 83-103.

22 Mysliwiec, J.; Miniewicz, A.; Nespurek, S.; Studenovsky, M.; Sedlakova, Z. Efficient Holographic Recording in Novel Azo-Containing Polymer. *Opt. Mat.* **2007**, *29*, 1756-1762.

23 Yadavalli, N. S.; Saphiannikova, M.; Lomadze, N.; Goldenberg, L. M.; Santer, S. Structuring of Photosensitive Material Below Diffraction Limit using Far Field Irradiation. *Appl. Phys. A* **2013**, *113*, 263-272.

24 König, T.; Goldenberg, L. M.; Kulikovska, O.; Kulikovsky, L.; Stumpe, J.; Santer, S. Reversible Structuring of Photosensitive Polymer Films by Surface Plasmon Near Field Radiation. *Soft Matter* **2011**, *7*, 4174-4178.

25 König, T.; Yadavalli, N. S.; Santer, S. Surface Plasmon Nanolithography: Impact of Dynamically Varying Near-Field Boundary Conditions at the Air-Polymer Interface. *J. Mater. Chem.* **2012**, *22*, 5945-5950.

26 Sobolewska, A.; Miniewicz, A. On the Inscription of Period and Half-Period Surface Relief Gratings in Azobenzene-Functionalized Polymers. *J. Phys. Chem. B* **2008**, *112*, 154526-4535.

27 Labarthet, F. Lagugné; Buffeteau, T.; Sourisseau, C. Time Dependent Analysis of the Formation of a Half-Period Surface Relief Grating on Amorphous Azopolymer Films. *J. Appl. Phys.* **2001**, *90*, 3149.

28 Pagliusi, P.; Audia, B.; Provenzano, C.; Piñol, M.; Oriol, L.; Cipparrone, G. Tunable Surface Patterning of Azopolymer by Vectorial Holography: The Role of Photoanisotropies in the Driving Force. *ACS Appl. Mater. Interfaces* **2019**, *11*, 34471-34477.

29 Fabbri, F.; Lassailly, Y.; Monaco, S.; Lahlil, K.; Boilot, J. P.; Peretti, J. Kinetics of Photoinduced Matter Transport Driven by Intensity and Polarization in Thin Films Containing Azobenzene. *Phys. Rev. B* **2012**, *86*, 115440.

30 Fabbri, F.; Garrot, D.; Lahlil, K.; Boilot, J. P.; Lassailly, Y.; Peretti, J. Evidence of Two Distinct Mechanisms Driving Photoinduced Matter Motion in Thin Films Containing Azobenzene Derivatives. *J. Phys. Chem. B* **2011**, *115*, 1363-1367.

31 Yadavalli, N. S.; Santer, S. In-Situ Atomic Force Microscopy Study of the Mechanism of Surface Relief Grating Formation in Photosensitve Polymer Films. *J. Appl. Phys.* **2013**, *113*, 224304.

32 Jelken, J.; Henkel, C.; Santer, S. Solving an old Puzzle: Fine Structure of Diffraction Spots from an Azo-Polymer Surface Relief Grating. *Appl. Phys. B* **2019**, *125*, 218.

33 Jelken, J.; Henkel, C.; Santer, S. Polarization Controlled Fine Structure of Diffraction Spots from an Optically Induced Grating. *Appl. Phys. Lett*. **2020**, *116*, 051601.

34 Yadavalli, N. S.; König, T.; Santer, S. Selective Mass Transport of Azobenzene-Containing Photosensitive Films towards or away from the Light Intensity. *J. Soc. Inf. Display* **2015**, *23*, 154-162.

35 Yadavalli, N. S.; Saphiannikova, M.; Santer, S. Photosensitive response of Azobenzene containing Films towards pure Intensity or Polarization Interference Patterns. *Appl. Phys. Lett.* **2014**, *105*, 051601.

TOC

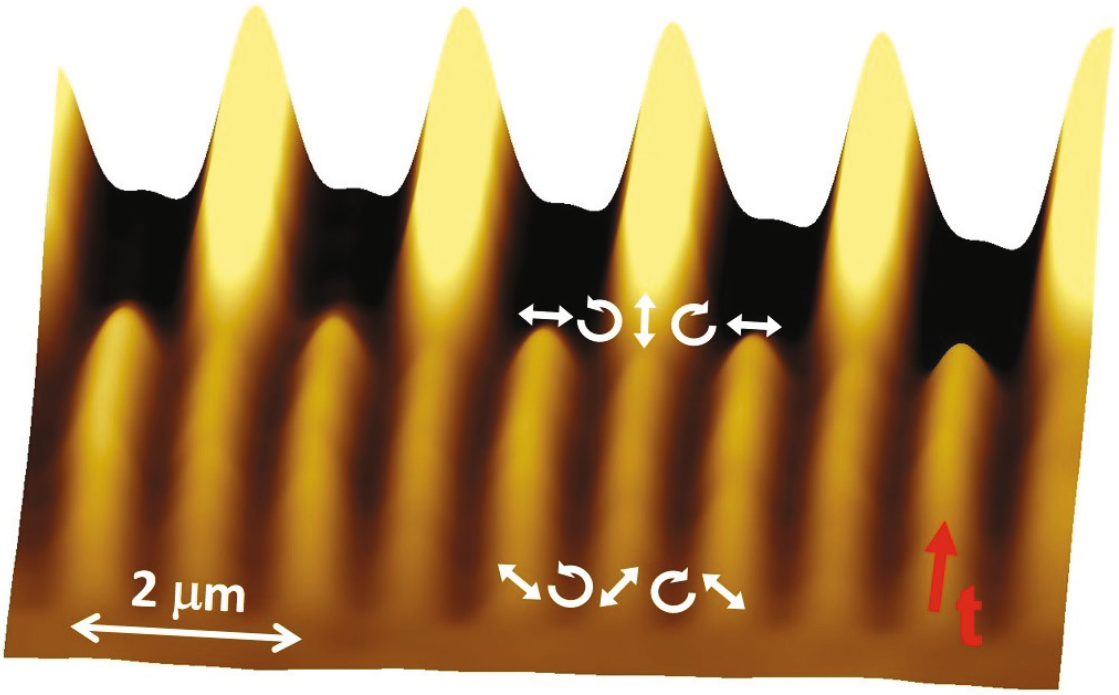

Supplementary Materials

Formation of Half-Period Surface Relief Gratings in Azobenzene Containing Polymer Films

Joachim Jelken, Carsten Henkel and Svetlana Santer*

Institute of Physics and Astronomy, University of Potsdam, 14476 Potsdam, Germany

AUTHOR EMAIL ADDRESS: santer@uni-potsdam.de

RECEIVED DATE

KEYWORDS: Photo-sensitive polymers, azobenzene containing molecules, surface relief grating formation, sub-diffraction gratings, photo-structuring of polymer films

* Corresponding author: santer@uni-potsdam.de

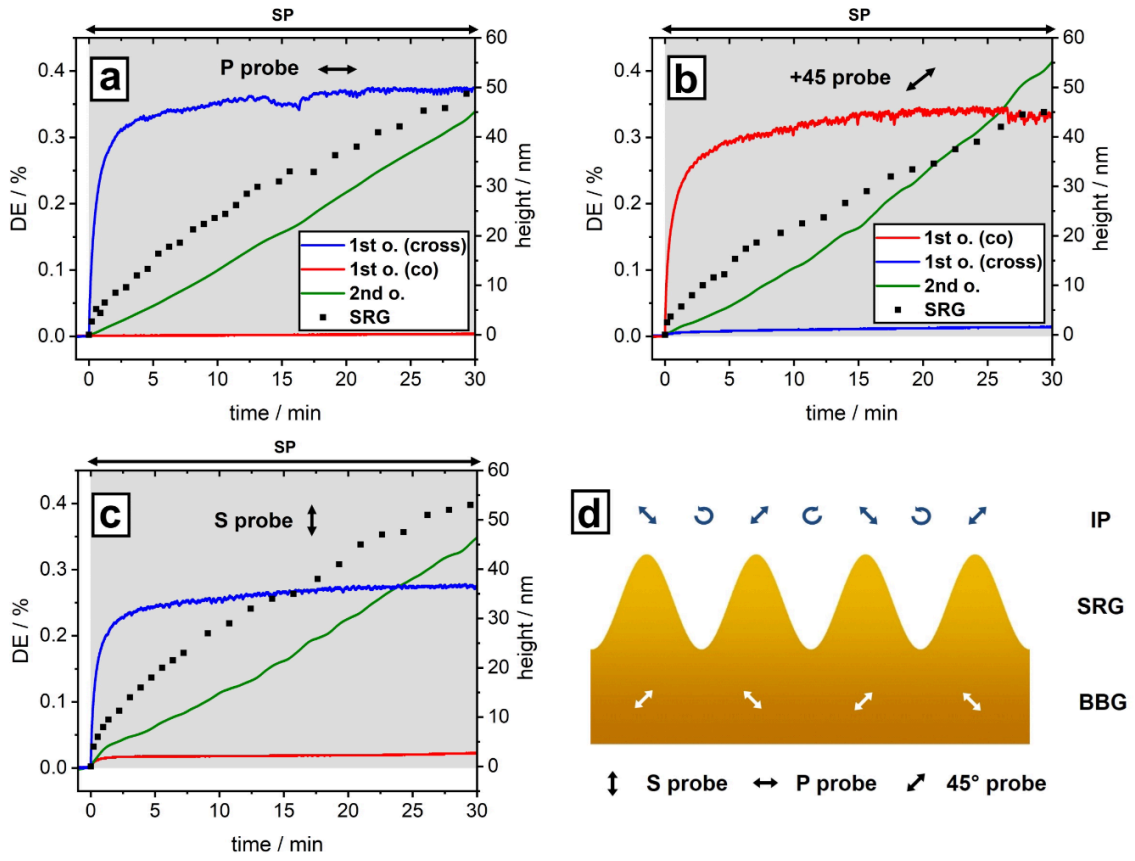

Figure S1. *In situ* recorded surface relief grating amplitude (black dots) and probe beam ($\lambda_{\mathrm{probe}} = 632\mathrm{nm}$) DE (colored lines) for a PAZO polymer film under irradiation with SP-IP ($\lambda_{\mathrm{pump}} = 491\mathrm{nm}$, $I = 200\ \mathrm{mW/cm^2}$, $\Lambda = 2\ \mu\mathrm{m}$ grating period, PAZO film thickness $d = 1\mu\mathrm{m}$). The panels (a–c) show different polarizations of the probe beam: P-, +45°-, S-polarized. The blue and red curves show the cross (co)-polarized components of the 1st order diffraction efficiency (DE), respectively, while the green curve indicates the 2nd order DE (un-polarized detection). Irradiation with the SP-IP is applied between $t = 0$ and $t = 30\mathrm{min}$. (d) Scheme of the SRG with distribution of electrical field vector (arrows on the top) for the SP-IP. White arrows within the SRG depict the photo-stationary orientation of the azobenzene chromophores in the bulk (bulk birefringence grating, BBG) during irradiation. Polarizations and orientations are projected onto the film plane.

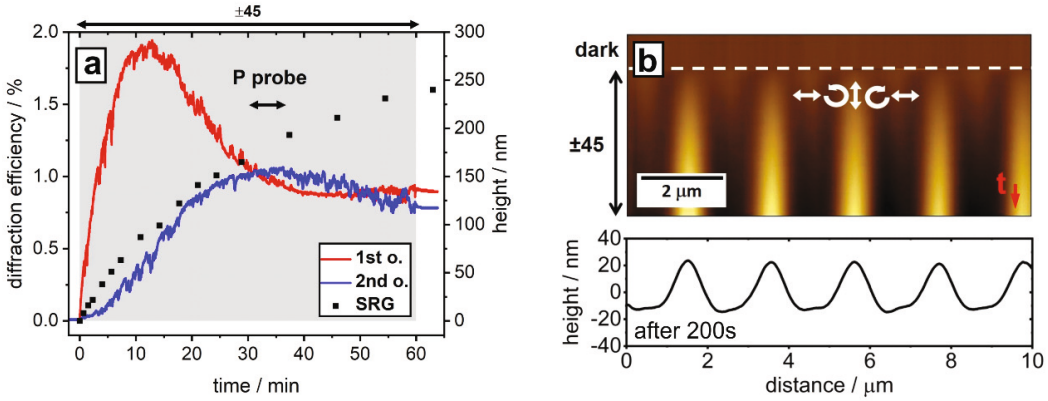

Figure S2. (a) SRG amplitude (black dots) and probe beam DE under irradiation with a ±45°-IP. The red and blue curve shows the 1st order (2nd order) DE, respectively. The grey rectangle marks the irradiation period with the ±45°-IP. (b) *In situ* recorded AFM micrograph of the SRG growth. Scanning is from top to bottom showing the temporal evolution of polymer topography (red arrow at bottom right). The AFM scan starts without irradiation (flat topography), the irradiation is switched on at the dashed white line. The local polarization state of the irradiation relative to the topographic maxima and minima is shown by white arrows. The lower panel shows a cross-section after 200s of irradiation.

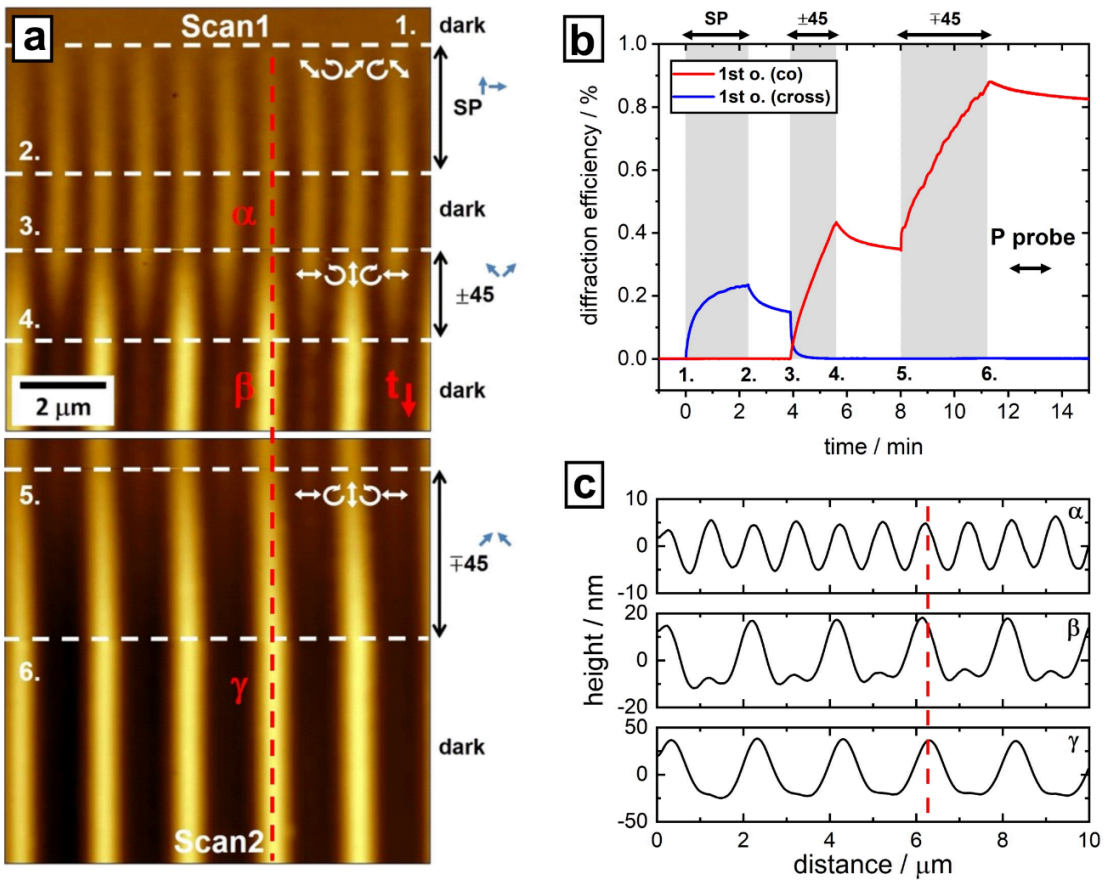

Figure S3. (a) AFM micrographs when the irradiation is switched from SP-IP to ±45°-IP (other parameters as in **Figure S1**). Between the white dashed lines 1 and 2, the SP irradiation is applied. The arrows illustrate the local polarization. The topography responds with a half-period grating ($\Lambda/2 = 1\mu m$). After a period in the dark, the sample is irradiated with a ±45°-IP between lines 3 and 4, whose local polarization is rotated by 45° relative to the SP-IP. The half-period structure is fading out and only the maximum located at vertical S-polarization remains. During the following dark period, the polarization of both beams is rotated by 90°, resulting in a ∓45°-IP. Irradiation is applied between lines 5 and 6, no change in the SRG is noticeable. At the line 6, irradiation is switched off. (b) *In situ* recorded 1st. order DE of a P-polarized probe beam (cross-(S)-polarized component in blue, co-(P)-polarized component in red) as a function of time (the grey rectangles mark the irradiation time). (c) AFM profile recorded during the scanning in dark after different irradiation schemes with SP- and ±45°-IP. Changing from SP to ±45° results in the disappearance of the half-period grating, while the switch from ±45°- to ∓45° does not affect the surface profile.

5. Discussion and Conclusions

The presented investigations address several aspects of the bulk birefringence gratings (BBGs) and surface relief gratings (SRGs) that form when one irradiates a film of polymer materials that contains azobenzene chromophores in the side-chains. A unique aspect of the experimental set-up in this thesis is the combination of an optical probe (diffraction efficiency, DE) and an atomic force microscope to measure *in situ* the evolution of the film properties. This is possible in real time while holographic irradiation is applied and can be switched in a controlled way between different configurations. New insights into the SRG formation are obtained by the simultaneous acquisition of the SRG and BBG amplitudes. In the following the questions formulated in the **Introduction** will be answered and discussed.

- Understanding optical diffraction data

One of the scientific findings of this work is the oscillation of the 1st-order DE, which can be attributed to large modulation amplitudes of the surface grating. It is explained by the special geometry of the set-up. In the present configuration the DE is detected in reflection configuration so that the optical path length is doubled in contrast to the transmission geometry usually used in the literature.[80,216–218] This results in a larger dynamic range with respect to changes in the DE. Additionally, more light is scattered forward compared to backward, which corresponds to a lower absolute value of the DE measured in reflection. The special geometry is necessary because of the integrated AFM which hinders the transmission measurement.

A fine structure in the 1st-order diffraction spot is observed and explained as resulting from the spatial inhomogeneity of the SRG and BBG amplitudes. The depth of the two gratings is following the intensity profile of the inhomogeneous (Gaussian shaped) irradiating beams. The theoretical modelling based on thin gratings (Raman-Nath approximation) reveals that the size and shape of the probe beam is an important parameter to understand quantitatively the temporal evolution of the DE. As soon as the size of the probe beam is increased, the DE differs from the one obtained with a small probe beam (as a result from an average over an inhomogeneous SRG). Using a narrow probe beam the same DE as in the case of a homogeneous SRG (constant SRG amplitude, described by a first-order Bessel function) is

obtained. Utilizing a probe beam of size comparable to the pump beam, it is possible to experimentally prove the theoretical predictions.

It turns out that the fine structure in the diffraction spot is changing from a Gaussian profile to a hollow beam and finally to a "Saturn"-like structure, with an increase in the grating modulation. The appearance of the fine structure is not universal and is only observed for large modulation amplitudes (in the few 100nm range) of the surface grating, which is usually achieved with interference patterns based on the polarizations ±45, RL and PP.

- Disentangling surface relief and bulk birefringence gratings

It is found that dependent on the polarization of the probe beam, a different diffraction efficiency is obtained. This results from combining the contributions of the BBG and SRG to the total DE. The probe beam senses a higher refractive index when the chromophores are aligned parallel to its polarization. This can result, for certain polarizations, in a spatial shift between the SRG and BBG. A constructive interference of the two gratings in the DE is observed when there is no shift between the gratings and destructive interference once there is a spatial shift of half the grating period. A rotation of the probe polarization by 90° switches between the two cases. In the latter case the total DE is first increasing due to the contribution of the BBG and starts to decrease as soon as the SRG is forming. The DE is increasing again for large modulation amplitudes of the SRG. This clearly shows the different kinetics of the two gratings: the BBG saturates to a maximum order parameter of molecular alignment, while the SRG grows monotonously, until its amplitude exceeds half the film thickness. This scenario applies for the extremely efficient polarization gradient patterns mentioned above.

The assignment of the relative position of topographic features to the local properties of the interference pattern is not trivial, especially for a polarization IP (constant intensity, local polarization is changing across the grating period). Usually the assignment for such an interference pattern is done with the help of an *in situ* performed surface analysis.[169,178] Therefore, the polymer film is illuminated through a mask and an AFM scan, executed afterwards, reveals whether the deformation is towards high or low intensity (material specific property). Knowing this assignment, the *in situ* illumination is first performed with an intensity IP and after some time changed to a polarization IP. Analyzing the deformation direction (SRG translation) during the change in the illumination, with the help of the

integrated AFM, permits to assign the local field of polarization interference patterns. The challenge of this method is that the change in the interference pattern (e.g. by rotating the half-wave-plates of the two-beam interference set-up) must not generate a phase shift between the two interfering beams. In this work, the method is further developed by comparing different types of IPs and in particular by switching between different patterns. A convenient reference situation is the PP-IP where the maximum of the SRG coincides with an intensity minimum.[169] In the new designed set-up, it is possible to switch, e.g. to an SP-IP while controlling the relative phase of the writing beams. The AFM scan reveals that the SRG maxima appear in the linearly polarized regions, where the electric field is oriented at +45° or -45°. The minima correlate with the (right or left) circularly polarized regions. The SP-IP plays a special role in this discussion. Experimentally, it shows no polarization dependency of the DE (for an S-, P- and +45° polarized probe beam). The explanation here is the unique half-period feature of the SRG which makes it impossible that BBG and SRG interfere in the 1st-order DE.

In this work an alternative way to assign the IP to the SRG and BBG, based on the analysis of the DE measured for different polarizations of the probe beam and a theoretical model (based on the Raman-Nath approximation for thin gratings) is found. The advantage of this method is that there is no need to add or change optical components during the experiment. It is found that the SRG maximum (minimum) appears at the position of a local S (P) polarization for $\pm$45-, RL- and LR-IP, respectively, which is in contrast to other publications.[183]

- Reversing the surface grating growth

A key question throughout this work concerned the origin of the strong mechanical stresses induced by holographic irradiation. The experiments, performed in this thesis, show the close relation between the BBG and the SRG. This is put into practical use and an efficient way of removing a SRG of ~50nm in amplitude within minutes is proposed. An IP with polarization gradients is shifted in such a way that the local polarization is rotated by 90°. This leads to a sign change of the molecular alignment (the local index ellipse exchanges its fast and slow axes). The consequence is a reversal of the photo-induced stresses and of the growth of the SRG.

The translation of the IP removes the SRG first (due to the generation of strong photo-induced forces) and the remaining BBG is removed by a single beam exposure afterwards. This combined method is several orders of magnitude faster (erasure within minutes) compared to (only) single beam exposure and the erase speed is even slightly faster than the grating inscription (due to the already existing anisotropy and the rotation of the local polarization by 90°).

These findings clearly support that SRG and BBG behave as two different gratings in the DE, but the photo-orientation of the azobenzene chromophores (bulk birefringence grating) occurs fast and is the driving force for the slow deformation of the polymer film which results in the SRG formation. The SRG kinetics is limited because the photo-mechanical stress has to work against viscosity, elastic force and yield stress for a bulk deformation.

It is also found for certain polymers (e.g. PAZO), having no T_g, that the SRG is optically flattened, but could not get thermally erased. Therefore, the cyclic local photo-isomerization of the azobenzene-unit of the polymer is more efficient than an increase in the temperature. It might be due to the local generation of free volume, which enables the polymer chains to re-orient.

Depending on the shifting speed and step length of the IP translation, the SRG is able to follow the change in the illumination ($\Lambda/4$-shift) or the modulation amplitude will start to decrease ($\Lambda/2$-shift). With this knowledge dynamically reconfigurable polymer topographies are generated.[150] This could give the possibility to move surface attached objects along the surface.[81,150] The optical induced generation of a fast changing dynamic surface is of high interest e.g. in biological applications where the temperature cannot be increase in order to erase the surface structure. Here, the cell seeding and growth is controlled by the change in the surface structure.[68,69,153]

- Photo-induced stresses

In order to irreversibly deform an amorphous polymer film large values of the photo-induced stress have to be generated.[100–103,163,199] These high values were experimentally measured but still there is a small gap with respect to the theoretical prediction. In order to close the gap a new experimental set-up is designed based on a polymer coated cantilever (see **Appendix Figure B.5** for more details). The irradiation of these special cantilevers results in a

deformation of the polymer film which is bending the cantilever upwards. Focusing a probe beam on the back side of the cantilever and detecting the deflection signal as a function of time permits to measure the kinetics of the photo-induced deformation. Using calibrated cantilevers delivers a photo-induced stress in the PAZO film of ca. 15MPa (see **Figure B.5**).

Nano-indentation measurements are performed to address the question of photo-softening upon illumination (see **Appendix Figure B.2** and **Figure B.3**). A change in the Young's modulus by a factor 4x under illumination is found which is not large enough to indicate a phase transition as suggested by the photo-fluidization concept. Additionally, the increase in temperature of the polymer film during irradiation is measured and found to stay below 10K (see **Appendix Figure B.1**). *In situ* performed Differential Scanning Calorimetry measurements (illumination of the polymer during the measurement) reveal that there is also no change in the glass transition temperature due to irradiation (see **Appendix**, **Figure B.4**).

- Probing the mass transport

The continuous grating translation (Λ/4-shift) is also used in order to probe the direction of the surface deformation. Therefore, a scratch was made within the polymer film and the initial coating height on the left- and right side of the scratch is measured. Afterwards the polymer film is irradiated with a continuously translated RL-IP which creates an SRG whose grooves are parallel to the scratch. The height of the polymer film is again characterized on both sides of the groove after the exposure. The measurement reveals that there is no significant change in height between both sides (side from where the material is taken and side where it is deposited), eliminating the possibility of a lateral mass transport of the polymer material over distances larger that the optical period of the IP. The same conclusion can be drawn by analyzing the motion of defects within the polymer film during the grating translation. They are stationary and appear once at the maximum and later in the minimum of the SRG. This indicates that the grating translation technique is continuously re-orienting the chromophores in the bulk which results in an up and down motion of the polymer film surface (similar to a water wave) but no significant large-scale mass transport. The data to these experiments are shown in **Appendix Figure D.1**, **Figure D.2** and **Figure C.12**.

- Complex surface gratings in mixed polarization- and intensity interference patterns

Utilizing slight changes in the polarization angle between the S- and P-polarized pump beams of the SP-IP permits the generation of topographical gratings with complex and asymmetric profiles. For instance, changing the IP from the SP to a +20:P configuration results in a SRG that contains harmonics both at the fundamental and the double period. A blazed structure is created, which is usually difficult to achieve in photo-lithography, because it requires a special local gradient in intensity. This illustrates the interplay of mechanical stresses due to gradients in intensity and polarization. It also indicates that polarization interference patterns are very sensitive to small changes in the polarization of the pump beams. Rotating the polarization of one beam in the SP configuration by only 1° leads to a fading of the half-period surface grating. The half-period SRG, created by illumination with a well aligned SP-IP, gives the possibility of generating sub-diffraction-limit structures of 250nm and smaller in size using far-field illumination ($\lambda_{\mathrm{pump}} = 491\mathrm{nm}$).

Outlook

- Applications in diffractive optics

Future work would be the direct application of the findings of this thesis. The polarization-dependent fine structure in the diffraction spot permits to shape a beam by an external stimulus. One could think of integrating such an optical device into an optical microscope, acting as an optical tweezer or for high resolution microscopy (e.g. STED, stimulated emission depletion). Changing from the “donut” to the “Saturn” structure inverts the spatial profile, which would e.g. invert the confinement in an optical trap.[219] It would also be of interest to study how this influences the motion of silica particles in a recently developed light-driven diffusioosmosis system.[220,221] The combined effect of the diffraction at the SRG and BBG is acting as a spatial light modulator (SLM). The costs of such an ultra-thin device would be much less compared to conventionally SLMs, based on liquid crystals or digital micromirror devices (DMD chips). The BBG is required in order to generate a strong phase modulation so that the hollow beam profile appears. This makes the presence of azobenzene chromophores essential. For some applications only the “donut” or “Saturn” structure is required. The necessary phase modulation can also be provided by the SRG only, but then a

larger surface grating amplitude is needed. Once this is achieved, the azobenzene containing polymer film can be used as a template for PDMS (Polydimethylsiloxane) molding to create replicas. The advantage of such a film is that it is transparent, which enables the use of a broad range of wavelengths.

In this work a simple way of producing a blazed surface grating using photo-lithography technique is presented. Future work could be the optimization of this process and the practical application. These gratings, and also their PDMS replicas, could be used in e.g. an optical spectrometer in order to optimize diffraction in a certain order.

- Optimization of a dynamically reconfigurable surface

A fast optical erase protocol of SRG and BBG, based on the translation of the interference pattern and a single beam exposure, is presented in this thesis. It is of interest if the grating formation could be accelerated in the same way. Starting from an anisotropic distribution of chromophores, induced e.g. by electrical poling or illumination, could reduce the inscription time significantly leading, together with the fast optical erasure technique to a faster response time of the surface gratings.

These results are also affecting the design of a dynamic reconfigurable surface, by performing a translation of the IP by a *quarter* of the grating period. The next step could be the practical demonstration of a large distance transport of e.g. silica particles, DNA origami or small droplets along the surface like it is already demonstrated for short distances.[81] Such a long distance transport of adsorbed objects can only be explained by a large scale mass transport and not by a mesoscopic deformation of the polymer film.

The grating inscription can also be enhanced by optimizing the IP used for the illumination. Mixed interference patterns permit to study the influence of gradients in polarization and intensity on the SRG formation. It might be that a circular or elliptical polarization at the bright areas of the IP results in a very efficient SRG formation, because it excites a large amount of chromophores which are only able to relax in the dark area of the IP. The Appendix shows results for interference patterns made of one circularly- and linearly polarized pump beam (see **Figure C.10**, **Figure C.11**, **Figure C.12**). Here, a strong difference in the SRG kinetics is observed by changing the polarization direction of the linearly polarized pump beam. This is rotating the orientation of the elliptical polarization in

the IP and permits to probe the influence of the orientation of the local polarization (along or perpendicular to the grating vector) on the SRG formation.[98,111]

The presented dissertation still leaves questions about the grating formation unanswered which could be addressed by continuing the work with the new designed set-up.

- Optimization of the experimental set-up

The presented set-up allows a direct microscopic view on the surface of the polymer film during changes in the illumination parameters and the correlation with changes in the DE. It has been reported several times[191,195,196] that by adding a third laser (the assisting beam, UV or blue laser) the grating inscription is optimized. Here, only the diffraction efficiency is analyzed and it is unclear whether there is an optimization in the BBG or SRG. This question could be clearly answered with the new developed set-up.

A further modification of the set-up could be the integration of an environmental chamber and analyzing the SRG formation as a function of e.g. humidity. The water molecules (small dipoles) are penetrating the polymer film and interact with the dipole moment of the azobenzene-chromophores, which might slow down the SRG inscription. This could be one way to explain the experimental observations that the ambient humidity (summer vs. winter season) plays a role in the efficiency of SRG formation.

The optical erasure is creating an isotropic chromophore orientation in the plane parallel to the surface and aligns a certain amount of chromophores along the beam propagation. The number of these chromophores can be quantified by probing e.g. the photo-induced birefringence under a certain angle.

- How much azobenzene is needed and where?

A long discussed and still unanswered question is how much azobenzene-chromophores are needed for the grating inscription and where they have to be located.[222] In order to address this question layer by layer structures made of alternating photo-active and non-photo-active layers could be prepared. This permits to vary the amount and the location of the azobenzene-chromophores in the system. Here, knowing the exact vertical distribution of the writing field within the polymer film would be helpful. **Figure C.9** shows an attempt to model the field within the film just by considering the reflection of the two pump beams at the flat polymer-air interface. The result is a set of bright and dark fringes parallel to the film plane,

which could lead to a non-trivial dependence of the SRG height on the film thickness. It might be that the SRG and BBG are disturbing the writing field.[223,224]

- Low dose/fluence exposure

Another interesting experiment addressing the question of the origin of the SRG formation is the short term light exposure or low intensity SRG inscription with subsequent SRG probing (see **Appendix**, **Figure C.13**, **Figure C.14** and **Figure C.15**). This provides the opportunity to obtain the energy balance of reversible and visco-plastic deformations as well as heat produced during the irradiation.

Further, the SRG formation can be probed in more detail. According to the "orientation approach",[99,163] it is expected that the BBG is the driving force of the SRG formation. Especially, the SP-IP reveals that the BBG is already saturated while the SRG is continuously increasing. This is in contradiction to the orientation approach. Here, the photo-induced mechanical forces, resulting in the SRG formation, appear only when the BBG is changing. Choosing the polarization of the probe beam in an appropriate way, the BBG and SRG kinetics are separated also for the ±45- and RL-IP. In the case of the ±45-IP this is done by choosing e.g. a -45° polarized probe beam and detecting the co- and cross-polarized component of the 1st-order DE (see **Appendix**, **Figure C.7**). It is found that indeed (similar to the case of the SP-IP, see **Figure C.6**) first the birefringence grating is developing due to the fast photo-orientation and later, with a certain delay, the SRG starts to form. The same analysis but with a circularly polarized probe beam can also be performed for the RL-IP (see **Figure C.8**).

In situ AFM scans near the border of the grating inscription area, where the illumination intensity due to the Gaussian spatial profile already drops down, can give hints for a nonlinear response of the SRG formation on intensity and can provide a value for the threshold between elastic and plastic deformation. The same information can also be obtained from one experiment by measuring the spatial profile (Gaussian profile) of the illuminating field and the corresponding surface deformation with the help of a profilometer. This directly reveals the correlation between intensity and SRG amplitude. For very low intensities it is expected that the induced surface structure is not stable, because the photo-induced stress has not exceeded the material's irreversibility threshold.

The formation of a transient grating in the first 20s of illumination with a RL-IP (see **Figure C.8f**) is still an unanswered question. Here, the first relief which is inscribed is not stable and vanishes after a certain time. Afterwards a second, inverted SRG is formed. The second SRG appears at a later stage and its amplitude overcomes the first grating. The presence of two gratings might be a result of lateral forces or an optical feedback as a consequence from the anisotropic *cis*-concentration. The irradiation with the ±45-IP shows a similar effect (see e.g. publication II). Here, a half period grating appears in the first seconds of illumination (similar to the SP-IP) which is not stable in time and transforms into a SRG with a normal period. The question why this short-term grating remains stable in the SP-IP, which differs from the ±45-IP only by a 45° rotation of the local polarization, could be addressed in the future.

- Yield stress

The polymer network needs to be able to release stress internally, e.g. by opening loops or supramolecular bridges. The observations in this work support the idea that the *trans-cis* isomerization enhances the mechanical "activity" on the supramolecular scale so that stress-releasing processes happen at a larger rate. This can be translated as an effective reduction of the yield point or of the viscosity. The difference with respect to an increase in temperature or the naive picture of photo-fluidization is that the increased mechanical activity is somehow localized to the motion of small-scale units in the network. In a further experiment (tensile test) a change in the yield stress upon illumination of the polymer film could be probed. For this purpose, stress-strain curves, measured with and without illumination, could reveal if there is a change in the yield point. A modification of this value due to irradiation makes the transition from elastic to plastic deformation easily accessible.

In summary, this dissertation addresses several different problems of the photo-patterning of amorphous azobenzene containing side-chain polymer films and gave new insights in the driving force behind the SRG formation. This was only possible due to the *in situ* acquisition of the BBG and SRG amplitude with the help of the new designed set-up. It also permits to acquire the change in *cis-trans* population, the photo-orientation and the mesoscopic deformation.

Appendix

A. Photo-orientation

In the “basics and theory” chapter (chapter 2) it is discussed that the exposure of the amorphous polymer film, with azobenzene in the side-chain, to linearly polarized light results in a photo-orientation generating an anisotropy with a different absorbance along and perpendicular to the chromophore orientation (dichroism). A higher absorbance is probed parallel and a lower perpendicular to the azobenzene-chromophore orientation (in the case of PDR1, see **Figure 2.5**). This is not observed for the PAZO film. Here, the irradiation with linearly polarized light generates an anisotropy but the absorbance for both polarizations is reduced (see **Figure A.1a**), indicating a certain orientation in the plane perpendicular to the film surface. The chromophores aligned in the direction of the beam propagation are not probed in this configuration of the set-up. Exposing the polymer film first to circularly polarized light is not generating an anisotropy (orientation parallel to the film surface) but reduces the absorbance (see **Figure A.1b**). The illumination with linearly polarized light afterwards creates an anisotropy with a symmetric splitting of the absorbance (similar like it is observed for the PDR1 polymer). This indicates that in the case of the PAZO film a certain amount of chromophores are aligned perpendicular to the film surface, maybe due to the interaction of the charged polymer with the substrate. **Figure A.1c** shows the kinetics of this photo-induced dichroism after exposure to circularly polarized light for one hour. Therefore, the film is stepwise irradiated for 10min with linearly polarized light and the absorbance is probed parallel and perpendicular to the chromophore orientation afterwards. The calculated dichroism and order parameter as a function of exposure time are shown in **Figure A.1d**.

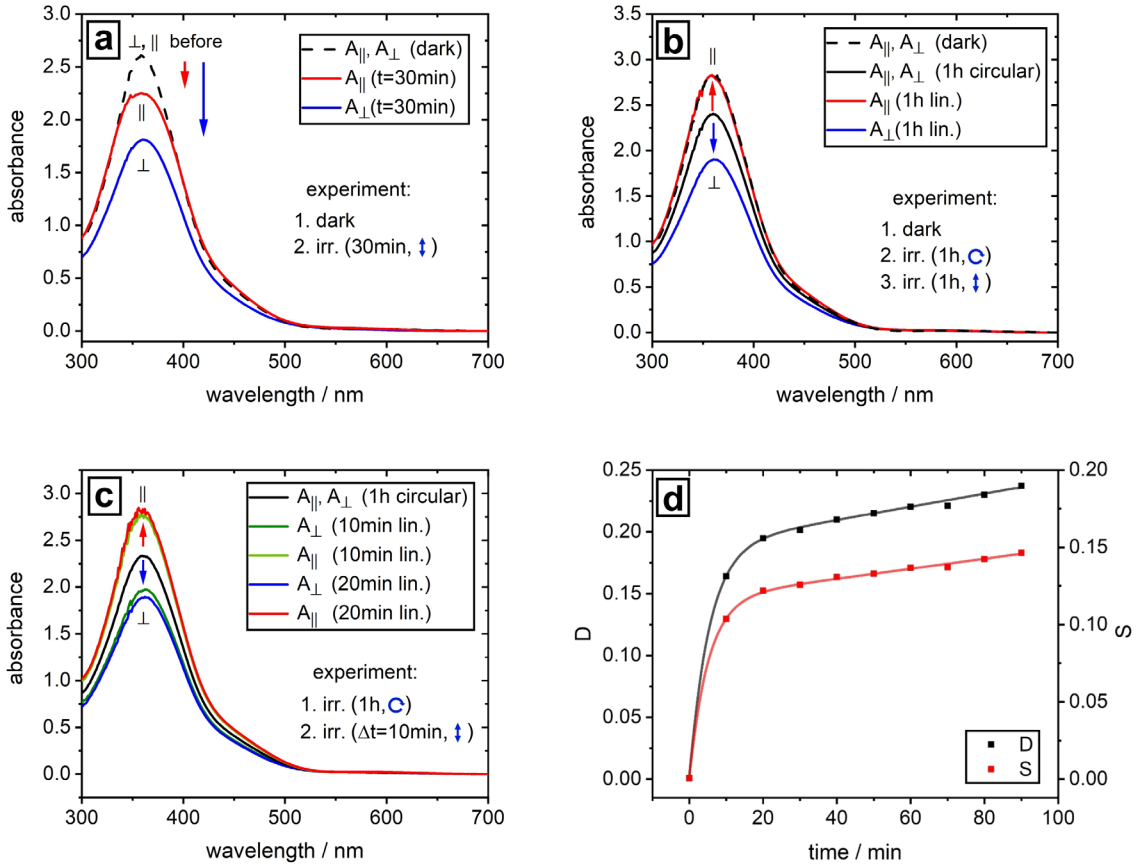

Figure A.1. Photo-induced dichroism in a PAZO film ($d = 450\text{nm}$). (a) The illumination with linearly polarized light ($\lambda_{\text{pump}} = 491\text{nm}$, $I = 100\text{mW/cm}^2$, $t = 30\text{min}$) results in a decrease of the absorbance probed parallel as well as perpendicular to the chromophore orientation. (b) Using circularly polarized light ($t = 1\text{h}$, other parameters same as before) is not generating an anisotropy but the absorbance is reduced compared to the initial state (shows chromophore orientation perpendicular to film surface). The exposure to linearly polarized light afterwards generates an anisotropy in the plane parallel to the film surface ($t = 1\text{h}$, other parameters same as before), so that a symmetric splitting of the absorption band is observed. (c) Kinetics of the photo-induced dichroism after exposure to circularly polarized light. The sample is stepwise exposed to linearly polarized light (for 10min) and the absorbance is probed afterwards. (d) Calculated dichroism and order parameter from the results of (c) as a function of exposure time (evaluated at the absorption maximum). The fitting is performed with a double exponential function ($\tau_1 = 5\text{min}$, $\tau_2 = 3 \cdot 10^{16}\text{min}$).

B. Mechanical properties

Temperature increase due to absorption

It was several times reported, that the SRG formation is caused by an increase in temperature due to the absorption of the light or is the result of an athermal phase transition into the viscoelastic state (photo-softening without heating as a result of the photo-isomerization).[204] **Figure B.1** is indeed showing an increase in the temperature of the two studied polymer films dependent on the intensity of the pump beams during SRG inscription. In (a**)** the results for a PAZO- ($d = 1\mu\text{m}$) and in (b) for PDR1 film ($d = 500\text{nm}$) are shown. The temperature of the PAZO film is increasing from room temperature (23°C) to 33°C as soon as the pump beam ($\lambda = 491\text{nm}, I = 200\text{mW/cm}^2$, intensity which is usually used for the SRG inscription) is switched on. The temperature increase is of course reducing the Young's modulus of the polymer (shown in the next chapter), but the change in modulus is still several orders of magnitude to low in order to induce a phase transition. The irradiation of the PDR1 film with the same intensity results in a temperature increase of 14°C. This is interesting because the polymer film is only 500nn thick, indicating a stronger absorbance at this wavelength. Nevertheless, this is still far away from the glass transition temperature ($T_g = 102°\text{C}$) of this polymer. In contrast there is no glass transition temperature found for the PAZO polymer. The temperature change is recorded with a IR-Laser thermometer (Optris Ls).

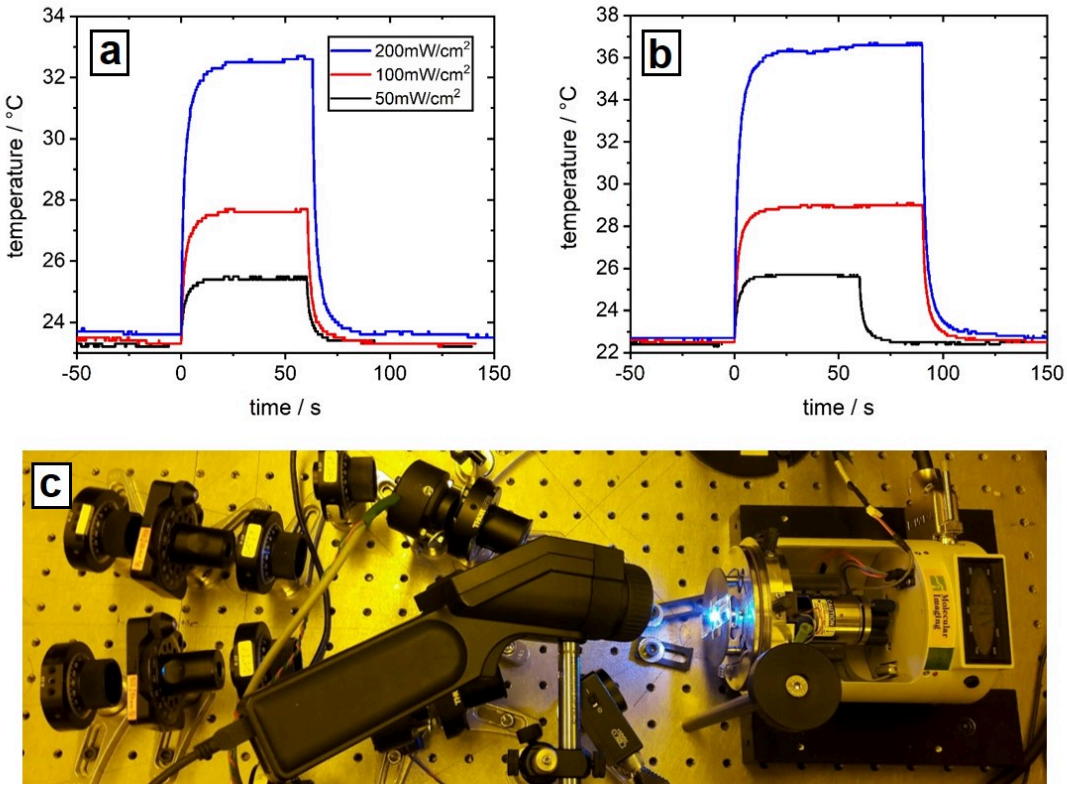

Figure B.1. *In situ* recorded temperature increase of the 1µm thick PAZO- (a) and 500nm thick PDR1- (b) film during irradiation with an IP using different intensities ($\lambda_{\mathrm{pump}} = 491\mathrm{nm}$). (c) Photo of the experimental set-up for the *in situ* temperature recording.

Indentation measurements

AFM indentation measurements are performed in order to characterize the change in the material properties (Young's modulus, adhesion) of the polymer film upon irradiation or an increase in the temperature. A spherical AFM cantilever (tipless cantilever with an attached sphere, 2µm in diameter, see **Figure B.2b**) is moved vertically with the help of a piezo scanner. Once the cantilever is approaching the surface further movement results in a deformation of the polymer film probed by analyzing the cantilever deflection. Therefore, a red probe laser is focused on the far end of the cantilever and the beam deflection is recorded with a four-segment photodiode. The cantilever deflection d is calculated from the optical deflection signal DFL using the cantilever sensitivity S and the equation $d = S \cdot DFL$. In order to determine the sensitivity S a hard surface is approached. Then, the cantilever displacement (Δz) is directly converted into a cantilever deflection (DFL) without a

deformation of the polymer film: $S = \frac{\Delta z}{\Delta DFL}$. The force is calculated from the cantilever deflection by means of the hooke's law $F = k \cdot d$, with the spring constant of the cantilever k. The sample deformation δ is obtained from the cantilever displacement Δz by subtracting the bending of the cantilever d: $\delta = z - d$. The elastic deformation of the polymer film by applying a certain force is explained, e.g. by the Hertz model.[225] Here, no adhesion force between the probe and the surface is assumed and the force F scales with deformation δ to the power of $3/2$:

$$F = E^* \sqrt{R} \delta^{\frac{3}{2}}. \tag{B.1}$$

R is the radius of the indenter. The proportionality factor E^* is the reduced modulus, which is a sum of the Young's modulus of the polymer film E and the Young's modulus of the indenter E_i ($\approx 130\text{GPa}$):

$$\frac{1}{E^*} = \frac{3}{4}\left(\frac{1 - v^2}{E} + \frac{1 - v_i^2}{E_i}\right). \tag{B.2}$$

Here, v_i is the Poisson's ration of the indenter (≈ 0.3) and v the one of the tested material (≈ 0.5). In the DMT-model[226] (Derjaguin, Muller, Toporov) the force scales with the same power as in the Hertz model but an adhesion force F_{ad} is added:

$$F = E^* \sqrt{R} \delta^{\frac{3}{2}} - F_{ad} \tag{B.3}$$

The JKR-model[227,228] (Johnson, Kendall, Roberts) assumes that the polymer film is very soft. During the approach a negative film deformation is observed, due to strong adhesion forces. Therefore, the force-deformation dependence is more complicated:

$$\delta = \frac{a^2}{R} - \frac{4}{3}\sqrt{\frac{aF_{ad}}{RE^*}} \qquad \text{with} \qquad a = \left[\frac{R}{E^*}\left(\sqrt{F_{ad}} + \sqrt{F + F_{ad}}\right)^2\right]^{1/3} \tag{B.4}$$

A typical force vs. distance curve is shown in **Figure B.2a** (recorded with a NTEGRA (NT-MDT) and Nanoscope V (Bruker) AFM). The tip-sample distance is continuously reduced during the approach (black curve). At a certain point the probe jumps into contact with the surface of the polymer film due to a strong adhesion force, which results in a negative cantilever deflection. Further motion of the probe causes a positive cantilever deflection and a deformation of the polymer film. Retracting the probe (red curve) reduces the force until a negative deflection is observed (due to the adhesion force). Once the retracting force is larger than the adhesion force the cantilever jumps out off contact. The slope of the approach curve contains the elastic and plastic deformation of the polymer film while the retract curve carries only the elastic deformation. The retract curve is used for the fitting with the different models in order to extract the Young's modulus of the polymer film. Additionally, also the adhesion force is extracted from this curve. Force vs. distance measurements permit to record changes in the Young's modulus of the photo-sensitive polymer film during illumination or a change in the temperature. **Figure B.2c** shows the change in the Young's modulus of a PAZO film upon illumination with a blue laser ($\lambda_{pump} = 491\text{nm}$, $P = 50\text{mW}$). The Hertz-model is applied for the fitting of the force vs. distance curve. Here, the modulus is reduced by 16% under illumination. These results indicate that there is no significant photo-softening upon illumination of the polymer film. The cantilever spring constant is an important parameter for these kind of measurements and has to fit to the expected Young's modulus of the polymer film. Choosing a cantilever which is "too" soft results only in a cantilever deflection but not in a deformation of the polymer film. The bending of the cantilever is "too" less and cannot sense the deformation of the polymer film, if the cantilever spring constant is "too" high. **Figure B.2d** shows the change in the modulus of a PAZO film for an increase in the temperature. Therefore, the polymer film is stepwise (10°C steps) heated up till 140°C which results in a change in the Young's modulus of one order of magnitude starting at the temperature of 80°C.

Performing indentation measurements is usually a challenging task which is the reason why the results shown above are only giving an overview about the different measurements. It is found that the modulus is showing a huge variation of several GPa dependent on the probe position on the film. Therefore, the modulus is averaged and the measurements are repeated several times. These measurements could be repeated with different polymers in the future.

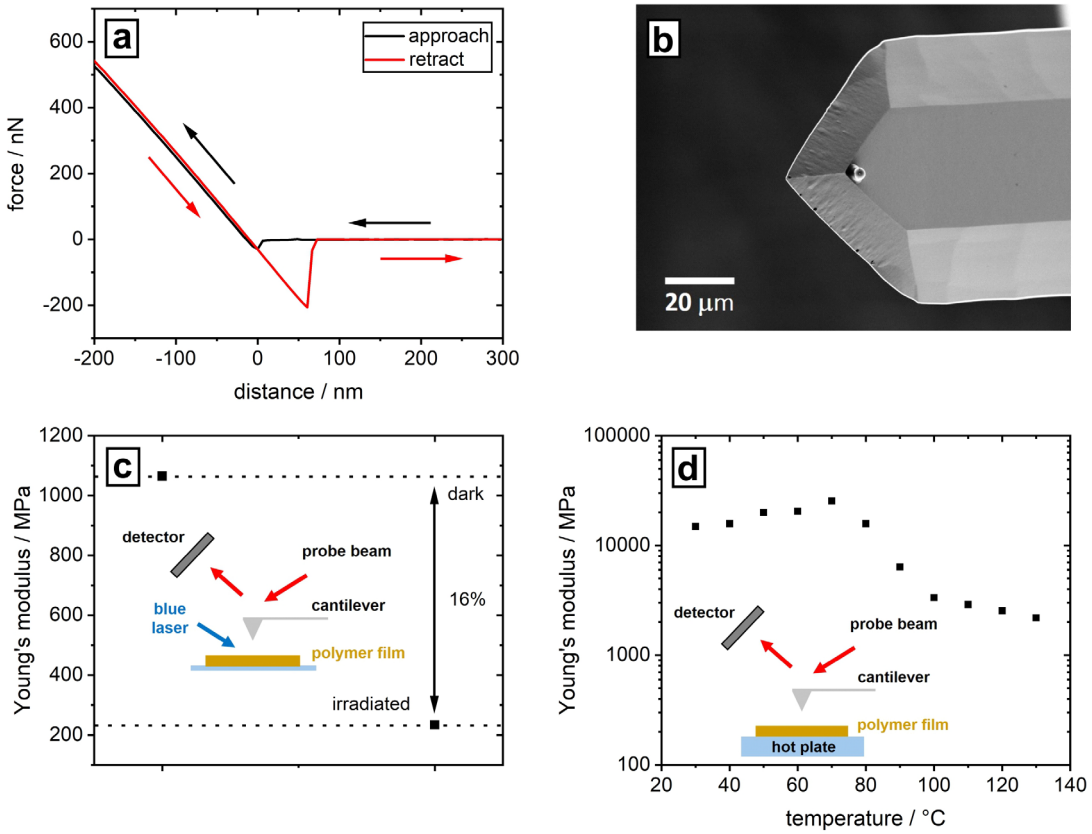

Figure B.2. (a) Typical force vs. distance curve obtained from a PAZO film ($d = 1\mu m$). (b) SEM image of the spherical indenter with a radius of $R = 1\mu m$ and a spring constant of $k = 42 N/m$. The change in the Young's modulus of the polymer film during irradiation ($\lambda_{pump} = 491nm$, $P = 50mW$) is shown in (c) and for an increase in temperature in (d). The fitting is performed according to the Hertz model.

Pulsed Force Mode

The pulsed force mode[229] (Witec, apha 300 SNOM) is not only performing a single force vs. distance curve, it is performing ~500 curves per second, which is averaging the mechanical properties. Here, a sinusoidal voltage modulation is applied on the piezo stack which is moving the cantilever in vertical direction. The frequency of this oscillation is around 500Hz and a typical force vs. distance cycle is shown in **Figure B.3a**. The topography is obtained from the maximum force point, the adhesion force from the snap off point and the Young's modulus from the slope of the curve. Moving the probe during the measurement (in x,y-

direction) permits a 2D mapping of the above mentioned parameters. **Figure B.3b** is showing the change in adhesion and Young's modulus of the PAZO film during illumination with a blue laser ($\lambda_{\mathrm{pump}} = 491\mathrm{nm}$, $P = 50\mathrm{mW}$). The adhesion force is increasing, while the Young's modulus is decreasing, as soon as the pump beam is switched on. These results show the effect of illumination on the mechanical properties only in a qualitative way, because the system is not calibrated. The calibration could be a task for the future in order to obtain an absolute value for the change in the mechanical properties.

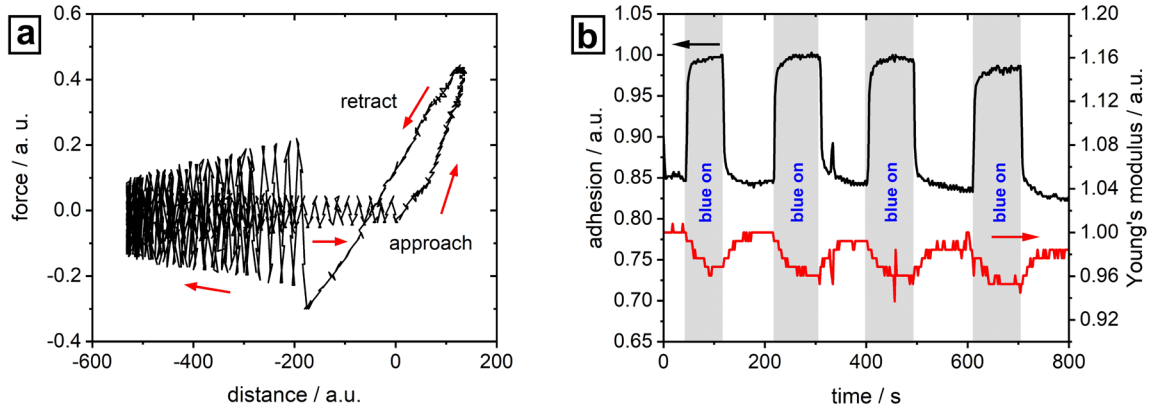

Figure B.3. (a) Typical force vs. distance cycle in the pulsed force mode. (b) Change in adhesion force and Young's modulus of a PAZO film ($d = 1\mu\mathrm{m}$) upon illumination with a blue laser ($\lambda_{\mathrm{pump}} = 491\mathrm{nm}$, $P = 50\mathrm{mW}$). The grey rectangles mark the irradiation sequence of the film. The adhesion force is increasing, while the Young's modulus is decreasing, as soon as the irradiation is switched on. A cantilever with a spring constant of $k = 2.8\mathrm{N/m}$ is used for these kind of measurements.

Differential Scanning Calorimetry

The previous experiments show that there is not a big change in the mechanical properties of the polymer film upon irradiation. A long discussed idea is that the glass transition temperature of the polymer might be affected by illumination, which would indicate a higher mobility of the polymer chains even at lower temperatures. In order to address this question differential scanning calorimetry (DSC, Photo-DSC 204 F1 Netzsch company) measurements first without and afterwards with *in situ* (during the measurement)

illumination of the polymer are performed (see **Figure B.4**). Therefore, the PDR1 sample is heated up to 120°C and cooled down to 25°C in three cycles with a heating/cooling rate of 10K/min and the heat flux is recorded as a function of temperature. The first heating of the DSC measurement reveals that at ≈70°C some lighter substances evaporate, because this peak is not present in the second and third heating. The second heating reveals that this polymer has two glass transition temperatures, one at 63°C and the second one at 101°C. The PDR1 polymer is a co-polymer made of PMMA and Poly(Disperse Red 1 acrylate), explaining the presence of two glass transition temperatures. The same experiment is repeated under blue light irradiation ($I = 100\mathrm{mW/cm^2}$). A small reduction in the first T_g of ≈1K is observed due to the illumination with blue light, which is not enough to significantly change the mobility of the polymer chains. On the other hand, the second T_g at 101°C is more pronounced in the case of the illumination.

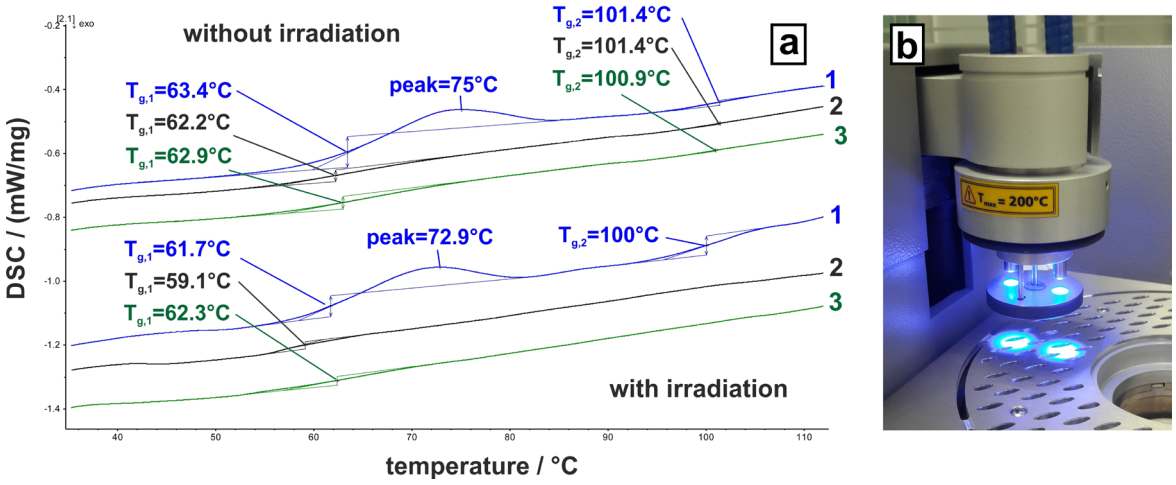

Figure B.4. (a) *In situ* DSC measurements of the PDR1 polymer without (top) and with (bottom) illumination (blue light, $I = 100\mathrm{mW/cm^2}$). The first three heating curves are shown for each experiment. The glass transition temperature of the polymer is reduced by ≈1K upon illumination. The measurements are performed in cooperation with the Netzsch company (Photo-DSC 204 F1). (b) Photo of the experimental set-up permitting the *in situ* illumination of the polymer during the DSC measurement.

Photo-induced forces

Of special interest in order to understand the SRG formation is to obtain an absolute value of the photo-induced forces during the grating inscription. A simple method for the direct measurement of the photo-induced stress is the coating of an AFM cantilever with the polymer film from the front side. This method is developed in the framework of this thesis. The irradiation of this photo-sensitive probe is bending the cantilever upwards due to the generation of a strong photo-induced stress caused by the photo-orientation of the azobenzene-chromophores and the resulting deformation of the polymer film. The cantilever deflection is measure by the displacement of a probe beam focused on the back side of the cantilever, similar like in the case of an AFM. The photo-induced stress Δs is calculated using the following equation:[230,231]

$$\Delta s = \frac{d E t_s^3}{12 l^2 t_c^2 \left(1 + \frac{t_s}{t_c}\right)(1 - \nu)}. \tag{B.5}$$

Here, l is the length of the cantilever, ν the poisson ratio (≈0,3) and d the cantilever deflection. E is Young's modulus of the cantilever (≈165GPa). t_s and t_c indicate the thickness of the cantilever and cantilever coating. The cantilever deflection d is calculated from the optical deflection signal DFL with the help of the sensitivity S and the equation $d = S \cdot DFL$ (see **indentation measurement**). In order to calculate the sensitivity of the cantilever a force vs. distance measurement on a hard surface is performed prior light exposure. As soon as the irradiation is switched on the cantilever is bending upwards indicating the generation of a photo-induced mechanical stress (**Figure B.5c)**. A certain relaxation of the cantilever deflection is observed once the illumination is switched off. The stress is not completely released indicating the plastic deformation of the polymer film. Using a cantilever with a spring constant of $k = 42\mathrm{N/m}$, a coating thickness of the PAZO film of $d \approx 2\mu\mathrm{m}$ and an irradiation power of $P = 50\mathrm{mW}$ ($\lambda_{pump} = 491\mathrm{nm}$) results in the generation of a photo-induced mechanical stress of $\Delta s \approx 20\mathrm{MPa}$ (**Figure B.5d**). The polymer coating is applied by spin coating after previous plasma cleaning.

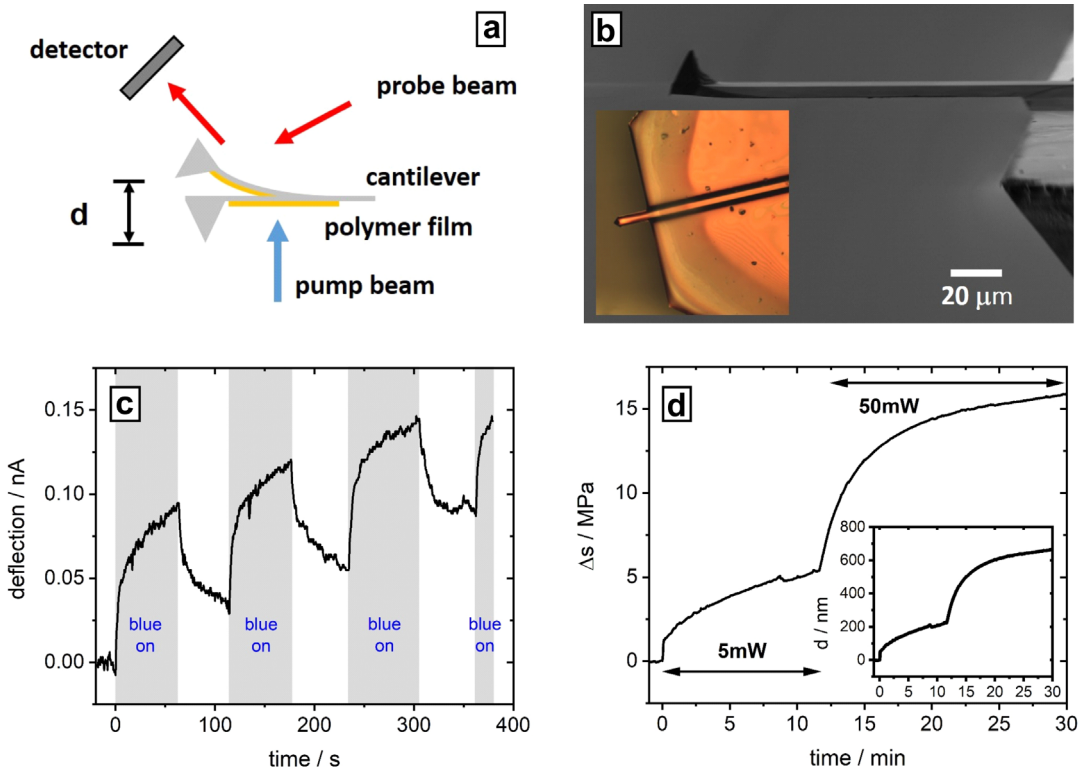

Figure B.5. (a) Schematic representation of the experimental set-up for the direct measurement of the photo-induced stress. The front side coated cantilever is irradiated from below ($\lambda_{\mathrm{pump}} = 491\mathrm{nm}$), generating a photo-induced stress and a polymer film deformation which results in a bending of the cantilever. The deflection is probed from the back side with a laser. (b) Scanning electron microscope image of the uncoated cantilever. The inset shows the optical microscope image of the polymer coated AFM cantilever (PAZO coating). The coating ($d \approx 2\mu\mathrm{m}$ thick) is applied on an uncoated silicon cantilever with a spring constant of $k = 42\mathrm{N/m}$. The optical deflection signal of four illumination cycles of the cantilever is shown in (c). The cantilever is bending upwards as soon the blue light irradiation is switched on and is relaxing once the light is switched off (the grey rectangles mark the irradiation sequence of the cantilever). The photo-induced bending is not completely relaxing so that the cantilever is more and more bended upwards with an increase in the exposure time. (d) Calculated photo-induced stress as a function of irradiation time for two different irradiation power ($P_1 = 5\mathrm{mW}$ and $P_2 = 50\mathrm{mW}$). The inset is showing the cantilever deflection.

C. *In situ* analysis of SRG and BBG formation

In order to correlate the *in situ* recorded DE with the SRG amplitude (measured with the *in situ* AFM), the two set-ups must be synchronized. **Figure C.1** is showing the wiring diagram of the DE set-up, AFM, Pockels cell, piezo stack and the communication between these different components. The voltage of the photodiodes (intensity of diffraction spot) is recorded with a AD/DA converter card in the computer (Kolter Electronic, PCI-AD12N-DAC2). This controller is also used to send a voltage signal (TTL or analogue) to the Shutter, which controls the irradiation, the piezo stack, which controls the position of mirror M_4 and to the Pockels cell, in order to drive it as a half- or quarter-wave plate. The connection between the PC and the AFM-controller might be the most important one, highlighted in red (see **Figure C.1**), because it enables the hardware synchronization of the different components in the set-up.

In order to control the new designed set-up a software was generated using the graphical programming software “Profilab-Expert” (Abacom). **Figure C.2a** is showing the graphical user interface (GUI) of the latest version of the software, while in (b) the corresponding block diagram is displayed.

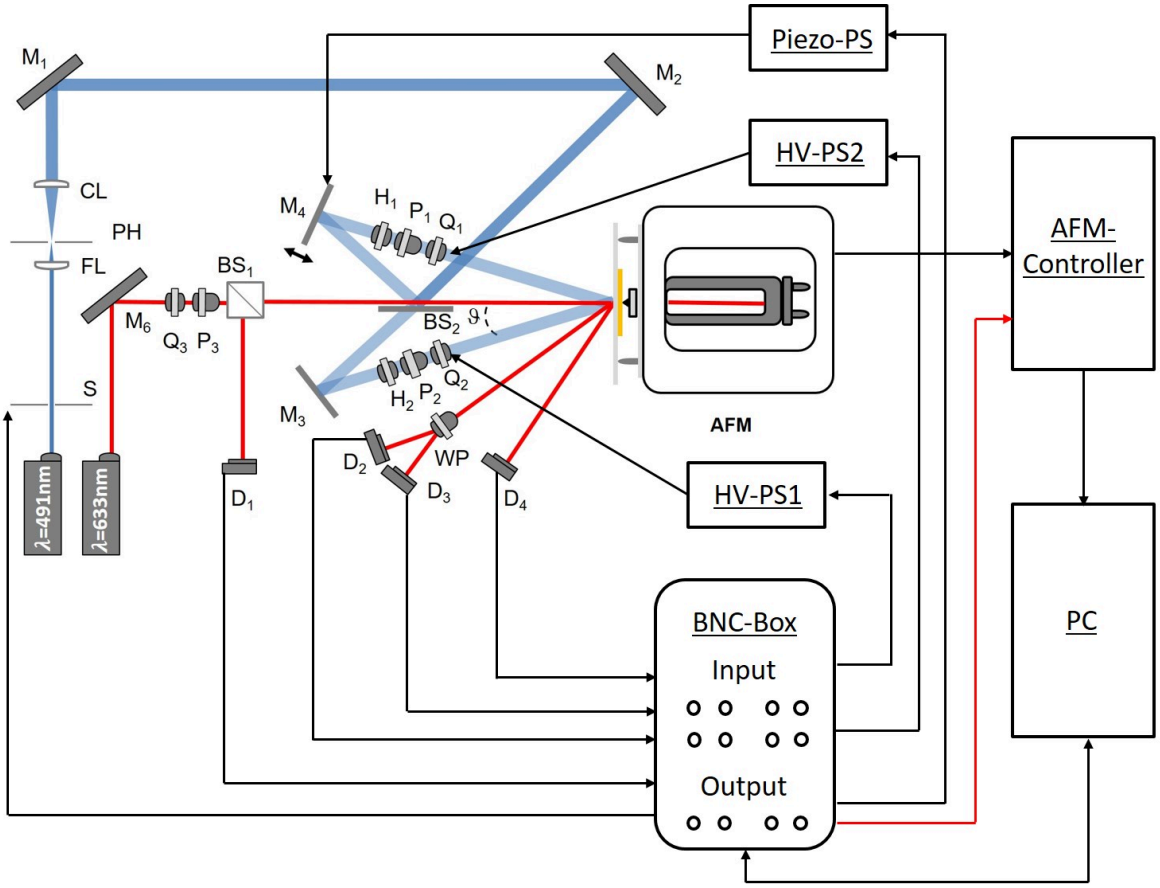

Figure C.1. Wiring diagram of the experimental set-up. HV-PS = high voltage power supply to drive the two Pockels cells (Q_1, Q_2). Piezo-PS = piezo power supply to control the position of mirror M_4 (other parameter same as in **Figure 2.14**).

The software permits to control the recording of the diffraction efficiency, the irradiation of the polymer film (shutter control), the voltage send to the Pockels cell (Thorlabs, EO-PC-550) and piezo stack (PiezoSystemJena, PA8-14 SG) and the synchronization of the DE setup with the AFM. The switch on the upper left side (see **Figure C.2a**) is opening and closing the shutter manually while on the upper right side a timer is integrated, which permits the precise illumination of the polymer film with the IP for a certain time. In the center and lower left side the voltage signals of the different photodiodes, Pockels cells, piezo stack and the voltage send to the AFM controller are displayed. The central and lower part on the right side is controlling the voltage which is send to the Pockels cells and to the piezo stack. Here, a voltage between 0 and 10 V is set, which is reaching the high voltage power supply (Trek 610D) of each Pockels cell or the controller of the piezo stack

(PiezoSystemJena, 12V40SG). The high voltage controller amplifies the control voltage by a factor 1000x. The high voltage is provided to the Pockels cells by using a special protected cable. This permits the precise control of the applied voltage on the Pockels cells in order to drive them as a half- or quarter-wave-plate. The fast switching between different IP became accessible with this special configuration of the set-up. The piezo-stack is controlled in the same way. Here, the voltage is send to the piezo controller and amplified by a factor 15x in order to precisely control the position of the mirror. The software also permits the modulation of the control voltage, so that e.g. the polarization of the probe beam is cyclically changed, the inscribed SRG is erased or the IP/SRG is continuously or stepwise translated in a certain direction. Three different graphical windows in the center of the GUI are showing the DE as a function of time, together with the control signals. In the first window (top) the back-reflected probe beam intensity (0^{th} diffraction order) as well as the intensity of the 2^{nd} diffraction order is shown together with the signal which is send to the AFM controller. In the central window the signals of two sensitive photodiodes (usually used to record the 1^{st}-order DE) as well as the control signal are displayed as a function of time. Additionally, the voltage applied on the first Pockels cell is recorded. The lower window is the control window. Here, the intensity of the probe beam is measured in order to calibrate the diffraction efficiency and to ensure that its intensity is constant during the experiment. Furthermore, the shutter and mirror position signal as well as the voltage applied on the second Pockels cell are shown. The data-set of the DE measurement consists of the files of these three graphs.

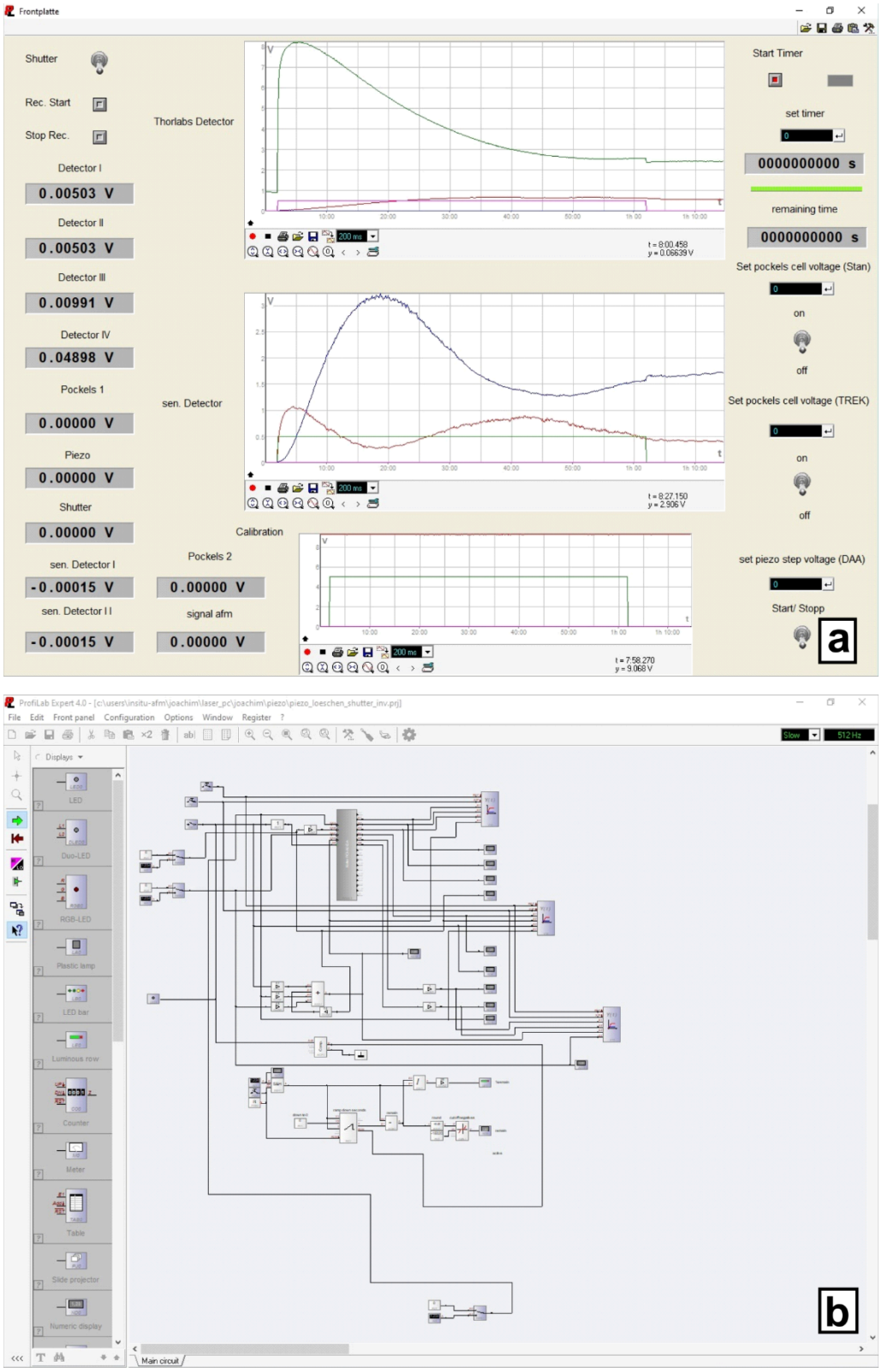

Figure C.2. (a) Graphical user interface (GUI) of the software designed with Profilab-Expert. (b) Block/ circuit diagram to the GUI of (a).

The signal send to the AFM controller enables the synchronization of the DE set-up with the integrated AFM. It is generated by the software and contains the illumination parameters, such as the voltage applied on the laser-shutter, piezo-stack, Pockels cell 1 and Pockels cell 2. These signals are summed up into one signal by multiplying each voltage with a certain pre-factor in order to distinguish the signals. The common signal is recorded in the DE set-up as well as with the AFM controller and provides the full information about the illumination parameter at each time of the experiment. The AFM data-set consist of three different images (see **Figure C.3**). The first information is the *in situ* recorded topography change. Additionally, also the phase map is recorded. The last part of the AFM-data-set is the map of the recorded voltage applied on the aux-input of the AFM controller. According to the previous description this signal contains the information of irradiation, mirror position and Pockels cell voltage. The correlation with the topography enables to track the exact experimental settings for each point of the topography. The whole *in situ* data-set consists of the three AFM-files and the three DE files.

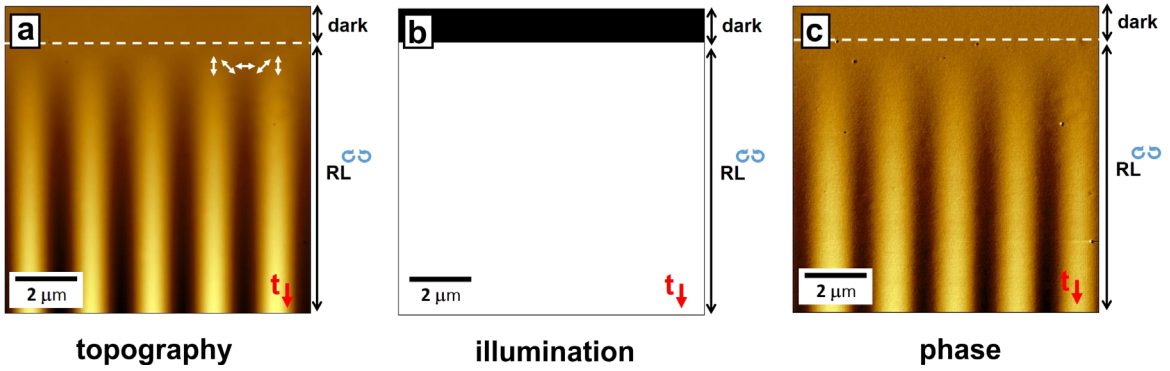

Figure C.3. Data-set recorded with the AFM during the *in situ* experiment: (a) SRG-amplitude (topography), (b) voltage applied to the aux-input of the AFM controller (shutter, Pockels cell, piezo-stack) and phase image (c).

Different interference patterns

In order to understand the grating inscription in an amorphous azobenzene containing polymer films the 1st- and 2nd-order DE as well as the SRG amplitude are measured *in situ* (during illumination) for different interference patterns and probe beam polarizations. **Figure C.4** is showing the results for a SS- (a) and PP- (b) interference pattern with a S- (left) or P-(right) polarized probe beam. In the case of an SS-IP the SRG amplitude and DE (1st- and 2nd-order) are increasing fast until both signals are saturating (at the SRG height of 70nm). In the case of a P-polarized probe beam the DE kinetics slows down, while the recorded SRG amplitude is the same as in the case of a S-polarized probe beam. The explanation is the destructive interference of the SRG and BBG in the total DE (see also publication II). A constructive interference is observed in the case of an S-polarized probe beam. A similar behavior is observed using a PP-IP for the illumination of the polymer film. Here, the fast kinetics is observed in the case of a P-polarized probe beam (constructive interference). In contrast to the SS-IP the DE is first increasing and then starts decreasing (at the SRG height of 100nm) while the SRG amplitude is continuously increasing. This behavior is predicted for the diffraction by a thin phase grating (in Raman-Nath approximation) and for large modulation amplitudes of the surface grating (described by a first-order Bessel function). The final SRG height is 200nm after one hour of illumination.

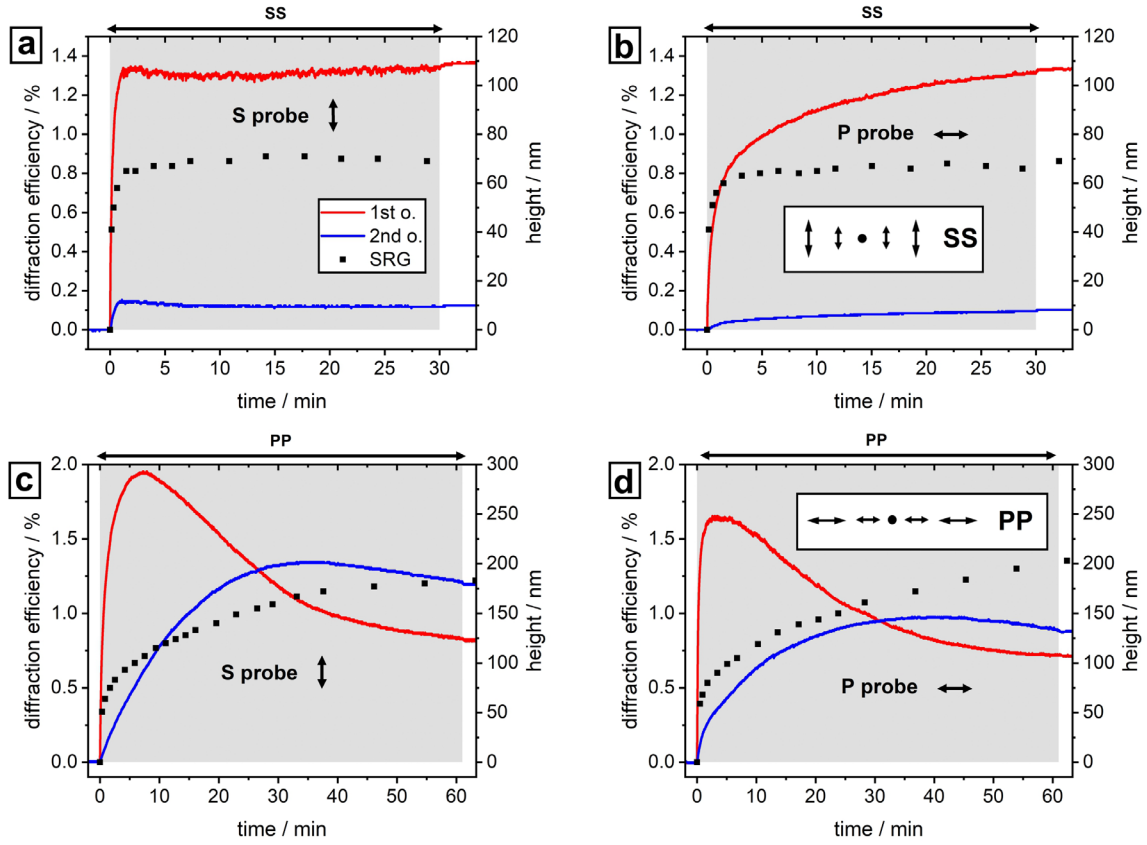

Figure C.4. *In situ* recorded DE (1st- and 2nd order) and SRG amplitude as a function of illumination time for different intensity interference patterns and probe beam polarizations. In (a) the results for the SS-IP with a S- (left) or P- (right) polarized probe beam are shown while in (b) the same for the PP-IP is presented (PAZO, same parameters as **Figure 3.1**). The inset shows the local polarization (black arrows) and the grey rectangle marks the irradiation sequence of the polymer film.

A different behavior is observed in the case of polarization interference patterns. **Figure C.5** is showing the results for a ±45- (a) and RL-IP (b) with a S- (left) or P- (right) polarized probe beam. The ±45- IP, as well as the RL-IP, shows an additional peak in the 1st-order DE within the first minutes of illumination (using a S-polarized probe beam). The explanation is a destructive interference of the SRG and BBG in the total DE (see publication II and IV). Using a P-polarized probe beam results in a constructive interference of these two gratings in the 1st-order DE. The final SRG height is 250nm in the case of ±45-IP and 300nm in the case of the RL-IP after 1h of illumination.

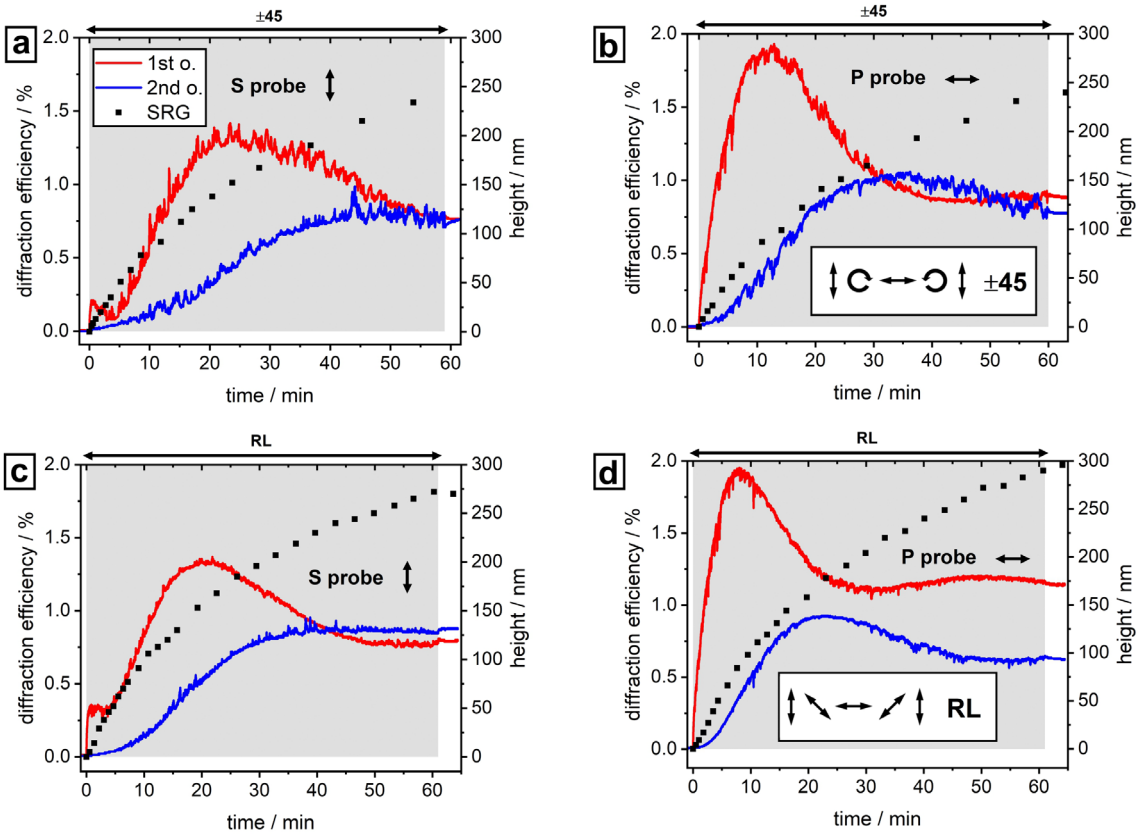

Figure C.5. *In situ* recorded DE (1st- and 2nd order) and SRG amplitude as a function of illumination time for different polarization interference patterns and probe beam polarizations. In (a) the results for the ±45-IP with a S- (left) or P- (right) polarized probe beam are shown while in (b) the same for the RL-IP is presented (PAZO, same parameters as **Figure 3.1**). The inset shows the local polarization (black arrows) and the grey rectangle marks the irradiation sequence of the polymer film.

A special interference pattern is the SP-IP. It is the only IP creating a surface grating with a period which is half the grating period of the IP. This results also in a unique behavior of the DE (see **Figure C.6** and publication V). The 1st- and 2nd-order DE is not dependent on the polarization of the probe beam. The 1st-order DE is increasing fast until the signal saturates during the illumination with the IP, while the 2nd-order DE is continuously increasing like the modulation amplitude of the SRG. The half-period grating is shifting the 1st diffraction order of the SRG to a higher diffraction angle, so that it coincides with the 2nd diffraction order of the BBG. This explains why the 1st-order DE contains only the BBG while the 2nd-order DE additionally carries the SRG.

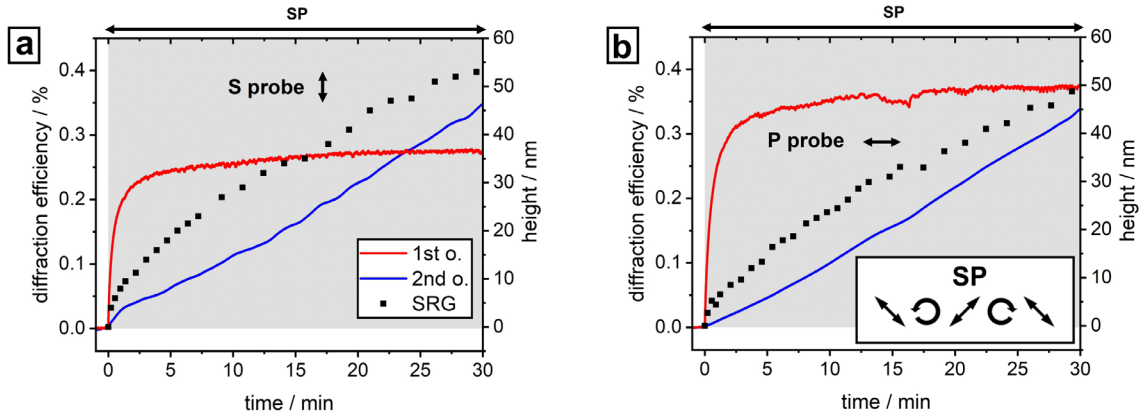

Figure C.6. *In situ* recorded DE (1st- and 2nd order) and SRG amplitude for the illumination with the SP-IP and different polarizations of the probe beam. In (a) the probe beam is S- and in (b) P- polarized (PAZO, same parameters as **Figure 3.1**). The inset shows the local polarization (black arrows) and the grey rectangle marks the irradiation sequence of the polymer film.

In order to also separate the BBG from the SRG in the DE in the case of other polarization interference patterns, a special polarization of the probe beam is used. For the ±45-IP this is a -45° or +45° polarization of the probe beam. The cross-polarized component of the 1st-order DE (+45° in the case of a -45° polarized probe beam) contains only the BBG while the co-polarized component (-45°) is a result of the SRG diffraction (see **Figure C.7**). The probe beam polarization is changed by the BBG due to the photo-induced anisotropy in the bulk (generation of a fast- and slow-axis), while the SRG is not affecting the polarization. Indeed, for a low SRG amplitude only the cross-polarized photodiode is detecting a signal, indicating the formation of the BBG. Once the SRG amplitude is increased also the co-polarized photodiode is measuring a signal. **Figure C.7b** is showing the theoretically predicted polarization of the +1st and -1st diffraction order of the BBG and SRG using a +45° or -45° polarized probe beam. The BBG is rotating the polarization of the probe beam by 90° while the SRG is maintaining the polarization. The cross-polarized component of the 1st-order DE is decreasing after some time due to an anti-symmetric coupling of the BBG and SRG (paper in preparation).

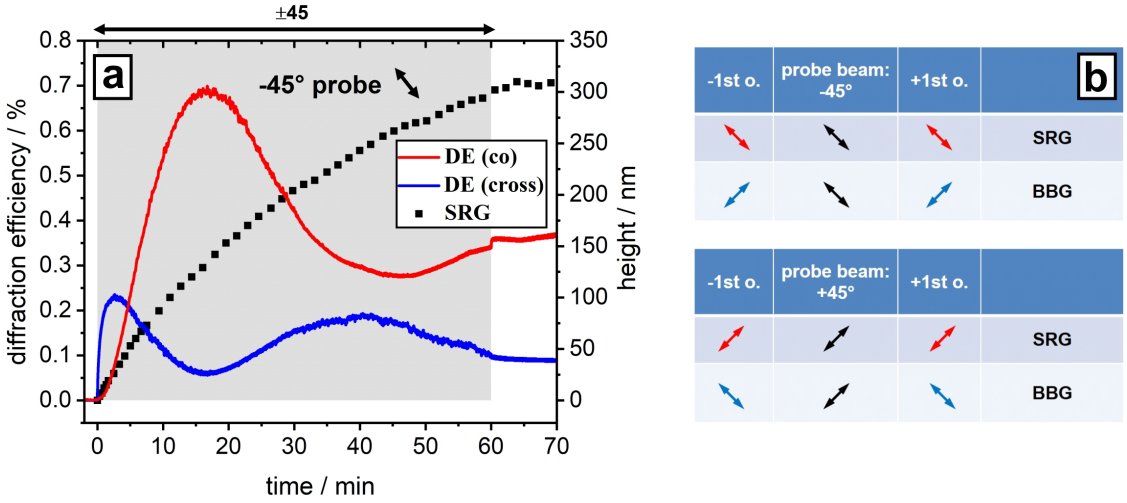

Figure C.7. (a) *In situ* recorded 1st-order DE and SRG amplitude (black dots) for the ±45 IP using a -45° linearly polarized probe beam. The red curve is showing the co(-45°)- and the blue curve the cross(+45°)-polarized component of the 1st-order DE (PAZO, same parameters as **Figure 3.1**). The grey rectangle marks the irradiation sequence of the polymer film. (b) Theoretically predicted polarization of the 1st-order diffraction spot for a -45°(top) or +45°(bottom) polarized probe beam. The bulk birefringence grating (BBG) is rotating the polarization of the probe beam (cross-polarized component of the DE) while the SRG is maintaining the probe beam polarization (co-polarized component of the DE).

A similar calculation reveals in the case of the RL-IP that a circularly polarized probe beam has to be used in order to separate the BBG from the SRG in the 1st-order DE. Here, the BBG is diffracting the probe beam only in the +1 diffraction order using a left-handed circularly polarized probe beam (LCP, see **Figure C.8c**) and is also converting its polarization from left- to right-handed circular polarization. The diffraction at the SRG is maintaining the probe beam polarization. The same behavior is observed in the case of a right-handed circularly polarized probe beam (RCP, see **Figure C.8d**). Here, only the -1 diffraction order (LCP-polarized) of the BBG appears, while the SRG is diffracting in both diffraction orders (-1 and +1). **Figure C.8** shows the *in situ* recorded 1st-order DE of the +1 diffraction order for a LCP- (a) or RCP- probe beam (b). The red curve is showing the co-polarized and the blue curve the cross-polarized component of the 1st-order DE. In the case of an LCP probe beam only the cross-polarized (RCP) detector is measuring a signal in the starting of the illumination with the RL-IP, indicating the formation of a BBG. As soon as the SRG amplitude is increasing also co-polarized photodiode (LCP) is detecting a signal (see **Figure C.8e**). The cross-polarized component is decreasing after some time due to an anti-

symmetric coupling of the BBG and SRG. Using a RCP probe beam only the co-polarized (RCP) detector is sensing a signal within the first minutes of illumination, indicating that the BBG is not diffracting in this order (as predicted by the theory). The co-polarized component is showing the same behavior as in the case of a LCP probe beam, representing the diffraction of the SRG. Here, the cross-polarized component is increasing after some time due to an anti-symmetric coupling of the BBG and SRG.

In the first 20s of irradiation with the RL-IP a transient surface grating is observed (see **Figure C.8f**). It is not stable and vanishes after a certain time. Afterwards, a second but inverted SRG is formed. It is stable and its amplitude overcomes the transient grating. The appearance of these two gratings might be due to an optical feedback as a result e.g. of the BBG formation. The diffraction efficiency set-up is further modified in order to analyze the circularly polarized 1st-order diffraction spot (see **Figure C.8g**). Therefore, a quarter wave plate in 45° orientation (angle to the optical axis) is added into the beam path of the 1st-order diffraction spot. The wave plate is converting circularly- into linearly-polarized light. A wollaston prism, integrated afterwards, is splitting the linearly polarized light into its components (S and P). These two components are recorded with two photodiodes. The S-polarized component represents the LCP- and the P-polarized component the RCP-polarized light or vice versa dependent on the polarization of the probe beam.

Therefore, an easy way of separating the BBG and SRG in the DE is found in the case of polarization interference patterns (together with publication V).

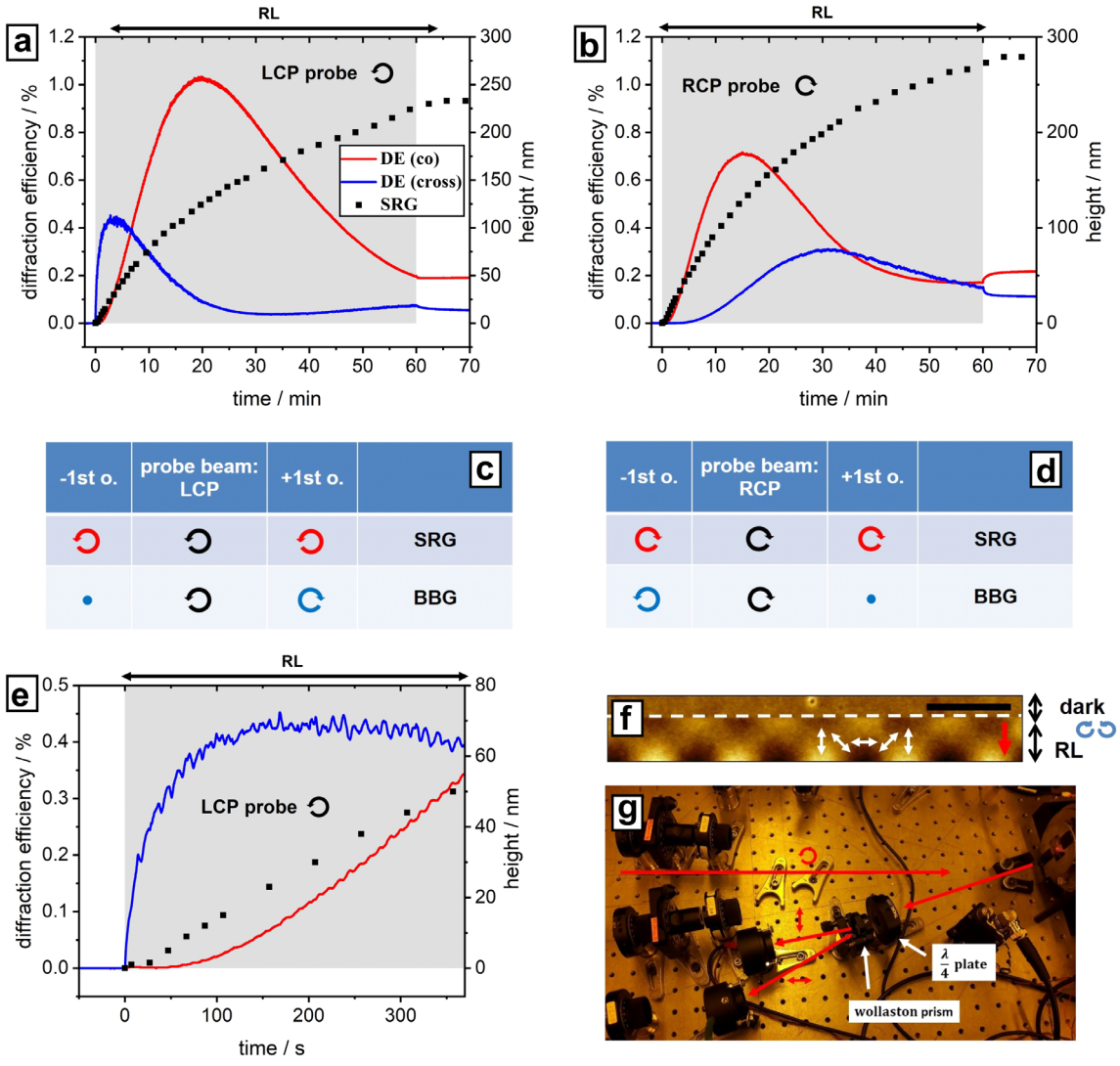

Figure C.8. *In situ* recorded 1st-order DE and SRG amplitude (black dots) for the RL-IP with a LCP (a) or RCP (b) polarized probe beam. The red curve is showing the co- and the blue curve the cross-polarized component of the +1st-order DE (PAZO, same parameters as **Figure 3.1**). The grey rectangle marks the irradiation sequence of the polymer film. The theoretical polarization prediction of the 1st-order diffraction spot for a LCP- and RCP- probe beam is shown in (c) and (d). The BBG is diffracting, dependent on the polarization of the probe beam, only in the +1 or -1 diffraction order (and changes the polarization of the probe beam). The SRG is not affecting the polarization of the probe beam. (e) Zoom in of (a) showing the first seconds of irradiation with the RL-IP. (f) *In situ* recorded AFM micrograph of the first seconds of illumination (RL-IP) showing the transient grating. The scan direction is from top to bottom. The illumination is started at the time of the white dashed line. The black scale bar indicates the grating period of $\Lambda = 2\mu m$. The white arrows show the local polarization. (g) Photo of the experimental set-up in order to separate left- from right-handed circularly polarized light in the 1st diffraction order.

Optical field within the polymer film

The knowledge of the exact optical field within the polymer film is an important parameter in order to understand the SRG formation induced by the illumination with an IP. Dependent on the polarization of the two interfering beams intensity- or polarization-interference patterns are formed (see main text of this dissertation). The interplay of the light field with the polymer film is still unknown, e.g. how the SRG and BBG are influencing the writing field (interference pattern). Knowing this relation permits the optimization of the grating inscription process. A first attempt to model the electric field within the polymer film is shown in **Figure C.9**. Here, the reflection of the illuminating field at the plane polymer-air interface is taken into account, which results in an intensity modulation also inside the polymer film (standing wave in the bulk). The false colors are representing the strength of intensity modulation. Additionally, the absorption of the pump beam is also added. **Figure C.9a** is showing the result for a polarization interference pattern (SP-IP) and in (c) the field map for an intensity interference pattern (PP-IP) is presented. A mixed interference pattern (intensity- and polarization gradient) is generated by using a +45°- and 90°- (P) polarized pump beam. The electric field map of such an IP is shown in (b). The calculations are performed by Prof. Dr. Carsten Henkel (University of Potsdam).

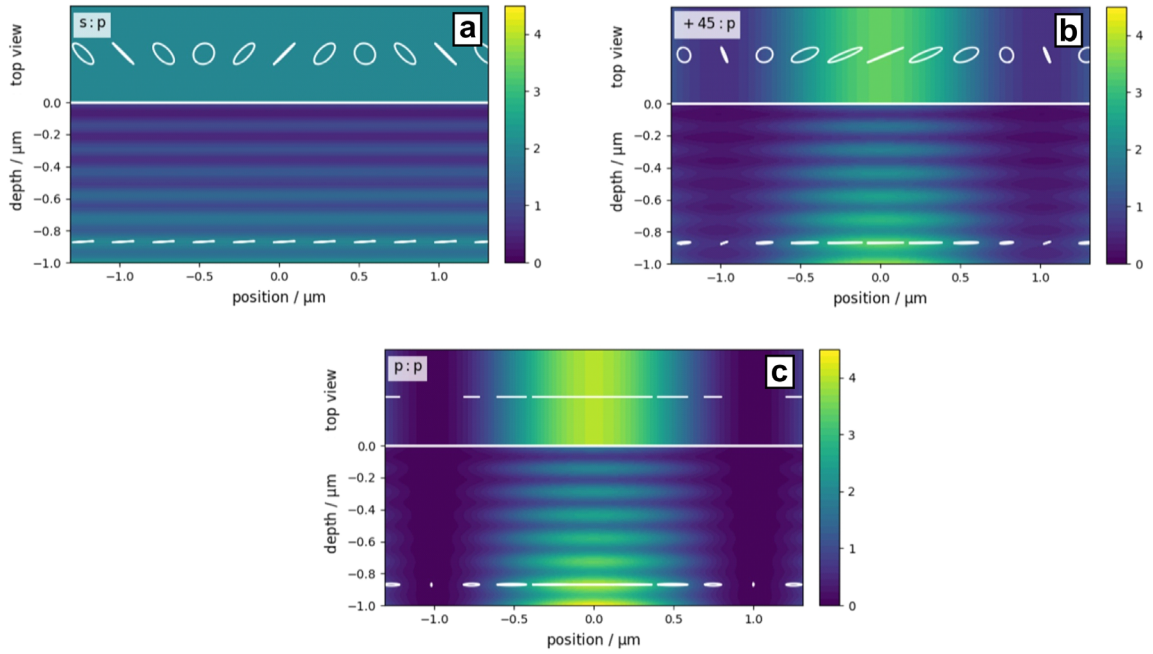

Figure C.9. Simulation of the electric field within the polymer film (field map) for different IPs assuming a reflection of the illuminating field (interference pattern) at the plane polymer-air interface. The reflected light is interfering with the illuminating field to a standing wave. Additionally, the absorption of the pump beam is also considered. The top part is showing the top view on the film surface and the lower part the cross-section though the film. The false colors indicate the intensity modulation and the white arrows the local polarization. (a) Field distribution in the case of an SP-IP (polarization interference pattern). Here, the intensity along the surface is constant only the polarization is changing with the grating period of the IP. (b) Field map for the +45:P-IP (mixed interference pattern made of an intensity- and polarization gradient). (c) Field map in the case of an intensity interference pattern (PP).

Mixed interference patterns

The two-beam interference set-up permits several different combinations in the polarization of the two interfering beams. Choosing a symmetric combination results in an intensity interference pattern with a sinusoidal intensity modulation (see **Figure C.10a**). For certain combinations a polarization interference pattern is formed with a constant intensity but the local polarization is changing along the grating period. The interference pattern generated by one linearly- and one circularly polarized pump beam is a mixed IP made of an intensity- and polarization variation. This permits to analyze the influence of a gradient in polarization and/or intensity on the SRG formation. The obtained results can help to optimize the surface

grating inscription on the polymer film. **Figure C.10a** shows the *in situ* recorded 1st-order DE (co-(red)- and cross-(blue)-polarized component) and SRG amplitude as a function of irradiation time for the illumination with an P:L-IP (one pump beam P- and the second one left-handed circularly polarized). A sinusoidal SRG is formed with a growth kinetics similar to the ±45- or RL-IP. The modulation amplitude has reached 230nm after 30min of irradiation. Taking a closer look to the field map (**Figure C.10c**) reveals that at the position of high intensity the light is elliptically polarized with an orientation along the grating vector. This is the explanation of the efficient SRG inscription, because from intensity interference patterns (PP-IP) it is known that a component of the polarization along the grating vector is required for an effective SRG formation. Additionally, the elliptical polarization is exiting the chromophores continuously, so that they only relax in the dark area of the IP.

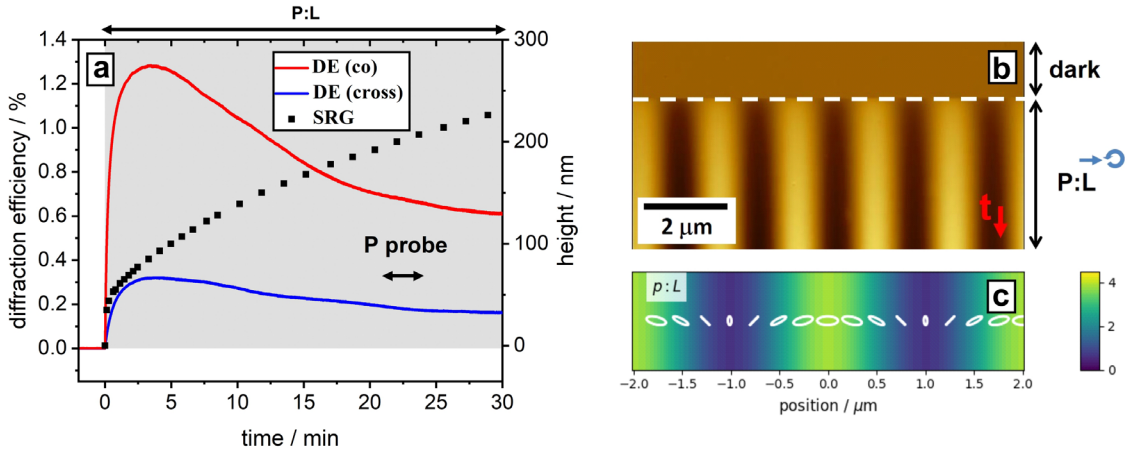

Figure C.10. (a) *In situ* recorded 1st-order DE (the red curve is showing the co-(P) and the blue curve the cross-(S) polarized component) and SRG amplitude (black dots) for the P:L-IP with a P-polarized probe beam (PAZO, same parameters as **Figure 3.1**). The grey rectangle marks the irradiation sequence of the polymer film. (b) *In situ* recorded AFM micrograph. The scanning starts at the top with a flat surface and at the time of the white dashed line the illumination with the P:L-IP is applied. (c) Calculated electric field map along the grating (top-view). In the P:L-IP the intensity (false colors) and the local polarization (white arrows) are spatially modulated.

Changing the orientation of the linearly polarized pump beam by 45° results in the +45:L-IP which is also a mixed interference pattern, showing an intensity- and polarization modulation (see **Figure C.11c**). Here, at the position of the intensity maximum the light is elliptically polarized with a +45° orientation. **Figure C.11b** is showing that also in the case of the

+45:L-IP a sinusoidal SRG is formed but with a slower growth kinetics compared to the P:L-IP, maybe because of the 45° orientation of the elliptical polarization in the bright areas of the IP. The SRG height has reached 250nm after 60min of illumination.

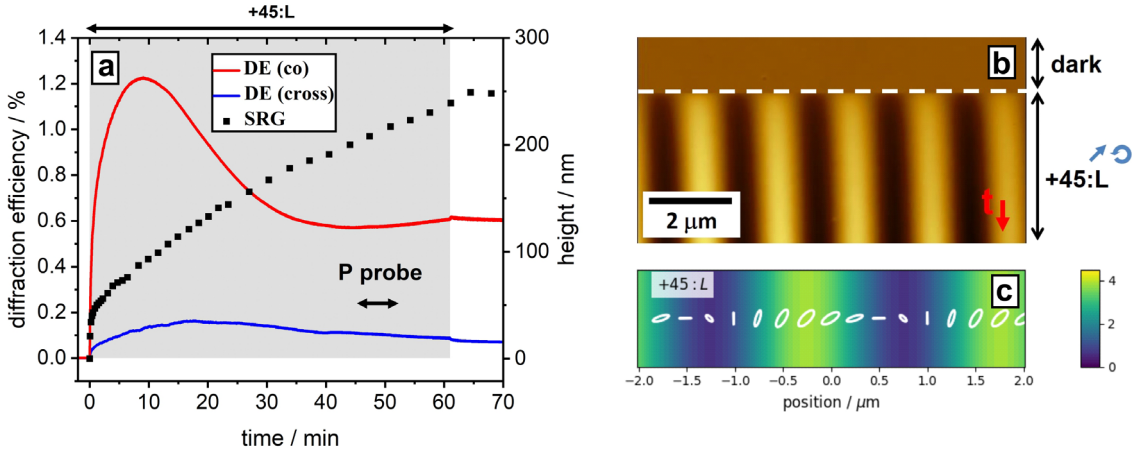

Figure C.11. (a) *In situ* recorded 1st-order DE (the red curve is showing the co-(P) and the blue curve the cross-(S)-polarized component) and SRG amplitude (black dots) for the +45:L-IP with a P-polarized probe beam (PAZO, same parameters as **Figure 3.1**). The grey rectangle marks the irradiation sequence of the polymer film. (b) *In situ* recorded AFM micrograph. The scanning starts at the top with a flat surface and at the time of the white dashed line the illumination with the +45:L-IP is applied. (c) Calculated electric field map along the grating (top-view). In the +45:L-IP the intensity (false colors) and the local polarization (white arrows) are spatially modulated.

A vertical polarized pump beam together with a LCP pump beam results in the S:L-IP. Here, the elliptically polarized light, located at the bright area of the IP, is oriented in vertical direction (perpendicular to the grating vector, see **Figure C.12c**). The illumination of the polymer film with such an IP shows an interesting effect in the starting of the exposure. The SRG amplitude is first rapidly increasing (see **Figure C.12a**) and drops down after 2min of irradiation (at the SRG height of 50nm). A minimum is reached after 25min of exposure. The SRG amplitude starts to increase afterwards and is reaching 150nm after 2h of illumination. The co-polarized component of the 1st-order DE (red curve in **Figure C.12a**) is mimicking the change in the topography, while the cross-polarized component (blue curve in **Figure C.12a**) increases fast until it saturates and starts to decrease afterwards. A translation of the SRG by half the grating period corresponds with the drop in the SRG amplitude (see **Figure C.12b**). This might indicate the interplay of two different processes.

The SRG, which appears within the first minutes of exposure, could be a result of the intensity modulation like in the case of an SS-IP. The second grating is formed by the competing effect of the grating formation by the intensity- and polarization modulation or an optical feedback. In the S:L-IP the elliptically polarized light in the bright area of the IP is oriented perpendicular to the grating vector. In the case of an intensity interference pattern (SS-IP) this results in a poor SRG amplitude and explains the slow kinetics in the case of the S:L-IP (as a result of the two competing SRGs).

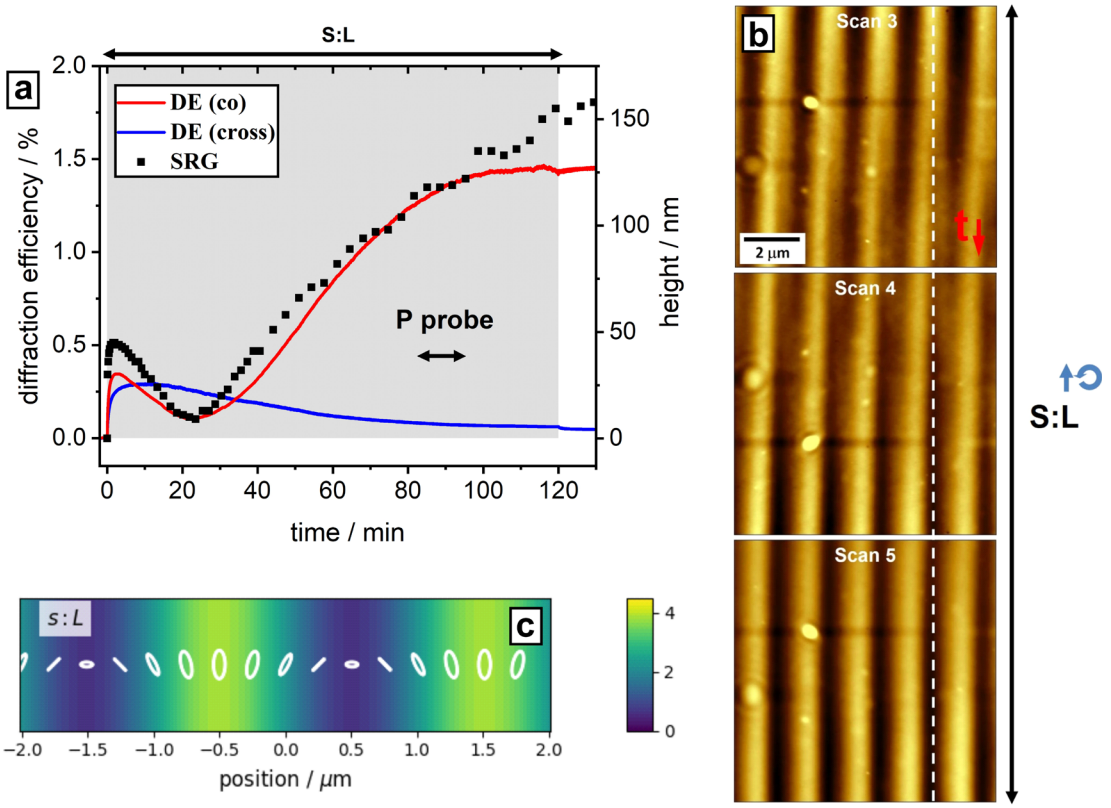

Figure C.12. (a) *In situ* recorded 1st-order DE (the red curve is showing the co-(P) and the blue curve the cross-(S) polarized component) and SRG amplitude (black dots) for the S:L-IP with a P-polarized probe beam (PAZO, same parameters as **Figure 3.1**). The grey rectangle marks the irradiation sequence of the polymer film. (b) *In situ* recorded AFM micrograph (Scan 3-5). The scanning starts at the top. A half-period drift of the SRG is observed with an increase in irradiation time. (c) Calculated electric field map along the grating (top-view). In the S:L-IP the intensity (false colors) and the local polarization (white arrows) are spatially modulated.

These data still have to get further analyzed but it may give the possibility to study the interplay of the SRG formation due to a gradient in local polarization and a gradient in intensity. Note, that the defects observed in the *in situ* AFM scan (**Figure C.12b**) are stationary, indicating the re-orientation of the bulk and not a mass transport over large distances. The SRG translation is a result of a change in the local polymer film deformation (similar to a transverse wave, up and down motion of the surface). A photo-induced stress is generated, which is inverting the grating formation (see also publication III and IV).

Low dose/fluence exposure

It is often reported, that no SRG is inscribed when the polymer film is exposed to the IP only for short time. That a certain minimum exposure time of more than 5s is required.[182] In order to further study the SRG formation in the case of low energy doses, the polymer film is exposed to several light pulses one by one and the DE and the SRG amplitude are probed in between. Additionally, this proves that the BBG appears first, followed by the SRG. **Figure C.13** shows the *in situ* recorded DE and SRG height for several 1s illumination pulses with the SS-IP. After the pulse the response of the SRG and DE is probed for 10s before the next 1s illumination pulse is applied. The SRG amplitude and DE are increasing as soon as the polymer film is exposed to light. The DE is decreasing in dark, indicating the relaxation of the BBG while the SRG amplitude is stable. During the first illumination pulse the SRG amplitude is increased by 15nn. The growth-rate slows down with exposure dose indicating the grating saturation. These results show that a SRG is inscribed on the polymer film even with an illumination pulse of one second using a moderate intensity ($I = 200\mathrm{mW/cm^2}$). The next step is the further reduction in illumination time in order to probe the time delay between the BBG- and SRG formation.

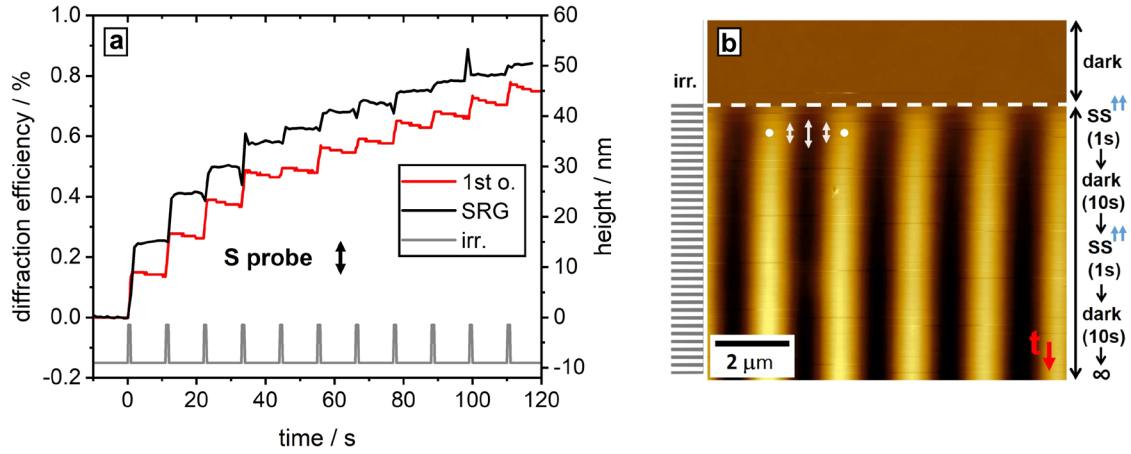

Figure C.13. (a) *In situ* recorded 1st-order DE (red curve) and SRG amplitude (black curve) of the pulsed illumination (1s) with a SS-IP (PAZO, same parameters as **Figure 3.1**). Afterwards the SRG amplitude and DE are probed for 10s in dark. The grey curve indicates the light exposure cycle. The DE and SRG amplitude are increasing as soon as the polymer film is illuminated. Once the light is switched off the DE is relaxing indicating the relaxation of the BBG while the SRG amplitude is constant. (b) *In situ* recorded AFM micrograph. The scanning starts at the top with a flat surface and the irradiation is switched on at the time of the white dashed line (the grey line on the left shows the irradiation cycle). The white arrows indicate the local polarization.

Figure C.14 shows the results for a pulsed illumination of the PAZO film with a polarization interference pattern (±45-IP) and two different polarizations of the probe beam. Here, the pulse length is changed to 1min of illumination and 3min of probing in dark due to the slow kinetics of the SRG and BBG.

The SRG and BBG are interfering constructively in 1st-order DE in the case of a P- polarized probe beam (see **Figure C.14b** and publication II). The DE is increasing as soon as the polymer film is illuminated and relaxes once the light is switched off. The growth kinetics slows down with an increase in exposure dose indicating the grating saturation. A destructive interference of the SRG and BBG in the 1st-order DE is observed using a S-polarized probe beam (see **Figure C.14a** and publication II). Here, right after the exposure the DE is increasing and relaxes in dark. The DE goes through a minimum in the following and increases again afterwards (with an increase in exposure dose). At this state the DE becomes noisy during the illumination pulse and increase slightly in dark, indicating the relaxation of the BBG because of the destructive interference.

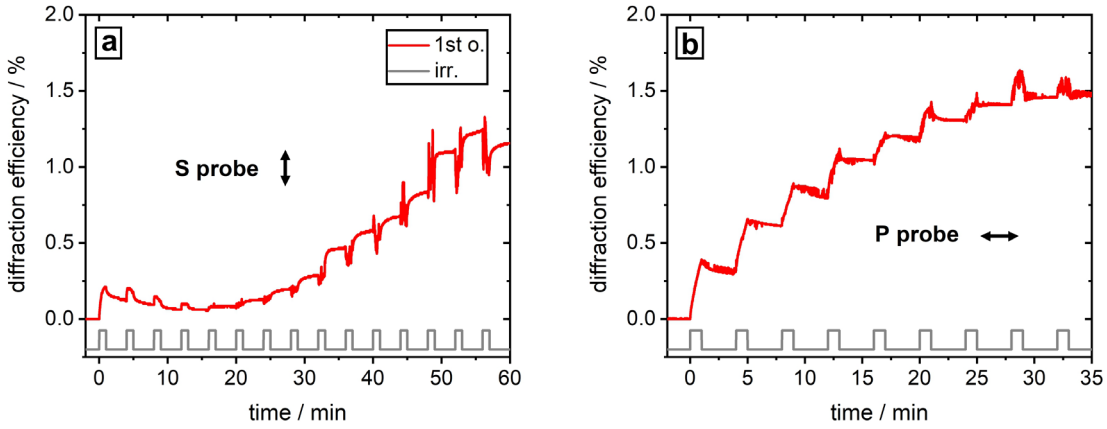

Figure C.14. *In situ* recorded 1st-order DE (red curve) in the case of a pulsed illumination of the PAZO film with a polarization interference pattern (±45-IP). The pulse length is 1min of irradiation and 3min of probing in dark (other parameters same as **Figure 3.1**). The grey curve indicates the light exposure cycle. In (a) the results for a S-polarized probe beam while in (b) the kinetics for a P polarization of the probe beam are shown.

In publication V it is shown that the SP-IP is the only interference pattern generating a surface grating with a period which is half the period of the IP. The 1st-order DE contains only the BBG, while the 2nd-order DE additionally gives information about the SRG. Therefore, it is of high interest to study the grating formation in the case of the SP-IP using pulsed illumination, because it permits the direct separation of the SRG and BBG kinetics. **Figure C.15a** shows the *in situ* recorded 1st- (red curve) and 2nd- (blue curve) order DE as well as the SRG amplitude (black curve) in the case of a pulsed illumination with the SP-IP (20s illumination, 80s dark). The diffraction efficiency and the SRG amplitude are increasing immediately after the exposure of the polymer film to light. The 1st-order DE is relaxing once the illumination is switched off indicating the relaxing of the BBG, while the SRG amplitude is almost constant. After five illumination cycles the amplitude of the BBG is already saturated, while the SRG amplitude, as well as the 2nd-order DE, is further increasing. This indicates a certain delay of the SRG formation on the photo-orientation. A change in the 2nd-order DE is observed for larger energy doses. During the first illumination pulses the 2nd-order DE is increasing once the illumination is applied. This behavior is inverted with time. Then, the DE is decreasing when the polymer film is illuminated and increasing after the light is switched off. This is the opposite behavior in respect to the 1st-order DE.

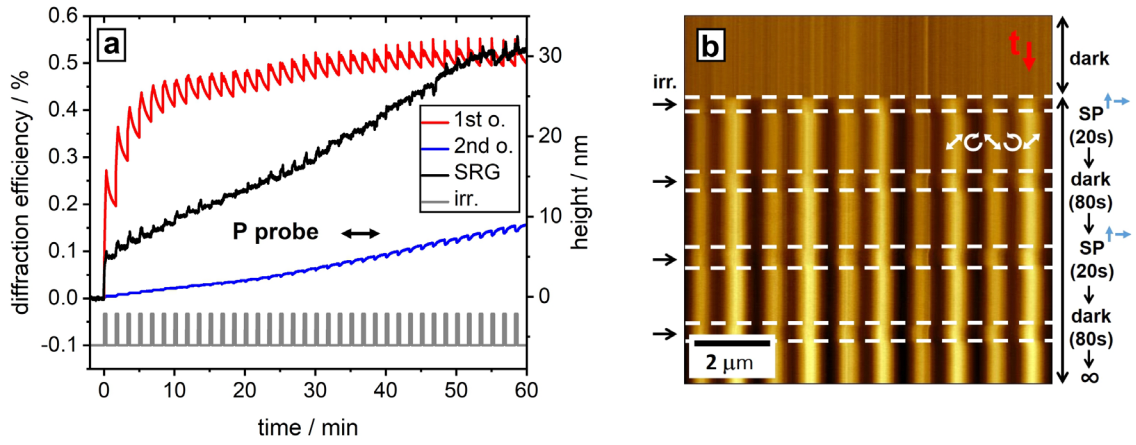

Figure C.15. (a) *In situ* recorded DE and SRG amplitude (black line) for pulsed illumination (20s) of the PAZO film with the SP-IP (same parameters as **Figure 3.1**). Afterwards the SRG amplitude and DE are probed for 80s in dark. The red curve is showing the 1st- and the blue curve the 2nd-order DE. The grey curve indicates the light exposure cycle. The DE and SRG amplitude are increasing as soon as the polymer film is exposed to light. After the light is switched off the 1st-order DE is relaxing while the SRG height is almost constant. The BBG (1st-order DE) is saturating after the first five illumination cycles while the SRG amplitude and 2nd-order DE are continuously increasing. In (b) the *in situ* recorded AFM micrograph is shown. The scanning starts at the top with a flat surface and the irradiation is switched on at the time of the first white dashed line. The black arrows on the side indicate the irradiation of the polymer film.

Changing the interference pattern during inscription

The re-orientation dynamics of the azobenzene-chromophores is beside the grating inscription kinetics of special interest. It is studied in different ways, e.g. like in publication III and IV due to several write and erase cycles. The translation of the RL-IP by half the grating period corresponds with a rotation of the local polarization, as well as the azobenzene-chromophores, by 90°. Here, the re-orientation of the chromophores generates strong photo-induced stresses resulting in the formation of an inverted SRG. The intensity for this polarization interference pattern is constant along the grating period.

The re-orientation dynamics in the case of intensity interference pattern is studied by the fast switching between the SS- and PP-IP. Here, the intensity is sinusoidal modulated and the chromophores are re-aligned by 90° as soon as the IP is changed. The fast switching between the IP is achieved by integrating a Pockels cell in the optical path of each beam of the two-

beam interference set-up. The polymer film is illuminated with the SS-IP without applied voltage on the Pockels cell. The PP-IP is irradiating the film once the half-wave-voltage is used to drive the Pockels cell. **Figure C.16** shows the results of such a fast switching experiment for a P- (a) or S- (b) polarized probe beam. In the case of a P-polarized probe beam SRG and DE are increasing when the polymer film is exposed to the SS-IP, but the increase in DE is rather slow due to the destructive interference of SRG and BBG in the total DE. This is changed as soon as the film is illuminated with a PP-IP. Here, the SRG amplitude is still but slowly increasing while the DE rapidly increases due to the change to constructive interference of the SRG and BBG in the 1st-order DE as a result of the fast photo-orientation. The change in the IP is not resulting in a translation of the SRG. Switching back to the SS-IP shows, that the SRG amplitude is not further increasing because the surface grating is already saturated. The DE rapidly decreases and saturates fast due to the change to destructive interference. The second exposure to the PP-IP is increasing the SRG amplitude again, because the surface grating is not yet saturated for this IP. The DE is also increasing again because of the change to constructive interference of the SRG and BBG as well as the increasing modulation amplitude of the surface grating. The same experiment is performed with an S-polarized probe beam (see **Figure C.16b**). Here, the SRG and BBG are interfering constructively in the DE using the SS-IP for the illumination. The change to the PP-IP results in a destructive interference and a drop in DE until the signal saturates while the SRG amplitude is still increasing. The second irradiation with the SS-IP is increasing the DE again due to the symmetric coupling of SRG and BBG in the DE. The repeated illumination with the PP-IP results in a destructive interference (drop of DE in the beginning) and an increase of the DE as soon as the SRG amplitude is rising. These results show that the probe beam polarization is an important parameter in the interpretation of the recorded DE. Additionally, it demonstrates the fast re-orientation of the azobenzene-chromophores in the case of an intensity interference pattern.

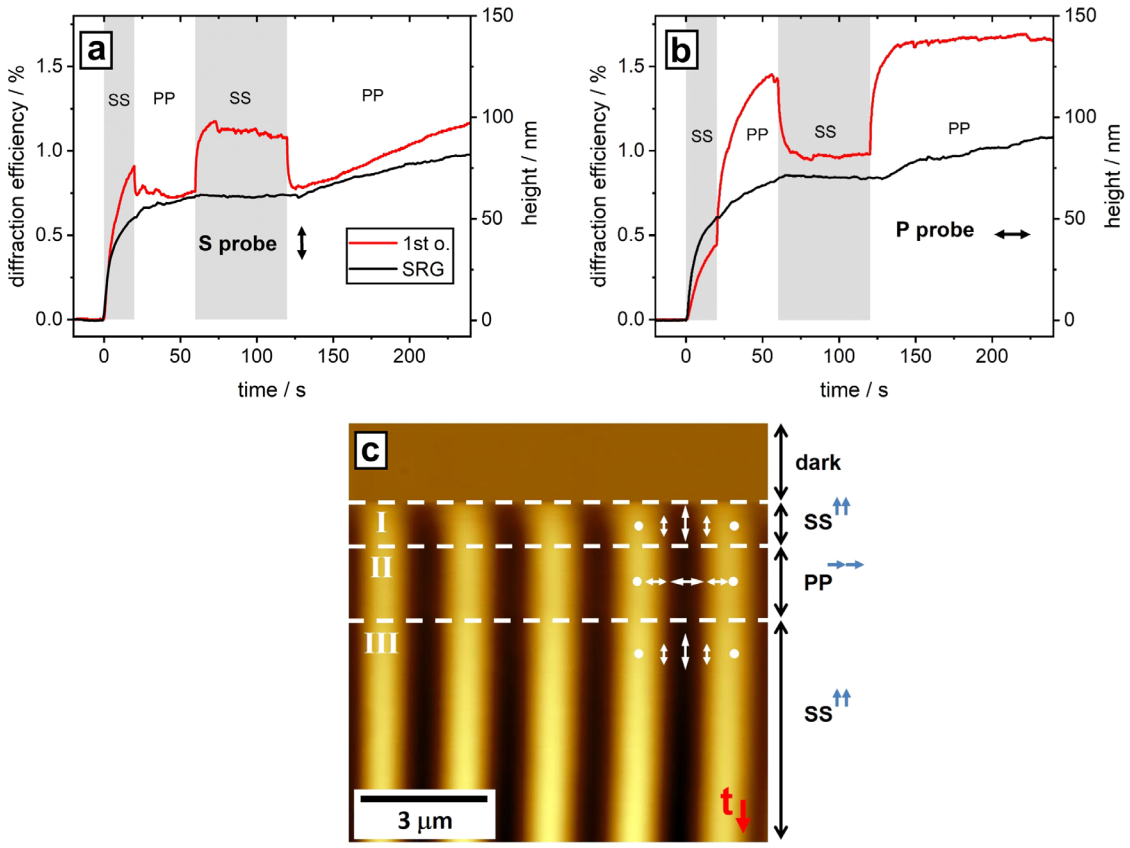

Figure C.16. *In situ* recorded 1st-order DE (red curve) and SRG height (black line) in the case of a fast switching between two intensity interference patterns (SS- and PP-IP). In (a) the results for a S- and in (b) for a P-polarized probe beam are shown (PAZO, same parameters as **Figure 3.1**). The grey rectangles indicate the exposure to the SS-IP. (c) *In situ* recorded AFM micrograph. The scanning starts at the top with a flat surface. The irradiation with a SS-IP is switched on at the time of the 1st white dashed line. At the time of the 2nd white dashed line the IP pattern is changed to PP-IP and at the 3rd white dashed line the polymer film is exposed again to a SS-IP. The white arrows indicate the local polarization.

Translating an intensity interference pattern is changing the local intensity but is not affecting the local polarization. This is in contrast to the other experiments from above (fast switching between intensity interference patterns and translation of a polarization interference pattern). **Figure C.17** shows the results of such an intensity shifting experiment in the case of an SS-IP. The polymer film is fist irradiated for 8s with the IP which results in a SRG of 50nm in height and a strong 1st-order DE signal. These two signals are decreasing as soon as the IP is translated by half the grating period. The DE goes through a minimum corresponding with a drift of the surface grating. The former maximum of the SRG splits up into two maxima and they are combining with the one next to them. The new common

maximum is shifted by half the grating period. At the same time also the DE starts increasing again but with a slower kinetics compared to the first writing process. The exposure of the polymer film to a sinusoidal intensity modulation aligns the azobenzene-chromophores perpendicular to the local polarization only in the bright areas of the IP. In the minimum of the intensity modulation (SRG maximum) the chromophores are still isotropic distributed. The half-period translation of the IP aligns the previously unexposed regions of the polymer film. This process is rather slow but results also in an inverted SRG due to the generation of strong photo-induced forces. In this method the orientation of the linearly polarized components of the light field are not changed only the absolute value of the local intensity. The mechanical stresses induced by the orientation in the bright areas are disturbing the orientation in the dark areas which might be the origin of the inverted SRG.

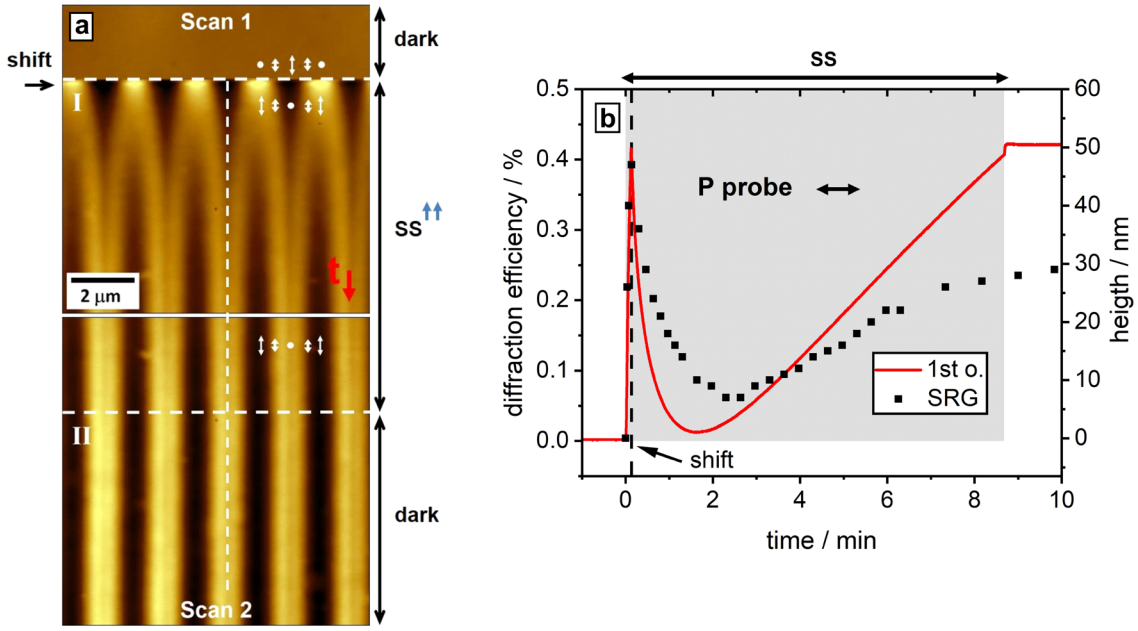

Figure C.17. (a) *In situ* recorded AFM micrograph in the case of a translation of the SS-IP (PAZO, same parameters as **Figure 3.1**). The scanning starts at the top with a flat surface and the irradiation is switched on at the time of the 1st white dashed line. After 8s of irradiation the IP is translated by half the grating period (indicated by the small black arrow at the side). At the time of the 2nd white dashed line the illumination is switched off. The local polarization is indicated by the white arrows. (b) *In situ* recorded 1st-order DE (red curve) and SRG amplitude (black dots) for the half-period translation of an intensity interference pattern (SS-IP). The grey rectangle marks the irradiation of the polymer film.

Summarizing the last three experiments: In the case of a half-period translation of a polarization interference pattern, the local polarization is rotated by 90° but the intensity is constant. The re-orientation of the azobenzene-chromophores in the bulk is generating strong photo-induced stresses, which are inverting the SRG formation. The fast switching between intensity interference patterns (SS- to PP-IP and vice versa) results in the cyclic re-orientation of the chromophores by 90°, which is not affecting the SRG position. Additionally, the intensity is sinusoidal modulated. The translation of an intensity interference pattern by half the grating period results in a change of the local intensity but the local polarization of the IP is not affected. Nevertheless, the SRG starts to drift after the translation of the IP. These three different experiments probe the SRG formation and re-orientation of the azobenzene-chromophores in the bulk under different constraints (I: constant intensity but gradient in local polarization, II: gradient in intensity and polarization, III: gradient in intensity but constant local polarization).

The assignment of the local polarization with respect to the SRG and BBG in the case of polarization interference patterns is usually done by the *in situ* change from an intensity interference pattern to a polarization interference pattern (see also publication V). **Figure C.18** shows the results of such a change from SS- to ±45-IP for different polarizations of the probe beam. The assignment in the case of the intensity interference pattern is done by performing the illumination of the polymer film through a mask. The direction of the photo-induce deformation is obtained from an AFM-scan performed after the light exposure. At the position of high intensity the PAZO film shows a dent, indicating a deformation away from the regions of high intensity. This information is used for the assignment of the local polarization with respect to the SRG and BBG in the case of the illumination with a polarization interference pattern (±45-IP, see **Figure C.18**). The SRG height is increasing during the illumination with a SS-IP but as soon as the IP is changed to the ±45-IP the amplitude is decreasing corresponding with a half-period translation of the SRG. The grating amplitude recovers again with an increase in the exposure time. The 1^{st}-order DE is increasing during the illumination with the SS-IP (for 20s) but as soon as the IP is changed to the ±45-IP it starts to decrease. A constructive interference of the SRG and BBG in the DE appears in the case of a S-polarized probe beam and the illumination with the SS-IP. These two gratings interfere destructively using a P-polarized probe beam, which results in a lower absolute value of the DE (see **Figure C.18c**). After the change to the ±45-IP the DE goes through a minimum for both polarizations of the probe beam. A certain delay between the SRG and DE signal is observed dependent on the polarization of the probe beam and is explained by the difference in the interplay of these two gratings in the DE. The change of the IP from SS to ±45 results in the case of a S-polarized probe beam in the switching from constructive- to destructive interference of the SRG and BBG. These two gratings interfere destructively in the case of an SS-IP and constructively using an ±45-IP for the illumination and a P-polarized probe beam.

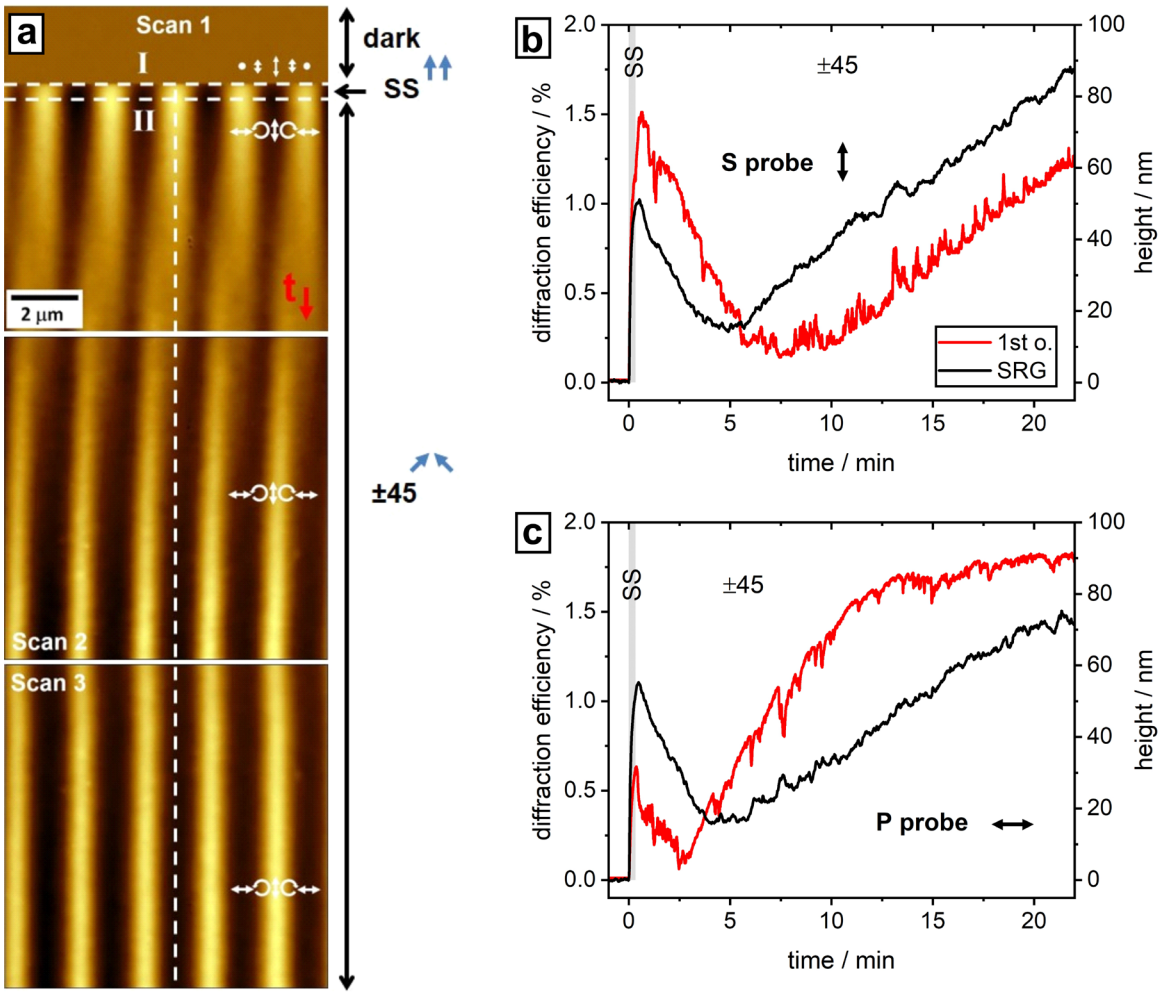

Figure C.18. (a) *In situ* recorded AFM micrograph of the change from an intensity- to a polarization IP (from SS to ±45). The scanning starts at the top and at the position of the 1st white dashed line (I) the illumination with the SS-IP is started. At the position of the 2nd white dashed line (II) the illumination is changed to the ±45-IP. The SRG is translated by half the grating period after the change in the IP. The local polarization is indicated by the white arrows. The *in situ* recorded 1st-order DE (red curve) and SRG amplitude (black curve) as a function of irradiation time for an S- or P-polarized probe beam are shown in (b) and (c). The grey rectangle indicates the illumination with the SS-IP. The SRG amplitude is increasing as long as the sample is irradiated with an SS-IP. After the change to the ±45-IP the amplitude is decreasing to 20nm until it starts to increase again, corresponding with a SRG translation by half the grating period. The 1st-order DE shows a certain offset with respect to the SRG amplitude dependent on the polarization of the probe beam (PAZO, same parameters as **Figure 3.1**).

In the new developed set-up the diffraction efficiency is recorded in reflection geometry, due to the integrated AFM. **Figure C.19** is comparing the 1st-order DE measured in transmission- (blue curve) and reflection (red curve) configuration. The DE recorded in transmission is continuously increasing, while the DE measured in reflection is first increasing and then starts to decrease. The explanation for this different behavior of the diffraction efficiency is a strong phase modulation in the case of the reflection geometry, because the light is traveling twice through the material. On the other hand, also the absolute value differs, because more light is forward than backward scattered, resulting in a higher DE in the transmission geometry.

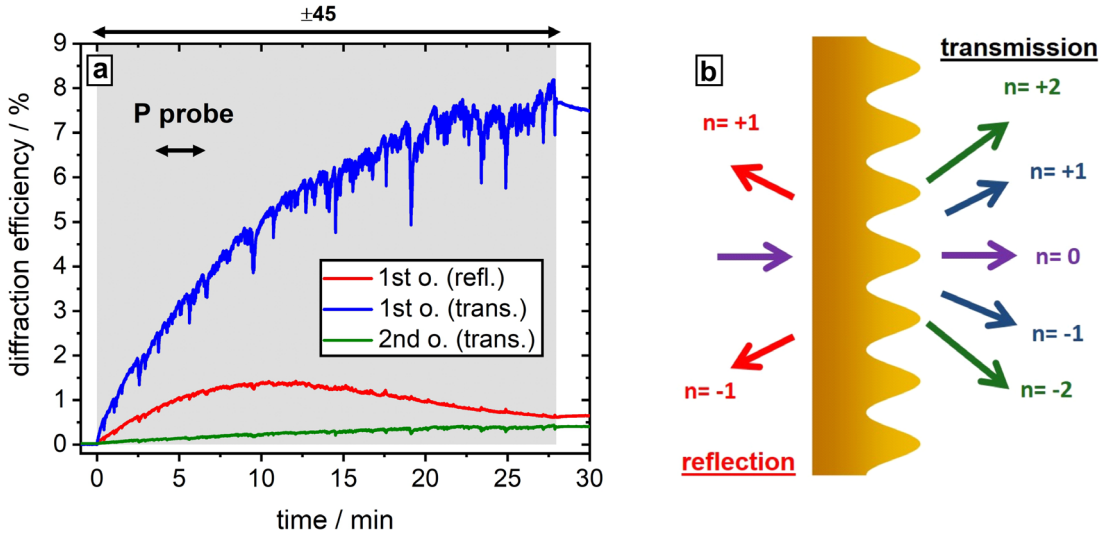

Figure C.19. (a) *In situ* recorded DE in transmission- and reflection geometry during the illumination with a ±45-IP and using a P-polarized probe beam (PAZO, same parameters as **Figure 3.1**). The grey rectangle indicates the illumination. The blue curve is showing the 1st-order DE and the green the 2nd-order DE measured in transmission geometry. The red curve is the corresponding 1st-order DE recorded in reflection geometry. (b) The sketch is explaining the DE recording geometry for the results presented in (a).

The SRG inscription is very sensitive to small changes in the illumination parameters (changes in the IP). **Figure C.20** is showing the difference in the 1st-order DE (the blue curve is representing the cross-(S) and the red curve the co-(P) polarized component) for the illumination with a ±45-IP and a P-polarized probe beam without (a) and with (b) a covered set-up. The DE signal is very noisy without encapsulation (a). Applying the cover results in

a smooth signal (b). A small air flow, produced by the air condition, is reaching the set-up in the case without a cover. This stream results in small density fluctuations which are causing a phase shift between the two interfering beams. As a result, the IP is not stable during the illumination which creates the small fluctuations of the DE. The noise disappears as soon as the pump beam is switched off. These fluctuations are very pronounced for polarization interference patterns and less for intensity interference patterns. This shows that the system is very sensitive to small changes in the environment and is the reason why it is very important to cover the set-up. Additionally, the homemade encapsulation of the set-up, produced by Florian Dornack in the workshop, permits to keep the room light switched on during the experiment.

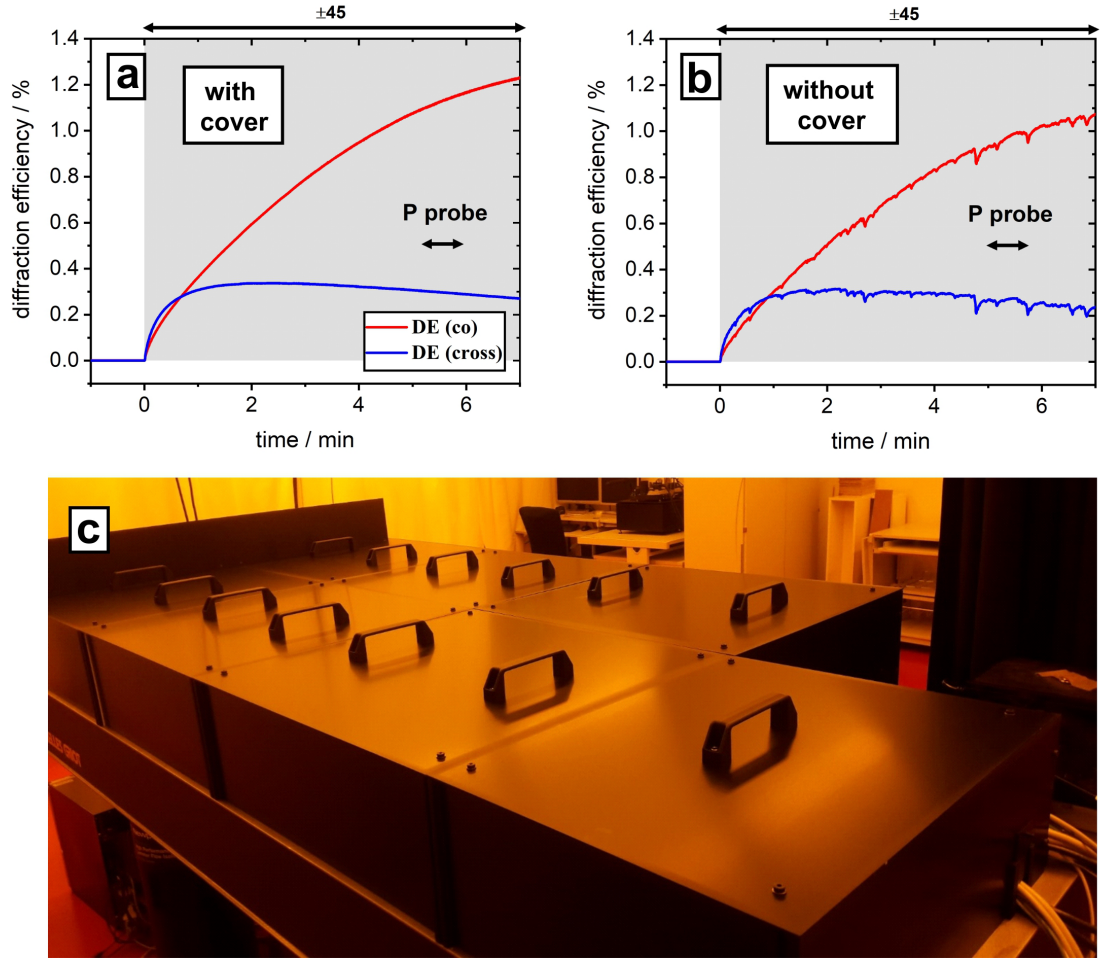

Figure C.20. Dependence of the 1st-order DE (red curve shows the co-(P)- and the blue curve the cross-(S)- polarized component) on the environment in the case of irradiation with the ±45-IP. In (a) the set-up is covered. (b) Recorded DE without encapsulation. The probe beam is P-polarized (PAZO, same parameters as **Figure 3.1**). The grey rectangle indicates the illumination. (c) Photo of the homemade encapsulation of the set-up.

D. Probing the mass transport

In order to address the question if the SRG is formed due to a large scale mass transport several different experiments are performed. Additionally, it is still unknown if the mass transport appears only on the surface or also in the bulk of the polymer film. Therefore, a scratch within the polymer film is made and afterwards the height is measured on the left- ($d_{left} = 474\text{nm}$) and right ($d_{right} = 480\text{nm}$) side of the scratch. The continuous translation of the RL-IP parallel to the scratch (with the help of the integrated piezo stack, which creates an SRG with grooves parallel to the scratch) in such a way that the SRG can follow, should result in a continuous mass transport (also in the bulk) in the direction of the IP translation according to the mass transport hypothesis (see also publication III). This may result in a different height of the polymer film on the left- (side form where the material is taken) and right side (side where the material is deposited) of the scratch. Surprisingly, the AFM scan reveals that there is no significant difference in the height before and after the exposure to the IP (see table in **Figure D.1c**).

The polymer film thickness is only slightly reduced, indicating that the mass transport in the bulk appears only over short distances. Moreover, the grating translation is interpreted as a cyclic re-orientation of the azobenzene-chromophores in the bulk which results in the local mass transport forming the SRG. The polymer chains orient and migrate only on the length scale of half the grating period. Then, the SRG behaves under shifting conditions like a transversal wave, indicating that the position of the polymer chains is almost fixed (up and down motion of the polymer surface). On the other hand, it is observed that the width of the structure is reduced by 5µm after the illumination. This may indicate a stretching of the polymer film.

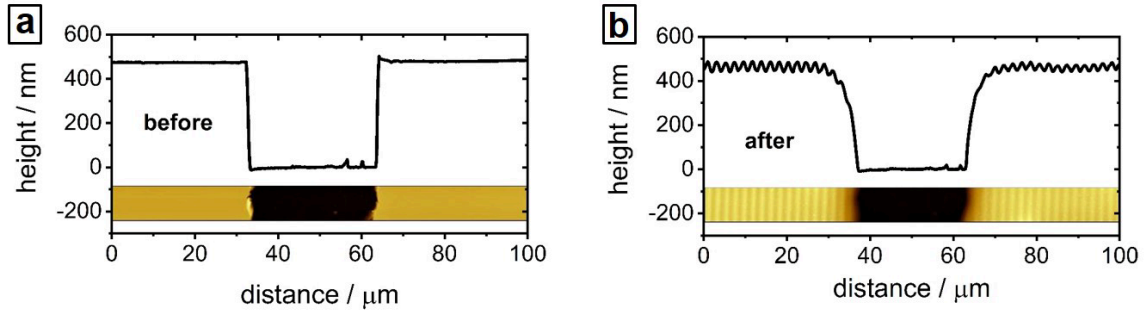

c	height left	height right	width
before	474nm	480nm	30µm
after	439nm (min.) 485nm (max.) 462nm (av.)	452nm (min.) 482nm (max.) 467nm (av.)	25µm

Figure D.1. *Ex situ* AFM micrographs in order to address the question of a macroscopic mass transport. The experiment is as follows: first a scratch is made within the polymer film (PDR1) in order to measure the thickness on the left- and right side of the structure before illumination (a). The SRG is inscribed afterwards and the RL-IP is continuously translated parallel to the nano-structure for one hour (which creates an SRG with grooves parallel to the scratch, same parameters as **Figure 3.1**). In this way the SRG is able to follow the grating translation which might result in a large scale mass transport. Afterwards the height is measured again (b). The results of this experiment are summarized in a table (c). The width of the structure is reduced by 5µm after the illumination but the film thickness on the left- and right side of the scratch is almost unchanged.

The mass transport is also addressed in another experiment. Here, a Ag-mask (200nm thickness) is prepared with a slit of 60µm in width. The back side of this mask is covered with the photo-sensitive polymer. Afterwards the sample is exposed to the RL-IP through the mask. An SRG, aligned along the slit, is only generated in the areas without metal coating. The translation of the IP perpendicular to the micro-structure (with the help of a piezo stack) in such a way that the SRG is able to follow, may result in a macroscopic mass transport. As a result, a trench should appears on the side from where the material is taken and a hill on the opposite side, indicating the deposition of the material. **Figure D.2b** shows the *ex situ* performed AFM micrograph of the experiment described above after the exposure of the polymer film to the light (shift of the IP for 1hour and 14µm). In (a) the IP is not

shifted. Comparing these two result may indicate that in the case of the grating translation (b) a trench on the left side is formed, while a small hill is observed on the right side. Unfortunately, these features are not pronounced. A small trench appears also on the right side. Together with the results of the previous experiment this may also indicate, that a large scale macroscopic mass transport is not happening.

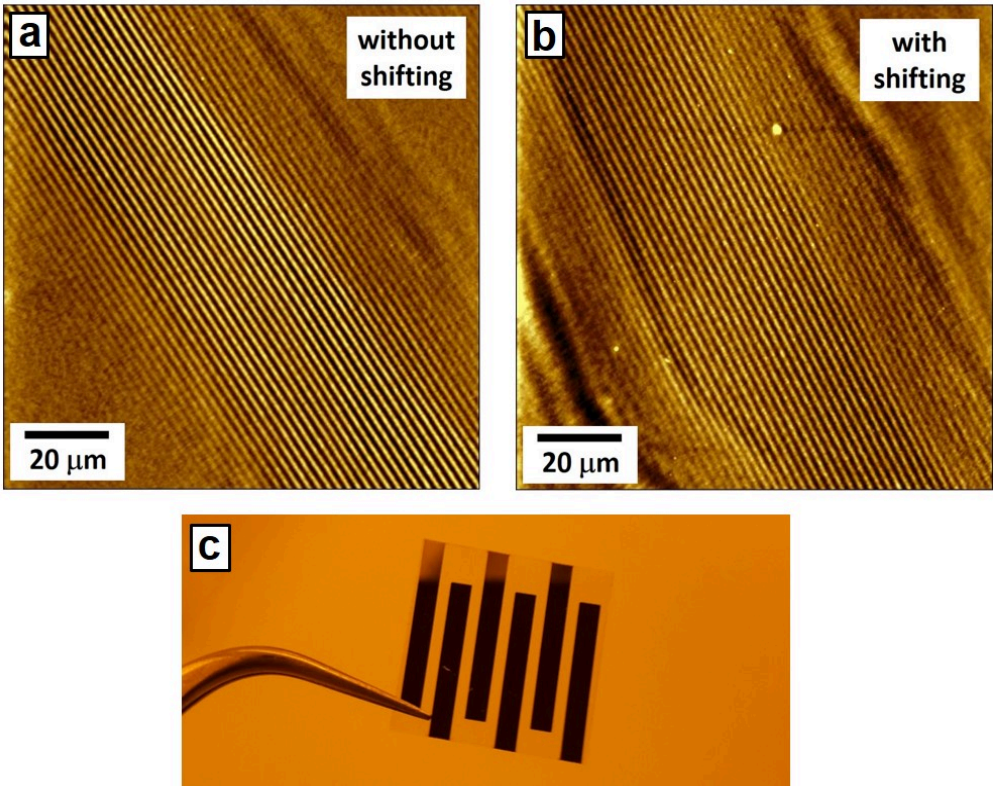

Figure D.2. *Ex situ* AFM micrographs in order to address the question of a large scale macroscopic mass transport. The experiment is as follows: A Ag-mask is back side covered with a 1µm thick PAZO film. Afterwards the film is exposed to the RL-IP. This creates a SRG along the micro-structure (a). The translation of the IP might result in a macroscopic mass transport and should create a trench at the side from where the material is taken and a hill on the opposite side (deposition of the material). In (b) the AFM micrograph of such an experiment is presented (PAZO, shifting for one hour and 14µm, same parameters as **Figure 3.1**). A photo of the uncoated Ag-mask is shown in (c).

Bibliography

1. Zarrintaj, P. *et al.* Thermo-sensitive polymers in medicine: A review. *Eur. Polym. J.* **117**, 402–423 (2019).
2. Karimi, M. *et al.* Temperature-Responsive Smart Nanocarriers for Delivery of Therapeutic Agents: Applications and Recent Advances. *ACS Appl. Mater. Interfaces* **8**, 21107–21133 (2016).
3. Yavuz, M. S. *et al.* Gold nanocages covered by smart polymers for controlled release with near-infrared light. *Nat. Mater.* **8**, 935–939 (2009).
4. Lendlein, A. & Kelch, S. Shape-Memory Effect From permanent shape. *Angew. Chem. Int. Ed. Engl.* **41**, 2034–2057 (2002).
5. Kocak, G., Tuncer, C. & Bütün, V. PH-Responsive polymers. *Polym. Chem.* **8**, 144–176 (2017).
6. Zhu, D. *et al.* PH-responsive drug release from porous zinc sulfide nanospheres based on coordination bonding. *RSC Adv.* **4**, 33391–33398 (2014).
7. Gupta, P., Vermani, K. & Garg, S. Hydrogels: From controlled release to pH-responsive drug delivery. *Drug Discov. Today* **7**, 569–579 (2002).
8. König, T. *et al.* Reversible structuring of photosensitive polymer films by surface plasmon near field radiation. *Soft Matter* **7**, 4174–4178 (2011).
9. Yin, S. N., Wang, C. F., Liu, S. S. & Chen, S. Facile fabrication of tunable colloidal photonic crystal hydrogel supraballs toward a colorimetric humidity sensor. *J. Mater. Chem. C* **1**, 4685–4690 (2013).
10. Fuller, E. G. *et al.* Externally Triggered Heat and Drug Release from Magnetically Controlled Nanocarriers. *ACS Appl. Polym. Mater.* **1**, 211–220 (2019).
11. Liu, T. Y., Hu, S. H., Liu, K. H., Liu, D. M. & Chen, S. Y. Preparation and characterization of smart magnetic hydrogels and its use for drug release. *J. Magn. Magn. Mater.* **304**, 397–399 (2006).
12. Camponeschi, E., Vance, R., Al-Haik, M., Garmestani, H. & Tannenbaum, R. Properties of carbon nanotube-polymer composites aligned in a magnetic field. *Carbon N. Y.* **45**, 2037–2046 (2007).
13. Li, Y. *et al.* Magnetic hydrogels and their potential biomedical applications. *Adv. Funct. Mater.* **23**, 660–672 (2013).
14. Mirfakhrai, T., Madden, J. D. W. & Baughman, R. H. Polymer artificial muscles. *Mater. Today* **10**, 30–38 (2007).
15. Shiga, T. & Kurauchi, T. Deformation of polyelectrolyte gels under the influence of electric field. *J. Appl. Polym. Sci.* **39**, 2305–2320 (1990).
16. Jeong, S., Park, S. J., Shin, M. S. & Kim, S. I. Characteristics of electrical responsive chitosan/polyallylamine interpenetrating polymer network hydrogel. *J.*

Appl. Polym. Sci. **86**, 2290–2295 (2002).

17. Kim, S. J. *et al.* Behavior in electric fields of smart hydrogels with potential application as bio-inspired actuators. *Smart Mater. Struct.* **14**, 511–514 (2005).

18. del Barrio, J. & Sánchez-Somolinos, C. Light to Shape the Future: From Photolithography to 4D Printing. *Adv. Opt. Mater.* **7**, 1900598 (2019).

19. Yoon, J., Kim, K. & Park, W. Modulated grayscale UV pattern for uniform photopolymerization based on a digital micromirror device system. *Appl. Phys. Lett.* **111**, 033505 (2017).

20. Carbonell, C. *et al.* Polymer brush hypersurface photolithography. *Nat. Commun.* **11**, 1–8 (2020).

21. Habault, D., Zhang, H. & Zhao, Y. Light-triggered self-healing and shape-memory polymers. *Chem. Soc. Rev.* **42**, 7244–7256 (2013).

22. Zhong, H. Y. *et al.* Azobenzene-containing liquid crystalline polyester with π-π interactions: diverse thermo- and photo-responsive behaviours. *J. Mater. Chem. C* **5**, 3306–3314 (2017).

23. Abdallh, M., Hearn, M. T. W., Simon, G. P. & Saito, K. Light triggered self-healing of polyacrylate polymers crosslinked with 7-methacryloyoxycoumarin crosslinker. *Polym. Chem.* **8**, 5875–5883 (2017).

24. Feldmann, D., Arya, P., Lomadze, N., Kopyshev, A. & Santer, S. Light-driven motion of self-propelled porous Janus particles. *Appl. Phys. Lett.* **115**, 263701 (2019).

25. Palagi, S. *et al.* Structured light enables biomimetic swimming and versatile locomotion of photoresponsive soft microrobots. *Nat. Mater.* **15**, 647–653 (2016).

26. Shahsavan, H. *et al.* Bioinspired underwater locomotion of light-driven liquid crystal gels. *Proc. Natl. Acad. Sci. U. S. A.* **117**, 5125–5133 (2020).

27. Singh, D. P., Uspal, W. E., Popescu, M. N., Wilson, L. G. & Fischer, P. Photogravitactic Microswimmers. *Adv. Funct. Mater.* **28**, 1–10 (2018).

28. Dicker, M. P. M. *et al.* Light-triggered soft artificial muscles: Molecular-level amplification of actuation control signals. *Sci. Rep.* **7**, 1–8 (2017).

29. Liles, K. P. *et al.* Photoredox-Based Actuation of an Artificial Molecular Muscle. *Macromol. Rapid Commun.* **39**, 1–7 (2018).

30. Han, B. *et al.* Plasmonic-Assisted Graphene Oxide Artificial Muscles. *Adv. Mater.* **31**, 1–7 (2019).

31. Dübner, M., Naoum, M. E., Spencer, N. D. & Padeste, C. From pH- to Light-Response: Postpolymerization Modification of Polymer Brushes Grafted onto Microporous Polymeric Membranes. *ACS Omega* **2**, 455–461 (2017).

32. Jelken, J., Pandiyarajan, C. K., Genzer, J., Lomadze, N. & Santer, S. Fabrication of Flexible Hydrogel Sheets Featuring Periodically Spaced Circular Holes with Continuously Adjustable Size in Real Time. *ACS Appl. Mater. Interfaces* **10**,

30844–30851 (2018).

33. Hvilsted, S., Sánchez, C. & Alcalá., R. The volume holographic optical storage potential in azobenzene containing polymers. *J. Mater. Chem.* **19**, 6641–6648 (2009).

34. Liu, S. *et al.* UV-resistant holographic data storage in noble-metal/semiconductor nanocomposite films with electron-acceptors. *Opt. Mater. Express* **8**, 1143 (2018).

35. Arya, P., Jelken, J., Lomadze, N., Santer, S. & Bekir, M. Kinetics of photo-isomerization of azobenzene containing surfactants. *J. Chem. Phys.* **152**, 024904 (2020).

36. Beharry, A. A. & Woolley, G. A. Azobenzene photoswitches for biomolecules. *Chem. Soc. Rev.* **40**, 4422–4437 (2011).

37. Klajn, R. Spiropyran-based dynamic materials. *Chem. Soc. Rev.* **43**, 148–184 (2014).

38. Gossweiler, G. R. *et al.* Mechanochemical activation of covalent bonds in polymers with full and repeatable macroscopic shape recovery. *ACS Macro Lett.* **3**, 216–219 (2014).

39. Li, M., Zhang, Q., Zhou, Y. N. & Zhu, S. Let spiropyran help polymers feel force! *Prog. Polym. Sci.* **79**, 26–39 (2018).

40. Waldeck, D. H. Photoisomerization Dynamics of Stilbenes. *Chem. Rev.* **91**, 415–436 (1991).

41. Waldeck, D. H. Photoisomerization dynamics of stilbenes in polar solvents. *J. Mol. Liq.* **57**, 127–148 (1993).

42. Lubbe, A. S., Szymanski, W. & Feringa, B. L. Recent developments in reversible photoregulation of oligonucleotide structure and function. *Chem. Soc. Rev.* **46**, 1052–1079 (2017).

43. Irie, M. Diarylethenes for Memories and Switches. *Chem. Rev.* **100**, 1685–1716 (2000).

44. Irie, M. Discovery and development of photochromic diarylethenes. *Pure Appl. Chem.* **87**, 617–626 (2015).

45. Wani, O. M., Zeng, H. & Priimagi, A. A light-driven artificial flytrap. *Nat. Commun.* **8**, 1–7 (2017).

46. Zeng, H., Wani, O. M., Wasylczyk, P., Kaczmarek, R. & Priimagi, A. Self-Regulating Iris Based on Light-Actuated Liquid Crystal Elastomer. *Adv. Mater.* **29**, 1–7 (2017).

47. Zeng, H., Wani, O. M., Wasylczyk, P. & Priimagi, A. Light-Driven, Caterpillar-Inspired Miniature Inching Robot. *Macromol. Rapid Commun.* **39**, 1–6 (2018).

48. Gelebart, A. H. *et al.* Making waves in a photoactive polymer film. *Nature* **546**, 632–636 (2017).

49. Yuan, Q. *et al.* Photon-manipulated drug release from a mesoporous nanocontainer controlled by azobenzene-modified nucleic acid. *ACS Nano* **6**, 6337–6344 (2012).

50. Schimka, S. *et al.* Photosensitive microgels containing azobenzene surfactants of different charges. *Phys. Chem. Chem. Phys.* **19**, 108–117 (2017).

51. Yadav, S., Deka, S. R., Verma, G., Sharma, A. K. & Kumar, P. Photoresponsive amphiphilic azobenzene-PEG self-assembles to form supramolecular nanostructures for drug delivery applications. *RSC Adv.* **6**, 8103–8117 (2016).

52. Oscurato, S. L., Borbone, F., Maddalena, P. & Ambrosio, A. Light-Driven Wettability Tailoring of Azopolymer Surfaces with Reconfigured Three-Dimensional Posts. *ACS Appl. Mater. Interfaces* **9**, 30133–30142 (2017).

53. Zhao, Y., Lu, Q., Li, M. & Li, X. Anisotropic wetting characteristics on submicrometer-scale periodic grooved surface. *Langmuir* **23**, 6212–6217 (2007).

54. Choi, J. *et al.* Flexible and Robust Superomniphobic Surfaces Created by Localized Photofluidization of Azopolymer Pillars. *ACS Nano* **11**, 7821–7828 (2017).

55. Brüschweiler, B. J. & Merlot, C. Azo dyes in clothing textiles can be cleaved into a series of mutagenic aromatic amines which are not regulated yet. *Regul. Toxicol. Pharmacol.* **88**, 214–226 (2017).

56. Bobrovsky, A. *et al.* Photo-Orientation Phenomena in Photochromic Liquid Crystalline Azobenzene-Containing Polymethacrylates with Different Spacer Length. *Macromol. Chem. Phys.* **218**, 1–10 (2017).

57. Vapaavuori, J., Bazuin, C. G. & Priimagi, A. Supramolecular design principles for efficient photoresponsive polymer-azobenzene complexes. *J. Mater. Chem. C* **6**, 2168–2188 (2018).

58. Natansohn, A., Rochon, P., Gosselin, J. & Xie, S. Azo Polymers for Reversible Optical Storage. 1. Poly[4′-[[2-(acryloyloxy)ethyl]ethylamino]-4-nitroazobenzene]. *Macromolecules* **25**, 2268–2273 (1992).

59. Hagen, R. & Bieringer, T. Photoaddressable polymers for optical data storage. *Adv. Mater.* **13**, 1805–1810 (2001).

60. Kawata, S. & Kawata, Y. Three-Dimensional Optical Data Storage Using Photochromic Materials. *Chem. Rev.* **100**, 1777–1788 (2000).

61. Ishikawa, M. *et al.* Reflection-type confocal readout for multilayered optical memory. *Opt. Lett.* **23**, 1781 (1998).

62. Zhao, Y. & Ikeda, T. *Smart Light-Reponsive Materials: Azobenzene-Containing Polymers and Liquid Crystals*. (John Wiley & Sons., 2009).

63. Rochon, P., Batalla, E. & Natansohn, A. Optically induced surface gratings on azoaromatic polymer films. *Appl. Phys. Lett.* **136**, 136 (1995).

64. Barrett, C. J., Natansohn, A. L. & Rochon, P. L. Mechanism of optically inscribed high-efficiency diffraction gratings in azo polymer films. *J. Phys. Chem.* **100**, 8836–8842 (1996).

65. Bian, S. *et al.* Single laser beam-induced surface deformation on azobenzene polymer films. *Appl. Phys. Lett.* **73**, 1817–1819 (1998).

66. Vapaavuori, J., Ras, R. H. A., Kaivola, M., Bazuin, C. G. & Priimagi, A. From partial to complete optical erasure of azobenzene-polymer gratings: Effect of molecular weight. *J. Mater. Chem. C* **3**, 11011–11016 (2015).

67. Tofini, A., Levesque, L., Lebel, O. & Sabat, R. G. Erasure of surface relief gratings in azobenzene molecular glasses by localized heating using a CO2 laser. *J. Mater. Chem. C* **6**, 1083–1091 (2018).

68. Fedele, C., Netti, P. A. & Cavalli, S. Azobenzene-based polymers: Emerging applications as cell culture platforms. *Biomater. Sci.* **6**, 990–995 (2018).

69. Rianna, C. *et al.* Spatio-Temporal Control of Dynamic Topographic Patterns on Azopolymers for Cell Culture Applications. *Adv. Funct. Mater.* **26**, 7572–7580 (2016).

70. Rocha, L. *et al.* Azobenzene based polymers as photoactive supports and micellar structures for applications in biology. *J. Photochem. Photobiol. A Chem.* **291**, 16–25 (2014).

71. Barillé, R., Janik, R., Kucharski, S., Eyer, J. & Letournel, F. Photo-responsive polymer with erasable and reconfigurable micro- and nano-patterns: An in vitro study for neuron guidance. *Colloids Surfaces B Biointerfaces* **88**, 63–71 (2011).

72. Tripathy, S. K., Viswanathan, N. K., Balasubramanian, S. & Kumar, J. Holographic fabrication of polarization selective diffractive optical elements on azopolymer film. *Polym. Adv. Technol.* **11**, 570–574 (2000).

73. Paterson, J., Natansohn, A., Rochon, P., Callender, C. L. & Robitaille, L. Optically inscribed surface relief diffraction gratings on azobenzene-containing polymers for coupling light into slab waveguides. *Appl. Phys. Lett.* **69**, 3318–3320 (1996).

74. Berdin, A., Rekola, H., Sakhno, O., Wegener, M. & Priimagi, A. Continuously tunable polymer membrane laser. *Opt. Express* **27**, 25634 (2019).

75. Goldenberg, L. M., Lisinetskii, V., Gritsai, Y., Stumpe, J. & Schrader, S. Second order DFB lasing using reusable grating inscribed in azobenzene-containing material. *Opt. Mater. Express* **2**, 11 (2012).

76. Goldenberg, L. M., Lisinetskii, V., Gritsai, Y., Stumpe, J. & Schrader, S. Single step optical fabrication of a DFB laser device in fluorescent azobenzene-containing materials. *Adv. Mater.* **24**, 3339–3343 (2012).

77. Ubukata, T., Isoshima, T. & Hara, M. Wavelength-programmable organic distributed-feedback laser based on a photoassisted polymer-migration system. *Adv. Mater.* **17**, 1630–1633 (2005).

78. Na, S. I. *et al.* Surface relief gratings on poly(3-hexylthiophene) and fullerene blends for efficient organic solar cells. *Appl. Phys. Lett.* **91**, 1–4 (2007).

79. Schedl, A. E. *et al.* Confinement templates for hierarchical nanoparticle alignment prepared by azobenzene-based surface relief gratings. *Soft Matter* **15**, 3872–3878

(2019).

80. Sakhno, O., Goldenberg, L. M., Wegener, M. & Stumpe, J. Deep surface relief grating in azobenzene-containing materials using a low-intensity 532 nm laser. *Opt. Mater. X* **1**, 100006 (2019).

81. Loebner, S. *et al.* Motion of adsorbed nano-particles on azobenzene containing polymer films. *Molecules* **21**, 1–11 (2016).

82. Kim, M. H., Kim, J. D., Fukuda, T. & Matsuda, H. Alignment control of liquid crystals on surface relief gratings. *Liq. Cryst.* **27**, 1633–1640 (2000).

83. Lee, G. J. *et al.* Liquid crystal alignment by holographic surface relief grating inscribed on azo-polymer film. *Mol. Cryst. Liq. Cryst.* **424**, 75–83 (2004).

84. Chung, D. H. *et al.* Competitive effects of grooves and photoalignment on nematic liquid-crystal alignment using azobenzene polymer. *J. Appl. Phys.* **92**, 1841–1844 (2002).

85. Lomadze, N., Kopyshev, A., Bargheer, M., Wollgarten, M. & Santer, S. Mass production of polymer nano-wires filled with metal nano-particles. *Sci. Rep.* **7**, 1–10 (2017).

86. Lagugné Labarthet, F., Buffeteau, T. & Sourisseau, C. Time dependent analysis of the formation of a half-period surface relief grating on amorphous azopolymer films. *J. Appl. Phys.* **90**, 3149–3158 (2001).

87. Yadavalli, N. S., Saphiannikova, M., Lomadze, N., Goldenberg, L. M. & Santer, S. Structuring of photosensitive material below diffraction limit using far field irradiation. *Appl. Phys. A Mater. Sci. Process.* **113**, 263–272 (2013).

88. Bublitz, D., Fleck, B. & Wenke, L. A model for surface-relief formation in azobenzene polymers. *Appl. Phys. B Lasers Opt.* **72**, 931–936 (2001).

89. König, T., Yadavalli, N. S. & Santer, S. Near-Field Induced Reversible Structuring of Photosensitive Polymer Films: Gold Versus Silver Nano-antennas. *Plasmonics* **7**, 535–542 (2012).

90. Papke, T., Yadavalli, N. S., Henkel, C. & Santer, S. Mapping a plasmonic hologram with photosensitive polymer films: Standing versus propagating waves. *ACS Appl. Mater. Interfaces* **6**, 14174–14180 (2014).

91. König, T., Yadavalli, N. S. & Santer, S. Surface plasmon nanolithography: Impact of dynamically varying near-field boundary conditions at the air-polymer interface. *J. Mater. Chem.* **22**, 5945–5950 (2012).

92. König, T. & Santer, S. Visualization of surface plasmon interference by imprinting intensity patterns on a photosensitive polymer. *Nanotechnology* **23**, 485304 (2012).

93. Stiller, B., Geue, T., Morawetz, K. & Saphiannikova, M. Optical patterning in azobenzene polymer films. *J. Microsc.* **219**, 109–114 (2005).

94. Barrett, C. J., Natansohn, A. L. & Rochon, P. L. Mechanism and model of laser-driven mass transport in thin films of azo polymers. *Am. Chem. Soc. Polym. Prepr.*

Div. Polym. Chem. **38**, 542–543 (1997).

95. Baldus, O. & Zilker, S. J. Surface relief gratings in photoaddressable polymers generated by cw holography. *Appl. Phys. B Lasers Opt.* **72**, 425–427 (2001).

96. Kumar, J. *et al.* Gradient force: The mechanism for surface relief grating formation in azobenzene functionalized polymers. *Appl. Phys. Lett.* **72**, 2096–2098 (1998).

97. Pedersen, T. G., Johansen, P. M., Holme, N. C. R., Ramanujam, P. S. & Hvilsted, S. Mean-field theory of photoinduced formation of surface reliefs in side-chain azobenzene polymers. *Phys. Rev. Lett.* **80**, 89–92 (1998).

98. Lefin, P., Fiorini, C. & Nunzi, J. M. Anisotropy of the photo-induced translation diffusion of azobenzene dyes in polymer matrices. *Pure Appl. Opt.* **7**, 71–82 (1998).

99. Saphiannikova, M. & Toshchevikov, V. Optical deformations of azobenzene polymers: Orientation approach vs. photofluidization concept. *J. Soc. Inf. Disp.* **23**, 146–153 (2015).

100. Yadavalli, N. S., Linde, F., Kopyshev, A. & Santer, S. Soft matter beats hard matter: Rupturing of thin metallic films induced by mass transport in photosensitive polymer films. *ACS Appl. Mater. Interfaces* **5**, 7743–7747 (2013).

101. Yadavalli, N. S., Korolkov, D., Moulin, J. F., Krutyeva, M. & Santer, S. Probing opto-mechanical stresses within azobenzene-containing photosensitive polymer films by a thin metal film placed above. *ACS Appl. Mater. Interfaces* **6**, 11333–11340 (2014).

102. Florio, G. Di, Bründermann, E., Yadavalli, N. S., Santer, S. & Havenith, M. Graphene multilayer as nanosized optical strain gauge for polymer surface relief gratings. *Nano Lett.* **14**, 5754–5760 (2014).

103. Di Florio, G., Bründermann, E., Yadavalli, N. S., Santer, S. & Havenith, M. Confocal raman microscopy and AFM study of the interface between the photosensitive polymer layer and multilayer graphene. *Soft Mater.* **12**, S98–S105 (2014).

104. Kopyshev, A., Galvin, C. J., Genzer, J., Lomadze, N. & Santer, S. Polymer brushes modified by photosensitive azobenzene containing polyamines. *Polymer* **98**, 421–428 (2016).

105. Kopyshev, A., Lomadze, N., Feldmann, D., Genzer, J. & Santer, S. Making polymer brush photosensitive with azobenzene containing surfactants. *Polymer* **79**, 65–72 (2015).

106. Ilnytskyi, J. M., Toshchevikov, V. & Saphiannikova, M. Modeling of the photo-induced stress in azobenzene polymers by combining theory and computer simulations. *Soft Matter* **15**, 9894–9908 (2019).

107. Yager, K. G. & Barrett, C. J. Confinement of surface patterning in azo-polymer thin films. *J. Chem. Phys.* **126**, 1–8 (2007).

108. Sobolewska, A. & Miniewicz, A. Analysis of the Kinetics of Diffraction Efficiency during the Holographic Grating Recording in Azobenzene Functionalized Polymers.

J. Phys. Chem. B **111**, 1536–1544 (2007).

109. Lagugné Labarthet, F., Rochon, P. & Natansohn, A. Polarization analysis of diffracted orders from a birefringence grating recorded on azobenzene containing polymer. *Appl. Phys. Lett.* **75**, 1377–1379 (1999).

110. Lagugné Labarthet, F., Buffeteau, T. & Sourisseau, C. Azopolymer Holographic Diffraction Gratings: Time Dependent Analyses of the Diffraction Efficiency, Birefringence, and Surface Modulation Induced by Two Linearly Polarized Interfering Beams. *J. Phys. Chem. B* **103**, 6690–6699 (1999).

111. Lefin, P., Fiorini, C. & Nunzi, J. M. Anisotropy of the photoinduced translation diffusion of azo-dyes. *Opt. Mater.* **9**, 323–328 (1998).

112. Naito, T., Horie, K. & Mita, I. Photochemistry in Polymer Solids. 11. The Effects of the Size of Reaction Groups and the Mode of Photoisomerization on Photochromic Reactions in Polycarbonate Film. *Macromolecules* **24**, 2907–2911 (1991).

113. Brown, C. J. A refinement of the crystal structure of azobenzene. *Acta Crystallogr.* **21**, 146–152 (1966).

114. Oscurato, S. L., Salvatore, M., Maddalena, P. & Ambrosio, A. From nanoscopic to macroscopic photo-driven motion in azobenzene-containing materials. *Nanophotonics* **7**, 1387–1422 (2018).

115. Lednev, I. K., Ye, T. Q., Hester, R. E. & Moore, J. N. Femtosecond time-resolved UV-visible absorption spectroscopy of trans-azobenzene in solution. *J. Phys. Chem.* **100**, 13338–13341 (1996).

116. Kobayashi, T., Degenkolb, E. O. & Rentzepls, P. M. Picosecond spectroscopy of 1-phenylazo-2-hydroxynaphthalene. *J. Phys. Chem.* **83**, 2431–2434 (1979).

117. Pavlenko, E. S. *et al.* Azobenzene-functionalized polyelectrolyte nanolayers as ultrafast optoacoustic transducers. *Nanoscale* **8**, 13297–13302 (2016).

118. Nishimura, N. *et al.* Thermal Cis-to-Trans Isomerization of Substituted Azobenzenes II. Substituent ans Solvent Effects. *Bull. Chem. Soc. Jpn.* **49**, 1381–1387 (1975).

119. Brown, E. V. & Granneman, G. R. Cis-Trans Isomerism in the Pyridyl Analogs of Azobenzene. A Kinetic and Molecular Orbital Analysis. *J. Am. Chem. Soc.* **97**, 621–627 (1975).

120. Beharry, A. A., Sadovski, O. & Woolley, G. A. Azobenzene photoswitching without ultraviolet light. *J. Am. Chem. Soc.* **133**, 19684–19687 (2011).

121. Bléger, D., Schwarz, J., Brouwer, A. M. & Hecht, S. O -fluoroazobenzenes as readily synthesized photoswitches offering nearly quantitative two-way isomerization with visible light. *J. Am. Chem. Soc.* **134**, 20597–20600 (2012).

122. Siewertsen, R. *et al.* Highly efficient reversible Z-E photoisomerization of a bridged azobenzene with visible light through resolved S1(nπ*) absorption bands. *J. Am. Chem. Soc.* **131**, 15594–15595 (2009).

123. Oliveira, O. N., Dos Santos, D. S., Balogh, D. T., Zucolotto, V. & Mendonça, C. R. Optical storage and surface-relief gratings in azobenzene-containing nanostructured films. *Adv. Colloid Interface Sci.* **116**, 179–192 (2005).

124. Mart, R. J. & Allemann, R. K. Azobenzene photocontrol of peptides and proteins. *Chem. Commun.* **52**, 12262–12277 (2016).

125. Ikeda, T. & Tsutsumi, O. Optical switching and image storage by means of azobenzene liquid-crystal films. *Science* **268**, 1873–1875 (1995).

126. Xie, S., Natansohn, A. & Rochon, P. Recent Developments in Aromatic Azo Polymers Research. *Chem. Mater.* **5**, 403–411 (1993).

127. Taniguchi, T., Asahi, T. & Koshima, H. Photomechanical azobenzene crystals. *Crystals* **9**, 1–14 (2019).

128. Bobrovsky, A. *et al.* The effect of spacer and alkyl tail lengths on the photoorientation processes in amorphousized films of azobenzene-containing liquid crystalline polymethacrylates. *Liq. Cryst.* **47**, 377–383 (2020).

129. Shibaev, V. P. Liquid-crystalline polymer systems: From the past to the present. *Polym. Sci. - Ser. A* **56**, 727–762 (2014).

130. Birabassov, R. *et al.* Thick dye-doped poly(methyl methacrylate) films for real-time holography. *Appl. Opt.* **37**, 8264 (1998).

131. Barrett, C., Choudhury, B., Natansohn, A. & Rochon, P. Azocarbazole polymethacrylates as single-component electrooptic materials. *Macromolecules* **31**, 4845–4851 (1998).

132. Viswanathan, N. K. *et al.* Surface relief structures on azo polymer films. *J. Mater. Chem.* **9**, 1941–1955 (1999).

133. Han, M. & Ichimura, K. Tilt orientation of p-methoxyazobenzene side chains in liquid crystalline polymer films by irradiation with nonpolarized light. *Macromolecules* **34**, 82–89 (2001).

134. Silva, J. R., Dall'Agnol, F. F., Oliveira, J. N. & Giacometti, J. A. Temperature dependence of photoinduced birefringence in mixed Langmuir-Blodgett (LB) films of azobenzene-containing polymers. *Polymer* **43**, 3753–3757 (2002).

135. Evans, S. D., Johnson, S. R., Ringsdorf, H., Williams, L. M. & Wolf, H. Photoswitching of azobenzene derivatives formed on planar and colloidal gold surfaces. *Langmuir* **14**, 6436–6440 (1998).

136. Yu, Y., Nakano, M. & Ikeda, T. Directed bending of a polymer film by light. *Nature* **425**, 145 (2003).

137. Ichimura, K., Oh, S. K. & Nakagawa, M. Light-driven motion of liquids on a photoresponsive surface. *Science* **288**, 1624–1626 (2000).

138. Toshchevikov, V., Petrova, T. & Saphiannikova, M. Kinetics of light-induced ordering and deformation in LC azobenzene-containing materials. *Soft Matter* **13**, 2823–2835 (2017).

139. Buffeteau, T., Lagugné Labarthet, F., Pézolet, M. & Sourisseau, C. Dynamics of photoinduced orientation of nonpolar azobenzene groups in polymer films. Characterization of the cis isomers by visible and FTIR spectroscopies. *Macromolecules* **34**, 7514–7521 (2001).

140. Buffeteau, T., Lagugné Labarthet, F., Pézolet, M. & Sourisseau, C. Photoinduced orientation of azobenzene chromophores in amorphous polymers as studied by real-time visible and FTIR spectroscopies. *Macromolecules* **31**, 7312–7320 (1998).

141. Priimagi, A. *et al.* Hydrogen-bonded polymer-azobenzene complexes: Enhanced photoinduced birefringence with high temporal stability through interplay of intermolecular interactions. *Chem. Mater.* **20**, 6358–6363 (2008).

142. Medvedev, A. V. *et al.* Phase behavior and photooptical properties of liquid crystalline functionalized copolymers with low-molecular-mass dopants stabilized by hydrogen bonds. *Macromolecules* **38**, 2223–2229 (2005).

143. Natansohn, A. *et al.* Azo Polymers for Reversible Optical Storage. 4. Cooperative Motion of Rigid Groups in Semicrystalline Polymers. *Macromolecules* **27**, 2580–2585 (1994).

144. Holme, N. C. R., Hvilsted, S. & Ramanujam, P. S. 10,000 Optical Write, Read, and Erase Cycles in an Azobenzene Sidechain Liquid-Crystalline Polyester. *Opt. Lett.* **21**, 902 (1996).

145. Nadtoka, O., Syromyatnikov, V. & Tarasenko, V. Photoinduced orientation of azobenzene groups in polymer films. Characterization by UV/visible spectroscopy. *Mol. Cryst. Liq. Cryst.* **536**, 122/[354]-129/[361] (2011).

146. Blanche, P.-A., Lemaire, P. C., Dumont, M. & Fischer, M. Photoinduced orientation of azo dye in various polymer matrices. *Opt. Lett.* **24**, 1349 (1999).

147. Bobrovsky, A. & Shibaev, V. Photo-optical properties and photo-orientation phenomena in an immiscible blend of cholesteric copolymer with azobenzene-containing polymer. *Liq. Cryst.* **34**, 411–419 (2007).

148. Elhani, S. *et al.* Quantitative analyses of optically induced birefringence in azo dye containing polymers. *J. Opt.* **21**, 115401 (2019).

149. Goldenberg, L. M., Kulikovska, O. & Stumpe, J. Thermally stable holographic surface relief gratings and switchable optical anisotropy in films of an azobenzene-containing polyelectrolyte. *Langmuir* **21**, 4794–4796 (2005).

150. Jelken, J. & Santer, S. Light induced reversible structuring of photosensitive polymer films. *RSC Adv.* **9**, 20295–20305 (2019).

151. Tong, F., Chen, Z., Lu, X. & Lu, Q. Thermostable birefringent copolyimide films based on azobenzene-containing pyrimidine diamines. *J. Mater. Chem. C* **5**, 10375–10382 (2017).

152. Oscurato, S. L., Salvatore, M., Borbone, F., Maddalena, P. & Ambrosio, A. Computer-generated holograms for complex surface reliefs on azopolymer films. *Sci. Rep.* **9**, 1–8 (2019).

153. Puliafito, A. *et al.* Driving Cells with Light-Controlled Topographies. *Adv. Sci.* **6**, 1801826 (2019).

154. Ambrosio, A. *et al.* Realization of submicrometer structures by a confocal system on azopolymer films containing photoluminescent chromophores. *J. Appl. Phys.* **107**, 083110 (2010).

155. Makushenko, A. M., Neporent, B. S. & Stolbova, O. V. Reversible orientational photodichroism and photoisomerization of aromatic azo compounds. I: model of the system. *Opt. Spectrosc* **31**, 295–299 (1971).

156. Makushenko, A. M., Neporent, B. S. & Stolbova, O. V. Reversible orientational photodichroism and photoisomerization of complex organic compounds in viscous solutions. *Opt. Spectrosc* **31**, 397–404 (1971).

157. Shvetsov, S. A., Emelyanenko, A. V., Bugakov, M. A., Boiko, N. I. & Zyryanov, V. Y. Photo-orientation of nematic liquid crystal without preliminary cell surface treatment. *Opt. Mater. Express* **9**, 2595 (2019).

158. Eich, M., Reck, B., Ringsdorf, H. & Wendorff, J. H. Reversible Digital And Holographic Optical Storafe In Polymeric Liquid Crystals (PLC). *Mol. Polym. Optoelectron. Mater.* **0682**, 93 (1987).

159. Ho, M. S., Natansohn, A. & Rochon, P. Azo Polymers for Reversible Optical Storage. 7. The Effect of the Size of the Photochromic Groups. *Macromolecules* **28**, 6124–6127 (1995).

160. Natansohn, A., Xie, S. & Rochon, P. Azo Polymers for Reversible Optical Storage. 2. Poly[4′-[[2-(acryloyloxy)ethyl]ethylamino]-2-chloro-4-nitroazobenzene]. *Macromolecules* **25**, 5531–5532 (1992).

161. Fiorini, C. *et al.* Molecular migration mechanism for laser induced surface relief grating formation. *Synth. Met.* **115**, 121–125 (2000).

162. Hattori, T., Shibata, T., Onodera, S. & Kaino, T. Fabrication of refractive index grating into azo-dye-containing polymer films by irreversible photoinduced bleaching. *J. Appl. Phys.* **87**, 3240–3244 (2000).

163. Toshchevikov, V., Ilnytskyi, J. & Saphiannikova, M. Photoisomerization Kinetics and Mechanical Stress in Azobenzene-Containing Materials. *J. Phys. Chem. Lett.* **8**, 1094–1098 (2017).

164. Toshchevikov, V., Saphiannikova, M. & Heinrich, G. Microscopic theory of light-induced deformation in amorphous side-chain azobenzene polymers. *J. Phys. Chem. B* **113**, 5032–5045 (2009).

165. Lagugné Labarthet, F., Buffeteau, T. & Sourisscau, C. Analyses of the diffraction efficiencies, birefringence, and surface relief gratings on azobenzene-containing polymer films. *J. Phys. Chem. B* **102**, 2654–2662 (1998).

166. Geue, T. *et al.* Formation of a buried density grating on thermal erasure of azobenzene polymer surface gratings. *Colloids Surfaces A Physicochem. Eng. Asp.* **198**–**200**, 31–36 (2002).

167. Henneberg, O. *et al.* X-ray and VIS light scattering from light-induced polymer gratings. *Zeitschrift fur Krist.* **219**, 218–223 (2004).

168. Pietsch, U. X-ray and visible light scattering from light-induced polymer gratings. *Phys. Rev. B - Condens. Matter Mater. Phys.* **66**, 1–9 (2002).

169. Yadavalli, N. S. & Santer, S. In-situ atomic force microscopy study of the mechanism of surface relief grating formation in photosensitive polymer films. *J. Appl. Phys.* **113**, 224304 (2013).

170. Yadavalli, N. S., Saphiannikova, M. & Santer, S. Photosensitive response of azobenzene containing films towards pure intensity or polarization interference patterns. *Appl. Phys. Lett.* **105**, 051601 (2014).

171. Lagugné-Labarthet, F., Buffeteau, T. & Sourisseau, C. Optical erasures and unusual surface reliefs of holographic gratings inscribed on thin films of an azobenzene functionalized polymer. *Phys. Chem. Chem. Phys.* **4**, 4020–4029 (2002).

172. Stracke, A., Wendorff, J. H., Goldmann, D., Janietz, D. & Stiller, B. Gain effects in optical storage: Thermal induction of a surface relief grating in a smectic liquid crystal. *Adv. Mater.* **12**, 282–285 (2000).

173. Yadavalli, N. S., König, T. & Santer, S. Selective mass transport of azobenzene-containing photosensitive films towards or away from the light intensity. *J. Soc. Inf. Disp.* **23**, 154–162 (2015).

174. Helgert, M., Wenke, L., Hvilsted, S. & Ramanujam, P. S. Surface relief measurements in side-chain azobenzene polyesters with different substituents. *Appl. Phys. B Lasers Opt.* **72**, 429–433 (2001).

175. Bublitz, D. *et al.* Photoinduced deformation of azobenzene polyester films. *Appl. Phys. B Lasers Opt.* **70**, 863–865 (2000).

176. Holme, N. C. R. *et al.* Optically induced surface relief phenomena in azobenzene polymers. *Appl. Phys. Lett.* **74**, 519–521 (1999).

177. Bian, S. *et al.* Photoinduced surface deformations on azobenzene polymer films. *J. Appl. Phys.* **86**, 4498–4508 (1999).

178. Yadavalli, N. S. *et al.* A comparative study of photoinduced deformation in azobenzene containing polymer films. *Soft Matter* **12**, 2593–2603 (2016).

179. Sekkat, Z. Optical tweezing by photomigration. *Appl. Opt.* **55**, 259 (2016).

180. Ambrosio, A., Marrucci, L., Borbone, F., Roviello, A. & Maddalena, P. Light-induced spiral mass transport in azo-polymer films under vortex-beam illumination. *Nat. Commun.* **3**, 989 (2012).

181. Jelken, J., Henkel, C. & Santer, S. Solving an old puzzle: fine structure of diffraction spots from an azo-polymer surface relief grating. *Appl. Phys. B Lasers Opt.* **125**, 1–11 (2019).

182. Henneberg, O. *et al.* Atomic force microscopy inspection of the early state of formation of polymer surface relief gratings. *Appl. Phys. Lett.* **79**, 2357–2359

(2001).

183. Sekhar Yadavalli, N. Advanes in Experimental Methods to Probe Surface Relief Grating Formation Mechanism in Photosensitive Materials. (University of Potsdam, 2014).

184. Geue, T., Henneberg, O. & Pietsch, U. X-ray reflectivity from sinusoidal surface relief gratings. *Cryst. Res. Technol.* **37**, 770–776 (2002).

185. Lagugné-Labarthet, F., Buffeteau, T. & Sourisseau, C. Inscription of holographic gratings using circularly polarized light: Influence of the optical set-up on the birefringence and surface relief grating properties. *Appl. Phys. B Lasers Opt.* **74**, 129–137 (2002).

186. Kogelnik, H. Coupled Wave Theory for Thick Hologram Gratings. *bell Syst. Tech. J.* **48**, 2909–2947 (1969).

187. Yeh, P. & Gu, C. *Optics of Liquid Crystal Displays*. (New Jersey: Wiley, 2009).

188. Raman, C. V. & Nagendra Nathe, N. S. The diffraction of light by high frequency sound waves: Part I. *Proc. Indian Acad. Sci. - Sect. A* **2**, 406–412 (1935).

189. Moharam, M. G. & Young, L. Criterion for Bragg and Raman-Nath diffraction regimes. *Appl. Opt.* **17**, 1757 (1978).

190. Ono, H., Tamoto, T., Emoto, A. & Kawatsuki, N. Holographic recording in photoreactive monomer/polymer composites. *Japanese J. Appl. Physics, Part 1 Regul. Pap. Short Notes Rev. Pap.* **44**, 1781–1786 (2005).

191. Fabbri, F. *et al.* Kinetics of photoinduced matter transport driven by intensity and polarization in thin films containing azobenzene. *Phys. Rev. B - Condens. Matter Mater. Phys.* **86**, 1–6 (2012).

192. Fabbri, F. *et al.* Evidence of two distinct mechanisms driving photoinduced matter motion in thin films containing azobenzene derivatives. *J. Phys. Chem. B* **115**, 1363–1367 (2011).

193. Garrot, D., Lassailly, Y., Lahlil, K., Boilot, J. P. & Peretti, J. Real-time near-field imaging of photoinduced matter motion in thin solid films containing azobenzene derivatives. *Appl. Phys. Lett.* **94**, 3–6 (2009).

194. Hendrikx, M. *et al.* Re- and Preconfigurable Multistable Visible Light Responsive Surface Topographies. *Small* **14**, 1803274 (2018).

195. Yang, K., Yang, S., Wang, X. & Kumar, J. Enhancing the inscription rate of surface relief gratings with an incoherent assisting light beam. *Appl. Phys. Lett.* **84**, 4517–4519 (2004).

196. Rahmouni, A., Bougdid, Y., Moujdi, S., Nesterenko, D. V. & Sekkat, Z. Photoassisted Holography in Azo Dye Doped Polymer Films. *J. Phys. Chem. B* **120**, 11317–11322 (2016).

197. Reinke, N., Draude, A., Fuhrmann, T., Franke, H. & Lessard, R. A. Electric field assisted holographic recording of surface relief gratings in an azo-glass. *Appl. Phys.*

B Lasers Opt. **78**, 205–209 (2004).

198. Zhou, B. *et al.* Theoretical and experimental studies of photomechanical materials [Invited]. *J. Opt. Soc. Am. B* **36**, 1492 (2019).

199. Linde, F., Sekhar Yadavalli, N. & Santer, S. Conductivity behavior of very thin gold films ruptured by mass transport in photosensitive polymer film. *Appl. Phys. Lett.* **103**, 253101 (2013).

200. Yager, K. G. & Barrett, C. J. All-optical patterning of azo polymer films. *Curr. Opin. Solid State Mater. Sci.* **5**, 487–494 (2001).

201. Karageorgiev, P. *et al.* From anisotropic photo-fluidity towards nanomanipulation in the optical near-field. *Nat. Mater.* **4**, 699–703 (2005).

202. Vapaavuori, J. *et al.* Nanoindentation study of light-induced softening of supramolecular and covalently functionalized azo polymers. *J. Mater. Chem. C* **1**, 2806–2810 (2013).

203. Kim, K.-H. & Jeong, Y.-C. Nanoindentation study of optically patterned surface relief grating of azobenzene polymers. *Opt. Express* **24**, 25242 (2016).

204. Hurduc, N. *et al.* Direct observation of athermal photofluidisation in azo-polymer films. *Soft Matter* **10**, 4640–4647 (2014).

205. Baranovskii, S. D. Theoretical description of charge transport in disordered organic semiconductors. *Phys. Status Solidi Basic Res.* **251**, 487–525 (2014).

206. Akamatsu, M. *et al.* Photoinduced viscosity control of lecithin-based reverse wormlike micellar systems using azobenzene derivatives. *RSC Adv.* **8**, 23742–23747 (2018).

207. Irie, M. & Suzuki, T. Photoresponsive polymers. Reversible solution viscosity change of poly(dimethylsiloxane) with azobenzene residues in the main chain. *Die Makromol. Chemie, Rapid Commun.* **8**, 607–610 (1987).

208. Kulikovska, O., Gharagozloo-Hubmann, K., Stumpe, J., Huey, B. D. & Bliznyuk, V. N. Formation of surface relief grating in polymers with pendant azobenzene chromophores as studied by AFM/UFM. *Nanotechnology* **23**, 485309 (2012).

209. Baldus, O., Leopold, A., Hagen, R., Bieringer, T. & Zilker, S. J. Surface relief gratings generated by pulsed holography: A simple way to polymer nanostructures without isomerizing side-chains. *J. Chem. Phys.* **114**, 1344–1349 (2001).

210. Viswanathan, N. K., Balasubramanian, S., Li, L., Tripathy, S. K. & Kumar, J. A Detailed Investigation of the Polarization-Dependent Surface-Relief-Grating Formation Process on Azo Polymer Films. *Japanese J. Appl. Physics, Part 1 Regul. Pap. Short Notes Rev. Pap.* **38**, 5928–5937 (1999).

211. Pagliusi, P. *et al.* Tunable Surface Patterning of Azopolymer by Vectorial Holography: The Role of Photoanisotropies in the Driving Force. *ACS Appl. Mater. Interfaces* **11**, 34471–34477 (2019).

212. Saphiannikova, M., Geue, T. M., Henneberg, O., Morawetz, K. & Pietsch, U. Linear

viscoelastic analysis of formation and relaxation of azobenzene polymer gratings. *J. Chem. Phys.* **120**, 4039–4045 (2004).

213. Pedersen, T. G. & Johansen, P. M. Mean-field theory of photoinduced molecular reorientation in azobenzene liquid crystalline side-chain polymers. *Phys. Rev. Lett.* **79**, 2470–2473 (1997).

214. Frank, T. D. Maier-Saupe model of liquid crystals: Isotropic-nematic phase transitions and second-order statistics studied by Shiino's perturbation theory and strongly nonlinear Smoluchowski equations. *Phys. Rev. E - Stat. Nonlinear, Soft Matter Phys.* **72**, 1–8 (2005).

215. Loebner, S. *et al.* Light-Induced Deformation of Azobenzene-Containing Colloidal Spheres: Calculation and Measurement of Opto-Mechanical Stresses. *J. Phys. Chem. B* **122**, 2001–2009 (2018).

216. Kulikovska, O., Goldenberg, L. M. & Stumpe, J. Supramolecular azobenzene-based materials for optical generation of microstructures. *Chem. Mater.* **19**, 3343–3348 (2007).

217. Moujdi, S. *et al.* Surface relief gratings in azo-polymers revisited. *J. Appl. Phys.* **124**, 213103 (2018).

218. Sobolewska, A., Bartkiewicz, S., Miniewicz, A. & Schab-Balcerzak, E. Polarization dependence of holographic grating recording in azobenzene-functionalized polymers monitored by visible and infrared light. *J. Phys. Chem. B* **114**, 9751–9760 (2010).

219. Ashkin, A. Optical trapping and manipulation of neutral particles using lasers. *Opt. Photonics News Photonics News* **10**, 41 (1999).

220. Feldmann, D. *et al.* Manipulation of small particles at solid liquid interface: Light driven diffusioosmosis. *Sci. Rep.* **6**, 1–10 (2016).

221. Arya, P., Feldmann, D., Kopyshev, A., Lomadze, N. & Santer, S. Light driven guided and self-organized motion of mesoporous colloidal particles. *Soft Matter* **16**, 1148–1155 (2020).

222. Koskela, J. E., Vapaavuori, J., Ras, R. H. A. & Priimagi, A. Light-driven surface patterning of supramolecular polymers with extremely low concentration of photoactive molecules. *ACS Macro Lett.* **3**, 1196–1200 (2014).

223. Naydenova, I. *et al.* Diffraction from polarization holographic gratings with surface relief in side-chain azobenzene polyesters. *J. Opt. Soc. Am. B* **15**, 1257 (1998).

224. Huang, T. & Wagner, K. H. Holographic diffraction in photoanisotropic organic materials. *J. Opt. Soc. Am. A* **10**, 306 (1993).

225. J. Roa, J., Oncins, G., Diaz, J., Sanz, F. & Segarra, M. Calculation of Young's Modulus Value by Means of AFM. *Recent Pat. Nanotechnol.* **5**, 27–36 (2011).

226. Lin, D. C., Dimitriadis, E. K. & Horkay, F. Robust strategies for automated AFM force curve analysis - II: Adhesion-influenced indentation of soft, elastic materials. *J. Biomech. Eng.* **129**, 904–912 (2007).

227. Lin, D. C. & Horkay, F. Nanomechanics of polymer gels and biological tissues: A critical review of analytical approaches in the Hertzian regime and beyond. *Soft Matter* **4**, 669–682 (2008).

228. Ebenstein, D. M. Nano-JKR force curve method overcomes challenges of surface detection and adhesion for nanoindentation of a compliant polymer in air and water. *J. Mater. Res.* **26**, 1026–1035 (2011).

229. Krotil, H. *et al.* Pulsed force mode: a new method for the investigation of surface properties. *Surf. Interface Anal.* **27**, 336–340 (1999).

230. Bumbu, G. G., Wolkenhauer, M., Kircher, G., Gutmann, J. S. & Berger, R. Micromechanical cantilever technique: A tool for investigating the swelling of polymer brushes. *Langmuir* **23**, 2203–2207 (2007).

231. Brenner, A. & Senderoff, S. Calculation of stress in electrodeposits from the curvature of a plated strip. *J. Res. Natl. Bur. Stand. (1934).* **42**, 105 (1949).

List of Publications authored by J. Jelken

Publications composing this work

I. J. Jelken, C. Henkel and S. Santer; Solving an old Puzzle: Fine Structure of Diffraction Spots from an Azo-Polymer Surface Relief Grating, *Applied Physics B*, **125** (2019), 218

II. J. Jelken, C. Henkel and S. Santer; Polarization Controlled Fine Structure of Diffraction Spots from an Optically Induced Grating, *Applied Physics Letters*, **116** (2020), 051601, selected as **Editor's pick**

III. J. Jelken and S. Santer; Light Induced Reversible Structuring of Photosensitive Polymer Films, *RSC Advances*, **9** (2019), 20295

IV. J. Jelken, M. Brinkjans, C. Henkel and S. Santer; Rapid Optical Erasure of Surface Relief and Bulk Birefringence Gratings in Azo-Polymer Thin Films, *SPIE Proceedings*, **11367** (2020), 1136710

V. J. Jelken, C. Henkel and S. Santer; Formation of Half-Period Surface Relief Gratings in Azobenzene Containing Polymer Films, *Applied Physics B*, **126** (2020), 149

Other publications

VI. P. Arya, J. Jelken, D. Feldmann, N. Lomadze and S. Santer; Light Driven Diffusioosmotic Repulsion and Attraction of Colloidal Particles, in print *Journal of Chemical Physics* (2020)

VII. P. Arya, J. Jelken, N. Lomadze, S. Santer and M. Bekir; Kinetics of Photo-Isomerization of Azobenzene containing Surfactants, *Journal of Chemical Physics*, **152** (2020), 024904

VIII. J. Jelken, C.K. Pandiyarajan, J. Genzer, N. Lomadze and S. Santer; Fabrication of Flexible Hydrogel Sheets Featuring Periodically Spaced Circular Holes with Continuously Adjustable Size in Real Time, *ACS Applied Materials and Interfaces*, **10** (2018), 30844–30851

IX. S. Loebner, J. Jelken, N. S. Yadavalli, E. Sava, N. Hurduc and S. Santer; Motion of Adsorbed Nano-Particles on Azobenzene Containing Polymer Films, *Molecules*, **21** (2016), 1663

Talks

April 2020

Presentation at SPIE Photonics Europe Digital Forum 2020

Title: "Rapid Optical Erasure of Surface Relief and Bulk Birefringence Gratings in Azo-Polymer Thin Films"

September 2019

Talk at "Polydays 2019" conference in Berlin, Germany

Title: "Reversible Surface Structuring of Photosensitive Polymer Films: *In situ* Atomic Force Microscopy and Diffraction Efficiency Measurements"

June 2019

Invited talk at "PIERS 2019" conference in Rome, Italy

Title: "Reversible Surface Structuring of Photosensitive Polymer Films: *In situ* Atomic Force Microscopy and Diffraction Efficiency Measurements"

April 2019

Talk at the "DPG-Spring Meeting 2019" in Regensburg, Germany

Title: "Reversible Surface Structuring of Photosensitive Polymer Films: *In situ* Atomic Force Microscopy and Diffraction Efficiency Measurements"

September 2017

Talk at the Helmholtz-Zentrum Geesthacht "MacroBio Summer School 2017", Potsdam, Germany

Title: "Biocompatible Membranes with Reversible Tunable Pore Size"

March 2017

Talk at the "DPG-Spring Meeting 2017" in Dresden, Germany

Title: "Near-Field Induced Structuring of Photosensitive Polymer Films: SNOM and AFM Measurements"

October 2016	Talk at the "Science and Progress 2016" conference in St. Petersburg, Russia Title: "Near-Field Induced Structuring of Photosensitive Polymer Films: SNOM and AFM Measurements"

Poster

September 2019	Poster presentation at "Polydays 2019" conference in Berlin, Germany Title: "Reversible Surface Structuring of Photosensitive Polymer Films: *In situ* Atomic Force Microscopy and Diffraction Efficiency Measurements"
June 2018	Poster presentation at "PhoSM" conference in Tampere, Finland Title: "*In situ* Atomic Force Microscopy and Diffraction Efficiency Study of the Mechanism of Surface Relief Grating Formation in Photosensitive Polymer Films"
October 2016	Poster presentation at the "Science and Progress 2016" conference in St. Petersburg, Russia Title: "Near-Field Induced Structuring of Photosensitive Polymer Films: SNOM and AFM Measurements"
September 2016	Poster presentation at the "Polydays 2016" conference, Potsdam, Germany Title: "Near-Field Induced Structuring of Photosensitive Polymer Films: SNOM and AFM Measurements"

Research Stay

December 2019	One week visit of the Group of Prof. Arri Priimägi (Tampere University, Tampere, Finland) and Prof. Jaana Vapaavuori (Aalto University, Helsinki, Finland)
May 2019	One month visit of the Group of Prof. Valery P. Shibaev and Prof. Alexey Bobrovsky at the Moscow State University, Moscow, Russia
June 2017	One month visit of the Group of Prof. Irina Zvereva at the Saint Petersburg State University, St. Petersburg, Russia
April 2017	Two weeks visit of the Group of Prof. Jan Genzer at the North Carolina State University, Raleigh, North Carolina, United States

Acknowledgements

My first and foremost gratitude goes to Prof. Dr. Svetlana Santer for her supervision. I'm also thankful to her for giving me the opportunity to excel my knowledge and skills by implementing my own ideas in this work.

In addition, I want to thank my mentor Prof. Dr. Carsten Henkel for valuable and fruitful discussions. A major part of this work would not exist without his help. He was all the time accessible and interested in my results. We had very inspiring discussions, which motivated me to go on and to try out new experiments. I really learned a lot from him. Thank you for that!

Next I would like to thank Dr. Marina Grenzer (Saphiannikova) and Prof. Dr. Arri Priimägi for reviewing this thesis.

Furthermore, I would like to thank Burkhard Stiller and Andreas Pucher, who were not only supporting me during my PhD thesis, also during my Diploma thesis they were a big help. Without their support I would not have been able to finish my thesis. They motivated me to do my best in saying that the science which I'm doing is nothing new and was already done 20 years back. Whenever I had a problem, they were willing to help, but they invited me only three times to their coffee meeting. I will never forget the support they gave and the discussions we had! Finally, after I have submitted my thesis, Burkhard is allowed to cut my hair, which he was asking for all the time.

Dr. Nino Lomadze and Dr. Alexey Kopyshev were helping me whenever I had a problem in the lab. I appreciate that!

Dr. David Feldmann, Dr. Selina Schimka and Maren Umlandt were the best colleagues you can think of and I really enjoyed the time with you guys!

I also want to thank my bachelor students Marius Brinkjans and Victor Krüger, they did an excellent job.

Not least my gratitude goes to all other members of the Experimental Physics group, especially to Dr. Jürgen Reiche, who was proofreading this thesis.

A special thanks is dedicated to the Ü60 group (Andreas Horka, Dagmar Stabenow and Elke Derlig). We had a lot of fun and it was nice to talk with you guys about topics beside work. They helped me a lot with the administration or whenever something was missing in the lab. In addition, my work related wife (Elke) helped me a lot in saving taxes.

I want to thank my diploma thesis supervisor Prof. Dr. Dieter Neher that I could use the lab equipment of the PwM group and for gifting the old group dishwasher to me. It was saving a lot of time of cleaning dishes which I could spent in the lab.

Dr. Frank Jaiser found a solution for every problem which I had, also during my diploma thesis. Thank you for that.

Without the brilliant work of Florian Dornack in the workshop a big part of my thesis would not exist. He was not only preparing the encapsulation of the *in situ* set-up, he was also a very big help in setting up the new optical microscope or whenever something was prepared/ designed in order to perform a specialized experiment.

I also want to thank Dr. Stefan Schmölzer (Netzsch company) for the *in situ* DSC measurement.

Very big thanks also goes to the university devils (Sohini, Manu, Vittoria, Vasu, Sam, Sarah, Amin, Yousuf, Meysam, Krishna) who became very good friends and made me realize that there is also a life existing beside work. I relay enjoyed the time and will never forget the fun we had. Thank you for that! Kilian was here!

In addition, a very special thanks goes to my colleague Pooja Arya in whom I found a friend for the rest of my life. I'm blessed that I found my best friend in my own group. It was a very intensive time we spent together but we were able to maintain the friendship also during the time of the PhD thesis. She was listening to me whenever I needed her help and I will never forget the time we spent and the fun we had. Now, we only have to fulfill the several contracts we made (including the business plan) and I have to perform a dance during her wedding.

The last thanks goes to my parents and sister, they were supporting me during my whole life and especially in the difficult time of the PhD thesis.

Declaration

I hereby certify that the work presented in this thesis has not been submitted to any other university or higher education institute and that this work is my own and that all sources and aids used are listed within. Any results not of my own creation are clearly indicated as such.

Place, Date	Joachim Jelken